

GROWTH OF INDIUM NITRIDE AND GALLIUM NITRIDE ON SILICON USING METAL
ORGANIC HYDRIDE VAPOR PHASE EPITAXY

By

VAIBHAV UDAY CHAUDHARI

A DISSERTATION PRESENTED TO THE GRADUATE SCHOOL
OF THE UNIVERSITY OF FLORIDA IN PARTIAL FULFILLMENT
OF THE REQUIREMENTS FOR THE DEGREE OF
DOCTOR OF PHILOSOPHY

UNIVERSITY OF FLORIDA

2012

© 2012 Vaibhav Uday Chaudhari

To Aai and Baba

ACKNOWLEDGMENTS

I am very fortunate that I got to work with Dr. Timothy J Anderson. He always gives students lot of independence to work and encourages everyone to define their own research problem. Though it was tough initially, I think it is only through his guidance, encouragement as well as patience and trust in me, I have been able to become any good researcher that I am today. I will be eternally thankful to Dr. Anderson for being my Guru.

I am also thankful to all my current committee members, Dr. Fan Ren, Dr Kirk Ziegler, Dr Mark Davidson. I am especially thankful to Dr. Kirk Ziegler that he accepted to be on my committee on such a short notice. I am also thankful to Dr. Olga Kryliouk for introducing and guiding me in the research initially.

I am thankful to Dr. Josh Mangum and Dr. Joseph Park for all the help they have provided. My research could not have taken direction without enormous amount of background work they have provided. I got to work with people of diverse background and culture in Dr. Anderson's Electronic Materials Processing Group (EMPG). I would like to thank all the people in EMPG for help and support they have provided.

My work would not have been possible without the support I received from all working at Microfabritech as well as Chemical Engineering. I would like to thank all of them especially to Maggie, Chuck, Ludie, Shirley, Debbie, Carolyn, Dennis and Jim.

In the end, I would like to thank my parents for their unconditional love, support and sacrifice. My father has always been my inspiration and my mother has always been my motivation. I am also thankful to my wife Milan and brother Gaurav for their support and making my time here at Gainesville more memorable.

TABLE OF CONTENTS

	<u>page</u>
ACKNOWLEDGMENTS.....	4
LIST OF TABLES.....	8
LIST OF FIGURES.....	9
ABSTRACT.....	13
CHAPTER	
1 INTRODUCTION	15
Promising GaN and InN Technology	15
Growth Techniques for Nitrides	16
Solution Based Methods and Involved Challenges	17
Heteroepitaxy Methods and Involved Challenges	18
Silicon carbide.....	19
Sapphire.....	19
Silicon	21
a Role of Silicon nitridation.....	21
b Epitaxial lateral overgrowth (ELO)	24
c Nanoheteroepitaxy (NHE)	25
d Use of buffer layers.....	27
Overview of Present Work	28
2 GROWTH OF VERTICAL INDIUM NITRIDE NANORODS ON SILICON IN MO-HVPE	38
InN Nanostructures in Literature	38
Metal-Organic Hydride Vapor Phase Epitaxy (MO-HVPE).....	39
Reactor Setup	39
MO-HVPE Operation.....	40
Indium Nitride Nanorods (InN _{NR}) Growth in MO-HVPE	42
InN _{NR} Growth Conditions.....	42
Use of Surface Treated Silicon.....	43
Nitride Nucleation Layers on Silicon	44
Results and Discussion.....	46
Effect of Surface Cleaning Treatments.....	47
Effect of Nucleation Layers.....	48
InN _{NR} Properties	52
Growth Mechanism of InN Nanorods	52
Summary and Conclusions	64

3	THEORITICAL MODEL FOR FINDING LIMITS OF COHERENCY FOR INDIUM NITRIDE NANORODS GROWN ON GALLIUM NITRIDE	91
	Overview.....	91
	Crystal Growth Modes.....	91
	Strain vs. Dislocation Model for Heteroepitaxy.....	94
	Formulation of Stress-Strain Relations in Hookian Transversely Isotropic Solids	95
	Formulation of Model for Nanorod Heteroepitaxy	97
	Rigid Substrate Model	97
	Coherent strain energy (E_c).....	99
	Energy of dislocated system (E)	102
	Flexible Substrate Model.....	105
	S-K growth and its effect on coherent diameter.....	113
	Summary and Conclusions	114
4	GROWTH OF GALLIUM NITRIDE ON SILICON IN MO-HVPE.....	132
	GaN Using InN in Litratue.....	132
	Growth of GaN in MO-HVPE Reactor.....	133
	Reactor Setup	134
	MO-HVPE Operation: HVPE mode	134
	MO-HVPE Operation: MOCVD mode.....	135
	Gallium Nitride Growth in MO-HVPE	136
	GaN Growth Conditions.....	136
	GaN Growth Stages	136
	Growth of low temperature GaN capping layer for InN nanorod template	136
	Growth of thick high temperature GaN.....	137
	Results and Discussion.....	137
	Properties of Low Temperature GaN Capping Layer	138
	Crystallinity of LT-GaN capping layer.....	139
	Compositional analysis of InN template capped with LT-GaN	145
	Properties of High Temperature GaN (HT-GaN) layer	149
	Growth conditions for thin and thick HT-GaN.....	149
	Properties of thinner HT-GaN	150
	Properties of thick HT-GaN.....	152
	Summary and Conclusions	152
5	EXPLORATORY STUDY ON GROWTH OF GALLIUM NITRIDE OVER INDIUM TEMPLATED SILICON	179
	Overview.....	179
	Growth Conditions for Different Layers in Growth.....	179
	Deposition of Indium Metal Film	180
	Deposition of GaN in MO-HVPE Reactor	180
	Thin GaN films	180
	Thick GaN films.....	181

Results and Discussion.....	181
Thin GaN films.....	182
Thick GaN films.....	183
Summary and Conclusions.....	185
6 CONCLUSIONS AND RECOMMENDATIONS OF FUTURE WORK.....	199
Conclusions.....	199
Recommendations for Future Work.....	201
Improvements in InN nanorod orientations.....	201
Growth of GaN and $\text{In}_x\text{Ga}_{1-x}\text{N}$ nanostructures in MO-HVPE.....	202
LIST OF REFERENCES.....	203
BIOGRAPHICAL SKETCH.....	214

LIST OF TABLES

<u>Table</u>		<u>page</u>
1-1	Common substrates for InN and GaN epitaxy	31
2-1	Peak ratios corresponding to (101).....	67
2-2	Relative peak intensity ratios for various surface treatments.....	68

LIST OF FIGURES

<u>Figure</u>	<u>page</u>
1-1 HRTEM of GaN grown on Si(111) with 2-3 nm Si ₃ N ₄ as intermediate layer	32
1-2 Epitaxial lateral overgrowth.....	33
1-3 Pendeo epitaxial growth.	34
1-4 Equilibrium phase diagram of Ga-O-N-Si system ⁷³ on Ga rich side	35
1-5 Strain relaxation in Nanoheteroepitaxy.....	36
1-6 GaN grown on nano-porous silicon ⁹⁶	37
2-1 MO-HVPE Reactor. A) Reactor Picture, B) Reactor Schmatic	69
2-2 InN growth map from MO-HVPE.	70
2-3 XRD θ -2 θ scan of InNNR on Si (100) Growth conditions V/III =250, Cl/III=4.0, T= 873K.....	72
2-4 Various InN nanorod orientations. Every nanorod orientation is forms specific angle with the surface.....	73
2-5 XRD θ -2 θ scans for nanorods grown on Si(100) showing effect of surface cleaning	74
2-6 XRD θ -2 θ scans for nanorods grown on Si(100) showing effect of surface cleaning with HCl.....	75
2-7 SEM images (10000x) showing effect of surface cleaning on InNNR.....	76
2-8 XRD θ -2 θ scans for nanorods grown on Si(100) showing effect of surface nitridation.....	77
2-9 SEM images showing effect of nitride layers	78
2-10 The XRD θ -2 θ scans for nanorods grown on Si (100) showing effect of using InN nucleation layer (Sample D) vs MOCVD GaN as nucleation layer (Sample E1).....	79
2-11 The XRD θ -2 θ scans for nanorods grown on HVPE GaN nucleation layer with Si(100) and Si(111) as substrates.....	80
2-12 SEM images of vertical InN nanorods	81
2-13 SEM images of vertical InN nanorods grown on MOCVD and HVPE GaN	82

2-14	Summary of effects of treatments on orientations of InN _{NR}	83
2-15	Pole figure of InNNR grown on HVPE GaN on Si (111) sample in [002] and [101] directions	84
2-16	ω -rocking curve of vertical InN _{NR} sample with Molybdenum X-ray source.....	85
2-17	TEM analysis of nanorods	86
2-18	EDS spectrum InN nanorods grown on HVPE GaN on Si (100).....	87
2-19	Effect of N/In ratio and Substrates on InN morphology at Cl/In=4 and T=873K..	88
2-20	Vertical InN nanorods grown on GaN nucleation layer on Si(100).....	89
3-1	Modes of epitaxial growth	116
3-2	Growth of InN film on GaN film viewed in $\langle 1\bar{1}00 \rangle$ direction.....	117
3-3	Schematic of InN nano structure growth on GaN film (with possible InN film)..	118
3-4	InN nanorod growth on GaN film	119
3-5	Stress field in nanorod.....	120
3-6	Strain Energy vs. nanorod radius	121
3-7	Strain Energy vs. nanorod height	122
3-8	Coherency map for InN nanorod on rigid GaN	123
3-9	Strain Energy vs. nanorod radius for flexible substrate model.....	124
3-10	Interfacial lattice constant vs. nanorod radius for flexible substrate model	125
3-11	Strain Energy vs. nanorod radius (flexible substrate)	126
3-12	Strain Energy vs. nanorod height (H _o) (flexible substrate)	127
3-13	Coherency map for InN nanorod on GaN	128
3-14	Coherency map for InN nanorod on GaN in S-K mode	129
3-15	SEM and COMPO images showing no evidence of films below InN	130
3-16	Relaxed strain in nanorod bulk	131
4-1	Schematic of MO-HVPE for GaN growth	155

4-2	Typical growth scheme for thick HT-GaN growth	156
4-3	SAED pattern for LT-GaN buffer in vertical InNNR template	157
4-4	Different stages of capping layer growth	158
4-5	XRD (θ -2 θ) pattern for vertically oriented InN nanorod capped by LT-GaN for 15 min.....	160
4-6	TEM image of InN-GaN core shell structure.....	161
4-7	HRTEM of GaN spike	162
4-8	GaN as viewed in $\langle 1\bar{2}10 \rangle$ direction represented in different models	163
4-9	GaN shell lattice fringe image.....	164
4-10	SAED patterns of InN – GaN core shell structure shown in Figure 4-6	165
4-11	TEM Image showing InN-GaN core shell structures filled with Indium nitride or Indium metal.....	166
4-12	Point scan and line scan EDS in TEM both showing absence of Indium in shell possibility of Indium liquid in dark regions	167
4-13	TEM and TEM EDS of InN template completely covered in LT-GaN.....	168
4-14	Annealing of LT-GaN/InN _{NR} /Si under ammonia atmosphere for 10 minutes at different temperatures showing decomposition of InN.....	169
4-15	Areas under (0002) GaN and InN peaks and area ratio vs. anneal temperature	170
4-16	Annealed LT-GaN/InN _{NR} /GaN sample.....	171
4-17	SEM EDS of annealed LT-GaN/InN _{NR} /GaN sample	172
4-18	SIMS depth profile showing In, Ga and Si for annealed LT-GaN/InN _{NR} /GaN sample.....	173
4-19	Cracked HT-GaN layer on Si (2 μ m) thick)	174
4-20	GaN (2 μ m thick) film without cracks	175
4-21	TEM cross sectional image of HT-GaN sample, 700 nm grain is single crystal growing in $\langle 000\bar{2} \rangle$ direction	176
4-22	SIMS depth profile of 1.5 micron thick GaN showing no diffusion of Indium in upper HT-GaN layer	177

4-23	SEM image of 50 μm thick GaN grown on InN template	178
5-1	SEM images of Indium on Silicon (100).....	187
5-2	SEM images of GaN grown at $T=873\text{K}$ for 10 min.....	188
5-3	XRD θ - 2θ scan of GaN grown on In/Si template for 10 min at 973K	190
5-4	SEM images of growth on In/Si at higher temperatures for 10 min.....	191
5-5	XRD θ - 2θ scan of GaN grown on In/Si template for 10 min at 1123K	193
5-6	SEM images of thick MOCVD GaN growth on In/Si at 1123K for 120 min	194
5-7	XRD θ - 2θ scan of GaN wafers grown at 1123K in MOCVD mode	195
5-8	SEM images of $40\mu\text{m}$ thick HVPE GaN growth on LT-GaN/In/Si at 1123K for 240 min.....	197
5-9	XRD θ - 2θ scan of thick GaN grown on LT-GaN/In/Si template at 1123K	198

Abstract of Dissertation Presented to the Graduate School
of the University of Florida in Partial Fulfillment of the
Requirements for the Degree of Doctor of Philosophy

GROWTH OF INDIUM NITRIDE AND GALLIUM NITRIDE ON SILICON USING METAL
ORGANIC HYDRIDE VAPOR PHASE EPITAXY

By

Vaibhav Uday Chaudhari

August 2012

Chair: Timothy J. Anderson
Major: Chemical Engineering

Well aligned catalyst free InN nanorods were grown on Si by metal organic hydride vapor phase epitaxy (MO-HVPE). The effect of different surface treatments and nucleation layers was studied on the orientations of nanorods and it was found out that nanorod orientations were highly dependent on surface conditions, giving signature of epitaxy. MO-HVPE grown low temperature GaN buffer layer was found to be best surface layer for archiving vertical nanorods. Nanorods were found to be defect free single crystals, growing in $\langle 000\bar{2} \rangle$ direction with no specific rotational preference with silicon substrate.

The single crystalline nature of InN nanorods was thought to be because of possible lateral relaxation in nanostructures as they grow. The strain vs dislocation energy model, which used minimization of total energy approach, was used to calculate coherency limits of nanorod. It was found that if substrate is also assumed to be flexible, the coherency limit of InN nanorod can double. The model predicts the coherent diameter of nanorod for which nanorod of any length would be defect free. It also shows

that dislocations will be only confined to stained bottom of the nanostructure which is consistent with the literature and observations.

The developed vertical InN template was used for growth of 50 μ m thick and crack free GaN without cracks on Si. GaN was free standing but polycrystalline. It was also found that the polycrystalline nature is as a result of polycrystalline nature of LT-GaN grown on the InN template. It was also shown that formation of completely enclosed uniformly distributed nanovoids were very essential to grow crack free thick GaN which is highly textured in $\langle 000\bar{2} \rangle$ orientation. The GaN grown was very high quality crystal free of Indium.

GaN growth on Indium metal deposited on Silicon was also studied. Depending on growth mode and conditions GaN 40 μ m thick film and 100nm x 5000nm GaN wafers were successfully grown in same reactor using this metal film template.

CHAPTER 1 INTRODUCTION

Promising GaN and InN Technology

The pseudo binary solid solution $\text{Ga}_x\text{In}_{1-x}\text{N}$ alloys exhibits a direct band gap in the range 3.4 to 0.7 eV. In addition to this, group III nitrides have very good mechanical and thermal stability. As a result, III-Nitrides materials have been extensively studied for various optoelectronic and photovoltaic applications¹⁻¹². The global optoelectronics market is growing rapidly and is projected to reach whopping US\$932 billion by the year 2015¹³. According to Solid State Lighting program, developed by the U. S. Department of Energy, advanced solid-state lighting technologies should be cost-competitive as compared to conventional lighting technologies by 2025. This would be done by developing technologies that create solid state light sources that are much more energy efficient, longer lasting but cheap to scale up. The set goals are to be achieved by targeting a product system efficiency of 50 percent with lighting that closely reproduces the visible portions of the sunlight spectrum¹⁴. These incentives have motivated the recent advancements in the sectors of solid state lighting and laser technologies. Still the continued advances in III – N materials, especially GaN, InN and $\text{Ga}_x\text{In}_{1-x}\text{N}$ alloys, are needed to make nitride technology and applications accessible to all.

The high brightness light emitting diodes (LEDs) made of GaN with $\text{Ga}_x\text{In}_{1-x}\text{N}$ active layer were first demonstrated in 1995-96 by Nakamura¹⁵⁻¹⁷ and Yang¹⁸. This was followed by blue laser diodes. As of now, various researchers have demonstrated use of nitrides for light emitting diodes and laser technology¹⁹⁻²². The recent advancement to green laser diodes 524 nm with 50 mW continuous wave output power using c-plane GaN^{19,20} will pave ways to advanced technology like mini RGB laser projectors. Along

with optoelectronics, III-nitrides also find applications in various other fields. The III-N materials direct bandgap can easily cover entire UV-visible electromagnetic spectrum and are stable at fairly high temperatures. This makes them ideal for photovoltaic applications. Various groups have demonstrated use of III-N films and nanostructures for photovoltaic applications theoretically^{23,24} as well as experimentally^{1,2,9-11,25-29}. High mobility, high drift velocities as well as high breakdown voltages make III-nitrides suitable for high power and high speed applications such as field effect transistors (FET)^{5,6,12,30}, high electron mobility transistors (HEMTs)^{3,4,8,31} etc. In addition to this, nanostructures find applications in sensing devices due to high surface area. The transformation of these demonstrated applications in nitride devices to commercial applications depend on ability to grow excellent quality nitride materials on large scale.

There are still various challenges in the growth of excellent quality GaN, InN and $Ga_xIn_{1-x}N$ alloys. The section below discusses the development in GaN and InN growth technology very briefly. The section mainly focuses on major challenges that growth of III-V semiconductors face.

Growth Techniques for Nitrides

The main that growth of nitride materials faces is availability of lattice matched substrates. Due to the lack of native substrates for growth of GaN and $Ga_xIn_{1-x}N$ alloys, heteroepitaxy is primary technique for growing these materials. It is only recently after heteroepitaxial grown seeds of better quality nitride materials have become available.that people have started looking at other approaches such as solution based techniques.

Solution Based Methods and Involved Challenges

Due to very high equilibrium pressures of nitrogen required (in the order of few GPa) bulk crystals of nitrides e.g. GaN are not possible by typical equilibrium methods such as Czochralski or Bridgman methods. Therefore, lower temperature and pressure methods such as ammonothermal synthesis are employed. These methods typically involve reactive solution that dissolves metal and ammonia to form metal nitrides. These nitrides in solution then precipitate out on seed crystals. The reactor operates at lower temperatures of the order of 773K to 873K and an order of magnitude less pressure than equilibrium pressure³²⁻³⁴. The GaN crystals grown by this method are the best quality to date as the crystals grow from solution and do not use any epitaxy on foreign substrates. Although researchers have grown crystals with less defects, the quality of product crystal still depends on seed crystal quality, reactant purities³⁵ etc. The product crystals size is not well controlled due to, firstly, challenges in design for such high pressures and, secondly, less understanding and control over flow and temperature patterns under reaction conditions. Getting rid of metallic impurities and oxygen also remains challenge in this method. As a result of these limitations, high quality GaN grown by this method are orders of magnitude expensive than that grown using other methods. Indium nitride growth has similar challenges as GaN by this method. In addition to requirement of having high equilibrium nitrogen pressure, it has low decomposition temperatures (~ 923K). This makes growth of InN difficult by any melt or high pressure method. Although ammonothermal method operates at lower temperatures than decomposition temperature, no studies have been yet reported on InN ammonothermal growth.

Heteroepitaxy Methods and Involved Challenges

The other way, which is probably more popular and traditional way, to archive InN and GaN crystal growth is deposit material at atmospheric pressure, sub-atmospheric pressures or vacuums. These processes involve little higher temperatures (ranging from approximately 773K to 1473K). The methods in this class are hydride vapor phase epitaxy (HVPE), metal-organic chemical vapor deposition (MOCVD), molecular beam epitaxy (MBE), reactive sputtering, atomic layer deposition (ALD) etc to name a few. Every method mentioned has its advantages and disadvantages. The common challenge that all these methods face is perhaps unavailability of native substrate. In addition to this, heteroepitaxy of InN becomes complicated owing to the low ammonia cracking efficiency at typical growth temperatures of 773 – 923K. The absence of lattice matched substrate remains to be the most critical issue for heteroepitaxy of nitrides. For any heteroepitaxy, finding compliant substrate is important for reducing defects like threading and screw dislocations. Lattice mismatch as well as thermal expansion coefficient mismatch between substrate and epilayer results in straining of epilayer. As epilayer grows in thickness, stress and strain in the epilayer are stored in the form of strain energy. This strain can be easily relieved partially or completely by formation of dislocations, thus minimizing total energy of the system. As a result, dislocations are naturally induced in epilayer in heteroepitaxy. The strained semiconductor's electrical behavior is different and it is more prone to developing cracks as well. This is undesirable for making devices. Thus, reducing strain, by finding compliant substrate or any other means such as buffer layers, developed in epilayer of GaN during heteroepitaxy is very essential.

The most common substrates, being used for growth in literature as well as commercially, are sapphire and silicon carbide. Table 1-1 summarizes some main substrates that are being used with their lattice mismatches with GaN and InN.

Silicon carbide

Silicon carbide has a lattice mismatch of 3.3% with GaN and it also has hexagonal structure like wurtzite GaN. It is available in various polytypes, but Si terminated SiC is the most preferred one. In Si terminated polytype, there are alternate hexagonal closed packed planes of Si and carbon with surface terminated with Silicon. It has been observed that GaN surface termination can be changed depending on the polytype of SiC used^{36,37}. The GaN film is Nitrogen and Gallium terminated respectively for Si terminated and C terminated silicon carbide substrate. The SiC substrates have high thermal and electrical conductivity, the properties that are preferred in electronic applications. Although all these properties make it a suitable substrate for GaN growth, SiC substrate has some limitations. Main limitation is high cost, with more than 3000\$ per 4 inch wafer³⁸. SiC substrate is hard to etch which limits its applicability in electronic devices. Also, gallium wetting properties of SiC are poor, which results in high defect density in GaN film. So, often a buffer layer such as AlN has to be used³⁹⁻⁴². This completely defeats the purpose of using SiC for its low lattice mismatch as AlN depositions add one more step in GaN deposition.

Sapphire

Sapphire has a larger lattice mismatch (~16%) with GaN and even higher (~28.6%) with InN that result in a high density of dislocations of the order of 10^{10} cm^{-2} . Although sapphire (0001) has a larger lattice mismatch with GaN, it is the most popular substrate. In 1983, Yoshida *et al*⁴³ first showed that use of a thin layer of AlN on a sapphire substrate

could improve quality of GaN grown on it greatly. This was confirmed by many other studies that followed⁴⁴⁻⁴⁷. This improvement in growth is attributed to two effects of AlN buffer layer. Firstly, reduction in microscopic fluctuations in crystallite orientation due to AlN layer reduces strain between GaN and sapphire⁴⁵. That is both AlN and GaN being wurtzite structurally results in effective reduction of the strain between GaN and Al₂O₃ surfaces. Secondly, greatly reduced lattice mismatch between AlN and GaN (~2.4%) reduces surface energy at AlN-GaN interface which promotes lateral growth of GaN. The same is true for InN growth, but reduction in mismatch to approximately 13.7 % is not as good as that in case of GaN. Thus, growth of InN film on sapphire remains more challenging. In spite of this challenge, and although very uncommon, use of InN film as a buffer layer for GaN on sapphire have been reported by two authors^{48,49} over span of more than a decade. Researchers have found that InN can be used as buffer layer to grow GaN on top because of soft nature of InN as well as low decomposition temperatures. Furthermore InN has same crystal structure as GaN. The relaxation of residual strain, developed during high temperature GaN growth, due to soft nature and decomposition of InN, resulted in better GaN growth. In addition to buffer layers like AlN, InN, various buffer layers like Al_xIn_{1-x}N, ZnO, BN, low temperature GaN have been reported by numerous authors. Sapphire substrates, although being popular, face various problems as well. Sapphire has very low thermal conductivity (5.43W/mK) as compared to GaN (130W/mK). As a result sapphire is very bad heat sink for high power devices made from GaN. This is problematic for device operation as well as device lifetimes. Low electrical conductivity of sapphire forces device contacts to be made on top or device side itself. This results in loss of important device area and complicates

device architecture. Also, thermal expansion coefficient of sapphire is more than that of GaN. This makes growth on large diameter substrates i.e. larger than 2 inch problematic due to cracking and bowing of GaN.

Silicon

It has been observed that every decade cost per lumen falls by factor of 10 whereas amount of light generated per LED package increases 20 times¹⁴. This progress of solid state lighting technology, calls for growth of better quality materials on cheaper substrates. The silicon substrate has unique advantage of availability in large sizes, high quality and lower cost. In this article, various approaches for using silicon as substrate for nitrides are discussed. The lattice mismatch between silicon and gallium nitride is very large (17%) and thermal expansion coefficient is also very high (33%). As a result, the GaN layer grown on silicon is constantly under tensile stress, which results in various defects such as high density of dislocations, unintentional n-type doping⁵⁰ as a result of silicon diffusion as well as cracks in GaN films. From the Table 1-1, silicon seems to be best substrate for InN with 7.9% lattice mismatch. But, with GaN mismatch with Si is very large (more than double that of InN). To add to this issue, silicon has diamond cubic crystal structure that does not match with GaN (more so for Si (1 0 0) than Si (1 1 1)). The Indium nitride, on the other hand, is more lattice matched substrate for GaN as compared to Silicon.

a Role of Silicon nitridation

Similar to nitridation of sapphire, nitridation of silicon has been shown to reduce the density of defects such as dislocations in overgrown GaN by few researchers. Nitridation of silicon produces ultra-thin film (2-3 nm Figure 1-1) of silicon nitride⁵⁰ or silicon oxynitride depending on conditions and temperatures used. The effect of silicon

nitride layer depends on the thickness of this Si_xN_y layer. It has been observed that thickness of this layer determines the quality of Si_xN_y layer. As thickness increases, the Si_xN_y layer tends to become amorphous and GaN grown on it tends to be polycrystalline i.e. a mixture of cubic and hexagonal GaN⁵⁰⁻⁵³. Such GaN also shows multiple in-plane alignments with respect to underlying Si. The wurtzite GaN over layer on Si generally shows up as two in-plane domains rotated by 30° ^{54,55} in XRD pole figures. The formation of Si_xN_y layer can be avoided altogether by introducing aluminum flux for small interval initially. Since thermodynamically Al-N bonds formation is highly favored over Si-N bond formation, introduction of Al results in very thin interlayer of AlN instead of Si_xN_y ⁵⁰⁻⁵². In the same effect, AlN buffer layer similar to that in case of sapphire can be used to grow good quality of GaN on Si^{54,56-68}. The AlN layer has lower lattice mismatch, similar structure and GaN is known to wet AlN completely⁶⁹. The AlN buffer layer also brings overgrown GaN under compressive stress rather than tensile stress, the stress that is thought to produce cracks in material. As a result, GaN grown using AlN buffer layer with lesser defects (reduction from 10^{10} to 10^8 cm^{-2}) and crack free thickness exceeding 1 micron have been shown to be grown on silicon substrate as well.

It has been shown that, the formation of Si_xN_y layer is not always detrimental for GaN overgrowth. Ultra-thin Si_xN_y layer has been used to grow high quality GaN by various researchers^{25,70-75}. Recent studies⁷⁵ show that use of high temperature Si_xN_y layer grown at 1173K produced better quality GaN films than that without nitridation or with low temperature nitridation. Most of the researchers, however, agree that thick Si_xN_y layer can detrimental to overgrown GaN quality. Thick Si_xN_y layer formation can

be avoided by initial nitridation at lower temperature. Contrary to thick layers, thin layer tends to maintain some epitaxial relationship with silicon. For example, β - Si_xN_y , which forms at lower temperatures, has hexagonal symmetry⁷⁶. This symmetry is similar to basal plane of wurtzite GaN with 16% lattice mismatch. Although lattice mismatch is high, GaN is able to maintain the epitaxial relationship due to its similar crystal structure. As a result GaN grown on nitridated silicon tends to be wurtzite as compared to mixed cubic wurtzite GaN grown on bare silicon⁷⁵. In addition to that ultra-thin Si_xN_y layer can act as barrier for Si diffusion into GaN avoiding unintentional n-type doping of GaN by Si. As a result of this, GaN grown has high structural quality as well as it is free from shallow or deep level traps. This is evident from the observations that GaN grown using Si_xN_y layer showed sharp XRD as well as PL peaks and PL was free of yellow shift or yellow sub-peak^{70,75}. This technique generally involves growth of ultra-thin Si_xN_y layer at temperatures lower than 850K followed by growth of low temperature GaN buffer layer⁷³. Thermodynamic analysis of Ga-O-N-Si system was done to understand equilibrium chemistry at GaN – Si interface. Oxygen was introduced in trace amount as quartz reactor tube and small impurity in all chemicals entering the reactor can act as source of oxygen. It was found that only temperatures above the 850K, amorphous Si_3N_4 is thermodynamically favorable to form (Figure1-2). So at lower temperature, Si surface can be partially covered with oxygen and partially covered in nitrogen. This oxinitride layer is thought to maintain epitaxial relationship with Si as well as GaN overlayer grown at low temperature. Another view on this process is that low temperature GaN buffer acts exactly similar to AlN layer. The GaN does not allow Si-N

bonds to form because GaN formation is favored over Si_3N_4 formation at lower temperatures according to equilibrium phase diagram in figure 4.

b Epitaxial lateral overgrowth (ELO)

Researchers have developed more complex methods such as pendeo-epitaxy to grow better quality GaN on silicon⁷⁷⁻⁸³. This technique is similar to epitaxial lateral overgrowth (ELO) methods⁸⁴⁻⁸⁶. The ELO methods generally involve growth in two to three steps. First low temperature and low quality GaN is grown on substrate. It is then covered with patterned oxide mask such as SiO_2 . Then high temperature GaN seed columns grow only through small holes that expose GaN below the mask and no seed growth takes place on SiO_2 mask itself. As growth continues, GaN from each seed column starts growing laterally to form high quality GaN. The pendeo-epitaxy method involves even more steps to grow GaN on Silicon. For growth on Si, silicon is carbonized to form thin SiC layer which has very small lattice mismatch with GaN. Since GaN does not wet SiC well, it is covered with thin layer of AlN. The GaN thin layer is then grown on the AlN which can be done at higher temperature to get better quality GaN. Then in the next step, the GaN is covered with Si_xN_y layer and patterned to expose $(11\bar{2}0)$ faces of GaN. The high temperature GaN grows from these seeds laterally. The GaN growing from pendeo seeds coalesce and grow to get very high quality GaN. The ELO and pendeo approaches are represented in cartoon in Figure 1-3 and Figure 1-4 respectively. With this method, it is possible to grow both thick and thin GaN films on silicon substrate with dislocation density as low as $10^5 - 10^6 \text{ cm}^{-2}$ ⁸³.

c Nanoheteroepitaxy (NHE)

Parallel to the idea of patterned substrates, nanostructures such as nanorods, nanowires or nano-patterned substrates can also be used as templates for growing GaN on silicon. The stress distribution in heated bimetal thermostat was found shown depend on the width of the thermostat⁸⁷. This idea was further applied to stresses developed in heteroepitaxy of materials with large lattice mismatch such as $\text{Si}_x\text{Ge}_{1-x}/\text{Si}$ system⁸⁸. Contrary to the plane 2D substrate as shown in Figure 1-5(A), if nanostructures such as seed pads, nanorods etc are used, the effective strained contact area in heteroepitaxy can be reduced to the area seed pads. Due to 3D nature of these seed pads or nanostructures, strain developed at heteroepitaxial interface can be confined to small thickness in the overgrown film. This is as a result of possible exponential lateral as well as vertical relaxation of strain in nanostructures over the characteristic length which is proportional to smallest dimension of nanostructure or seed pad Figure 1-5(B). Due to this relaxation process, theoretically strain energy can be kept below the energy required to form dislocations^{88,89}. As results, there is reduction in dislocations in grown GaN. This process is termed as nanoheteroepitaxy (NHE). The theory of nanoheteroepitaxy and its application to the growth of system with high lattice mismatch such as GaAs/Si and GaN/Si is developed in series of publications by Zubia and Hersee⁸⁹⁻⁹².

In comparison to the direct 2D growth such as growth of GaN film on thick or ultrathin silicon substrate, use of patterned Si with nano-stripes is more effective in reducing the defects in overgrown material. This later approach is based on the principles developed earlier by Luryi and Suhir⁸⁸. Due to the nano-patterned substrate, the effective contact between the substrate and epilayer is reduced. As a result stress is

effectively accommodated within first few nanometers of epilayer as a result of lateral as well as vertical relaxation. The nanoheteroepitaxy is more effective than this approach by Luryi and Suhir and is more effective for systems with very high lattice mismatches. The main difference in the approach above and nanoheteroepitaxy is the use of nano sized seed pads in NHE instead of nano-strip pattern. For example, instead of using patterned silicon, SOI with patterned silicon nano-pads can be used. The flow rates and temperatures can be adjusted such that GaAs or GaN will seed selectively on Si nano-pads. Due to the ability of lateral relaxation, the strain due to lattice mismatch is distributed between seeds of silicon as well as overgrown GaAs or GaN nuclei. As a result, strain as well as deformations, such as dislocations that form as a result of strain, are confined to small regions of nuclei. Also, all nuclei being away from each other, the dislocations can glide and terminate at the edge of nuclei. The overgrown layer is relaxed and highly crystalline ⁹⁰. The later approach (NHE) requires additional step of growing nano-pads for nucleation over SOI, as compared to the patterning of silicon stripes which can be simply integrated with available technology. The NHE techniques is, however, better for very high lattice mismatched systems such as GaN on silicon.

The NHE approach is used by different researchers to grow GaN on nano porous GaN on sapphire ⁹³, SiC ⁹⁴ as well as silicon ⁹⁵⁻⁹⁷. The approaches, however, do not follow NHE exactly to as described earlier, but by employing templates of substrate that is covered with seeding pads of nano-porous materials such as silicon and GaN. These nano-porous seed pads are formed by lithography techniques that used anodized porous aluminum oxide membrane as a mask. This produces porous pads on substrate

with uniform pore diameters typically 60nm. Use of such techniques has shown promise growth of quality GaN on silicon substrate (Figure 1-6).

d Use of buffer layers

There have been various other efforts to grow GaN on silicon using different buffer layers such as AlAs films⁹⁸, ZnO films⁹⁸⁻¹⁰², ZnO nanorods¹⁰³, boron phosphide films¹⁰⁴⁻¹⁰⁸. The ZnO has less than 2% lattice mismatch and same wurtzite crystal structure. This makes ZnO highly compliant buffer layer material for GaN growth. The GaN grown with such layers is shown to be high quality with dislocation densities as low as 10^{-8} cm^{-2} . Mainly two types of threading defects are more prominent in these systems, viz. stacking mismatch boundaries (SMB) and inversion domain boundaries (IDB). The SMB defects in GaN films are formed because of defective ZnO layer. The crystal structure of Si is very different from ZnO wurtzite structure. This difference in stacking sequence in substrate and ZnO epilayer often results in stacking faults in ZnO layer. The IDB defects are formed because of growth of opposite face or polarity materials on each other⁹⁹. It is often required to grow low temperature GaN layer over ZnO buffer layer. Direct exposure of ZnO to ammonia results in its deformation. As a result, Zinc diffuses out or into the GaN layer resulting in low quality GaN. Use of low temperature GaN to cover ZnO buffer layer protects this layer. It, however, has disadvantage of forming gallium oxide at interface. The use of nanostructured ZnO template also has similar disadvantages. Due to very large surface area of ZnO nanorods in this case results in complete decomposition of ZnO layer after GaN growth¹⁰³ forming GaO_x at interface. Not many studies are done for BP as potential compliant layer for GaN growth, but this approach becomes interesting as it provides possibility to grow cubic GaN. Boron phosphide has less than 0.6% lattice mismatch

with zinc blende GaN and both boron as well as phosphorus are used as dopants for silicon. It has been found that cubic GaN can be grown on Si (1 0 0) using BP buffer layers. The quality of GaN, however, depends on quality of BP layer. In some cases where BP layer is polycrystalline, GaN tends to be polycrystalline as well as cubic GaN mixed with more stable wurtzite GaN. Due to limited results as well as formation of multiple phases of GaN, this approach is still limited to research. Although not much work has been done on potential use of InN as buffer layer on silicon, the InN film as buffer on sapphire has been shown to be very promising^{48,49}. InN has lower lattice mismatch with silicon than sapphire. Thus, use of InN film and nanostructures as buffer on silicon is more plausible choice than that on sapphire.

Overview of Present Work

Former section presents a very brief overview of current status of GaN and InN growth. The most pressing issue in the growths of nitrides is absence of native substrates. As a result growths of both GaN and InN are predominantly via heteroepitaxy methods. Silicon technology is very mature and as a result in recent years lots of efforts are focused on growths of nitride materials on Silicon. GaN has especially created lot of interest in research community due to its applicability in high brightness optics applications as well as high power electronic devices. The current work presents one such technique to grow GaN on Silicon. This study has tried to use nanostructures of InN to grow GaN on Silicon. As discussed previously, InN has lower lattice mismatch with Silicon than GaN. InN can also form pseudo binary alloy $\text{In}_x\text{Ga}_{1-x}\text{N}$ with GaN. Also, in parallel with NHE approach discussed previously nanostructures can be better in relieving strain. They also have better crystal quality. Both of these things can be

effective in stress reduction in GaN if InN is used as buffer layer. As a result, InN nanostructured templates can be used as compliant substrates for GaN growth.

The study is divided into three main parts. First part of study, presented in Chapter 2, is growth of InN nanorod on Silicon. Chapter discusses in detail about effect of different surface treatments as well as buffer layer on orientation as well as morphology of InN nanorods. This study can be used as a guide for other similar growths. This Chapter gives unique and only recipe to grow catalyst and patterned-template free vertical InN nanorod growth on Silicon. This has never been achieved before on Silicon substrates even with catalyst use.

Similar to many other nanostructures grown in different studies, InN nanorods in this study showed high crystalline quality. When films grow, they tend to be rigid and developed strain results in high density of defects such as dislocation as well as cracks. Both dislocations and cracks act as strain relieving mechanisms in high strain systems such as III-N hetero epitaxial growths. Research shows, however, unlike two dimensional films, nanostructures are much less prone to defects. This is also widely observed with nanostructures grown on foreign substrates. This is often attributed to their high aspect ratio. Because of smaller diameters, and contact in only base plane, nanostructures can relax laterally as they grow. This enables them to quickly relax strain as they grow. Chapter 3 presents an energy minimization model for nanorod growth. It qualitatively describes critical dimensions for which nanorods will be free of defects. Although the model uses InN nanorods grown on GaN as case study, model is very general and can describe equilibrium limits of coherency for any hetero-epitaxial system.

With previous Chapters giving recipe for high quality vertical nano structures as well as idea about strain relaxation capability of the nanostructures, Chapter 4 discusses the growth of GaN on these novel nanostructured templates. Although InN films have been used as buffer layers for GaN growth on Silicon, this study distinguishes itself with use of InN nanorod template. The Chapter is divided into two subsections with low temperature GaN growth in first section and high temperature growth in the second section. The Chapter discusses various stages of GaN growth on InN as well as interesting roles that are played by InN template. Most interestingly, question of disappearance of Indium from final GaN growth, which is also observed by other researchers, is addressed here. Also, study has successfully shown the growth of thick GaN without cracks by using InN nanorod templates.

With InN decomposing, at high temperatures of GaN growth study of possible use of only Indium metal film for growth of GaN is discussed in Chapter 5. It will be shown in this Chapter that similar to InN nanorods as template In/Si can also be used as possible template for thick GaN growths. This Chapter also shows interesting results about growth of GaN wafers with uniform 100nm thickness and 8 μ m lengths can be grown with use of In/Si templates. Indium metals role as surfactant and oxide mediated growth is believed to be responsible for these nanostructures.

Final Chapter, along with some key conclusions, gives suggestions on future work that add to as well as improve this approach.

Table 1-1. Common substrates for InN and GaN epitaxy

Substrate	Structure	Lattice Constants (Å)		Lattice Mismatch (%)	
		a	c	GaN	InN
GaN	Wurtzite	3.189	5.185	0	10.9
InN	Wurtzite	3.537	05.704	-9.8	0
c-Al₂O₃	Rhombohedral	4.765	12.982	15.9*	28.6*
AlN	Wurtzite	3.112	4.982	2.4	13.7
6H-SiC	Wurtzite	3.086	15.117	3.3	14.6
Si	Diamond	5.431	-----	-16.9	-7.9

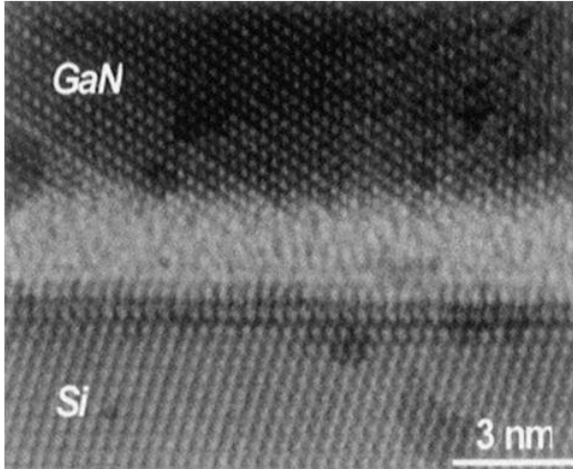


Figure1-1. HRTEM of GaN grown on Si(111) with 2-3 nm Si₃N₄ as intermediate layer⁵⁰

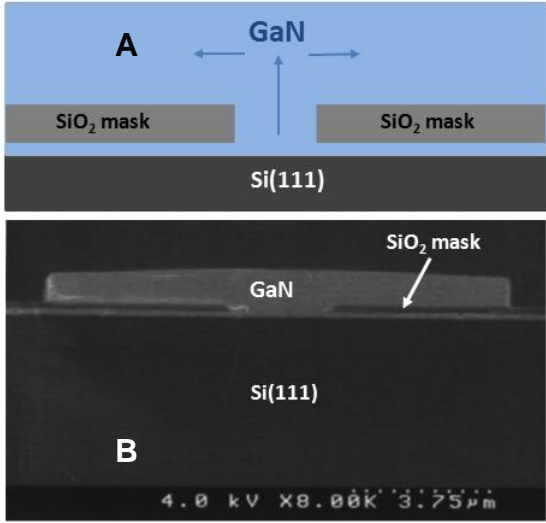


Figure 1-2. Epitaxial lateral overgrowth. A) schematic of growth, B) cross sectional SEM of ELO growth⁸⁵

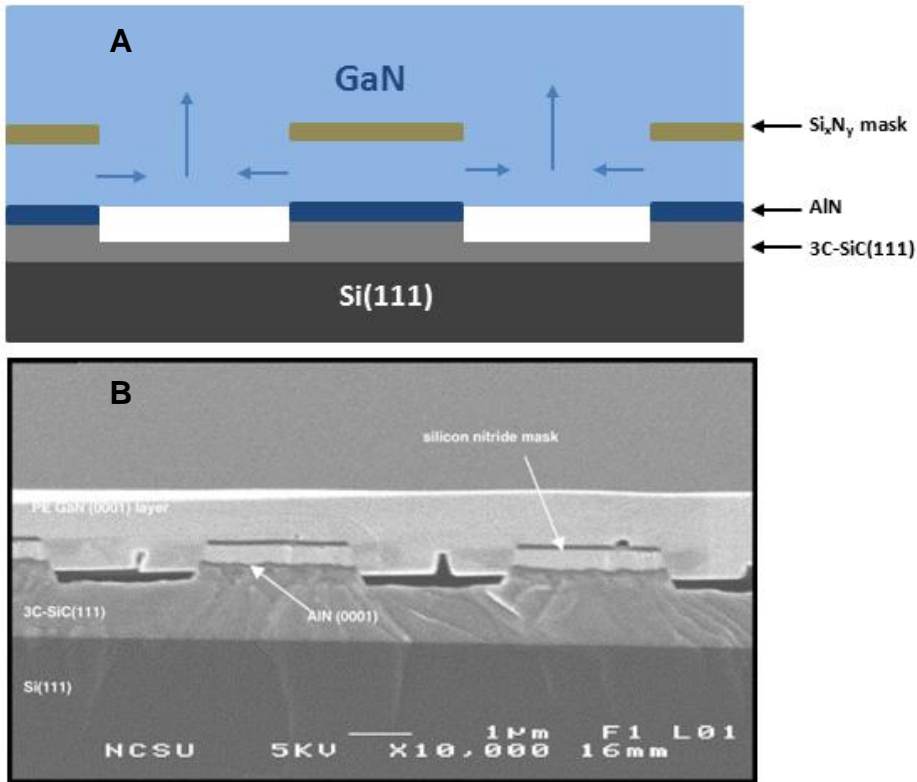


Figure 1-3. Pendeo epitaxial growth. A) schematic of growth, B) cross sectional SEM of PE growth⁷⁹

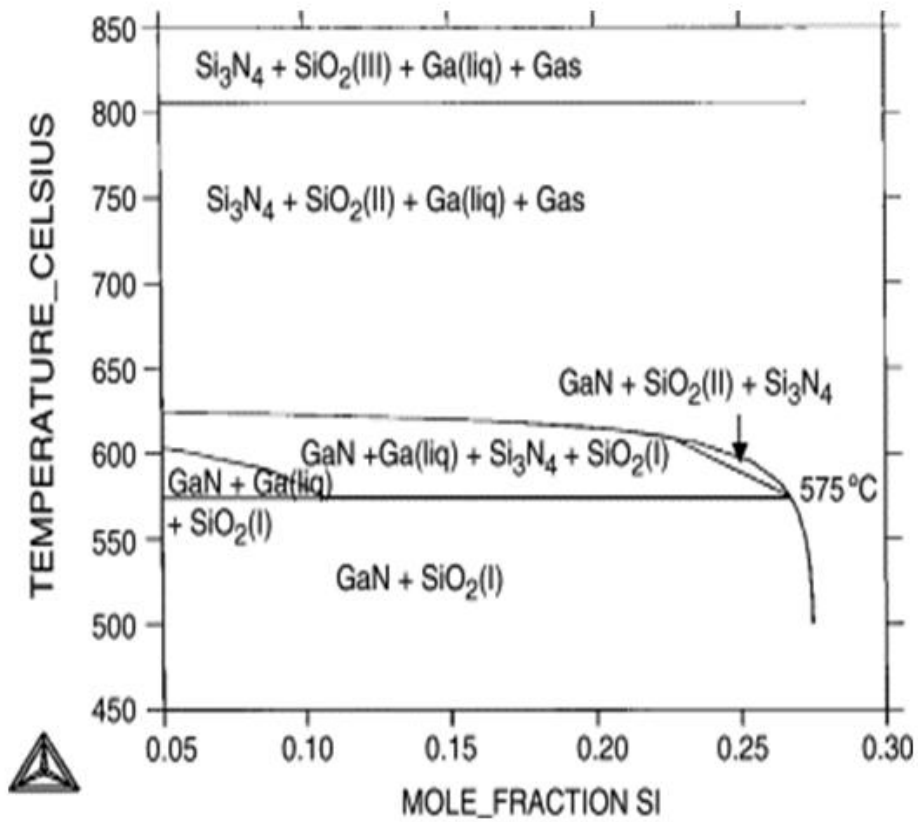


Figure 1-4. Equilibrium phase diagram of Ga-O-N-Si system⁷³ on Ga rich side

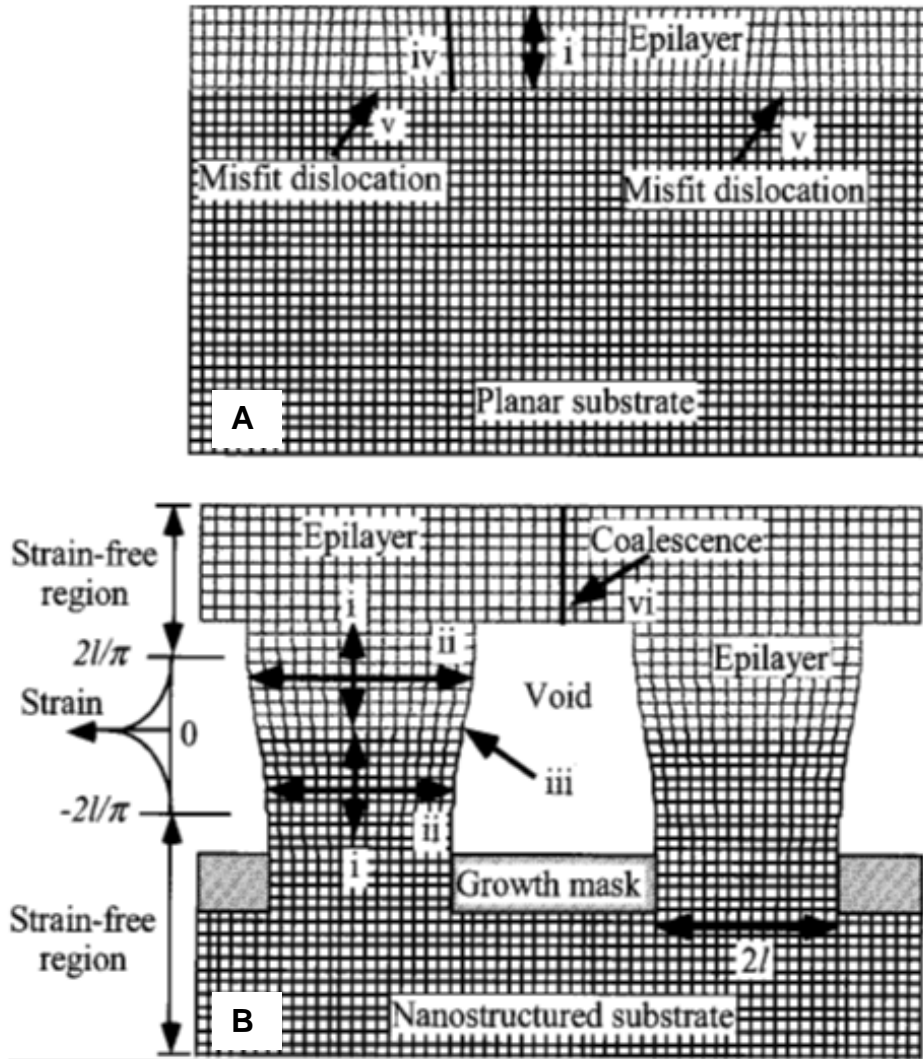


Figure 1-5. Strain relaxation in Nanoheteroepitaxy A) dislocation formation in 2D heteroepitaxial structures, B) strain relaxation in nanopads and seeds in NHE⁹⁰

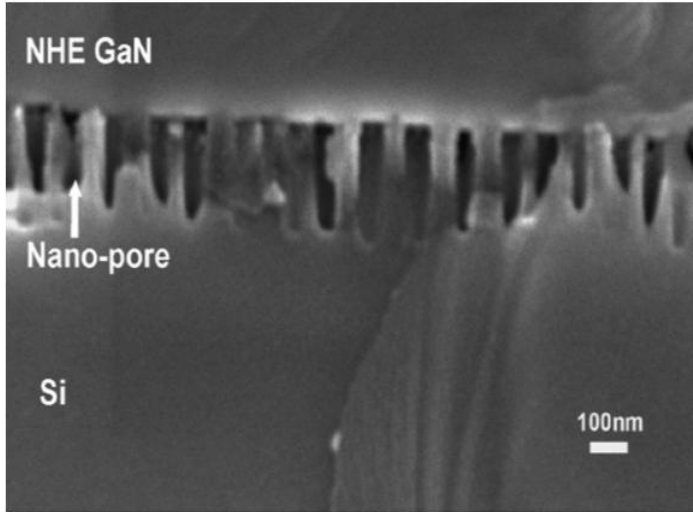


Figure 1-6. GaN grown on nano-porous silicon⁹⁶

CHAPTER 2 GROWTH OF VERTICAL INDIUM NITRIDE NANORODS ON SILICON IN MO-HVPE

InN Nanostructures in Literature

The global optoelectronics market is growing rapidly and is projected to reach whopping US\$932 billion by the year 2015¹³. This projected growth, however, relies greatly on continued progress in understanding of group III nitride growth and processing. Amongst the group III nitrides InN is least studied. It is now getting attention because of its interesting electronic properties. It has lowest direct bandgap of 0.7eV amongst the group III-nitrides¹⁰⁹, which has extended the coverage of nitride and alloys from deep ultraviolet to far infrared region in electromagnetic spectrum. Also, due lowest effective mass amongst group III-nitrides leading to superior electronic properties such as potentially higher mobility, higher drift velocities, there is increased interest using InN in optoelectronic applications such as laser diodes, solar cells, sensors and high frequency devices. The growth of high quality epitaxial InN has been a challenge, due to low decomposition temperatures of InN, high equilibrium nitrogen partial pressures¹¹⁰ at growth and lack of compliant substrates for InN. Various reported results, however, suggest that growth of highly crystalline InN is possible if it is grown in the form of nanostructures rather than films.¹¹¹⁻¹¹⁷

The growth of InN nanorods and nanowires have been studied and reported by various researchers^{109,111-114,116-121}. The metallic catalysts such as particles of gold, nickel etc. are most commonly used in growth as they provide preferential sites for reaction with growth taking place via vapor-liquid-solid (VLS) mechanism. The metal droplet often remains unreacted in this process and can be observed on tip of the nanowire. Although this method can be promising, size of metal droplet does not always

ensure the uniformity of shape and size of nanorods^{122,123}. Also, getting rid of metal droplets after growth, especially noble metals, can be a tedious as well as expensive. The other most common technique is by patterning of substrate¹¹⁹, but it has not been that successful in achieving single crystalline InN nanostructures. There are very few reports that demonstrate self-assembled growth of InN nanorods without patterning or catalyst^{111,113,124}. All the reports that mention catalyst and pattern free growth, use halide based approach to get nanorods. This works also presents on such halide based but unique approach.

Metal-Organic Hydride Vapor Phase Epitaxy (MO-HVPE)

Metal-Organic Hydride Vapor Phase Epitaxy (MO-HVPE), as name suggests, combines more conventional Metal Organic Chemical Vapor Deposition (MOCVD) and Hydride Vapor Phase Epitaxy (HVPE). Due to uniqueness of the method, no literature is available on this method except reports by Anderson group. Hyun Jong Park has previously reported InN nanorod growth on various substrates using this method^{111,112}.

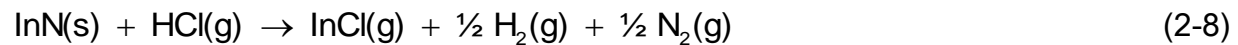
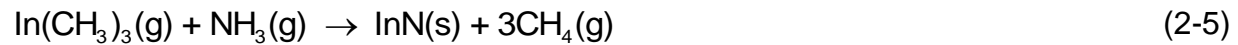
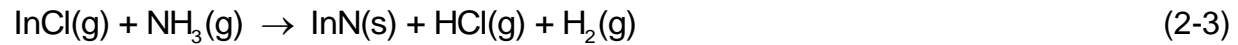
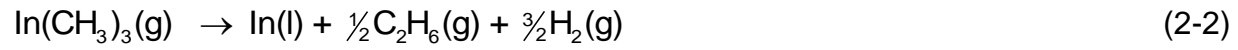
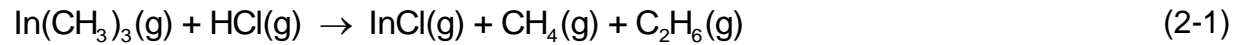
Reactor Setup

The reactor photograph and schematic are presented in Figure 2-1(A) and Figure 2-1(B) respectively. It is a hot wall quartz reactor fitted in resistively heated furnace which is typically operated at atmospheric pressure. The furnace has five individually controlled heating zones with heating capacity more than 1273K. But in current configuration heating is restricted to 1273K to avoid any damage to quartz reactor from possible softening at higher temperatures. Currently only three zones are in use and they act as source zone, mixing zone and reaction zone. The temperatures of the zones are adjusted in such a way that desired temperature profile is achieved. Substrates are loaded into the reactor with magnetic loading arm on tiled quartz susceptor. Load lock

separated by gate valve helps to minimize oxygen contamination into the reactor. The reactor can be operated with Nitrogen (N₂), Hydrogen (H₂), forming gas (4% H₂, balance N₂) and Helium (He) as sweeping and carrier gases. Typically, N₂ was used as carrier gas for InN growths. High sweep gas flows from inlet and gate valve are adjusted so as to minimize wall depositions and confining growth to growth zone.

MO-HVPE Operation

Typically temperature profile is adjusted in such a way that end of the inlet zone is maintained in the range of 573K to 673K. This ensures complete decomposition of metal organic as well as activation of other reactants before they enter the mixing zone. The typical overall reactions that are expected in InN formation are as follows.



Inlet consists of three concentric quartz tubes. Metal organic which in this case is Trimethyl-Indium (TMI) enters the reactor from central tube. Its shorter design ensures that metal organic reacts with 10% Hydrogen Chloride (HCl) gas to form Indium Chloride (InCl) (Reaction 2-1) as well as Indium trichloride (InCl₃) and other chloride

species, before it comes out in mixing zone. However, it has been known that formation of InCl_3 and other chloride species is less favorable thermodynamically especially at temperatures used^{125,126}. Indium chloride then reacts with ammonia to form InN which gets deposited on hot substrate (Reaction 2-3). If HCl gas is not used, Trimethyl-Indium decomposes to form Indium or reacts with ammonia directly after coming out in mixing zone, to form Indium nitride (Reactions 2-2, 2-4, 2-5). Thus, depending on presence and absence of HCl gas same reactor can be operated in HVPE mode and MOCVD mode respectively.

Typical growth temperatures used for InN are in the range of 773K to 823K. At these temperatures, ammonia decomposition is very limited. As a result, incomplete reaction of metal organic with ammonia or InN decomposition can result in Indium rich film or even Indium droplet formation (Reactions 2-2, 2-6 respectively). Kang's work¹²⁷, however, shows that addition of HCl gas can completely eliminate formation of Indium droplets (Reaction 2-7). The excess use of HCl can also result in etching of InN film (Reaction 2-8). It has been however observed that the etching of InN solid by HCl is not isotropic and results in etch pits rather than uniform etching¹²⁶.

Thermodynamic analysis of In-C-H-Cl-N , suggests that depending on HCl to Indium (HCl/TMI) ratios used, at constant V/III (i.e. ammonia to Indium) ratio different growths of InN are expected at different temperatures^{111,125}. These typically include InN growth with Indium liquid droplets, InN solid growth, and InN no growth. Droplets are expected for HCl/TMI ratios 1 and below. When excess HCl is used i.e HCl/TMI ratio > 1, InN can either form or can be completely etched away as a function of temperature as seen in Figure 2-2. In practice, the boundary between growth and no growth is not

sharp as predicted by theoretical calculations. As a result, near growth etch boundary, competition between formation reactions and decomposition reactions often results in decrease in nucleation and growth. Due to large lattice mismatch, surface energetics is such that, like many other heteroepitaxial semiconductor growths, nitride growths are in Volmer-Weber mode of film growth^{47,128,129}. In this mode of growth¹³⁰, nucleation is in the form of small islands, which grow and coalesce to form film. In fact, gas kinetics is also not simple in MO-HVPE and the amount of HCl in the reaction zone plays a role in kind of nucleation that follows. Raman spectroscopy studies and DFT calculations reveal that HCl/TMI ratio is 1 or less, InN 2D film growth is expected as InCl is predominant source of Indium. But when HCl/TMI ratio is 3-4, InCl₃ also is major source of Indium. It can form a H₃N:InCl₃ complex with ammonia. This complex is known to polymerize which can result in chain and ring compounds of $[-H_2N:InCl_2-]_n$ form¹³¹. The combination of all these factors results in growth of nanostructures. Figure 2-2(B) gives an idea on variety of possible growths of InN possible in the reactor.

Indium Nitride Nanorods (InN_{NR}) Growth in MO-HVPE

InN_{NR} Growth Conditions

Trimethyl Indium solution (TMI), Trimethyl Gallium (TMG) from Epichem and 99.999% pure ammonia from Airgas South were used as indium, gallium and nitrogen source respectively. For InN growth TMI was reacted with 10%HCl (balance nitrogen) from Airgas South in source zone at 573K to form chlorinated species of Indium. These species were then mixed with ammonia from the concentric inlet in mixing zone. The substrate temperature was maintained at 833K-873K for growth. The inlet HCl/TMI molar ratio and NH₃/TMI molar ratio were maintained at 4 and 250 respectively. The N₂

carrier gas flow rate of 1600 sccm was also maintained all along the 1 hour runs. These growth conditions ensured dense InN nanorod growth as established from previous studies^{111,112}. Silicon (100) and Silicon (111) were used as substrates and were loaded together in every run. As this study was done only to see the effect of different surface conditions of substrates, following sets of runs were carried out.

For this work following surface treatments were considered. The methods that clean the surface of foreign materials, particulate entities and that are helpful in passivation of silicon surface without adding considerable epitaxial layer of different material are treated as surface treatments. All other methods that form certain layer of material to Si surface are treated as nucleation layers.

Use of Surface Treated Silicon

A. Organic solvent degreasing and buffered oxide etching: In these sets of runs two types of silicon substrates were used. First set of silicon substrates were simply degreased using standard cleaning method. This method used baths of boiling trichloroethylene (TCE), acetone and methanol. The silicon wafers were cleaned by dipping in boiling baths organic solvents for 5 minutes each in the previously mentioned sequence. Then they were washed with deionized water and dried using nitrogen gas. This step removed any carbon or oily residues formed on silicon surface. In second set of silicon, in addition to surface degrease, substrate wafers were dipped in buffered oxide etch (BOE) for 1 min at room temperature. This step was done to remove some native oxide from silicon surface. InN samples grown on degreased and BOE cleaned Silicon would be called sample A1 and sample A2 in further discussion.

B. *In-situ* surface cleaning with 10% HCl : In these sets of runs, degreased Silicon wafers were loaded into the reactor and were treated with HCl for 10 min at

873K prior to actual InN_{NR} growth. The flow rate of 10% HCl gas was kept at 50 sccm. The HCl is very reactive and can be used as etching agent to remove oxide layer similar to hydrofluoric acid in BOE clean in previous section. Reaction of HCl with silicon oxide forms silicon oxychlorides which are thought to be volatile¹²⁶. As a result, HCl was thought to be effective agent for surface cleaning of silicon. Samples of InN_{NR} grown on HCl cleaned Si will be called sample B in further discussion.

Nitride Nucleation Layers on Silicon

The results from previous studies^{73,111} suggested that intermediate nitride layer can be used to grow better quality GaN and InN respectively on Silicon and Sapphire substrates. These studies markedly improved quality and orientation of nitrides grown using same method. The idea was to study if the use of nucleation layer changed the orientation distribution of InN to preferred orientation. Initially, Silicon substrates were nitridated by exposure to ammonia and then the MO-HVPE reactor system was used to grow films in two modes. The MOCVD mode films were grown when no HCl was used. The reactions took place by thermal decomposition of MO followed by reaction with ammonia. The HVPE mode films were grown when HCl was used and nitride was formed by reversible reaction between chloride species and hydride (which is ammonia in this case). In this study, in total, four types of nitride buffer layers were used, *viz.* Silicon oxynitride, InN using HVPE growth mode and gallium nitride using both MOCVD condition and HVPE conditions. Then, InN nanorods were grown on these nucleation layers. Then their effect was studied on further InN nanorod growth and orientation using XRD and SEM.

C. *In-situ* surface nitridation before growth: Nitridation of silicon is known to form amorphous silicon nitride SiN_x on its surface. Due to the amorphous nature, the

SiN_x layer is known to decrease the quality of nitrides grown. The nitridations were still carried out based on previous work. In previous work, equilibrium studies were done for Ga-O-N-Si system as well as actual growth experiments were conducted⁷³. The studies revealed that SiN_x formation embarked only at $\sim 848\text{K}$. The SiN_x formation deterred formation of good quality nitride on silicon. But, on the contrary the nitridation done at lower temperatures and for shorter time intervals resulted in silicon oxynitride $\text{SiO}_{1-x}\text{N}_x$ layer. This layer was shown to improve the quality nitrides grown on top. For these reasons, nitridation of silicon was carried out followed by InN nanorod growth. In these sets of runs after silicon substrates were loaded, in situ nitridation using ammonia at 1500 sccm was carried out. It was done by passing ammonia over hot silicon substrate at 833K for short time intervals of 10 minutes. After nitridation InN growths were carried out using conditions mentioned earlier. These samples would be called sample C in further discussions.

D. Low temperature Indium nitride film as nucleation layer: For growth of indium nitride film following conditions were used. The inlet HCl/TMI molar ratio and NH_3 /TMI molar ratio were maintained at 2 and 700 respectively. The growth zone temperature was kept at 873K while mixing and source zone were maintained at 723K. Indium nitride was not grown without HCl because absence of HCl results in bad quality of indium nitride films which had indium droplets on top. The InN samples grown on these layers would be called sample D.

E. Low temperature gallium nitride film as nucleation layer: Gallium nitrides films were grown in both HVPE mode and MOCVD mode. For HVPE mode GaN films growths were carried out as follows. The TMG from Epichem and NH_3 from Airgas south

were used as gallium and nitrogen sources. The TMG was mixed with 10% HCl in source zone to form chloride species of gallium. The HCl/TMG molar ratio was maintained at 2. These species then reacted with NH_3 in mixing zone to form GaN film on silicon substrates. Growth zone was maintained at 873K and NH_3 /TMG molar ratio was set at 570.

In separate sets of runs, GaN films in MOCVD mode were grown by maintaining high NH_3 /TMG molar ratio of about 3000 and temperature of 873K. These conditions were selected based on optimizations in previous studies, the details of which can be found elsewhere ⁷³. The InN nanorod samples that use MOCVD and HVPE GaN films as buffer layers would be called sample E1 and sample E2 respectively in further sections.

Results and Discussion

Samples grown on bare Si substrate tend to be randomly oriented. Figure 2-3 shows typical powder X-ray diffraction (XRD) pattern for randomly oriented InN nanorod samples grown on degreased silicon i.e. A1 samples. As seen from XRD θ - 2θ scan, the InN nanorods showed diffraction peaks for various families of planes such as $\{10\bar{1}0\}$, $\{0002\}$, $\{10\bar{1}1\}$, $\{10\bar{1}2\}$, $\{10\bar{1}3\}$ etc. The illustration in Figure 2-4 shows that to get particular peak in typical θ - 2θ scan, nanorods are required to be oriented at a particular angle to the substrate surface. For example, vertical nanorods have (002) plane horizontal, that is the [002] direction makes angle of 90° with horizontal plane or substrate plane. Similarly, to get diffraction from (100), (101), and (102) planes nanorods should be tilted at angles of 0° , 28° , 47° to the substrate. This angle is same as angle made by [002] direction to horizontal plane in respective cases. Two qualitative

approaches are employed in order to study if any orientation is preferred. Firstly, ratios of intensity of a particular peak to a reference peak in same sample are calculated. These ratios are then compared to corresponding intensity ratios reference powder XRD pattern. The PDF # 50-1239 powder XRD data for InN from International Centre for Diffraction Data (ICDD) was used as a reference. Only, first four major peaks are considered for further analysis. The (101) peak was chosen as reference peak in each sample, since it is highest intensity peak in reference PDF. In other words with (101) peak intensity as unity, the other peak intensities were calculated. These ratios for each sample are tabulated in Table 2-1. More the ratio for a certain peak, higher the preference of that sample to be oriented in that direction. In second approach relative intensity ratio R was determined for each peak. The ratio is defined as ratio of normalized intensity of observed peak to normalized intensity of same peak in reference. First approach only allows seeing preference in certain orientation as compared to (101) orientation in that particular sample. It does not say anything about the (101) orientation preference. The second approach, which is tabulated in Table 2-2, allows comparison of every peak in the reference sample but does not tell real comparison between peak ratios of same sample. It is however worthwhile to note here that these ratios strictly give information about orientation or texture qualitatively and not quantitatively. The SEM images are taken to supplement the results observed by XRD.

Effect of Surface Cleaning Treatments

The major difference in sample A1 and sample A2 is that later has native oxide layer partially removed. As silicon oxide is amorphous the nucleation in both cases can be different which can result in different orientations of nanorods. The XRD θ -2 θ scans are shown in Figure 2-5. The analysis of XRD θ -2 θ scan, using peak ratios (Table 2-1)

and relative intensity ratios (Table 2-2), suggested that there is not much difference in the samples. The sample B does not show any effect on any peak either (Figure 2-6). The calculations however show increased intensity of (102) peak indicating increase in that particular orientation. The reason behind this might be that HCl being anisotropic etchant, creates etch pits into the silicon. These sites are energetically favored for nucleation. As the nanorods growing from (111) Si planes from etch pits do not grow vertically, they add to the other orientation. As the random orientation would increase with more exposure to HCl prior to the reaction, no HCl clean was done for further studies. The SEM images of A1, A2 and B showed no differences in the morphology in Figure 2-7. Although, there is no significant difference visible in XRD, InN nanorods growing on HCl cleaned Si not only are random, but also have wide diameter distribution with diameters in the range from 50nm to 400nm. Wide distribution here also results from the fact that once nanorod becomes big enough, it serves as nucleation site, resulting in branching. Such secondary nucleations are clearly visible in Figure 2-7(C). The secondary nucleations or branching, however, is totally expected. The same behavior was observed by previous researchers^{125,126}. On the other hand, samples A1 and A2 in Figure 2-7(A) and (B) respectively show uniform distributions with InN_{NR} with diameters near 200nm and 100nm respectively, which is an indicator of uniform nucleating surface.

Effect of Nucleation Layers

Growth on nitridated Si: The InN_{NR} grown on nitridated silicon show definite improvement in (002) peak as compared to non nitridated sample A1 (Figure 2-8). This is because nitridation forms silicon oxynitride layer under the experimental conditions used. It was observed that nitridated Si surface consisted of a.7% Si-N bonds and 26%

Si-O bonds and rest bulk Si-Si bonds⁷³. Although exact mechanism of nanorod nucleation is not known on this surface, there is improved nucleation of nanorods in (002) direction due to presence of some Si-N bonds. Layer of SiN_x is believed to have hexagonal geometry, similar to wurtzite InN and GaN⁷⁶. The observed results are in agreement with improvements in GaN films quality that were reported previously on nitridated silicon⁷³. The A1 and A2 samples are perfectly random nanorods. The SEM picture in Figure 2-9 (A) confirms that sample C has visibly less number of random nanorods, and number of vertical nanorods has increased. This sheer increase in number of [002] nanorods increased corresponding peak intensity.

Comparison between InN film, MOCVD GaN film and HVPE GaN film as nucleation layers: One of the earlier studies reported improvement in GaN film quality on silicon using silicon oxynitride layer⁷³. Also, there was improvement in texture in InN nanorods on silicon due to nitridation. The combination of these observations led to studies in use of different nitride layers as nucleation layer for nanorod growth. Results from this approach are discussed next.

The use of MOCVD GaN and HVPE GaN further improves texture InN nanorods in [002] direction as expected. It is clear from the Table 1 and Table 2 that sample E1 and E2 are highly textured in [002]. But, the corresponding values of ratios for D samples revealed even more randomness than samples C. The Figure 2-10 compares XRD θ - 2θ scan for the D and E1 samples. The [002] texture of InN nanorods in E1 is evident. This means that nucleated nanorods on InN nucleation layer are random. This randomness is consequence of two reasons. Firstly, it might just be mainly because of any texture being absent in InN nucleation layers itself. It is but evident from previous observations

that InN by nature grows randomly on the silicon and nanorods follow texture of the film. Secondly, it is known that the nanorods tend to be randomly oriented if they originate from single big nucleation sites¹³². The indium droplet wetting of InN film surface is not uniform¹¹¹. The nanorod nucleation in this type of reactions goes through the $\text{Cl}_2\text{In}:\text{NH}_2$ adduct formation. These adducts then undergo oligomerization to form InN^{131} . If a bigger indium droplet of Indium forms on film during beginning of the reaction, the indium chlorine ammonia adduct forms at multiple points on same droplet, resulting in multiple nucleation from same spot. Moreover, Indium can readily wet InN as compared to GaN. As a result, many InN_{NR} on InN film can have larger diameters. This explains observed wide size distribution of InN nanorods in Figure 2-9 (B).

The Figure 2-11 illustrates that HVPE GaN nucleation layer can be used to get InN nanorods with very high [002] preferred orientation on both Si (100) and Si (111). This (002) texture on GaN nucleation layer is also confirmed from cross sectional SEM images in Figure 2-12. This means that the directional nature of nanorods is governed directly by the quality of nucleation layer it nucleates and not the actual substrate. This can be further explained by observing differences in InN nanorods grown on different GaN nucleation layers. The HVPE GaN nucleation layer growth after nitridation is highly textured in [002] directions; contrary to MOCVD GaN in which (101) GaN peak is also observed. In addition, the MOCVD grown GaN film tends to form small spherical features on surface, from which multiple nanorods can nucleate in different direction. One such multiple nanorod nucleation site on MO-GaN film is shown in Figure 2-13 (A), whereas Figure 2-13 (B) corresponds to initial growth on HVPE GaN surface. Here, randomness is arising only due to InN tripods formation. The InN tripods are formed

when zinc blend cubic core is formed at the base as a result of strain relaxation mechanism and wurtzite InN_{NR} grows from (111) faces of zinc blend core.

The nanorods grown on MO-GaN nucleation layer, however, tend to be more uniform and smaller in diameter. The differences in polarities of GaN grown in MOCVD and HVPE could be reason behind this. The MOCVD grown GaN is gallium terminated and is smooth. In comparison, the HVPE grown GaN films are rougher and tend to be N-terminated, because they are grown in presence of HCl. The HCl acts as metal scavenger and also makes surface rough because of its anisotropic etching. Thus, in sample D, due to smoother and uniform surface, nanorod nucleation tends to be more uniform in size, resulting in more uniform nanorods. Fully grown, InN_{NR} on MO-GaN films and HVPE-GaN films are shown in 2-13 (C) and 2-13 (D) respectively.

In the end all results are summarized graphically in Figure 2-14. It compares percentage relative ratio of each of the four major orientations considered in this study. Powder XRD only gives information about the dominance of certain orientation provided that the particular planes produce constructive interference in X-rays. Although, power scans show that InN nanorods on HVPE GaN films are oriented in [002] direction, pole figure gives exact rotation about the vertical axis and omega rocking curves gives qualitative information about certain orientation. Pole figures of vertical InN_{NR} on Si (111) using GaN are shown in Figure 2-15. The results show that indeed GaN and InN are have their c-axes aligned with [111] of Si. The phi scan for [101] peak of GaN reveals that GaN grown here does not have any preferred rotational orientation on Silicon substrate. InN_{NR} just follow the rotation of the GaN crystal, which is expected¹²⁵. Thus, there is a texture in [002] direction, but there is no rotational preference observed

in these samples. The omega rocking curve done on same sample using Molybdenum X-ray source is shown in Figure 2-16. The rocking curve has FWHM of 936 arcsec which is better than any reported values in literature for InN nanostructures.

InN_{NR} Properties

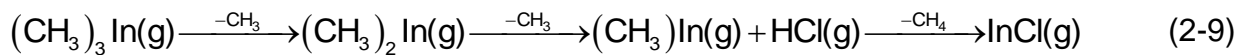
The nanorods are tested for crystal quality in JOEL 300CX transmission electron microscope. The Figure 2-17 shows individual flat ended as well as tipped nanorod. Lattice fringe image as well as SAED analysis revealed that nanorods were wurtzite with [002] growth axis along their length and {100} faces making the hexagonal shape. The TEM images also occasionally showed presence of some planer defects and evidence of secondary nanorod nucleation on nanorod main body. These nucleations could have also added to randomness of nanorods. The energy dispersive spectroscopy (EDS) in SEM of E2 samples (Figure 2-18) revealed that no oxygen was present in the films in detection limit, however, 0.77 atomic percent of chlorine was detected. Although the detection below 1% and cannot be considered in quantitative manner, it reveals presence of chlorine in sample. We speculate that the chlorine signal is coming from HVPE GaN films as nanorods by this process do not have any chlorine.

Growth Mechanism of InN Nanorods

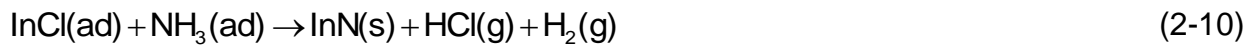
As seen in previous sections, MO-HVPE system is similar to HVPE system in operation when HCl is introduced into the system. The metal organic source seems to completely react with HCl to form Indium chloride and Indium trichloride, which act as primary Indium precursors. Increase in HCl results in increase in trichloride. At constant Indium metal flux, the value of Cl/In and N/In ratios indicate the amount of HCl and Ammonia in the system. In addition to these parameters, substrate temperatures, distance between inlet and substrate, type of substrate used, growth time etc. are the

parameters that influence the InN growth. As a result, for the study of effect of single parameter all other parameters need to be constant in order to see or state full effect of that parameter. However, it is to be noted that various parameters are interlinked and as a result, it is often not easy to isolate the effects of different parameters. The effects of change of some of the very important parameters are discussed below. Also, the effect of each variable is discussed at different conditions formed by change in other variable to better understand the complete mechanism of highly anisotropic crystals such as nanorods.

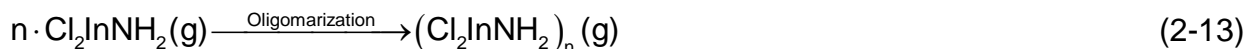
Effect of Cl/In ratio: The control on Cl/In ratio in MO-HVPE system, is perhaps the most unique feature that this system offers. The Cl/In ratio is very critical in suggested mechanism of nanostructures formation in MO-HVPE system at constant temperature as well as N/In conditions^{111,131}. The chlorine to indium ratio influences the formation of chloride species of Indium. The proposed growth mechanism of InN growth depending on Cl/In ratio are as follows. It is based on gas phase kinetics study using Raman Spectroscopy and density functional theory calculations.



For Cl/In=1



For Cl/In=3





At low Cl/In ratio of 1, as shown in equation 2-9, dominant chloride that forms is InCl. The InCl and ammonia then adsorb or chemisorb on surface as shown in equation 2-10. This results in formation InN film via layer by layer growth or islands coalescence depending on surface energetics.

In case of Cl/In ratio of 3, InCl_3 is dominant gaseous species. This species can undergo chain in of reactions as shown in equations 2-11 and 2-12 which results in monomer complex by elimination of HCl from $\text{Cl}_3\text{In}:\text{NH}_3$ adduct. This gaseous monomer can undergo polymerization owing to strong H-Cl polar interaction between monomer molecules. The oligomers such as $\text{Cl}_9\text{In}_6\text{N}_6\text{H}_9$ are ring compounds with wurtzite structure with InN at core¹³³ and Hydrogen and Chlorines on outside. Such oligomers are heavy and can form random nuclei on substrates. The supersaturation of Indium chloride species in gas phases then drives formation of InN nanorods. The oligomer nuclei have c-axis as a polar axis. The reactivity of polar precursors of Indium is higher along polar axis than the surfaces. This results in higher reactivity along c-axis, resulting in higher growth rates along $[000\bar{2}]$ direction.

Further increase in Cl/In ratio increases amount of HCl in the system. The HCl is reactant that drives formation of more InCl_3 as well as it is a product in formation of monomers as well as oligomers that are responsible for InN nucleation. As a result, increase in HCl generally drives equilibrium towards formation of more InCl_3 in chloride species. Increase in HCl also results in shifting equilibrium towards monomers of $\text{InCl}_3 - \text{NH}_3$ complex. This can be seen as more dominant etching reactions by HCl. As a result, increase in Cl/In ratio results in sparse nucleations, more etching and no growths.

Significant increase in NH_3 is required to drive reactions towards oligomers and nanostructures.

In general, at constant temperature and N/In ratio, the diameter of nanorods grown decreases with increase in Cl/In ratio. The effect can be attributed to more etching reactions. It is also seen that diameter distribution tends to become more and more uniform as Cl/In ratio increases. This effect however is complex function of gaseous oligomer formation and their interaction with substrates during heterogeneous nucleation.

Effect of N/In ratio: Effect of ammonia is most straight forward of all reactants.

Ammonia is always present in excess and as a result ammonia often is not a limiting reactant. As N/In ratio is increased, activity of ammonia increases and InN formation is favored according to Le Chatelier's principle. Independent of Cl/In ratio and temperature, at which InN is grown, increase in ammonia increases InN formation and as a result InN sows transition from nano or island growth to film growth. Effect of ammonia is profound on InN morphology. As seen from Figure 2-19,(taken from previous work in same reactor¹²⁵), although different substrate have different types of InN nanostructure morphologies, increased ammonia in the system results in transition of growth from nanostructures towards film growths. This is again result of shift of equilibrium towards products InN, HCl and ammonium chloride, due to ammonia rich atmosphere. As discussed in previous section, at high HCl concentrations, increase in ammonia can drive equilibrium towards oligomers and nanorods can form.

Relatively ammonia poor conditions are necessary for InN nanostructure formation in case of MOCVD growths, which proceed by Vapor Liquid Solid mechanism. For

example, the impinging jet geometry used by Josh¹²⁶, results in low apparent N/In ratio at surface of substrate. As a result of this nanostructures growth via VLS growth is observed. Indium flux in this case only controls the density of nucleations. As a result, most dense nucleations are at the center of impinging jet and nanostructures become sparse towards edges of subsector. It is also worth to note here that, ammonia poor conditions here do not translate to N/In ratios of less than 1. Such ratios are bound to result in Indium metal droplet formations at the surface of films.

In general it can be thus concluded that environments very rich in ammonia can result in bigger nucleations and growth. Ammonia poor environments, with optimum flows of other reactants can result in film as well as nanostructures.

Effect of temperature on InN growth: Temperature is always a very important parameter in material growths. InN starts to decompose above 923K, but NH₃ cracking is not effective below 773K, which limits the growth window of InN to very narrow temperature range. As a result, the InN formation gets better with increase in temperature, peaks and then declines. At lower temperatures growth is limited by ammonia cracking and at higher temperatures, decomposition dominates.

In MO-CVD mode or when there is no enough HCl around to form Indium chloride, often indium metal droplets form. Depending on flow patterns used, films as well as nanostructured growths are possible. For example, horizontal inlet results in film growth, whereas impinging reactants can result in nanostructures via VLS mechanism. Very high N/In ratio (≈ 50000) can avoid metal droplet formations at optimum growth temperatures around 873K. At lower temperatures, no active nitrogen is available. This

results in metal droplet formation even at very high N/In ratios. At temperatures 973K and above, no growth is possible as InN is unstable at these temperatures.

In presence of HCl, ($Cl/In > 1$), InCl and InCl₃ are present and InN is formed by reaction between these species. Unlike MOCVD growth, reactions in presence of HCl do not take place by radical mechanism, but direct reaction of ammonia with chlorides. As a result of different mechanism, the reaction is not limited by active nitrogen concentration resulting from cracking of ammonia. As a result, at lower temperatures, InN formation is possible in this mode. Effect of temperature; however is similar in terms of quality and morphology of InN formed. InN quality increases with increased temperature, as increase in energy of molecules allows them to form better crystals. InN films become more columnar, and when temperature is above 923K InN decomposition dominates and there is no growth. With increased Cl/In ratio, chemistry changes and InN grows as discontinuous film or nanostructures. This can be seen as a result of more corrosion due to increased HCl as well as corrosion due to hydrogen produced in cracking of ammonia. But effect of temperature remains similar.

Thus, a general trend is that crystal quality gets better with increase in temperature, followed by decrease in growth as temperature goes towards decomposition temperature of InN. Although crystalline quality increases, for higher Cl/In ratios nanorod diameters decrease and diameter distribution becomes narrower with increase in the temperature. The smaller diameter crystals are better at relaxing the strains, and as a result exhibit better crystalline quality than that of bigger nanorods. This trend is clearly visible in Figure 2-2. This effect is also explained in higher details in work by Hyun Jong Park^{112,125}.

Effect of substrate type: The effect of surface on quality and nucleation of InN film as well as nanorods is rather complex. The lattice mismatches of Sapphire, AlN, GaN and Si with InN are approximately -28%,-13%,-11% and +8% respectively. As a result Si can be seen as best lattice matched substrate for growth of InN. It was, however, seen that at constant Cl/In ratio, N/In ratio and temperature, nanorods grown on Silicon in general were bigger in diameter than that grown on Sapphire. The diameters were smallest for nanorods grown on GaN nucleation layer. The diameters had narrower distribution in case of GaN nucleation layer as compared to any other substrate used. Use of InN nucleation layer also accounted for larger diameters and wider size distribution. All nanorods showed faster growth along polar c-axis and all samples always showed some preference towards vertical orientation. The preference for vertical orientation with nucleating surface was most for GaN layer followed by Silicon and Sapphire. It has been consistently observed in this study as well as other works^{125,126}. Previous study¹²⁶ also suggested that InN nanorods tend to be flat tipped in case of polar substrates like c-GaN, a-Al₂O₃, c-Al₂O₃. InN nanorods have sharp tips in case of nonpolar substrate like r- Al₂O₃ and Silicon. On r- Al₂O₃ formation of nonpolar [11 $\bar{2}$ 0] InN or [11 $\bar{2}$ 0] GaN films is more common, but nanorods are found to be almost always [000 $\bar{2}$] oriented in these studies. In rare cases growth axis was found to be [1 $\bar{1}$ 00]. This study as well as study by Hyun Jong Park, however, did not always find the strong relation between surface polarity and shape of the tip of nanorod. It was often seen that densely nucleated nanorods tend to be flat tipped and rare nanorods tend to be sharp tipped. The flat as well as sharp tipped vertical nanorods grown on GaN nucleation layer are

shown in Figure 2-20. All nanorods had nitrogen polarity as Indium metal is taken away by HCl in the reactor.

All these observations are very hard to explain on the basis of gas phase nucleations alone. The random nucleation can be explained by the gas phase oligomer formation, which then gets deposited on surfaces at random locations. But distribution and difference in the diameter sizes of nanorods grown on different surfaces cannot be explained by random nucleation alone. Oligomers complexes can have random sizes, but if surfaces on which nanorods are grown did not have any role to play; random nanorods would show same diameter distributions independent of substrates used. The fact that this uniformity is not observed, points towards role of surface energetics on further growth of nanorods. The heterogeneous nucleation is highly influenced how surface energies are changed when nucleation occurs on foreign surface. Consider a nucleus having shape of hexagonal parallelepiped deposited on the substrate as shown in Figure 2-21. The energy change in the surface when such nucleus is deposited is given by

$$\Delta G = - \left(\frac{3\sqrt{3}}{2} \frac{L^2 H}{\Omega} \right) \Delta\mu + \frac{3\sqrt{3}}{2} L^2 \Delta\alpha + 6LH\alpha \quad (2-15)$$

where $\Delta\mu = \mu_v - \mu_c$ is difference in chemical potential of nucleating species in vapor and condensed phase, the driving force for nucleation

Ω is molar volume of nucleated InN

α is specific free energy of nonpolar vertical faces of nuclei

$\Delta\alpha = 2\alpha_o - \alpha_{ad}$ is variation of surface free energy at interface due to formation of nuclei

α_o is surface free energy of basal plane or polar plane

α_{ad} is specific free energy of adhesion of InN on substrate surface

The quantity $\Delta\alpha = 2\alpha_o - \alpha_{ad}$ can be seen as measure of how much more difficult is to split the crystal than to separate itself from substrate surface. When force of adhesion is stronger $\Delta\alpha$ is negative and adhesion is strong whereas positive values of $\Delta\alpha$ will indicate that adhesion is weak. The former gives rise to Frank-Van der Merwe or layer by layer type of growth and later gives rise to island growth which is also known as Volmer-Waber (V-W) type of growth. In some cases, initially few layers of layer by layer growth take place, but strain energy makes it more favorable to form islands thereafter. This type of growth mode is called Stranski-Krastanov (S-K) mode. The V-W mode and S-K mode are more common in semiconductor heteroepitaxy^{130,134}.

With the help of the above equations, many of the observations regarding differences in the diameters nanostructures formed on the different surfaces can be explained. Surface wetting or adhesion of InN on Si is weaker than sapphire¹³⁵. As a result nucleation in general tends to be better on sapphire substrate. But the InN grown on Si is under tensile stress as compared to the InN grown on other substrates. This also is very important factor to be considered when InN is grown on any surface. For the overgrown layer grown under tension, it is energetically more favorable to form films and bigger grains for dislocations are readily be introduced in growing material as growth takes place¹³⁶. As a result, the nanorods tend to be bigger in size when grown on Silicon as compared to the sapphire substrate. Nitridation of silicon produces layer of β -SiN_x which is often detrimental to the further semiconductor growth. But silicon nitride is known to have hexagonal structure similar to InN basal plane. As a result the growth

on nitridated sample becomes more oriented vertically. As far as surface wetting is considered, the adhesion decreases and different sizes of InN nuclei can form and grown under V-W growth mode. As a result, growth on nitridated silicon becomes more directional but overall diameter distribution is widened.

The use of GaN and InN nucleation layers show two very opposite results when InN nanorods nucleate on these surfaces. The InN nanorods nucleating on InN will have no specific preference for layer by layer vs island growth. But, due to strain in InN layer and growth conditions used, island growth prevails. As a result nanorods with wide diameter distribution and random nucleations originate. In case of GaN nucleation layer however, due to difference in the materials, the adhesion is weaker as compared to perfect InN crystal itself. As a result, nanorods with smaller and uniform nuclei nucleate. The GaN layer on which nanorods are growing was found to be oriented in polar c-axis. The oligomer complexes that are responsible for nucleation of nanorods also have polar c-axis. As a result, these nuclei tend to align with GaN grains to form vertical nanostructures. The alignment of exact hexagonal basal plane to hexagonal c-plane of GaN grain in nucleation layer is energetically most favorable. Thus, if GaN film is well oriented in $[000\bar{2}]$ direction and has epitaxial relationship with substrate, InN nanorods growth also exhibits similar alignment. This is clear from the results of vertically oriented nanorods on Si in this study and that on sapphire in previous study¹²⁵.

The molecular kinetic theory of crystal growth states that for film to nucleate and grow, work of nucleation has to be overcome. The principle kinetic equation for the growth rate V of a crystalline face is given by following equation.

$$V = V_o \cdot \exp\left(\frac{-\pi \cdot \Omega \cdot \kappa^2}{k \cdot T \cdot a \cdot \Delta\mu}\right) \quad (2-16)$$

where Ω is molar volume

κ is edge energy which is related to specific surface energy of growing face

k is Boltzman constant

T is temperature

a is lattice constant

$\Delta\mu$ is supersaturation

The nucleation on kink site is energetically more rewarding than growth on step site. The nucleation on flat faces is least rewarding energetically. Because of this the closed packed faces, which tend to be very flat, are slowest growing faces and large supersaturations are required to increase rate drastically. As a result in crystal or film growth, slowest growing faces are the faces that generally remain at the end. As seen from the equation above, high supersaturation will be required to grow $\ln N$ along $[000\bar{2}]$ direction, and growth rate in $[000\bar{2}]$ direction cannot be greater than any other face. The nanorod is very anisotropic crystal and growth along c-axis is certainly faster than other nonpolar m-faces. As a result, according to this theory growth of nanorods is highly improbable. Still nanorods are found to have formed experimentally. These contradictions in the theory and experimental results can be eliminated if energetically growth of $(000\bar{2})$ plane is favored. Often it has been found that growth on nanorods proceeds by tip formation. The tips of nanorods are typically planes like $(10\bar{1})$, $(10\bar{2})$, $(10\bar{3})$ which have higher growth rates than m faces that form sidewalls of the nanorods. The se faces that form tip of the nanorods have step sites which increase the growth

rates. Often defects such as screw dislocation and twin defects are found at the tips¹²⁶ in high resolution TEM analysis. If the defect such as screw dislocation forms in c plane, a spiral step is introduced in otherwise perfect closed packed plane. This dislocation then acts as the continuous source of growth. But most of the flat tipped nanorods were highly single crystalline with no defects such as dislocations. As a result, growth mechanism of such flat tipped nanostructured nanorods had to be different. In HVPE the c-plane is often nitrogen terminated and faces such as $(000\bar{2})$ that are nitrogen terminated tend to be rough as compared to the (0002) faces which are metal terminated. Also due to polarity of these faces the sticking coefficients of polar molecules such as InCl which act as precursors is more on these faces. It can be seen mathematically as decrease in edge energy κ to a very small value. Decrease in edge energy, results in drastic increase in growth rate along c-plane. In fact, it has been observed that, mobility of Indium on m-faces is higher under ammonia rich conditions. The indium species tend to get absorbed on all surfaces as well as substrate and migrate to c-faces which are rapidly growing faces¹³⁷. This Vapor –Solid mechanism for InN nanorod growth seems to drive InN growth to form highly anisotropic crystals on various substrates.

The presence of V-S growth mechanism can be further confirmed by different characteristics of Vapor Solid growth. First of all, in any conditions, no Indium droplets are detected in SEM as well as TEM. The nanorods tend to have constant or slightly tapering diameters. This is indicator of In diffusing from side walls to c-faces or tips where growth rate is maximum. The taper is especially observed on microrods. As length of rod increases, it becomes more difficult for Indium to diffuse from faces to the

tip. As a result, stems tend to be fatter at the bottom and become narrower towards tips. Second feature of typical S-V growth is independent growth of nanorods. Nanorods often tend to grow and intersect and still keep growing into each other. In VLS mechanism, the intersection sites are often worked as new nucleation sites, or nanorods fuse and grow into one. The branching is only rarely observed branches seem to grow independently like new nanorods, which is typical in V-S mechanism.

The formation of tripods and random nanostructures in this mechanism is discussed in detail in other parts of Chapter 2. In accordance with the theory developed here, branching of nanorods can be initiated by formation of oligomeric clusters of $\text{InCl}_3\text{-NH}_3$ that have cubic form¹³³. Such clusters can nucleate, with (111) faces forming a tetrahedron. From each face of tetrahedron, however, more stable wurtzite InN nanorods can grow. Since (111) faces are at 120° in tetrahedron, tripods of nanorods are formed. In similar manner, different flower like clusters of nanorods can originate from more complex ring oligomers. No liquid droplet as nucleus is necessary to explain presence of such clusters and growth can proceed via V-S growth mechanism.

Summary and Conclusions

To summarize, the effect of different surface cleaning steps on InN nanorod orientation is presented in this Chapter. The study has presented different nucleation layer approaches that can be used to get preferred orientation of InN nanorod on silicon. The nanorods cannot be grown in preferential direction on silicon alone. Nanorods require similar material nucleation layer to control nucleation directions. By using textured nucleation layers like MOCVD GaN and HVPE GaN, the InN nanorods can be grown in [0002] orientation without use of any catalyst and patterning. The orientations depend on quality and type of nucleation layer. The results also suggest

that the size of nuclei formed by oligomerization nucleation reaction between chlorinated species of Indium ammonia can vary depending on nucleation layer. Thus, diameter of nanorods is determined by nature of nucleation layer in addition to temperature, NH_3/TMI ratio and HCl/TMI ratio.

The study also shows that, InN_{NR} tend to follow exact texture of underlying film, if they have similar crystal structures. The nanostructures grown tend to be very uniform dimensions on smother uniform films. In all, nanorod show excellent crystal quality. They show no oxide layer formation on the surface and are highly crystalline in nature. The defects tend to be agglomerated at certain locations such as bottom of nanorods. In the end it can be concluded that choosing the right surface treatments and controlling the quality of nucleation layer is critical to control the orientations of InN nanorods. The vertical single crystalline nanorod growth on silicon is possible using textured GaN layer on silicon. Key to get even better textures on InN_{NR} lie only in improvement of nucleation layer.

The effect of various parameters considering both gas phase oligomerization mechanism as well as surface energetics is discussed at the end of the Chapter. Detailed analysis on observed results showed that possibly gas phase oligomerization and formation of $\text{InCl}_3\text{-NH}_3$ ring complexes was responsible for initial nucleation at high Chlorine to Indium ratios. The nucleation then proceeded to produce InN nanorods by Vapor Solid growth mechanism. The high aspect ratio of InN crystals to form nanorods, was the result of enhanced growth rates of c-direction because of various factors such as surface roughness, possibility of surface defects such as screw dislocations The tip formation can also lead to enhanced growth rates. Possibility of higher sticking

coefficients of polar species such as Indium Chlorides on polar faces and high surface mobility of Indium species resulting in migration of reactants to c-faces was also thought to be responsible for high growth rates of InN in $[000\bar{2}]$ direction. As a result, possible growth mechanism of random as well as vertical nanorods was discussed in its entirety.

Table 2-1. Peak ratios corresponding to (101)

Peak ratio	A1	A2	B	C	D	E1	E2 Si(100)	Si(111)
(100)/(101)	0.16	0.02	0.34	0.06	0.07	0.10	0.04	0.06
(002)/(101)	1.35	1.15	3.18	2.53	1.17	16.33	68.42	11.63
(101)/(101)	1.00	1.00	1.00	1.00	1.00	1.00	1.00	1.00
(102)/(101)	0.43	0.29	2.81	0.20	0.18	1.30	0.00	0.06

Table 2-2. Relative peak intensity ratios for various surface treatments

Peak ratio	A1	A2	B	C	D	E1	E2 Si(100)	Si(111)
(100)	0.25	0.04	0.23	0.08	0.13	0.02	0.00	0.02
(002)	2.28	2.32	2.18	3.30	2.40	4.32	4.88	4.51
(101)	0.69	0.82	0.69	0.54	0.84	0.11	0.03	0.16
(102)	1.65	1.33	1.93	0.59	0.82	0.78	0.00	0.06

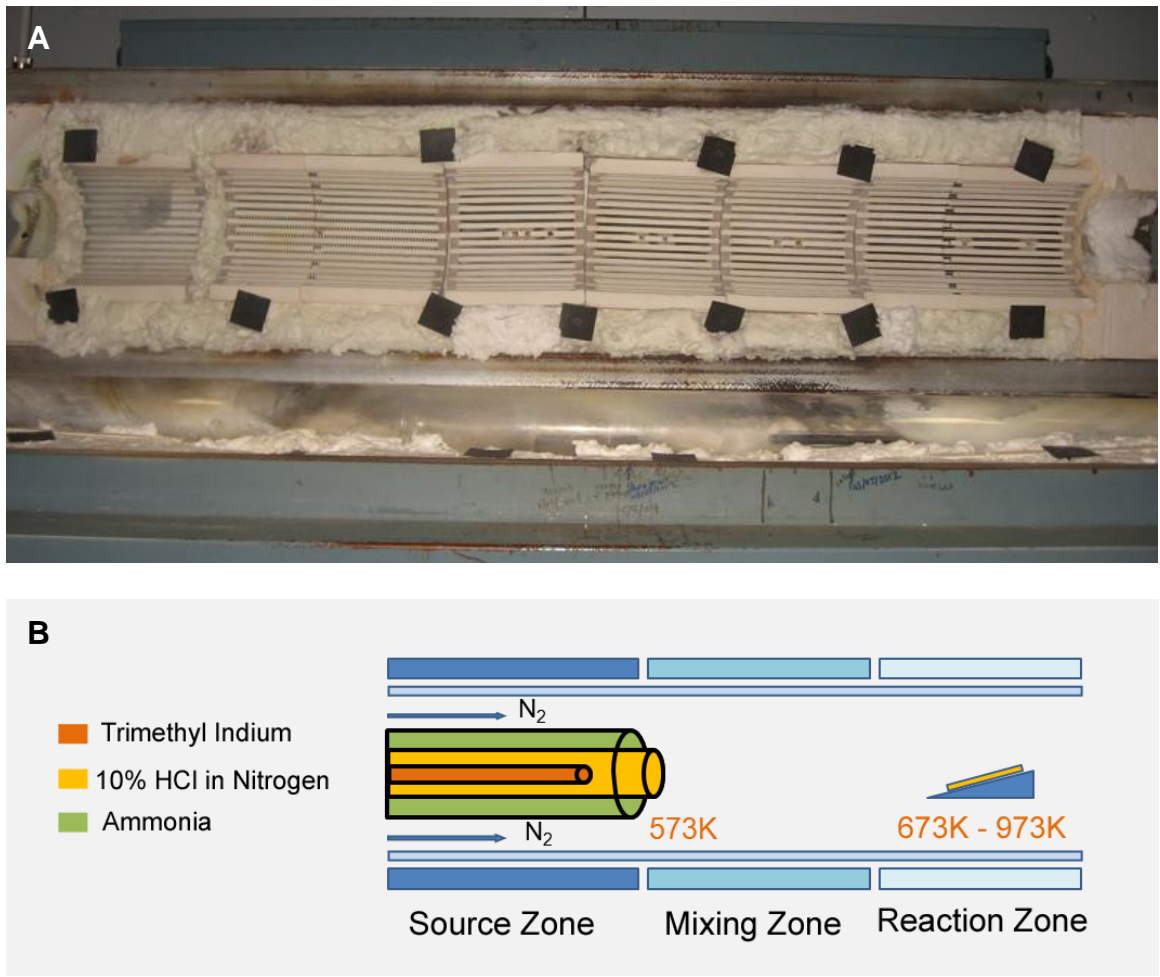


Figure 2-1. MO-HVPE Reactor. A) Reactor Picture, B) Reactor Schematic

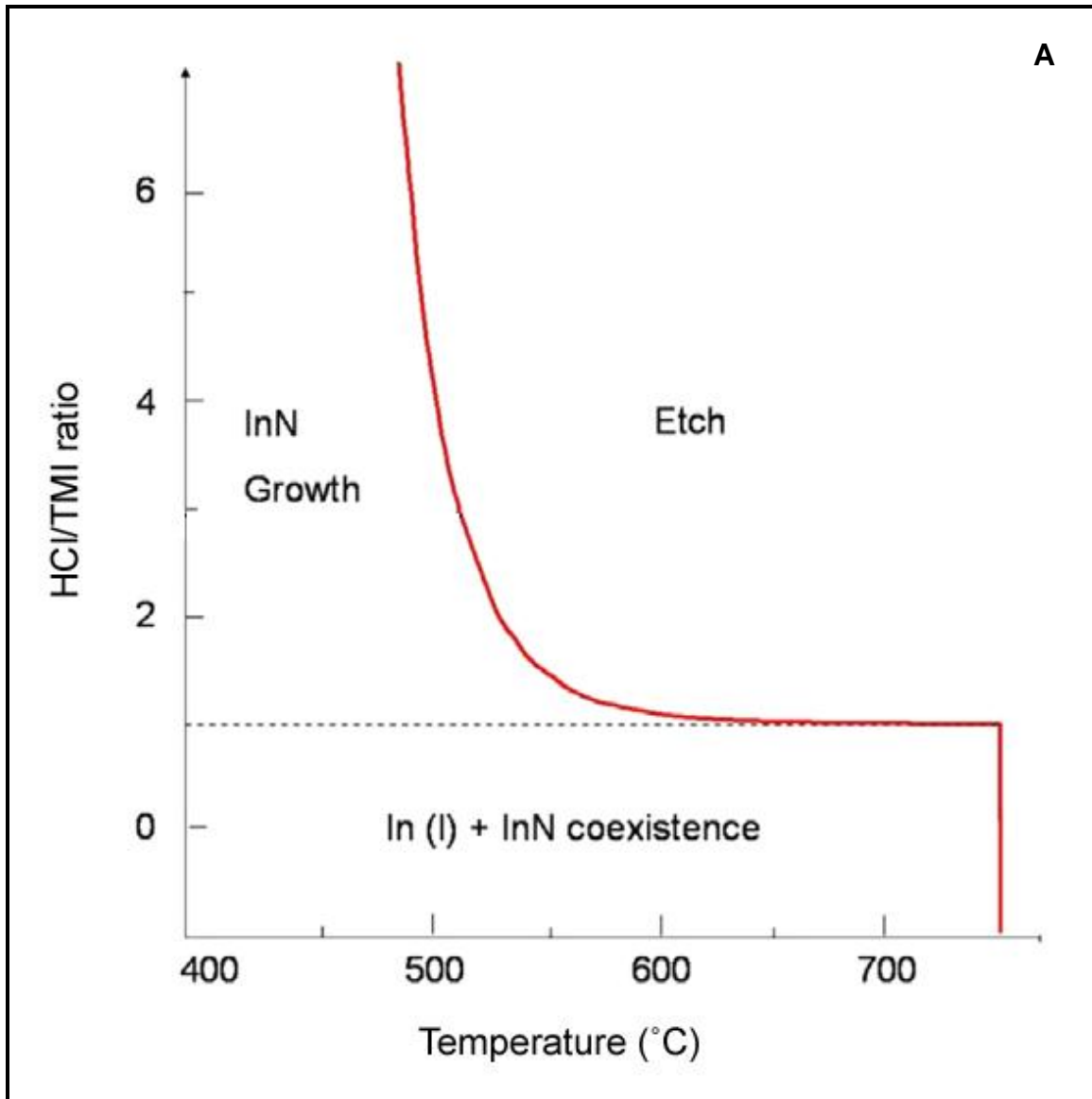


Figure 2-2. InN growth map from MO-HVPE. A) Growth etch transition temperature for InN as a function of HCl/TMI at constant $V/III = 250$, B) Transition temperature map with actual InN growths on c-Al₂O₃^{111,125}

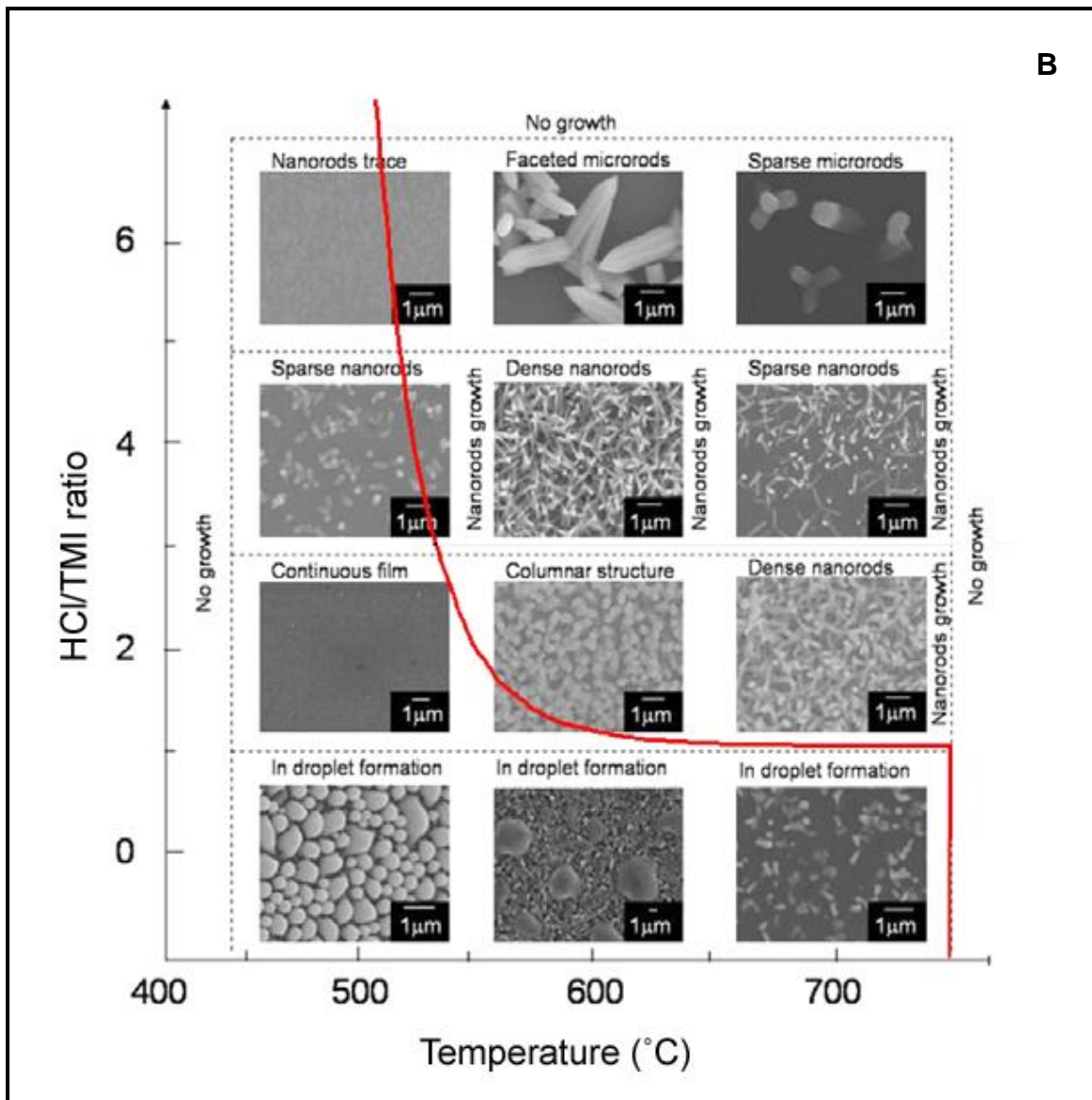


Figure 2-2. Continued

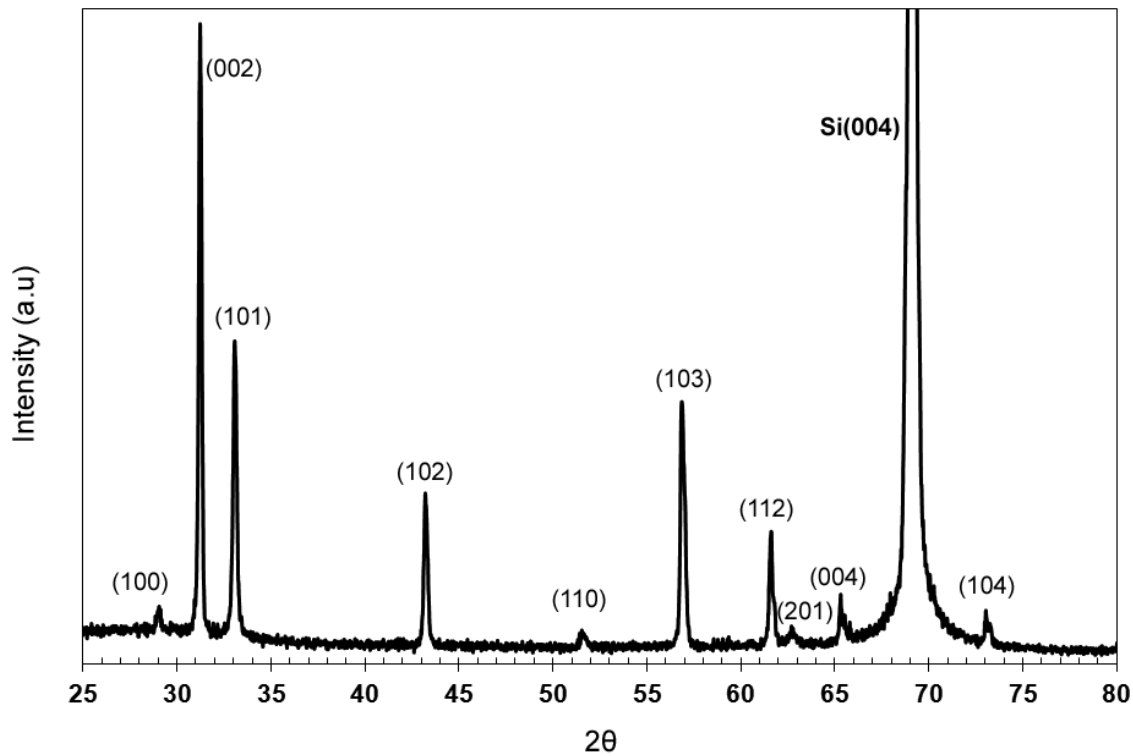


Figure 2-3. XRD θ - 2θ scan of InNNR on Si (100) Growth conditions V/III =250, CI/III=4.0, T= 873K

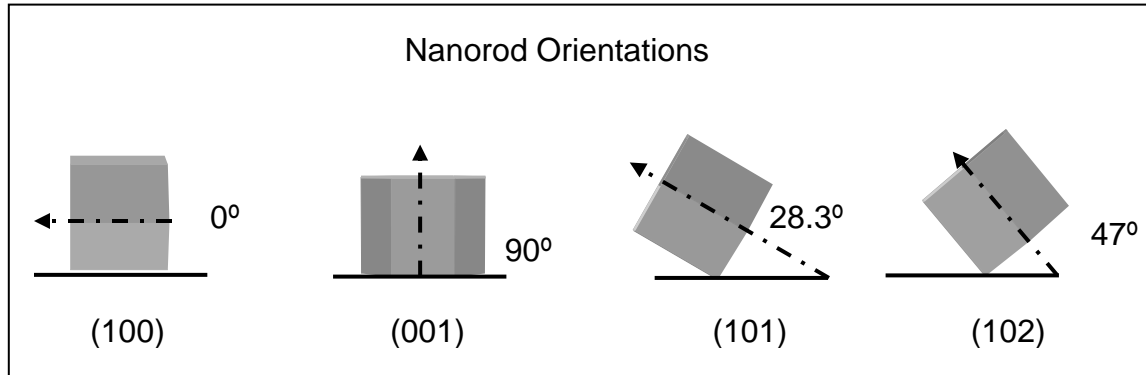


Figure 2-4. Various InN nanorod orientations. Every nanorod orientation forms specific angle with the surface

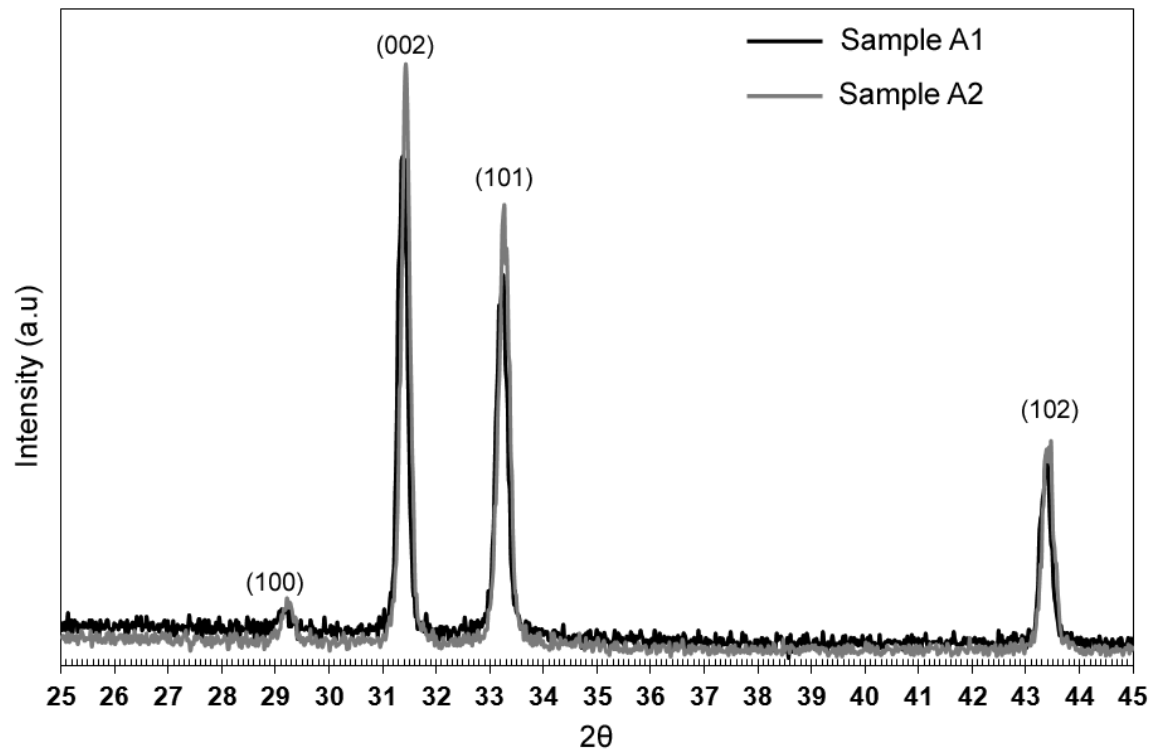


Figure 2-5. XRD θ - 2θ scans for nanorods grown on Si(100) showing effect of surface cleaning. Growth conditions $V/III = 250$, $Cl/III = 4.0$, $T = 600$ °C for 60 minutes

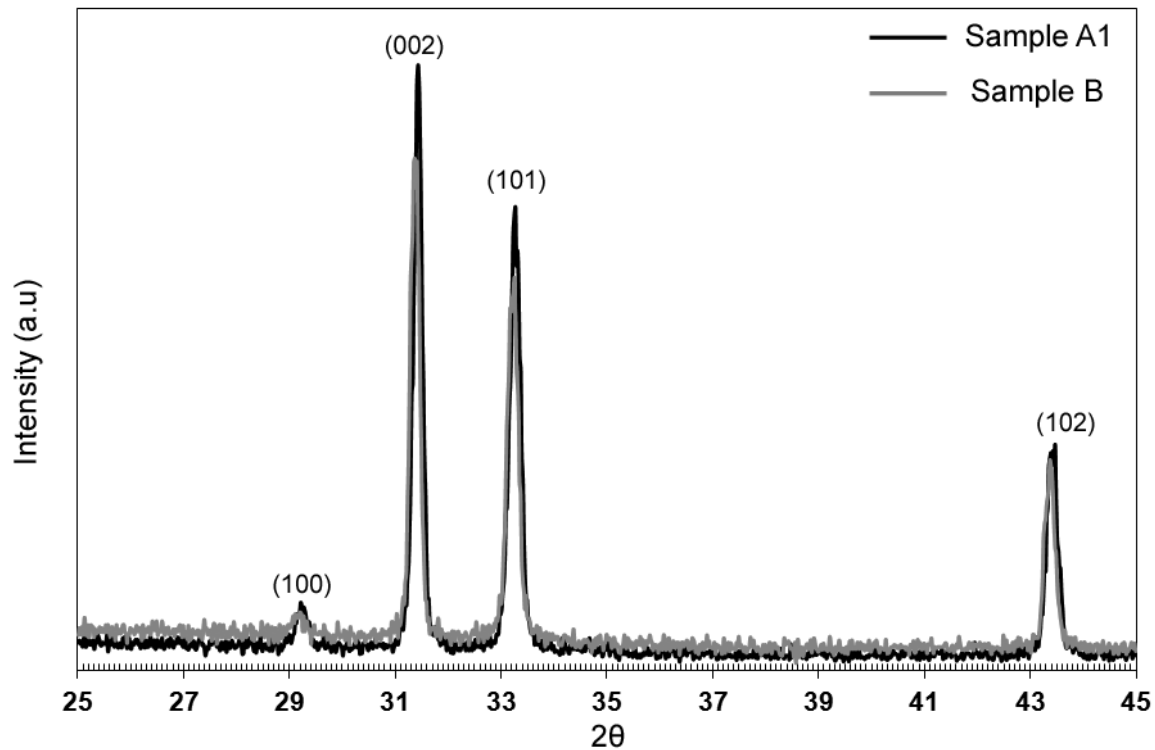


Figure 2-6. XRD θ - 2θ scans for nanorods grown on Si(100) showing effect of surface cleaning with HCl. Growth conditions: V/III =250, Cl/III=4.0, T= 873K for 60 minutes HCl cleaning conditions :FHCl=1500sccm, T= 873K for 10 minutes

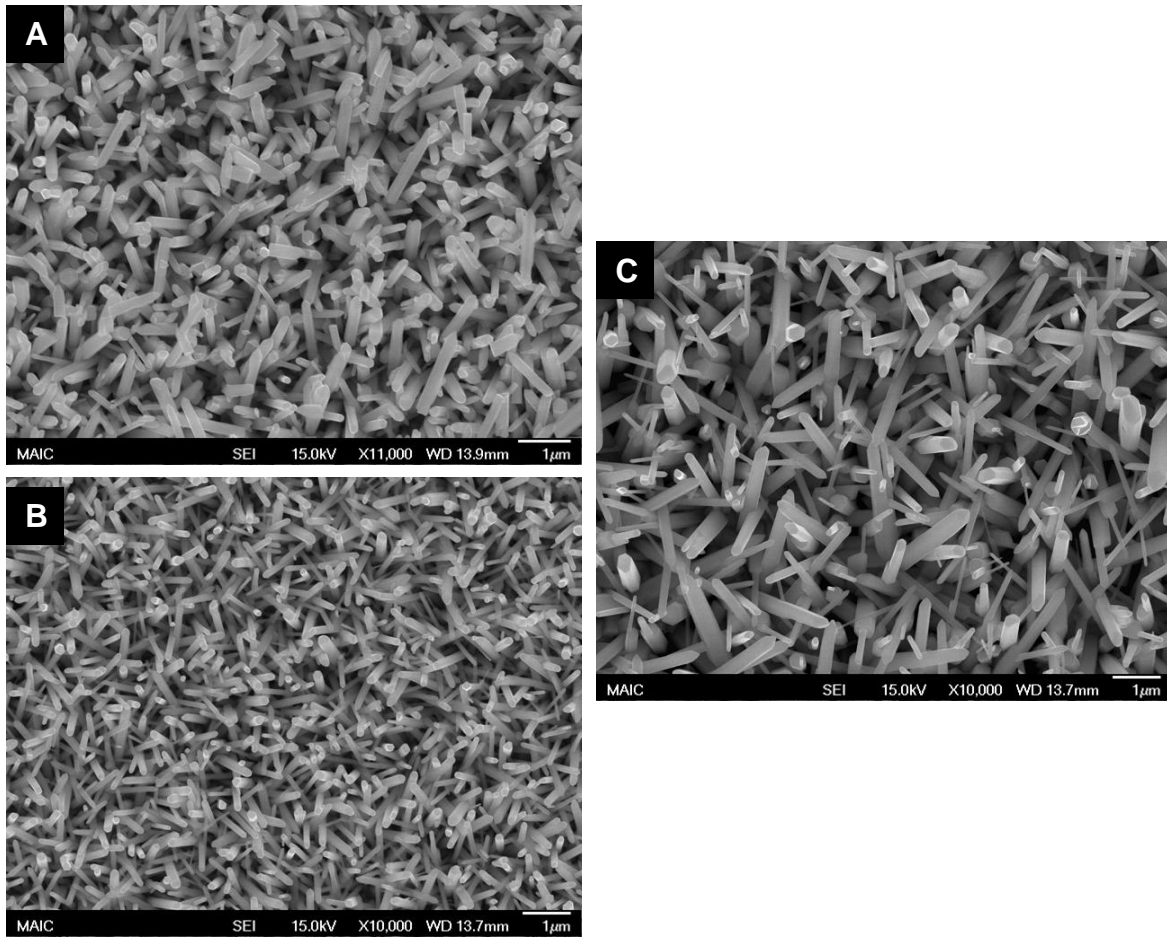


Figure 2-7. SEM images (10000x) showing effect of surface cleaning on InNNR. A) A1: InNNR on degreased Si (100), B) A2: InNNR nanorods on BOE cleaned Si (100), C) B: InN nanorods on nitridated Si (100)

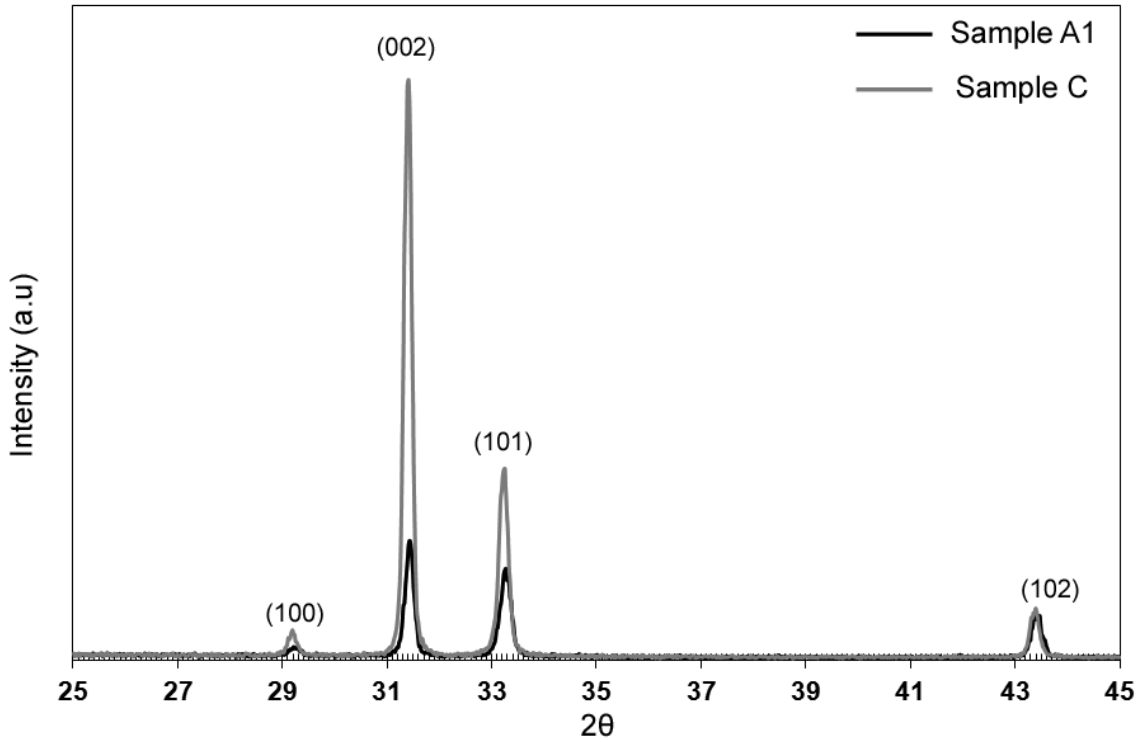


Figure 2-8. XRD θ - 2θ scans for nanorods grown on Si(100) showing effect of surface nitridation Growth conditions: V/III =250, Cl/III=4.0, T= 600 °C for 60 minutes Nitridation conditions:FNH₃=1500sccm, T= 560 °C for 10 minutes

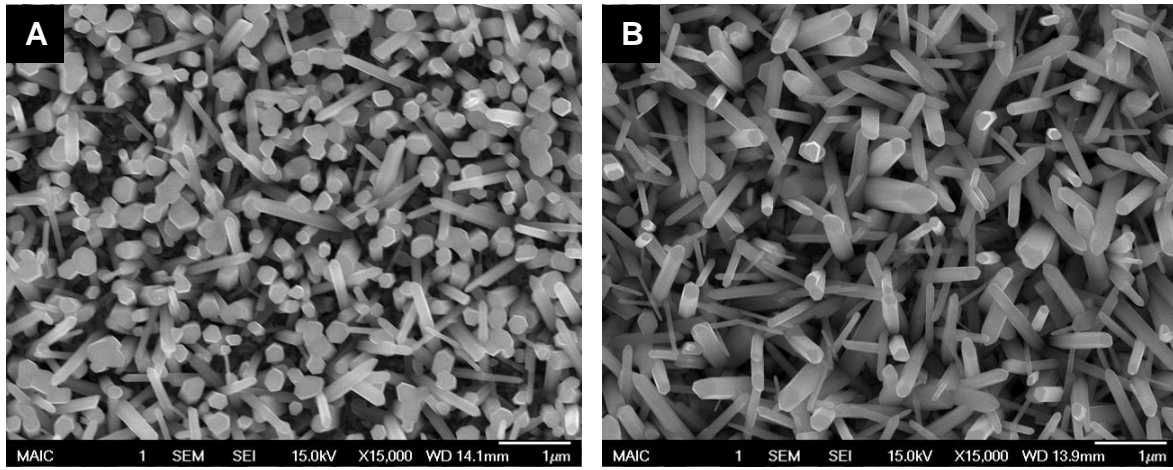


Figure 2-9. SEM images showing effect of nitride layers. A) InN_{NR} grown on nitridated Si (100), B) InN_{NR} grown on InN film as a nucleation layer

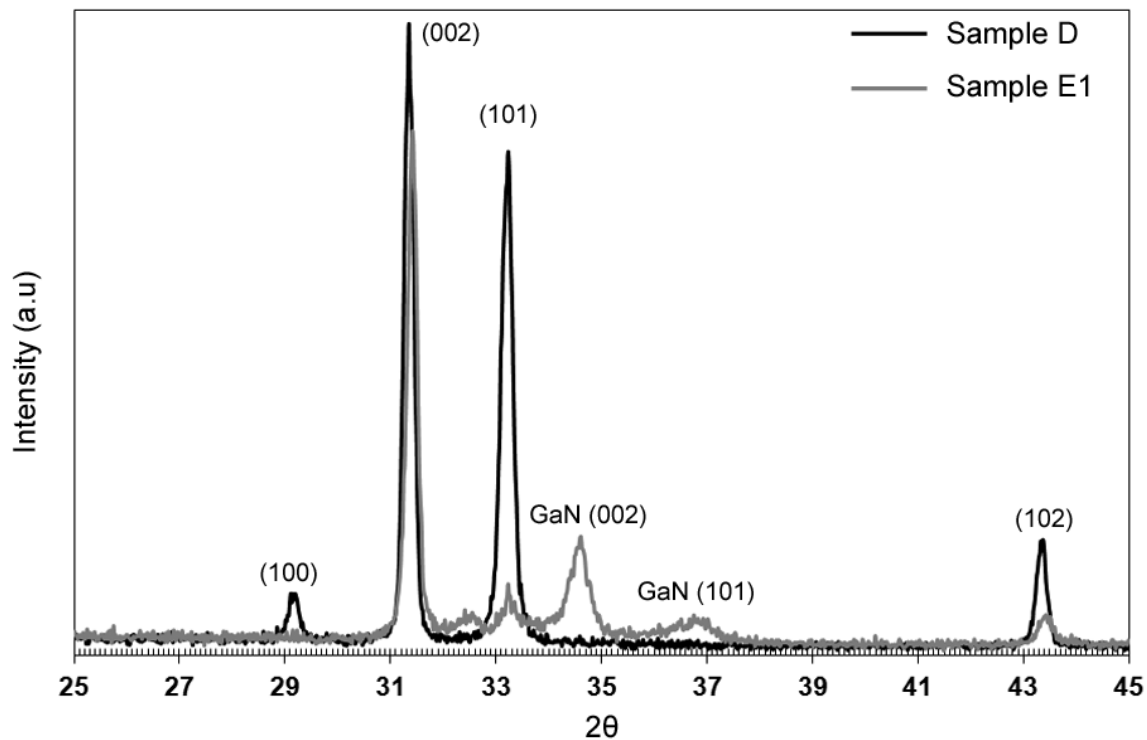


Figure 2-10. The XRD θ - 2θ scans for nanorods grown on Si (100) showing effect of using InN nucleation layer (Sample D) vs MOCVD GaN as nucleation layer (Sample E1). Growth conditions: Nanorods: V/III =250, Cl/III=4.0, T= 600 °C for 60 minutes, InN layer: V/III =700, Cl/III=2.0, T= 600 °C for 10 minutes, GaN layer: V/III =3000, Cl/III=0.0, T= 600 °C for 30 minutes

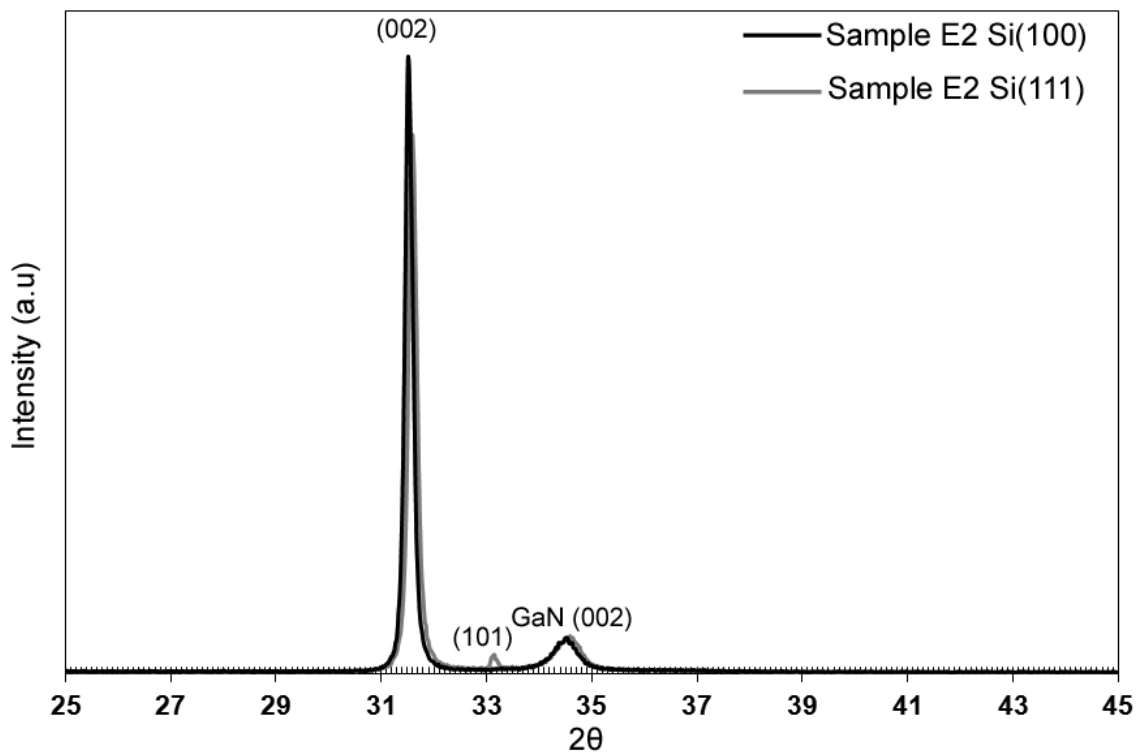


Figure 2-11. The XRD θ - 2θ scans for nanorods grown on HVPE GaN nucleation layer with Si(100) and Si(111) as substrates. Growth conditions: Nanorods: V/III =250, Cl/III=4.0, T= 600 °C for 60 minutes, GaN layer: V/III =570, Cl/III=2.0, T= 600 °C for 10 minutes

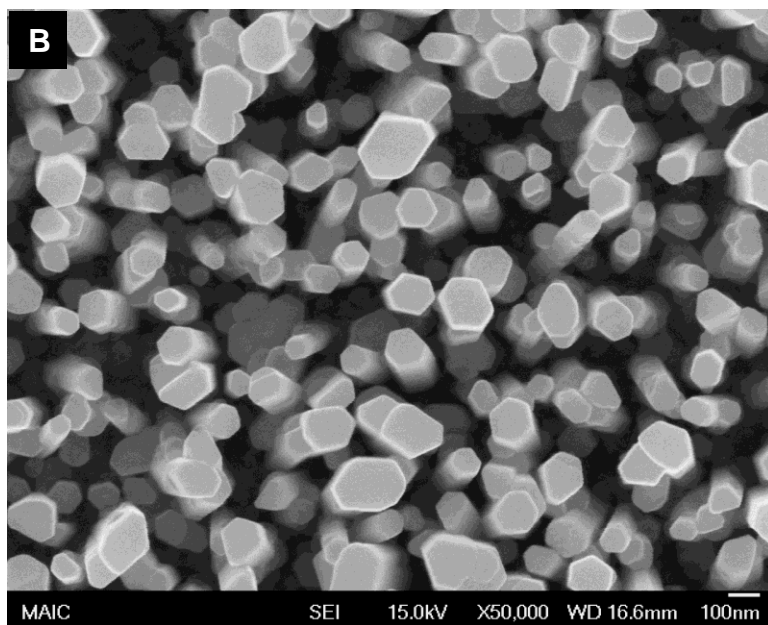
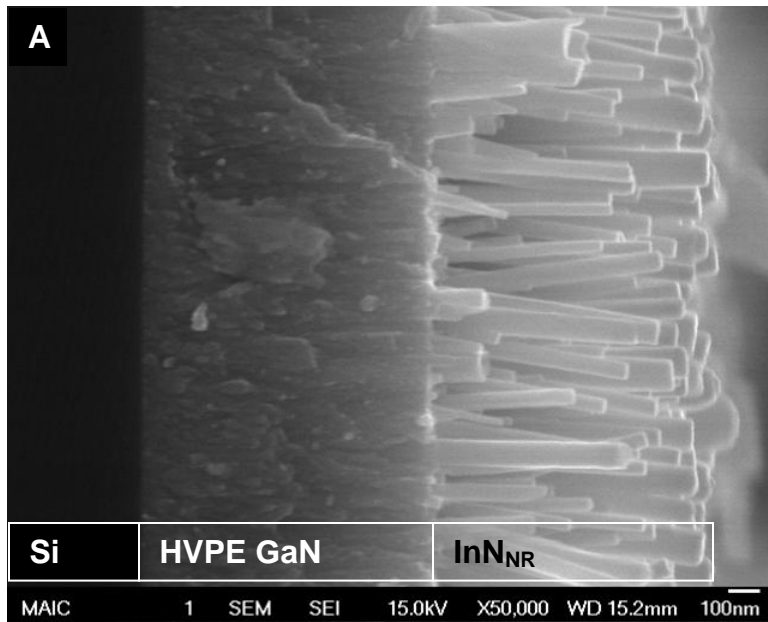


Figure 2-12. SEM images of vertical InN nanorods. A) cross sectional view showing InN nano/GaN/Si(100) structure B)top view

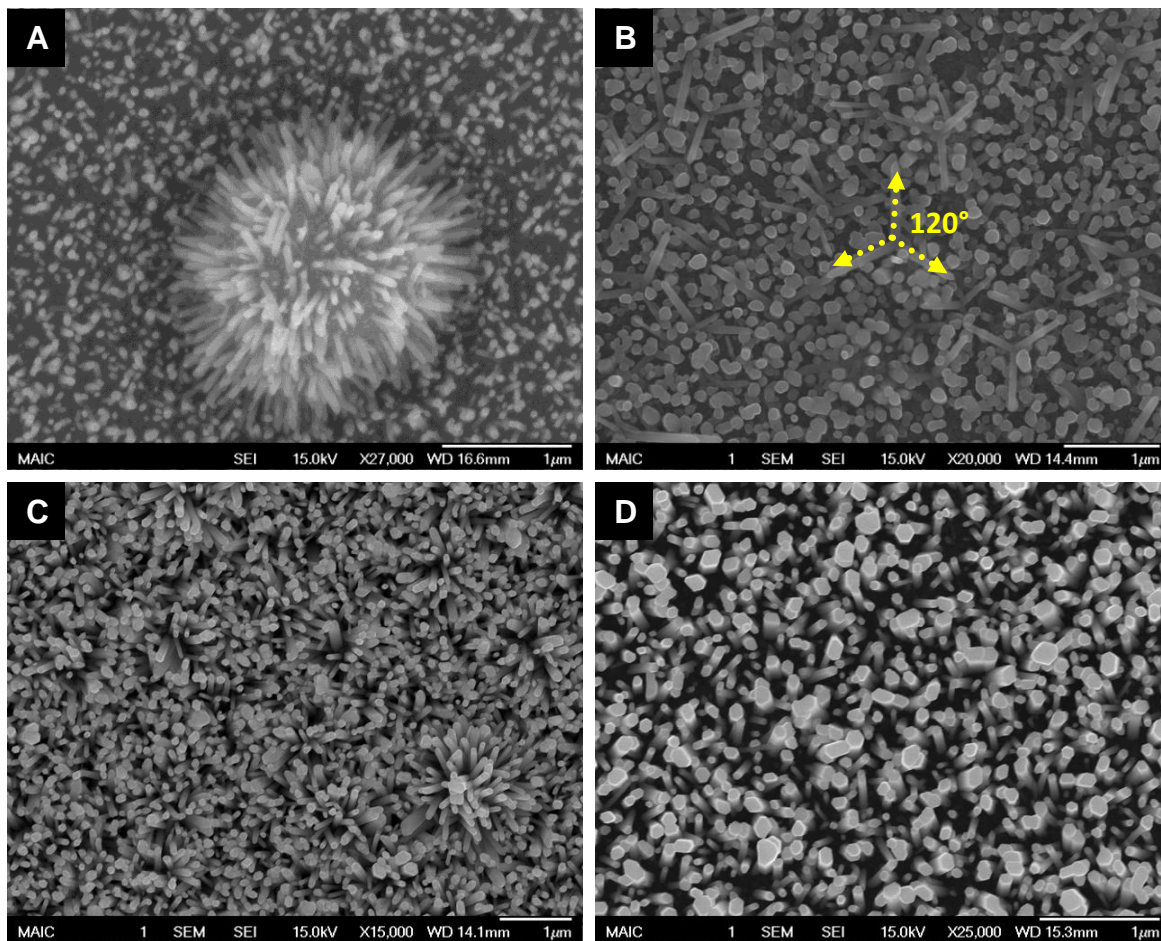


Figure 2-13. SEM images of vertical InN nanorods grown on MOCVD and HVPE GaN. A) Multiple nucleation spot on MO-GaN surface, B) Vertical nucleations with tripods on HVPE GaN, C) Dense growth with uniform diameters on MO-GaN, D) InN_{NR} grown on HVPE GaN

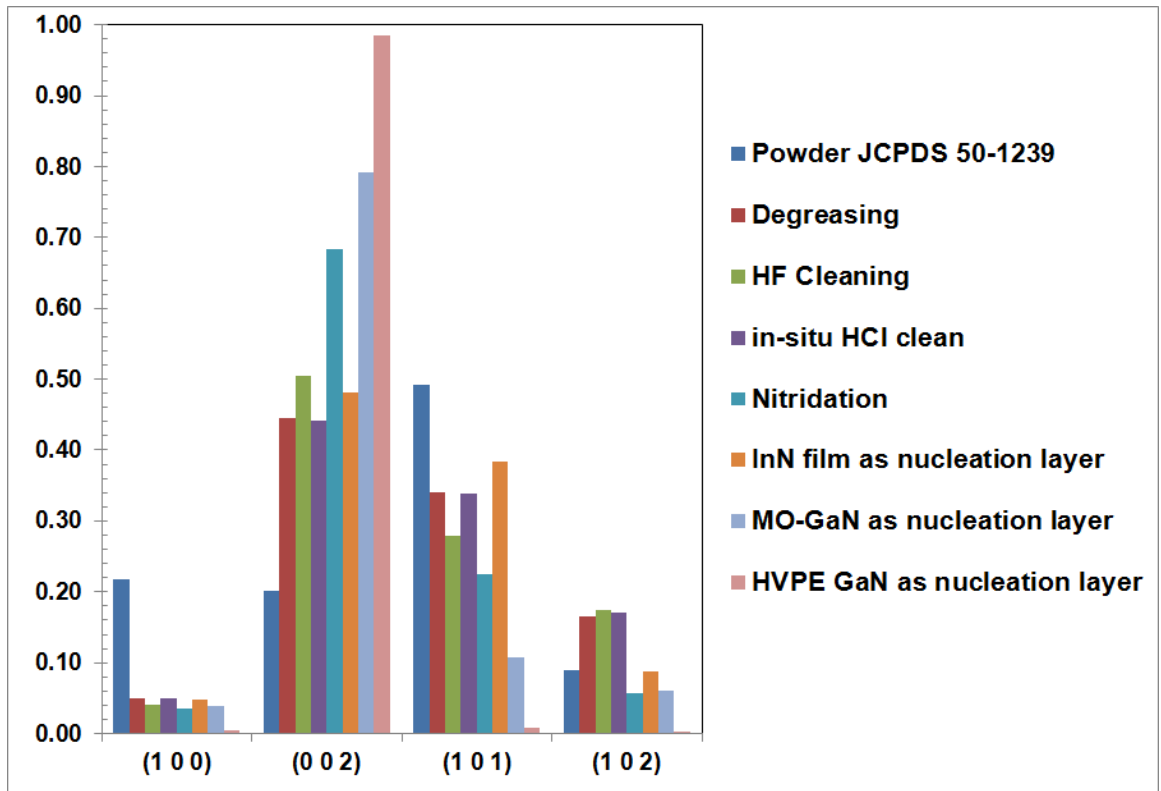


Figure 2-14. Summary of effect of treatments on orientations of InN_{NR}

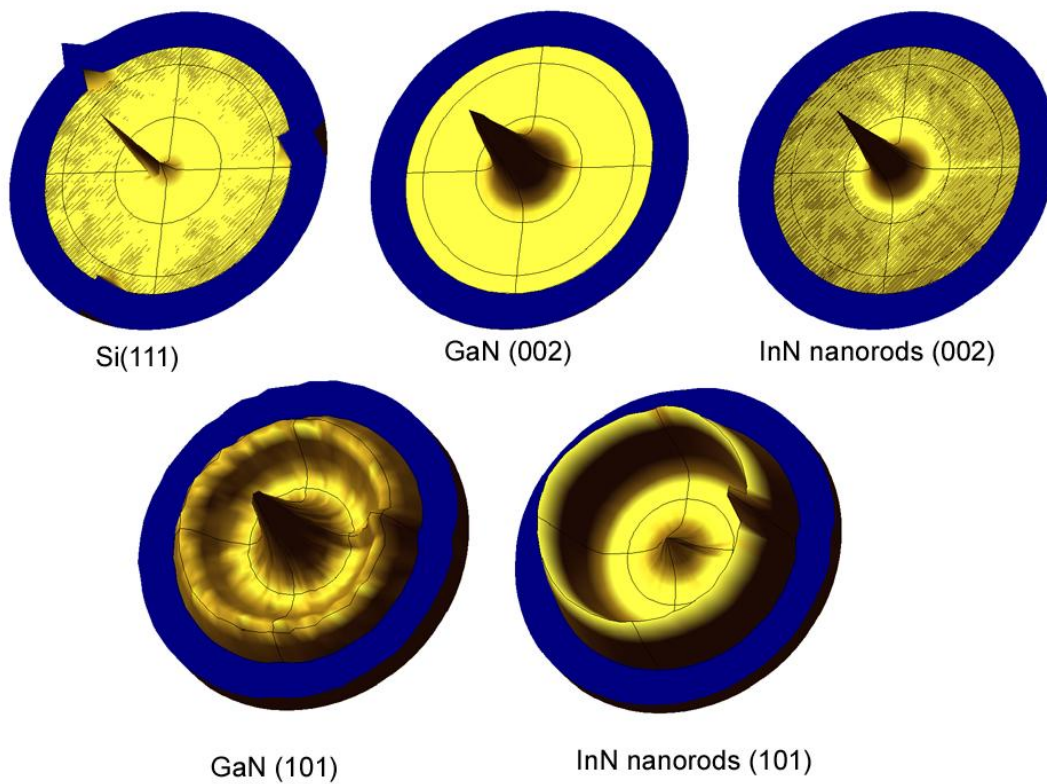


Figure 2-15. Pole figure of InNNR grown on HVPE GaN on Si (111) sample in [002] and [101] directions

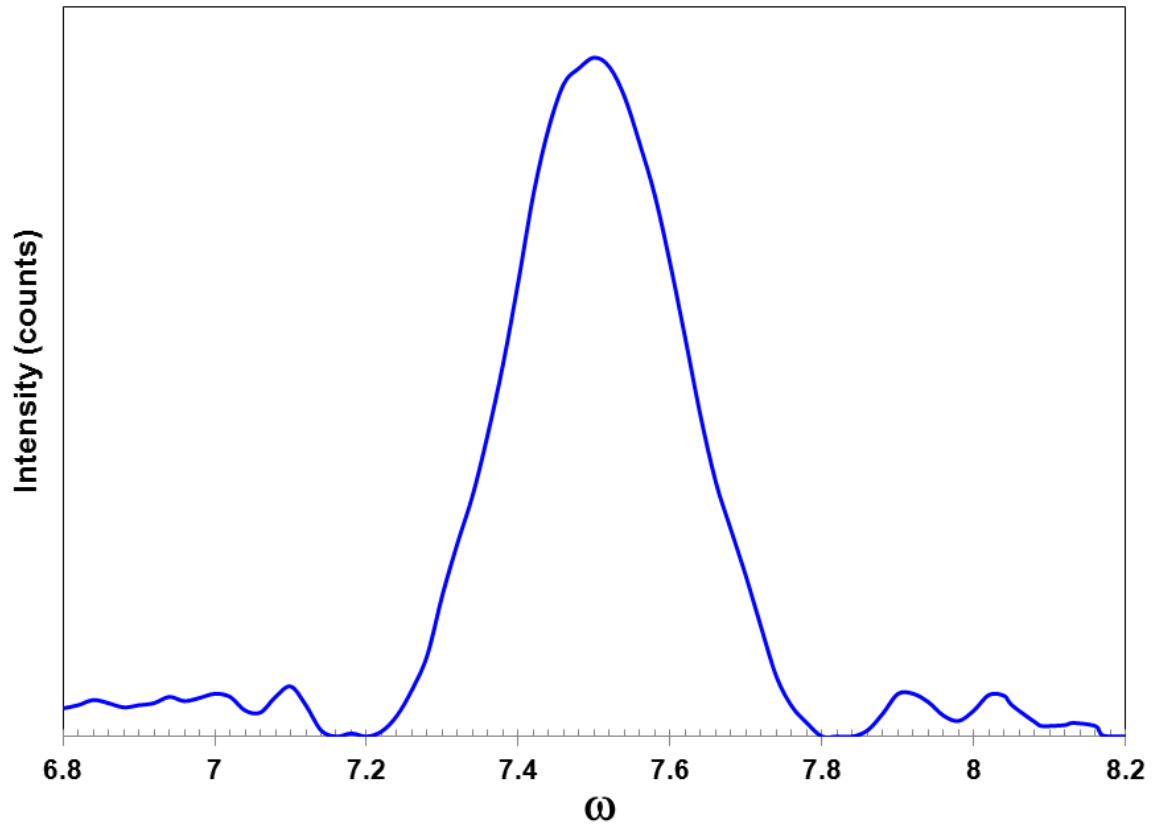


Figure 2-16. ω -rocking curve of vertical InN_{NR} sample with Molybdenum X-ray source

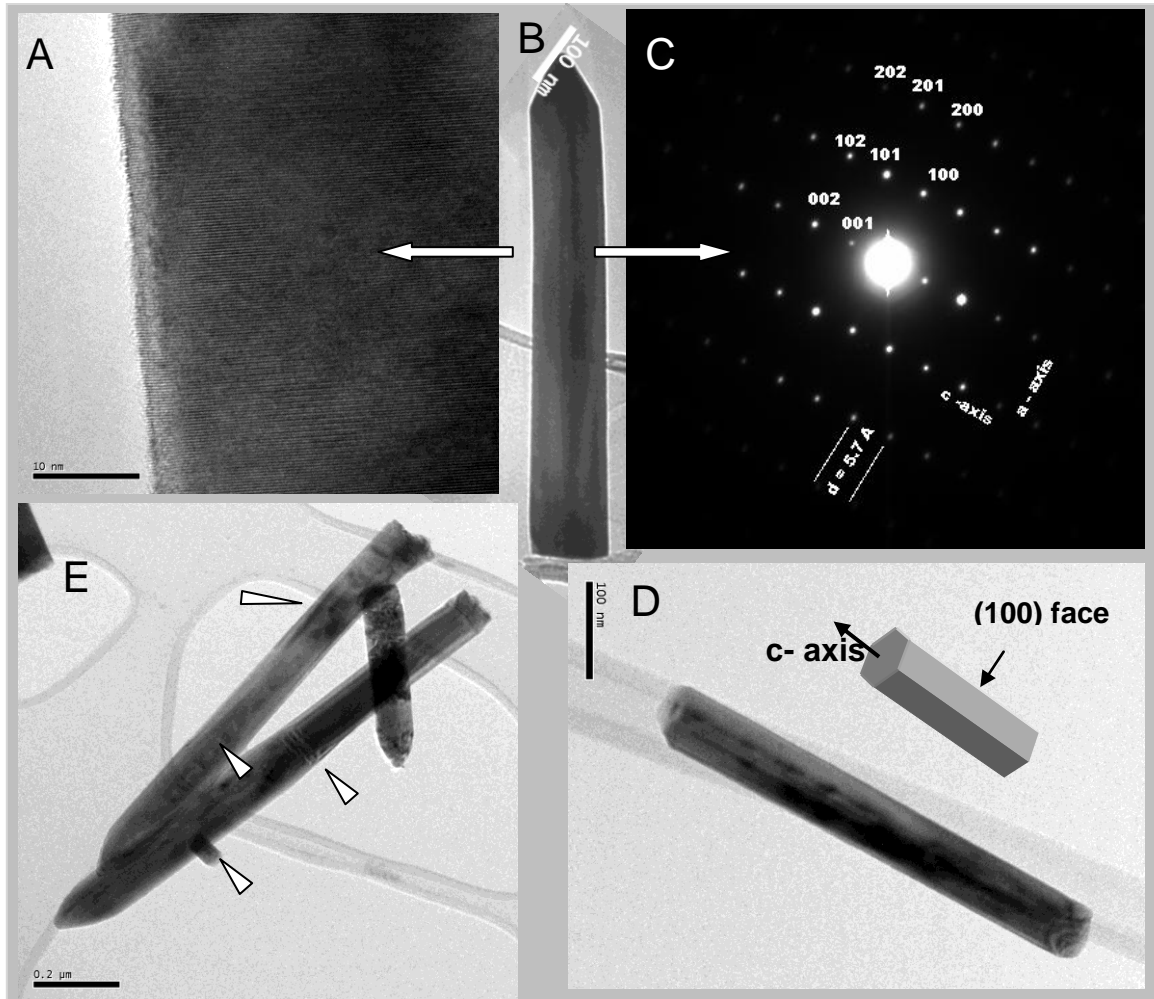


Figure 2-17. TEM analysis of nanorods A)lattice fringe image of nanorod in B, B) Tipped InN nanorod of 100 nm diameter, C)SAED pattern showing wurtzite pattern of nanorod in B, D)flat tipped InN nanorod with cartoon showing explanation for SAED orientation, E)Tipped nanorods with planar defects visible, also shows secondary nucleation.

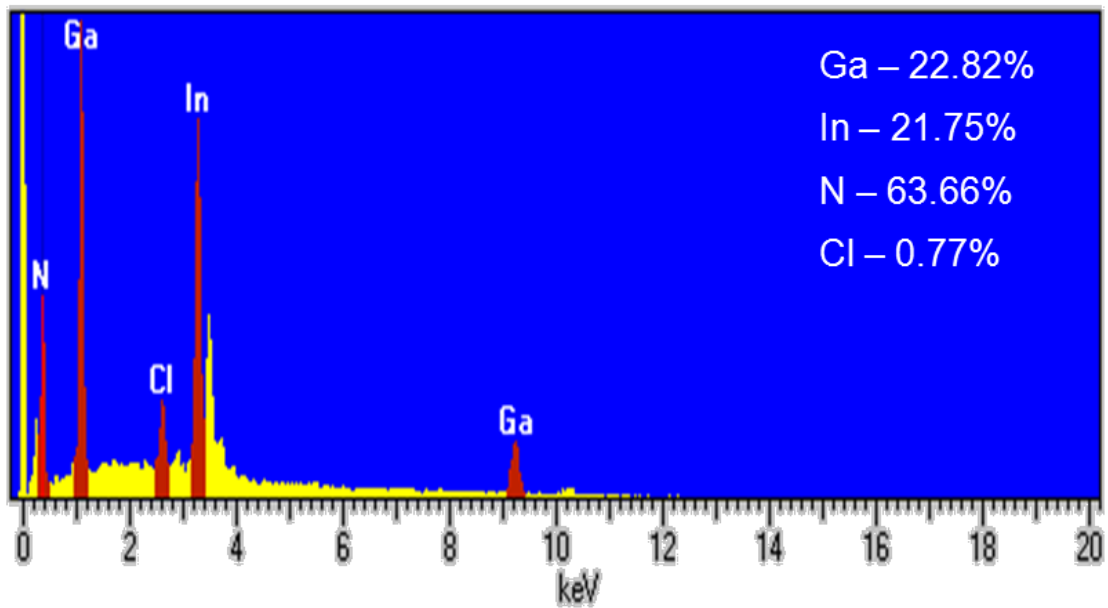


Figure 2-18. EDS spectrum InN nanorods grown on HVPE GaN on Si (100) (Sample E2)

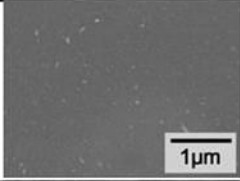
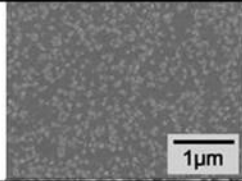
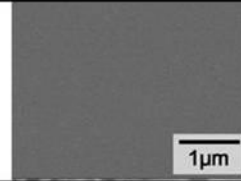
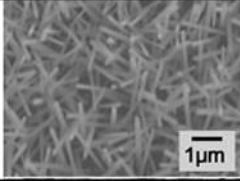
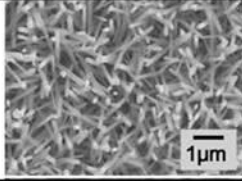
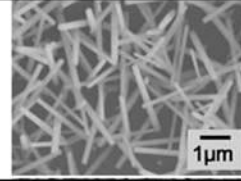
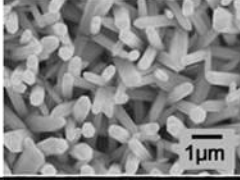
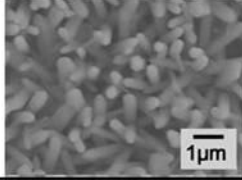
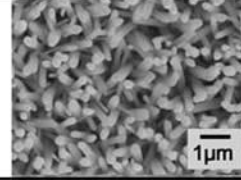
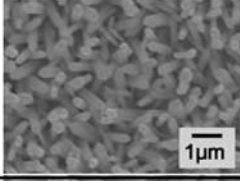
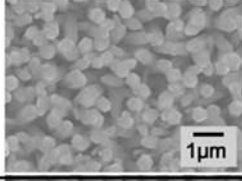
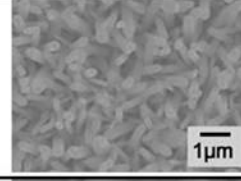
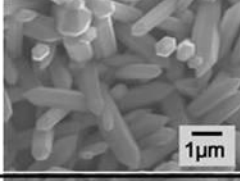
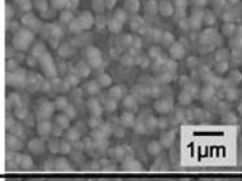
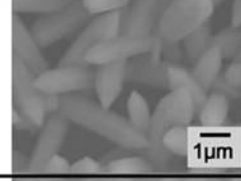
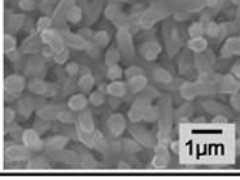
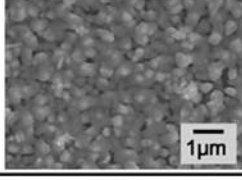
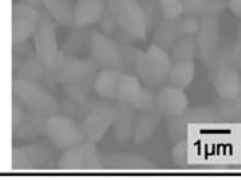
NH_3/TMIIn \backslash Substrate	c- Al_2O_3	GaN/c- Al_2O_3	Si (111)
100			
250			
500			
1000			
3000			
7000			

Figure 2-19. Effect of N/In ratio and Substrates on InN morphology at $\text{Cl}/\text{In}=4$ and $T=873\text{K}$ ¹²⁵

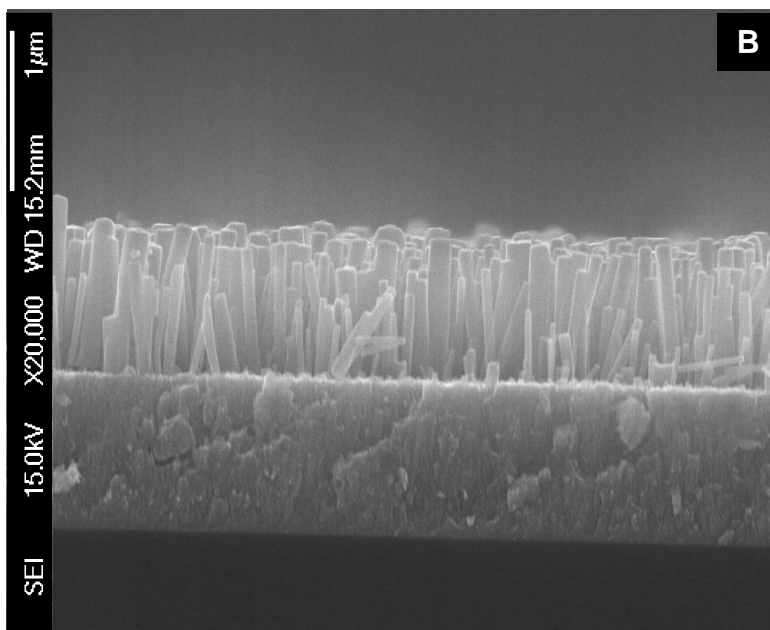
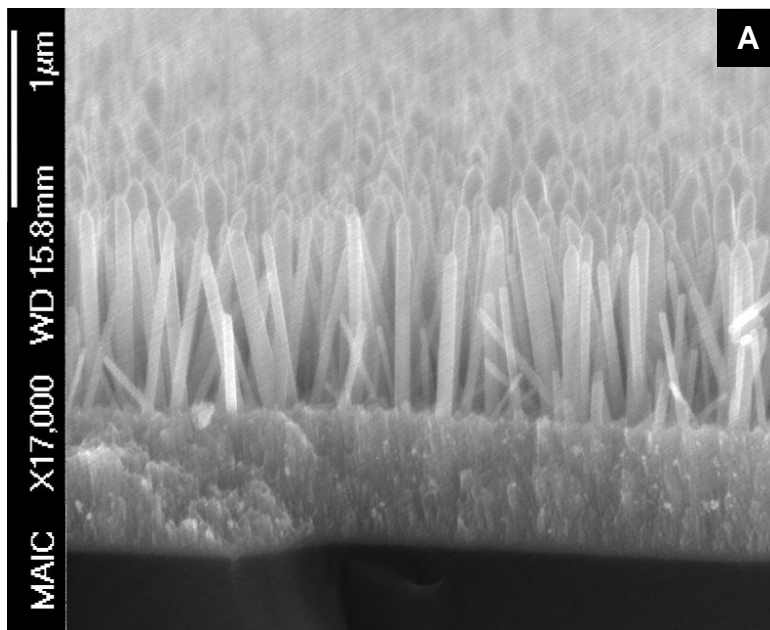


Figure 2-20. Vertical InN nanorods grown on GaN nucleation layer on Si(100) A) Conical tipped nanorods, B) Flat tipped nanorods

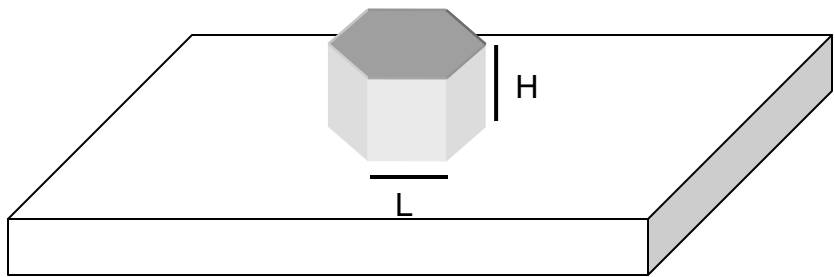


Figure 2-21. Heterogeneous nucleation of hexagonal parallelepiped on substrate

CHAPTER 3 THEORITICAL MODEL FOR FINDING LIMITS OF COHERENCY FOR INDIUM NITRIDE NANORODS GROWN ON GALLIUM NITRIDE

Overview

Traditionally used planar hetero-structures have various limitations. They have lower surface area resulting in lower efficiencies. Due to lattice mismatches, defects like dislocations are common at hetero-interfaces. Dislocations are preferred sites for impurity items. They act as high diffusivity path for dopants and also as nonradioactive recombination centers. They can be precursors for crack formations at interfaces with higher lattice mismatch. Nanostructures such as nanowires and nanorods, on the other hand, are going to be essential building blocks of the semiconductor technology. Due to properties like high surface area and single crystalline nature, nanostructures are one of the best candidates for applications like light emitting diodes (LEDs), laser diodes (LDs), detectors and solar cells. Various researchers have demonstrated formation of highly crystalline nanostructures despite of high lattice mismatches between substrate and deposited material^{111,112,117,120,138,139}. Moreover the use of highly crystalline nanostructured templates for improving the quality films in heteroepitaxy has been demonstrated by various researchers^{89-92,94-96}. The same was true in case of InN_{NR} grown on GaN in previous Chapter.

Crystal Growth Modes

In the field of crystal growth and heteroepitaxy, there are three basic accepted modes of the growth¹³⁰. The *figure1* shows schematic of these modes at different coverage. The Volmer-Weber (V-W) growth mode (Figure 3-1 (A)) is characterized by island growth. This mode is a result of stronger interactions amongst ad-atoms than that between ad-atoms and substrate atoms. When surface energies are significant and $\sigma_1 >$

$\sigma_2 + \gamma_{12}$, where σ_1 , σ_2 and γ_{12} are surface energy of substrate, surface energy of epilayer and interfacial energy between substrate and epilayer respectively, V-W growth is observed. The Frank-van der Merwe mode, on the contrary, is the layer by layer growth mode (Figure 3-1 (B)). In this mode, ad-atoms preferentially attach to the surface of substrate forming uniform layer. The monolayers cover surface completely before the next layer grows. This results in 2D growth resulting in smooth films. The third growth mode is intermediate case between the modes explained above. It is called Stranski-Krastanov (S-K) growth mode¹⁴⁰. In this mode, the layer by layer growth till critical thickness is followed by island growth. The transition of growth mode observed here depends on properties like surface energies, interaction energies, lattice mismatch between substrate and film. For example, in systems such as Ge/Si surface energies do not differ significantly, interfacial energy is not significant but there is a large lattice mismatch between the two. In such case, initially layer by layer growth occurs, which introduces strain energy. When strain energy reaches certain critical limit, it can be relieved by formation of dislocations or switching to V-W growth (island formation) or both. Thus, in semiconductor systems, that have large lattice mismatch, but similar structures, S-K growth mode is observed e.g. Ge/Si¹⁴¹, InAs/GaAs¹⁴². In the S-K mode, the island formation might be coherent or dislocated. In coherent S-K, the 3D island growing remains coherent below certain critical size. This can occur because the interface region where islands form remains strained with some radius of curvature. Moreover, dislocations can be introduced either in layers or islands if islands are close together or if islands exceed critical size.

In heteroepitaxy, the growth of epilayer can take place ideally in basically two ways viz. dislocated film growth and pseudomorphic film growth. Due to lattice mismatch the dislocations tend to form resulting in interfacial dislocations or dislocated film. This is the first type of growth. In later case, however, due to epitaxial nature of the growth, epilayer grows pseudomorphically or epilayer is homogeneously strained such that its lattice parameter matches with the substrate. These two extremes are shown in Figure 3-2 for the case of InN film growth on GaN film.

Ideally, observed growth tends to be the combination of both modes. That is, first few layers tend to grow pseudomorphic to the substrate. In these layers substrate and epilayer at interphase are coherently strained. This strain is stored in the form of strain energy. This pseudomorphic growth continues, until it is energetically favorable to form dislocation to relieve some strain. Over the years there have been various theoretical developments based on this approach that have helped engineering hetero interfaces. Initial theoretical developments by J. H. van der Merwe form fundamental approach to explain crystal interfaces in heteroepitaxy¹⁴³⁻¹⁴⁶. In 1975, Mathews improved this model further by adding mesh of non-interacting perpendicular dislocations to calculate critical thickness of coherency for 2D film growth^{147,148}. In nanostructures, however, approach that is applied to 2D film growth is not valid as it is. Extension of approach to calculate stresses in bimetal thermostats⁸⁷ to heteroepitaxy on patterned substrate predicted reduction in stress and higher coherent thickness of epilayer⁸⁸. It showed that the finite dimensions of the nanostructures, the strain is much reduced as a result of lateral relaxation away from interface. This theory formed basis of nanoheteroepitaxy⁸⁹ which has been widely used since, to reduce the defects in epilayer^{90-92,94-96}.

Strain vs. Dislocation Model for Heteroepitaxy

On the similar lines of nanoheteroepitaxy model⁸⁹ and Matthews' model¹⁴⁷, model for nanostructures was developed¹⁴⁹. The model was primarily developed for cubic material case which is modified for hexagonal or wurtzite crystal structure here. As discussed earlier, nanorods, due to the 1D nature of growth, tend to relieve the strain (arising due to lattice mismatch) both laterally and vertically away from interface unlike 2D films. As a result nanostructures tend to be single crystalline over wider dimensions. The heteroepitaxial films, on the other hand, form dislocations. This model captures this behavior of nanostructures. The model assumes strains in all three directions unlike 2D film growth models. The strain energy is function of all these strains as well as dimensions of nanostructures such as diameter and height (if nanostructures are cylindrical). For a given strain, below certain diameter nanostructures can be defect or dislocation free for any given height. This coherency limit for nanowire diameter is out of reach for conventional 2D film models that predict critical thickness of the films. The same model can be used to predict the critical coherent thickness by assuming very large radial spans.

There are various assumptions in the model in order to simplify model for system under study. The most important assumption in the model is that the principles of linear elasticity are applicable. That is, both substrate and epilayer are assumed to be continuum and not discrete atoms. Also, at each point in continuum each component of stress tensor can be expressed as linear combination of components of strain tensor. Since almost every function is linear at infinitesimal level, linear theory of elasticity can be assumed to be applicable provided deformations are small. Before discussing other

assumptions, it is important to revise the relationship between stress and strain as dictated by linear theory of elasticity.

Formulation of Stress-Strain Relations in Hookian Transversely Isotropic Solids

Hooke's law can be simply stated as *Ut tensio, sic vis*, meaning, "As the extension, so the force". In other words, in elastic solids stresses are directly proportional to strains and each component of stress tensor can be expressed as linear combination of components of strain tensors. In tensor form it can be stated as:

$$\sigma_{ij} = \sum_{k=1}^3 \sum_{l=1}^3 c_{ijkl} \epsilon_{kl} \text{ where } \{i,j=1,2,3\} \quad (3-1)$$

where σ_{ij} =stress tensor components, ϵ_{kl} =strain tensor components and c_{ijkl} = elements of stiffness constant tensor. Since the units of the stress-tensor components are N/m^2 , and the strain-tensor components are dimensionless, the units of the elasticity-tensor components are N/m^2 .

Since c_{ijkl} tensor relates two second rank tensors, it has $3^4=81$ components. But due to symmetry of stress tensor ($\sigma_{ij} = \sigma_{ji}$) and strain tensor ($\epsilon_{ij} = \epsilon_{ji}$), only 36 independent components remain to completely describe elasticity tensor. Thus, the relationship between stress and strain in matrix form is given by:

$$\begin{bmatrix} \sigma_{11} \\ \sigma_{22} \\ \sigma_{33} \\ \sigma_{23} \\ \sigma_{31} \\ \sigma_{12} \end{bmatrix} = \begin{bmatrix} C_{11} & C_{12} & C_{13} & C_{14} & C_{15} & C_{16} \\ C_{21} & C_{22} & C_{23} & C_{24} & C_{25} & C_{26} \\ C_{31} & C_{32} & C_{33} & C_{34} & C_{35} & C_{36} \\ C_{41} & C_{42} & C_{43} & C_{44} & C_{45} & C_{46} \\ C_{51} & C_{52} & C_{53} & C_{54} & C_{55} & C_{56} \\ C_{61} & C_{62} & C_{63} & C_{64} & C_{65} & C_{66} \end{bmatrix} \begin{bmatrix} \epsilon_{11} \\ \epsilon_{22} \\ \epsilon_{33} \\ 2\epsilon_{23} \\ 2\epsilon_{31} \\ 2\epsilon_{12} \end{bmatrix} \quad (3-2)$$

The elasticity tensor is further simplified depending on symmetry of the material. The materials InN and GaN have wurtzite structures. The wurtzite materials fall under

the category of transversely isotropic materials. Transversely isotropic materials are characterized by plane of isotropy and its properties are symmetric about an axis that is perpendicular to plane of isotropy. The basal plane of hexagonal lattice (wurtzite material) exhibits six folds symmetry. That is every $2\pi/6$ rotation around z-axis we get same structure with same properties.

If XYZ and X'Y'Z' represent original and transformed orthogonal space, then mathematically, the transformation of a vector in space can be done using direction cosine matrix given by A:

$$A = \begin{bmatrix} a_{11} & a_{12} & a_{13} \\ a_{21} & a_{22} & a_{23} \\ a_{31} & a_{32} & a_{33} \end{bmatrix} = \begin{bmatrix} \cos(\theta) & \sin(\theta) & 0 \\ -\sin(\theta) & \cos(\theta) & 0 \\ 0 & 0 & 1 \end{bmatrix} \quad (3-3)$$

Here, (a_{11}, a_{12}, a_{13}) are direction cosines of X' with respect to X, Y, Z axes respectively. Similarly, (a_{21}, a_{22}, a_{23}) and (a_{31}, a_{32}, a_{33}) are direction cosines of Y' and Z' with respect to X, Y, Z axes respectively. The angle θ represents angle by which XYZ is rotated about Z to get X'Y'Z system.

The transformation matrix for elasticity tensor matrix, however, is more complex as it involves tensor. It can be shown that it is given by M:

$$M = \begin{bmatrix} \cos(\theta)^2 & \sin(\theta)^2 & 0 & 0 & 0 & 2\cos(\theta)\sin(\theta) \\ \sin(\theta)^2 & \cos(\theta)^2 & 0 & 0 & 0 & -2\cos(\theta)\sin(\theta) \\ 0 & 0 & 1 & 0 & 0 & 0 \\ 0 & 0 & 0 & \cos(\theta) & -\sin(\theta) & 0 \\ 0 & 0 & 0 & \sin(\theta) & \cos(\theta) & 0 \\ -\cos(\theta)\sin(\theta) & \cos(\theta)\sin(\theta) & 0 & 0 & 0 & \cos(\theta)^2 - \sin(\theta)^2 \end{bmatrix} \quad (3-4)$$

Knowing θ , elasticity tensor can be transformed from one set of orthogonal axes to other as

$$C^{TRANS} = M^T C M \quad (3-5)$$

But for θ of $2\pi/6$ in order to satisfy rotational symmetry, transformed elasticity tensor C^{TRANS} is equal to actual elasticity tensor C . Thus, the transformation of elasticity tensor results in only five independent elements for stiffness constant tensor viz. C_{11} , C_{12} , C_{13} , C_{33} , and C_{44} .

As a result, in case of transversely isotropic materials the relationship between stress and strain can be given as:

$$\begin{bmatrix} \sigma_{11} \\ \sigma_{22} \\ \sigma_{33} \\ \sigma_{23} \\ \sigma_{31} \\ \sigma_{12} \end{bmatrix} = \begin{bmatrix} C_{11} & C_{12} & C_{13} & 0 & 0 & 0 \\ C_{12} & C_{11} & C_{13} & 0 & 0 & 0 \\ C_{13} & C_{13} & C_{33} & 0 & 0 & 0 \\ 0 & 0 & 0 & C_{44} & 0 & 0 \\ 0 & 0 & 0 & 0 & C_{44} & 0 \\ 0 & 0 & 0 & 0 & 0 & \frac{1}{2}(C_{11} - C_{12}) \end{bmatrix} \begin{bmatrix} \varepsilon_{11} \\ \varepsilon_{22} \\ \varepsilon_{33} \\ 2\varepsilon_{23} \\ 2\varepsilon_{31} \\ 2\varepsilon_{12} \end{bmatrix} \quad (3-6)$$

If material shows rotational invariance about an axis for an angle of $2\pi/n$, where $n \geq 5$, then it can be shown to be invariant for all the angles about that axis¹⁵⁰. This implies that transversely isotropic materials like InN and GaN have equivalent properties along any direction in hexagonal basal plane (Figure 3-3(A)). Thus, these materials can be modeled with cylindrical coordinates with uniform properties in circular bases and symmetry around transverse z-axis (Figure 3-3(A)).

Formulation of Model for Nanorod Heteroepitaxy

Rigid Substrate Model

The Figure 3-4 explains model for nanostructure growth that allows for lateral relaxation. The Figure 3-4(A) shows InN nanostructure growing in $\langle 0002 \rangle$ direction on GaN film. It is highly strained at interface as a

result of lattice mismatch. If the nanorod grows pseudomorphically like 2D film (Figure 3-4(B)), then it will result in high levels stress and strain. This strain if possible will be partially relieved by edge or mixed dislocations. As a result, it is not possible to grow very long nanowires without dislocations in pseudomorphic mode. This is contrary to experimentally observed results. From literature it is also known that nanostructures have better ability to accommodate strain as compared to film because of lateral relaxation. As a result nanostructure is homogeneously strained and strain is relaxed as nanostructure grows, with negligible strain in bulk material (Figure 3-4(C)). This results in single crystal nano structures with very high aspect ratio such as nanorods and nanowires.

Incorporation of lateral relaxation in model should be able to explain existence of very large aspect ratio single crystal nanowires. All nanowires or rods are assumed to be cylindrical to apply cylindrical coordinates. When the nanostructures grow, the epitaxial layer is assumed to be pseudomorphic at interface i.e. the lattice of epilayer is exactly mapped on to the substrate. To allow for lateral relaxation away from interface, all the strains are assumed to exponentially vanish away from the interface. As a result, there is negligible strain in bulk material. This is achieved by incorporating characteristic relaxation length α into the model. The relaxation length is dependent on elastic properties of material. Also, the interaction between strains fields of different nanorods are considered to be negligible. This can be assumed if nanorods are not very close to each other. Both the cases of rigid as well as flexible substrate are considered.

First strain energy of coherent nanorod is calculated which is the function of elastic constants, lattice mismatch, strain distribution and dimensions of nanostructure such as

radius and height. The nanorod initially grows coherently on the substrate with interface exactly mapped like substrate. As a result this nanostructure is coherently strained and strain is stored in the form of strain energy. The nanorod can continue to grow this way until it reaches certain critical diameter R^* for given height and lattice mismatch. The radius R^* is such that above this radius, system can deform and introduce a defect such as dislocation to partially relieve its strain as well as minimize strain energy. In this model, strain energy of coherent system (E_c) and dislocated system (E) are calculated as a function of R for known H as well as misfit f . The radius at which E_c becomes more than E is coherent radius for that H and misfit f .

The model is described below in detail in general terms. The epilayer material is InN and substrate is GaN. Epilayer and substrate are denoted with subscripts 'e' and 's' respectively. First, calculation of coherent strain energy is discussed.

Coherent strain energy (E_c)

The lattice mismatch between substrate and epilayer is given by

$$f = \frac{(a_s - a_e)}{a_s} \quad (3-7)$$

The radius and height of nanorod are denoted as R and H respectively. Initially, epilayer will be coherently mapped onto the substrate. Thus, for a nanorod of coherent radius R strain will be stored only as strain energy. The uniformly stretched interface in radial direction and decaying displacement along Z-axis or growth direction can be represented as follows:

$$u_r = fre^{\frac{1-z}{2\alpha R}}$$

$$u_\theta = 0$$

$$u_z = (Pr + QR) e^{-\frac{1}{2\alpha R} z}$$

Here, f represents the total lattice mismatch, α is the relaxation constant and P, Q are constants related to deformation in radial directions. The unknown constants (P, Q and α) are determined by minimization of total energy approach. That is, system always tends to go to state of lowest energy, and constants will have value such that energy of system is minimized. Based on the displacements, the strains in all the directions are

$$\varepsilon_{rr} = \frac{\partial}{\partial r} u_r = f e^{-\frac{1}{2\alpha R} z}$$

$$\varepsilon_{\theta\theta} = \frac{u_r}{r} + \frac{1}{r} \cdot \frac{\partial}{\partial \theta} u_\theta = f e^{-\frac{1}{2\alpha R} z}$$

$$\varepsilon_{zz} = \frac{\partial}{\partial z} u_z = -\frac{1}{2} \frac{(Pr + QR) e^{-\frac{1}{2\alpha R} z}}{\alpha R}$$

$$\varepsilon_{z\theta} = \frac{1}{2} \cdot \left(\frac{\partial}{\partial z} u_\theta + \frac{1}{r} \cdot \frac{\partial}{\partial \theta} u_z \right) = 0$$

$$\varepsilon_{rz} = \frac{1}{2} \cdot \left(\frac{\partial}{\partial z} u_r + \frac{\partial}{\partial r} u_z \right) = \frac{1}{4} \frac{e^{-\frac{1}{2\alpha R} z} (-fr + 2P\alpha R)}{\alpha R}$$

$$\varepsilon_{r\theta} = \frac{1}{2} \cdot \left(\frac{\partial}{\partial r} u_\theta + \frac{1}{r} \cdot \frac{\partial}{\partial \theta} u_r \right) = 0$$

The stresses are related to strains through equation (3-6). Thus, stress vector is given by:

$$\begin{bmatrix} \sigma_{rr} \\ \sigma_{\theta\theta} \\ \sigma_{zz} \\ \sigma_{z\theta} \\ \sigma_{rz} \\ \sigma_{r\theta} \end{bmatrix} = \begin{bmatrix} C_{11}\varepsilon_{rr} + C_{12}\varepsilon_{\theta\theta} + C_{13}\varepsilon_{zz} \\ C_{12}\varepsilon_{rr} + C_{11}\varepsilon_{\theta\theta} + C_{13}\varepsilon_{zz} \\ C_{13}\varepsilon_{rr} + C_{13}\varepsilon_{\theta\theta} + C_{33}\varepsilon_{zz} \\ 2C_{44}\varepsilon_{z\theta} \\ 2C_{44}\varepsilon_{rz} \\ 2\left(\frac{1}{2}C_{11} - \frac{1}{2}C_{12}\right)\varepsilon_{r\theta} \end{bmatrix} \quad (3-8)$$

The hydrostatic stress field and stress field is shown in Figure 3-5. As it follows exponential decay in about $6\alpha R$, the stress decreases to less than 5% of maximum stress. The strain energy density of nanorod is given by

$$w = \frac{1}{2} \sigma \cdot \varepsilon \quad \text{J/m}^3 \quad (3-9)$$

$$w = \frac{1}{2} \frac{1}{\alpha^2 R^2} \left(\left(\left((2C_{11} + 2C_{22})f^2 + C_{44}P^2 \right) \alpha^2 - 2f\alpha C_{13}Q + \frac{1}{2}Q^2 C_{33} \right) R^2 + \left(\frac{1}{2}P \left(-4f \left(C_{13} + \frac{1}{2}C_{44} \right) \alpha + QC_{33} \right) rR + \frac{1}{4}r^2 \left(P^2 C_{33} + C_{44}f^2 \right) \right) e^{-\frac{z}{\alpha R}} \right) \text{J/m}^3$$

Thus, integrating strain energy density over the volume of nanorod gives total strain energy of the system

$$E_c = \int_0^H \int_0^{2\pi R} \int_0^R w r dr d\theta dz \quad \text{J}$$

$$E_c = \frac{\pi R^3}{16\alpha} \left(\left((16C_{11} + 16C_{22})f^2 + 8C_{44}P^2 \right) \alpha^2 - \frac{32}{3} \left(\left(C_{13} + \frac{1}{2}C_{44} \right) P + \frac{3}{2}C_{13}Q \right) f\alpha \right) \left(1 - e^{-\frac{H}{\alpha R}} \right) + C_{44}f^2 + \left(2Q^2 + P^2 + \frac{8}{3}PQ \right) C_{33}$$

This function was minimized numerically to get the values of parameters P, Q and α . The minimum values are independent of R and H as long as the two are not comparable. The values of P, Q and α for InN nanostructure are found to be -0.0521,

0.0149 and 0.1120 respectively. Minimized coherent strain energy for nanorod of radius 100nm and height 1000nm was found to be 1.9125×10^{-12} Joules.

Energy of dislocated system (E)

As discussed before the radius of nanorod increases above certain critical value R^* , system no longer remains coherent as it is energetically favorable to form dislocation. When energetics is favorable, perfect coherency or pseudomorphism between substrate and epilayer is broken by local degeneracy. The degeneracy is introduced by extra half plane in one of the layers. In Figure 3-2(A) for example the GaN substrate has two extra half planes (one shown by dotted yellow line). This can be also viewed as if half plane from InN layer is squeezed out due to the compressive stress. This allows for relaxation for partial relaxation for upper layers. This type of degeneracy is viewed as negative dislocation along $\langle 10\bar{1}0 \rangle$ direction, the line perpendicular to the plane of the figure2a. This dislocation has burger's vector in $\langle 11\bar{2}0 \rangle$ direction as shown in figure2a. The burger's vector essentially relates to magnitude and direction of strain relief here. These types of dislocations are called edge dislocations in which burgers vector is perpendicular to the dislocation line. The dislocations in which burger's vector is along the line of dislocation are called screw dislocations. These types of dislocations do not relieve any type of strain. For edge dislocation to relive strain, its burger's vector should be perpendicular to the line of dislocation as well as it should be in or parallel to interfacial plane. For example, in growth of InN on GaN both growing in $\langle 000\bar{2} \rangle$ direction, for dislocation line along $\langle 1\bar{1}00 \rangle$ direction, edge dislocation with burger's vector in $\langle 000\bar{2} \rangle$ direction will not relieve any strain. But an edge dislocation with burger's vector in $\langle 000\bar{2} \rangle$ direction will relieve strain.

In this study, perpendicular sets of pairs of dislocations in $\langle 11\bar{2}0 \rangle$ direction and $\langle 1\bar{1}00 \rangle$ direction are assumed to be formed when degeneracy is introduced in coherent systems. These types of dislocations are common in hexagonal crystals¹⁵¹⁻¹⁵³. The dislocation is the introduction of localized regions of degeneracy in order to accommodate lattice mismatch strain. It requires energy to form, which is again related to elastic properties of materials and magnitude of burger's vectors. The energy for n pairs dislocations in $\langle 11\bar{2}0 \rangle$ direction is given by¹⁵³

$$E_d = (2n) \cdot (2R) \cdot \frac{(C_{11}^2 - C_{12}^2)}{C_{11}} \frac{b^2}{4\pi} \ln\left(\frac{4R}{b}\right) \quad (3-10)$$

Here, b is the magnitude of burger's vector for edge dislocation. As seen from the equation, dislocation energy is proportional to square of burger's vector. This is because the localized strain field of degeneracy is proportional to magnitude of burger's vector. To minimize dislocation energy, dislocations tend to form with lowest magnitude of b possible. As a result, dislocations in closed packed direction and closed packed planes are common. In our system also, dislocations form in closed packed $\langle 11\bar{2}0 \rangle$ direction and closed packed $(000\bar{2})$ planes are gliding planes. The burger's vector has magnitude equivalent to lattice constant 'a' as it is the shortest distance between atoms in $\langle 11\bar{2}0 \rangle$ direction.

Due to formation of dislocation strain is partially relaxed. The residual strain in the nanorod of radius R is

$$|f_r| = |f| - \left| \frac{nb}{2R} \right| \text{ where } (0 \leq b \leq Rf) \quad (3-11)$$

This strain is again stored in nanostructure as residual strain energy. Thus, total energy for dislocated system (E) is summation of residual strain energy and energy to form a pair of dislocation.

$$E = E_c|_{f=f_r} + E_d \quad (3-12)$$

$$E = \frac{\pi R^3}{16\alpha} \left[\begin{aligned} & \left((16C_{11} + 16C_{22})f_r^2 + 8C_{44}P^2 \right) \alpha^2 \\ & - \frac{32}{3} \left(\left(C_{13} + \frac{1}{2}C_{44} \right) P + \frac{3}{2}C_{13}Q \right) f\alpha \left(1 - e^{-\frac{H}{\alpha R}} \right) + (4R) \cdot \frac{(C_{11} - C_{12}^2)}{C_{11}} \frac{b^2}{4\pi} \ln \left(\frac{4R}{b} \right) \\ & + C_{44}f_r^2 + \left(2Q^2 + P^2 + \frac{8}{3}PQ \right) C_{33} \end{aligned} \right] \quad (3-13)$$

As energy of dislocation only partially relieves the strain, the constants P, Q and α do not change. This is also verified by again optimizing the total energy function for dislocated system.

The Figure 3-6 shows the curves for coherent strain energy (green curve) and total energy of dislocated system (red curve) very high aspect ratio i.e. very large height. Initially E is greater than E_c and as a result it is not energetically favorable to form a dislocation. But as radius increases E becomes smaller than E_c and system forms dislocation rather being coherent. The coherent radius for system of InN nanorod on GaN substrate was found to be 5.25nm.

It means that InN nanorods with almost infinite length would be possible to grow coherently if their diameters are less than 5.25nm on GaN film purely. It is expected then that if height of nanorod is decreased then for nanorod of even higher diameters are possible to form coherently. This is indeed observed in the model. When at a constant radius coherent strain energy and total energy of dislocated system are plotted, for nanorods with radius 4nm, E is always greater than E_c . As a result at this

radius any height nanorod would be coherent (Figure 3-7(A)). But for nanorod with radius of 6nm for examples if height is more than 2nm it will not be coherent (Figure 3-7(B)). The heights vs. radius can thus be plotted for various radius and heights. It is shown in Figure 3-8. Below the curve nanorods will be coherent and grow as single crystalline almost in island or Volmer-Weber growth mode. Above the curve it is expected that nanorods will either have dislocations or will grow in Stranski-Krastanov growth mode. It has been observed that nanorods with much greater diameter can be coherently on GaN. In S-K mode, InN strained and dislocated film first forms on the GaN film and then 3D growth starts. Due to growth on partially relaxed film of same material, much larger coherent diameter is energetically favored. Another reason behind higher coherency diameter is the flexibility of substrate. It is not completely right to assume rigidity of substrate. As the InN grows on GaN, InN is elastically compressed. But, at the same time GaN film underneath itself is getting strained, thus sharing some part of strain. This case is discussed next in flexible substrate mode. The actual growth can be combination of both cases.

Flexible Substrate Model

To incorporate the flexibility of substrate, InN nanorod (over-layer) of radius R_o is assumed to be growing on GaN substrate (under-layer) such that area inscribed by nanorod basal plane is coherently matched to substrate layer. (Note: Henceforth, epilayer and substrate are referred to as over-layer and underlayer. They are denoted by subscripts o and u respectively.) Since actual lattice constant of over-layer (a_o) and under-layer (a_u) are different, former is under tensile stress and later is under compressive stress in this case. As a result, although coherently mapped at interface,

the relaxed over-layer radius of R_o corresponds to the relaxed under-layer layer radius of R_u . The values of R_o and R_u are related by overall lattice mismatch, given by f .

$$f = \frac{(a_u - a_o)}{a_u} \quad (3-14)$$

$$R_o = (1-f)R_u \quad (3-15)$$

Also, the overlayer and underlayer coherent mapping onto each other in a dislocation free system requires that at $z=0$ both radial and vertical displacements for overlayer and underlayer should be equal. This condition can be represented numerically as follows:

$$\text{for } 0 \leq r_u \leq R_u \left\{ \begin{array}{l} u_{zo}(r_u(1-f), z=0) = u_{zu}(r_u, z=0) \\ \text{and} \\ r_u(1-f) + u_{ro}(r_u(1-f), z=0) = r_{uo} + u_{ro}(r_u, z=0) \end{array} \right. \quad (3-16)$$

The negative value of lattice mismatch (f) indicates over-layer under compression. The strain gets distributed, between overlayer and underlayer such that the interfacial lattice constant assumes intermediate value of a . The radial strains at the interface, in overlayer and underlayer, are given by

$$\varepsilon_{rro}(r, z=0) = B = \frac{(a - a_o)}{a_o} \quad (3-17)$$

$$\varepsilon_{rru}(r, z=0) = \frac{(a - a_u)}{a_u} \equiv B(1-f) - f \quad (3-18)$$

To be consistent with rigid substrate model, equations would be written in terms of B instead of interface lattice constant a . The other variables to be optimized are taken as P , Q , α_u and α_o . Here, α_u and α_o are relaxations constants for underlayer and overlayer respectively. As elastic properties of overlayer and underlayer material are

very different strain relaxation in these materials is expected to happen over different lengths. As seen from equations (3-16)-(3-18), overlayer which is located in $0 \leq r \leq R_o$ and $0 \leq z \leq H_o$ is compressed and underlayer which is located in $0 \leq r \leq R_u$ and $H_u \leq z \leq 0$ is stretched.

Following the formulation in rigid substrate model, various strains in overlayer and underlayer are given by

$$\varepsilon_o = \begin{bmatrix} \varepsilon_{rro} \\ \varepsilon_{\theta\theta o} \\ \varepsilon_{zz o} \\ \varepsilon_{z\theta o} \\ \varepsilon_{rzo} \\ \varepsilon_{r\theta o} \end{bmatrix} = \begin{bmatrix} Be^{\frac{1}{2\alpha_o R_o} z} \\ Be^{\frac{1}{2\alpha_o R_o} z} \\ -\frac{1}{2} \frac{(Pr + QR_o) e^{\frac{1}{2\alpha_o R_o} z}}{\alpha_o R_o} \\ 0 \\ -\frac{1}{2} \frac{Bre^{\frac{1}{2\alpha_o R_o} z}}{\alpha_o R_o} + Pe^{\frac{1}{2\alpha_o R_o} z} \\ 0 \end{bmatrix} \quad (3-19)$$

$$\varepsilon_u = \begin{bmatrix} \varepsilon_{rru} \\ \varepsilon_{\theta\theta u} \\ \varepsilon_{zzu} \\ \varepsilon_{z\theta u} \\ \varepsilon_{rzu} \\ \varepsilon_{r\theta u} \end{bmatrix} = \begin{bmatrix} (B(1-f) - f) e^{\frac{1}{2\alpha_u(1-f)R_u} z} \\ (B(1-f) - f) e^{\frac{1}{2\alpha_u(1-f)R_u} z} \\ \frac{1}{2} \frac{(P(1-f)r + Q(1-f)R_u) e^{\frac{1}{2\alpha_u(1-f)R_u} z}}{\alpha_u(1-f)R_u} \\ 0 \\ \frac{1}{2} \frac{(B(1-f) - f) r e^{\frac{1}{2\alpha_u(1-f)R_u} z}}{\alpha_u(1-f)R_u} + P(1-f) e^{\frac{1}{2\alpha_u(1-f)R_u} z} \\ 0 \end{bmatrix} \quad (3-20)$$

Knowing the relation between stress and strain from equation (3-6), stress vectors can be expressed in terms of strains similar to expressions in (3-8). Strain energy densities in overlayer and underlayer can be calculated as

$$w_o = \frac{1}{2} \sigma_o \varepsilon_o \quad (3-21)$$

$$w_o = \frac{1}{8} \frac{1}{\alpha_o^2 R_o^2} \left(\left((8O_{11} + 8O_{12})B^2 + 4O_{44}P^2 \right) \alpha_o^2 - 8B\alpha_8 O_{13}Q + O_{33}Q^2 \right) R_o^2 - \left(8rP \left(B \left(O_{13} + \frac{1}{2}O_{44} \right) \alpha_o - \frac{1}{4}O_{33}Q \right) R_o + r^2 (O_{33}P^2 + O_{44}B^2) \right) e^{\frac{-z}{\alpha_o R_o}} \quad (3-22)$$

$$w_u = \frac{1}{2} \sigma_u \varepsilon_u \quad (3-23)$$

$$w_u = \frac{1}{\alpha_u^2 (1-f)^2 R_u^2} \left((K)(1-f)^2 R_u^2 + L \right) e^{\frac{z}{\alpha_u (1-f) R_u}} \quad (3-24)$$

$$\text{where } K = \left(\begin{array}{l} \alpha_u^2 \left((U_{11} + U_{12})B^2 + (2U_{11} + 2U_{12})B + U_{11} + U_{12} + \frac{1}{2}U_{44}P^2 \right) f^2 \\ -2 \left(\left((U_{11} + U_{12})B^2 + (U_{11} + U_{12})B + \frac{1}{2}U_{44}P^2 \right) \alpha_u + \frac{1}{2}U_{13}Q(1+B) \right) \alpha_u f \\ + \left((U_{11} + U_{12})B^2 + \frac{1}{2}U_{44}P^2 \right) \alpha_u^2 + \alpha_u U_{13}QB + \frac{1}{8}U_{33}Q^2 \end{array} \right)$$

$$\text{and } L = \left(\begin{array}{l} -r \left(\left(U_{13} + \frac{1}{2}U_{44} \right) \alpha_u (1+B)f - B \left(U_{13} + \frac{1}{2}U_{44} \right) \alpha_u - \frac{1}{4}QU_{33} \right) P(1-f)^2 R_u \\ + \frac{1}{8} r^2 \left(\left(U_{44}B^2 + U_{33}P^2 + U_{44} + 2BU_{44} \right) f^2 - (2BU_{44} + 2U_{33}P^2 + 2U_{44}B^2) f \right) \\ + U_{44}B^2 + U_{33}P^2 \end{array} \right)$$

It is to be noted here that elastic constants for overlayer and underlayer are represented by O_{11} - O_{44} and U_{11} - U_{44} respectively. Sum of integration of energy densities

over corresponding volumes of underlayers and overlayers gives total coherent strain energy of system.

$$E_c = E_{co} + E_{cu}$$

$$\text{where } E_{co} = \int_0^{H_o} \int_0^{2\pi R_o} \int_0^R w_o r dr d\theta dz \text{ and } E_{cu} = \int_{-H_u}^0 \int_0^{2\pi R_u} \int_0^R w_u r dr d\theta dz \quad (3-25)$$

$$E_{co} = \frac{\pi R_o^3}{\alpha_o} \left[\begin{array}{l} \left((O_{11} + O_{12})B^2 + \frac{1}{2}O_{44}P^2 \right) \alpha_o^2 \\ -\frac{2}{3}B \left(\left(O_{13} + \frac{1}{2}O_{44} \right) P + \frac{3}{2}QO_{13} \right) \alpha_o \\ + \frac{1}{16}O_{33} \left(2Q^2 + \frac{8}{3}QP + P^2 \right) \end{array} \right] \left(1 - e^{\frac{-H_o}{\alpha_o R_o}} \right)$$

$$E_{cu} = \frac{\pi R_u^3}{\alpha_u(1-f)} \left[\begin{array}{l} \left((U_{11} + U_{12})(B(1-f) - Bf)^2 + \frac{1}{2}U_{44}P^2 \right) (1-f)^2 \alpha_u^2 \\ -\frac{2}{3}(B(1-f) - Bf) \left(\left(U_{13} + \frac{1}{2}U_{44} \right) P + \frac{3}{2}QU_{13} \right) (1-f) \alpha_u \\ + \frac{1}{16}U_{33} \left(2Q^2 + \frac{8}{3}QP + P^2 \right) \end{array} \right] \left(1 - e^{\frac{-H_u}{(1-f)\alpha_u R_u}} \right)$$

Similar to case of rigid substrate model, this function was minimized numerically to get the values of parameters P, Q, B, α_o and α_u . The minimum values of the most parameters are independent of R and H (except for B in some conditions) as long as the two are not comparable. For example, the values of P, Q, B, α_o and α_u for InN nanostructure on flexible GaN base are found to be -0.0240, 0.0088, -0.0585, 0.1039 and 0.1171 respectively. Minimized coherent strain energy for nanorod of radius 100nm and height 1000nm was found to be 9.8357×10^{-13} Joules.

It is to be noted here that values of P and Q are approximately half of that in rigid substrate model. The value of α_o , although relaxed a little bit, has value similar to that in rigid substrate model. This can be explained easily by understanding the physical

significance of these values. Due to flexible nature of substrate, effective lattice mismatch at interface is given by B instead of f. Thus, lattice mismatch experienced by overlayer in flexible substrate case is -0.0585 instead of -0.1079. This is the first factor that affects the values of the parameters P and Q that decide mapping at the interface. Since mapping structure is the same, mapping parameters P and Q decrease proportional to the effective lattice mismatch at interface. Secondly, due to incorporation of flexible substrate, a part of strain is shared by underlayer. Thus, values of P and Q are also affected by elastic properties of both overlayer and underlayer instead of only overlayer (rigid substrate assumption). The value of α_0 , the relaxation parameter, on the other hand depends on elastic parameters of materials. Thus, this value remains constant. Also, Figure 3-9 illustrates that value of total coherent strain energy when flexible substrate is assumed is decreased substantially. It means that flexible substrate structure will be better relaxed than the rigid substrate case.

In coherence with rigid substrate model, perpendicular sets of pairs of dislocations in $\langle 11\bar{2}0 \rangle$ direction and $\langle 1\bar{1}00 \rangle$ direction are assumed to be formed when degeneracy is introduced in coherent systems. The energy to form dislocation is given by following equation similar to equation (3-10).

$$E_d = (2n) \cdot (2R_o) \cdot \frac{(O_{11}^2 - O_{12}^2)}{O_{11}} \frac{b^2}{4\pi} \ln\left(\frac{4R_o}{b}\right) \text{ J} \quad (3-26)$$

From equation (3-26), it is clear that dislocation is assumed to be introduced in the overlayer. This assumption is done on the basis that dislocation is introduced while nanostructures grow as overlayer. As a result of formation of a pair of dislocation,

however, total lattice mismatch is relaxed from f to f_r given by equation (3-27) below which is exactly same as equation (3-11).

$$|f_r| = \left| f - \frac{nb}{2R_o} \right| \text{ where } (0 \leq b \leq 2R_o f) \quad (3-27)$$

Again, condition that $(0 \leq b \leq 2R_o f)$ assures that formed dislocation cannot overcompensate the mismatch in the system. The burger's vector b assumes value of lattice constant 'a' which is the interfacial lattice constant. The value of interfacial lattice constant is dynamic and depends on the optimum value of B through equations (3-17) and (3-18). In flexible substrate model, introduction of dislocation changes the total lattice mismatch which changes B to B_r . Dislocation energy in turn depends on depends on changes in B . This interdependence of E_d on B and vice versa requires B to be optimized again on introduction of dislocation.

After dislocation forms total energy of system is, thus, given by equation as follows

$$E = E_c \Big|_{f=f_r, B=B_r} + E_d \quad (3-28)$$

The expression total energy of dislocated system can be easily calculated by substituting for f_r from equation (3-27) and $B=B_r$ in equation (3-25) and knowing expression for E_d from (3.26). The actual expression for E will not be given here because of length limitation of word processor.

The values of all the parameters except B remain constant except at the very small values of radius. At smaller radii, dislocation formation can compensate lattice mismatch substantially. This reflects into large deviations in P and Q values. But, at the same time for smaller radii, coherency at interface is energetically favored. As a result,

dislocations do not tend to form at smaller radii and these deviations in values of P and Q do not affect the results.

From optimized values of B, the lattice parameters of relaxed overlayer and underlayer can be calculated using relations in equations (3-17) and (3-18). They are plotted in Figure 3-10. It shows that for smaller radius nanorods formation of dislocations will relieve greater strain and lattice constant on both sides will tend to relax to their bulk lattice constants. But the formation of dislocation itself can be seen as introduction or reduction of plane of atoms in the material and it introduces local strain fields. This requires energy equivalent to dislocation energy. The Figure 3-11 shows plot of total energy of coherent as well as dislocated system for the case of flexible substrate model. Below 10.7nm, coherent strain energy is lower than strain energy of dislocated system. As a result below 10.7nm system will be coherent. So, critical coherency diameter for InN nanorod in case of flexible substrate model is 21.4nm as compared to 10.5nm in case of rigid substrate model. The increase in critical coherency radius is due to the flexibility of substrate. It is also illustrated in Figure 3-12. The Figure 3-12(A) and Figure 3-12(B) show the plot of height of nanorod versus strain energies of dislocated as well as coherent systems for nanorod radius of 10nm and 12nm respectively. Since 10nm is below critical coherency limit, coherent nanowire with any height is possible in this case. On the other hand, if nanostructure height exceeds 4nm for 12nm radius nanorod, dislocations would be introduced. Thus, for every radius, there is a critical height below which structure can be coherent. All such heights versus radii are plotted in Figure 3-13. The figure also compares the results for two approaches. The

introduction of flexibility of substrate means more compliance with overlayer that result in increased coherent diameter.

S-K growth and its effect on coherent diameter

The S-K growth mode is simply a film growth followed by the 3D island growth. When two like compounds are grown epitaxially, initially different surface interactions are such that 2D film growth dominates. After few layers, however, strains arising due to lattice mismatch make 3D growth more favorable. In addition to that, 3D growth also provides both lateral and vertical relaxation. As a result, 3D nanostructures can grow strain free by acquiring S-K growth mode.

The S-K growth can then be incorporated in given model by assuming lower lattice mismatch between substrate and epilayer. This is because initially epilayer grows either coherently or dislocated mode on the substrate. Depending on value of (α) and grain size (D), strain is reduced below 10% of original value within distance equivalent to $3\alpha D$. For example, if InN film with grains of 100nm is formed on GaN, then within 30nm the strain would be below 10% of original. This film then can be precursor to nanostructures with at least 100 nm diameters with no dislocations.

The Figure 3-14 shows R-H coherency map for S-K mode growth with different lattice mismatch. Below the curve the nanostructures tend to be coherent for any height. Above the curves the nanostructures will be dislocated. In S-K mode, by formation of dislocated film has dual effect on heteroepitaxy. Firstly lattice mismatch is reduced and as a result strain is reduced. Secondly, materials become similar in terms of elastic properties, thus stress is distributed uniformly amongst the layers. The exponential decay of strain means that strain will fall to 0.3679 of original value in αD length. It means that for InN with grain size of 100 nm, strain will be 0.3679 f within 30 nm. From

Figure 3-14 it is clear that for S-K growth with 0.3 lattice mismatch, more than 100nm radius coherent nanorod growth is possible for InN on GaN system.

However, no S-K growth mode was visible in the InN_{NR} grown in Chapter 2. This can be clear from Figure 3-15 which is a cross sectional SEM image of InN_{NR} grown on Silicon as well as GaN buffer layer. But nanorods grown have very good crystalline quality. As seen from the model it is clear that nanorods will tend to form dislocations at very early stage of growth. If nanorods form pair of dislocations at 5 nm radius, the relaxed nanorod would be able to grow to 20 nm radius without further dislocation formation. Also, as seen from the strains plotted from the model, it is clear that nanorod is mostly strained at the bottom (Figure 3-16). As a result dislocations tend to be concentrated only at the bottom center of nanorod^{154,155}. Result of this is maximum relaxation at the interface and grown nanorod is defect free. The similar results are predicted by the theoretical model.

Summary and Conclusions

This Chapter presents a model for heteroepitaxial nanorod growth for transversely isotropic materials. The model predicts limit of coherency of particular nanorod growing heteroepitaxially. Unlike films, nanorod basal planes that are epitaxially bound to substrate are very small. All other faces of nanorod are free to expand and contract as no stress is applied to them on any free faces. As a result, physics of the problem requires them to relax laterally as they grow. The model characterizes relaxation by relaxation constant α . This relaxation constant is not arbitrary, but is decided by material properties along with other parameters P and Q. The model employs the minimization of free energy approach to optimize parameters and make predictions. Every system

tends to attain least energy state. A strained nanorod can attain minimized energy state with either growing coherently or forming misfit dislocation. Misfit dislocation can be viewed as missing plane or extra plane of atoms introduced in either epilayer or substrate. When dislocation forms it creates dangling bonds as well as localized strain field. As a result, dislocation to form requires some energy. The model easily predicts state of system by energy minimization approach. Model suffers few disadvantages. It generally overestimates critical diameter. Although, model overestimates the predicted coherent region as compared to literature, it presents a qualitative picture of strain relaxation in nanostructures. It predicts rapid lateral relaxation of strain in the nano material, such that bulk is almost strain free. Secondly model should not be used for predicting formation of second sets of dislocations as once dislocation form linear elasticity model does not hold. But barring that model perfectly predicts formation of dislocations only in basal region, which is also observed experimentally. Model is also able to qualitatively describe how SK growth mode, which is common in heteroepitaxy, is able to increase coherency in the epilayer and reduce dislocation density. In all, this model is very general and can be applied or modified for any system in the heteroepitaxy.

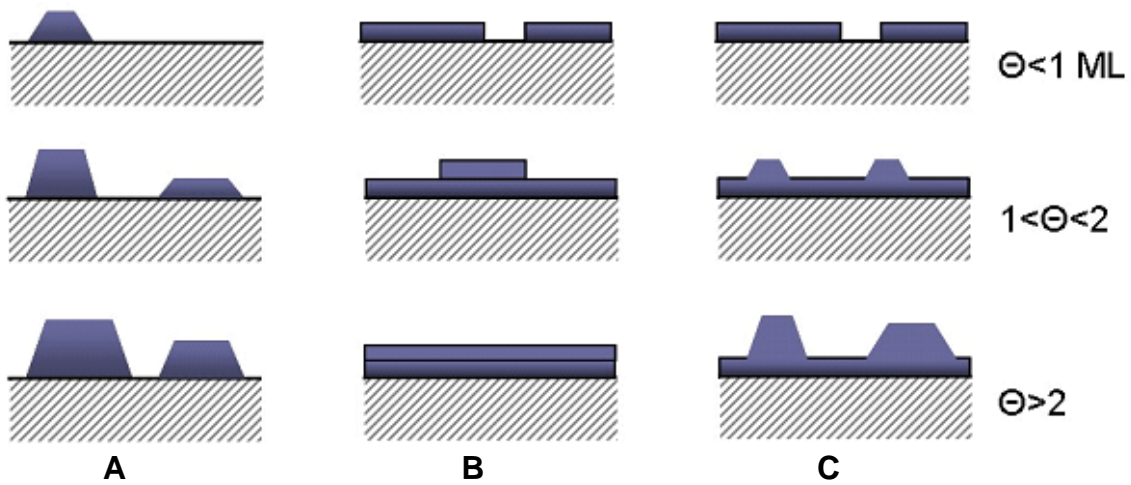


Figure 3-1. Modes of epitaxial growth: A) Island or Volmer-Weber growth mode, B) Film or Frank-van der Merwe growth mode and C) Stranski-Krastanov growth mode¹³⁰

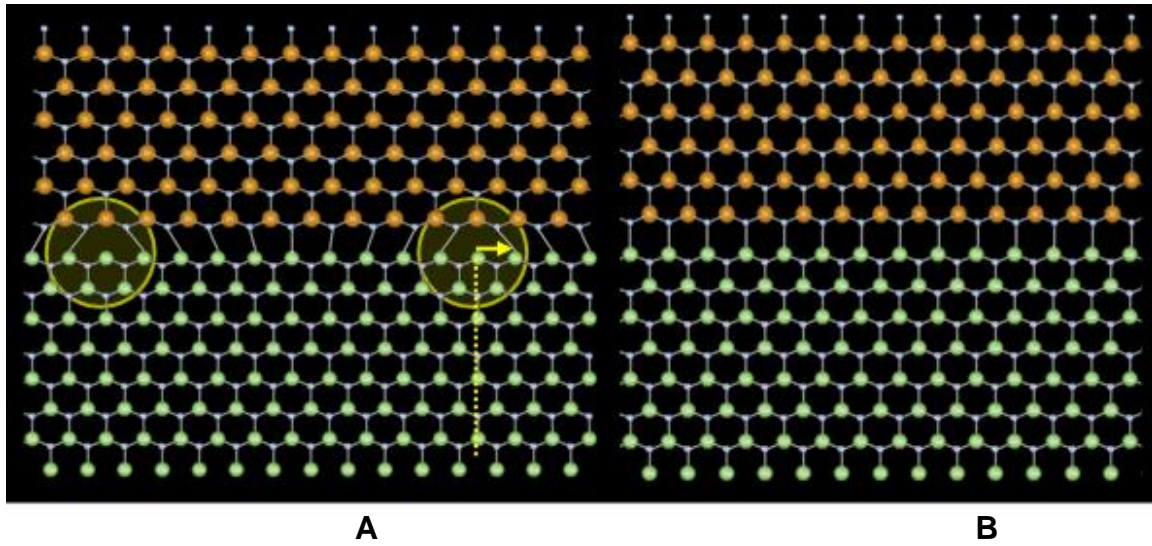


Figure 3-2. Growth of InN film on GaN film viewed in $\langle 1\bar{1}00 \rangle$ direction A) Dislocated growth with pair of dislocation at interface, yellow arrow shows Burgers vector in $\langle 11\bar{2}0 \rangle$ direction B) pseudomorphic growth with homogeneously strained InN film

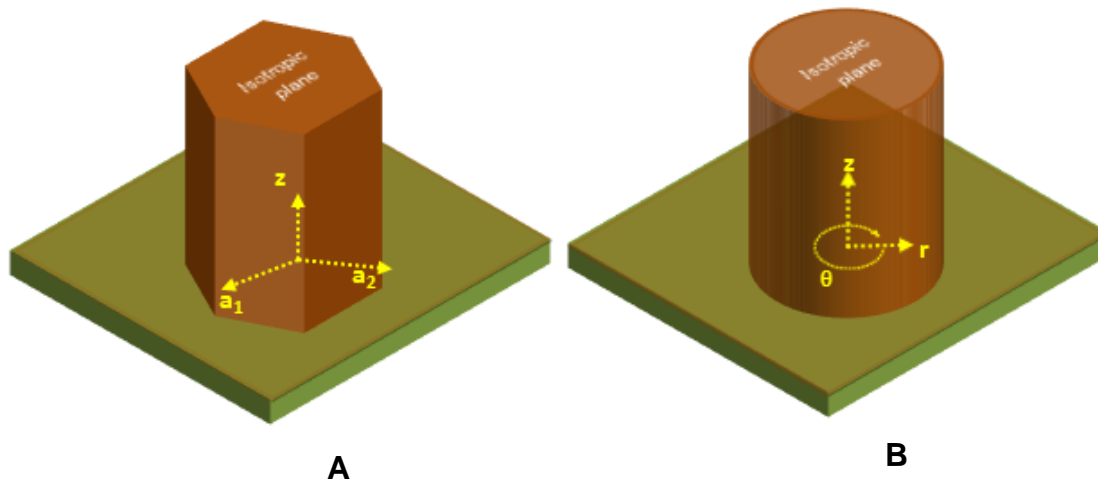


Figure 3-3. Schematic of InN nano structure growth on GaN film (with possible InN film): A) hexagonal nanorod geometry with growth in z direction, hexagonal plane is isotropic in properties, B) equivalent cylindrical geometry used for model

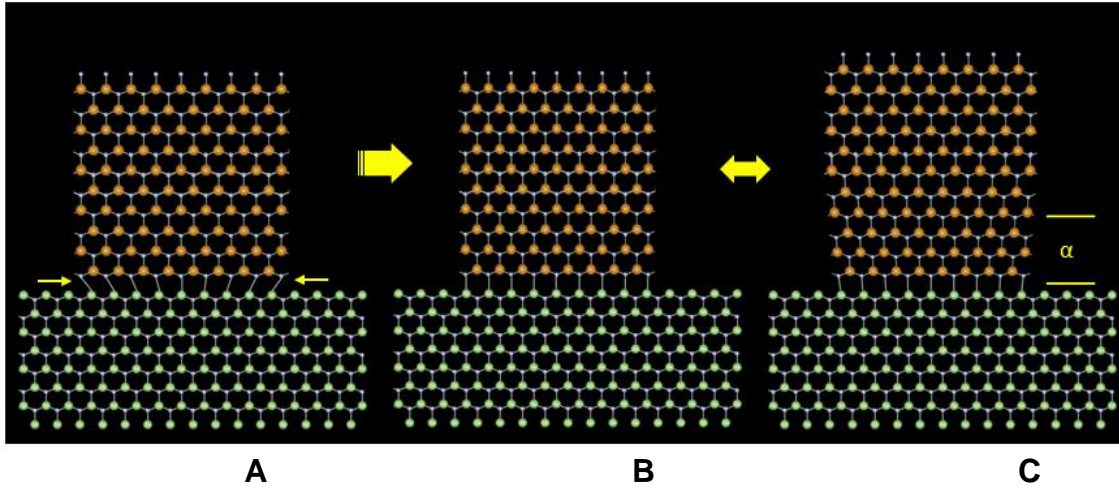


Figure 3-4. InN nanorod growth on GaN film A) InN experiences compression at interface, B) nanorod pseudomorphic growth with high compressive strain in crystal, C) nanorod has ability of lateral relaxation results in no strain in bulk(model), α is relaxation length

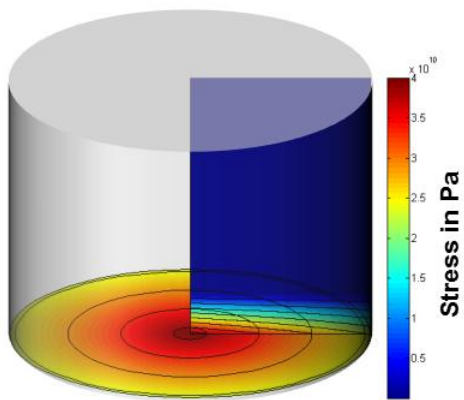


Figure 3-5. Stress field in nanorod. Figure shows both lateral as well as longitudinal contour. Overall stress is at its maximum at the center. There is no stress in bulk due to lateral relaxation over length of αR .

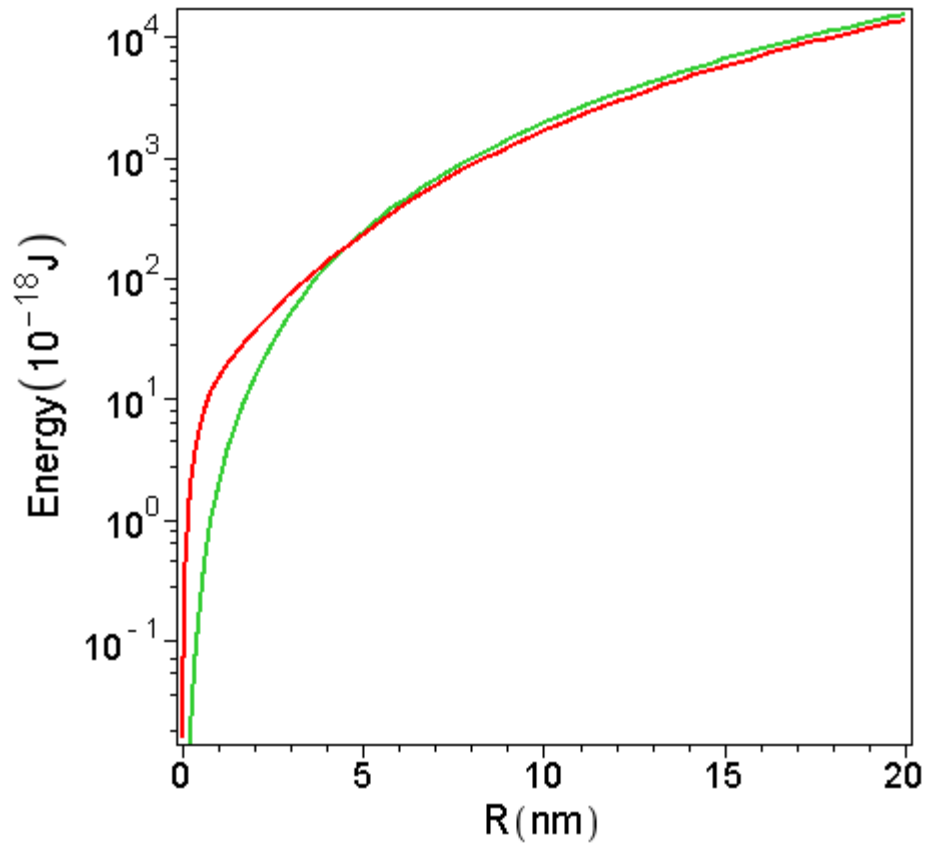


Figure 3-6. Strain Energy vs. nanorod radius: Red curve is total energy of dislocated system; green curve is coherent strain energy

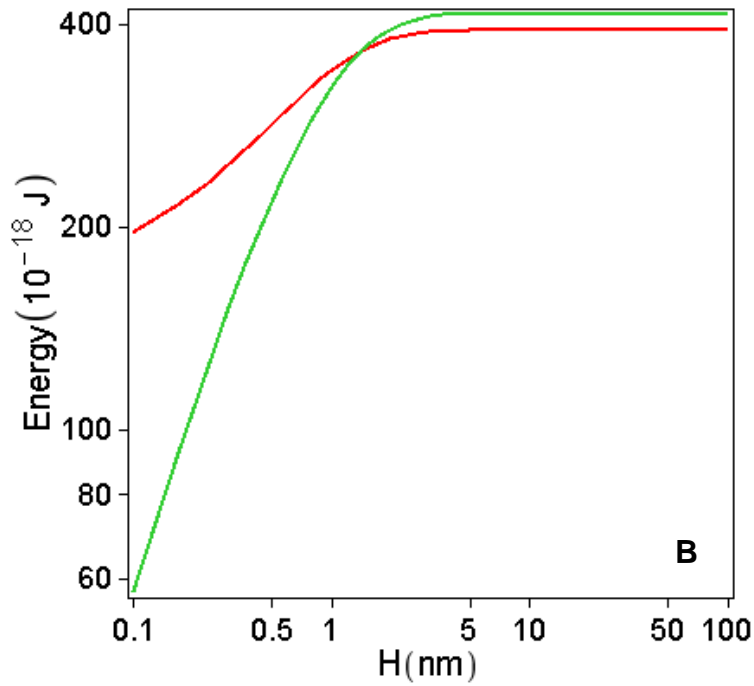
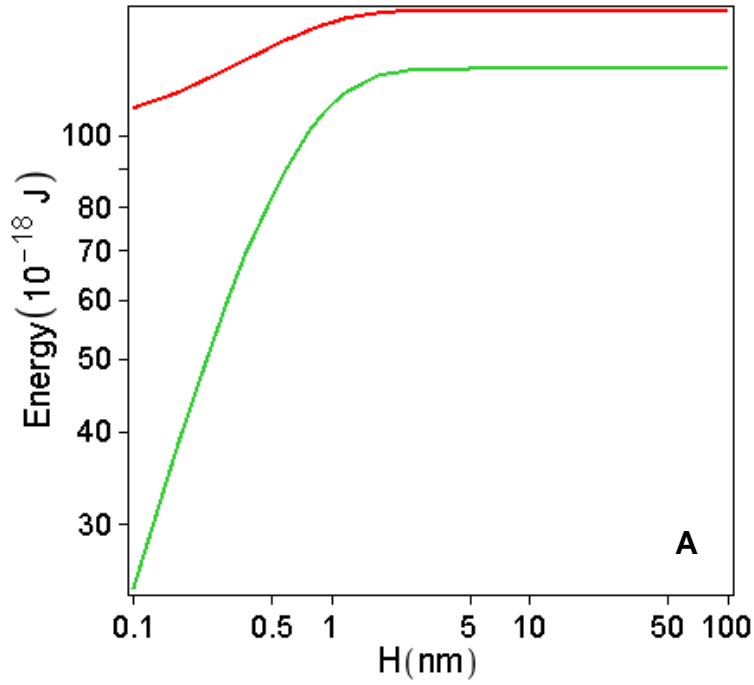


Figure 3-7. Strain Energy vs. nanorod height: Red curve is total energy of dislocated system, green curve is coherent strain energy, A) for $R = 4$ nm nanorod is coherent at any height, B) for $R=6$ nm nanorod is coherent only below 2 nm height

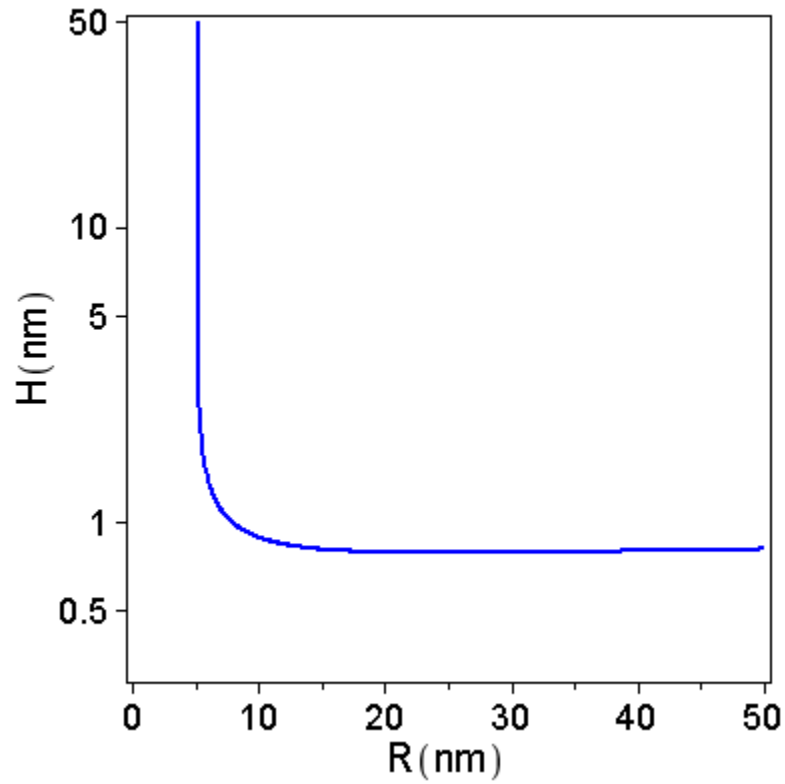


Figure 3-8. Coherency map for InN nanorod on rigid GaN In area above the curve dislocations will tend to form or system might acquire S-K growth mode to increase compliance of substrate.

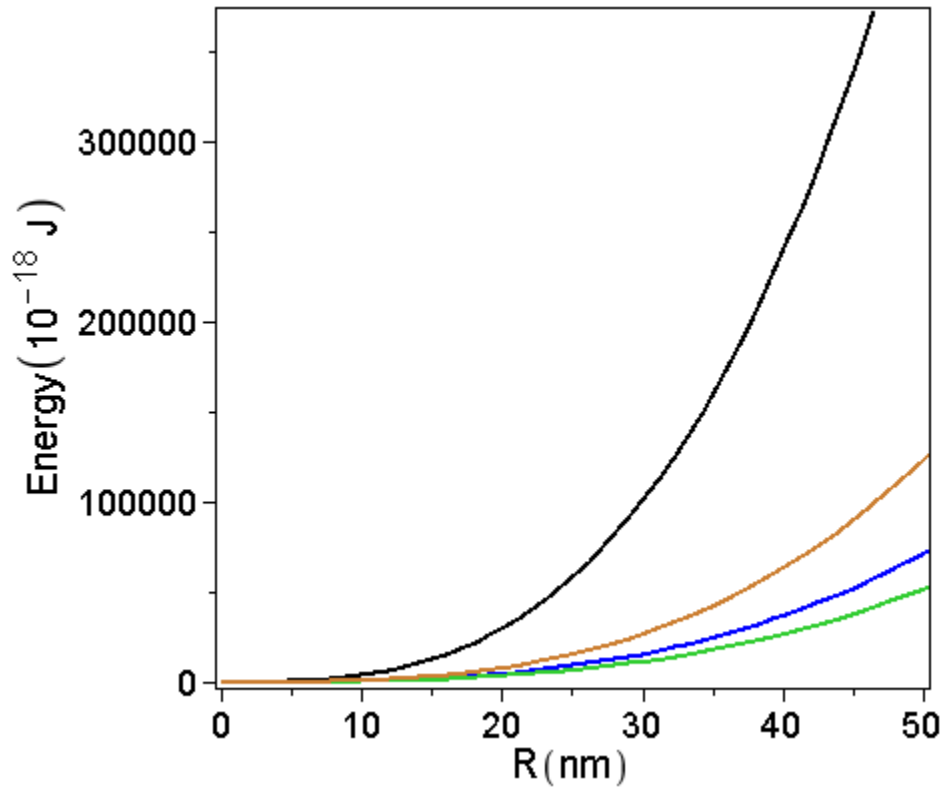


Figure 3-9. Strain Energy vs. nanorod radius for flexible substrate model. Curves show coherent energy for rigid substrate case is much more than flexible substrate case. Black line: Total coherent strain energy with rigid substrate assumption, Gold line: Total coherent strain energy with flexible substrate assumption, Blue and green lines are strain energies in overlayer and underlayer respectively

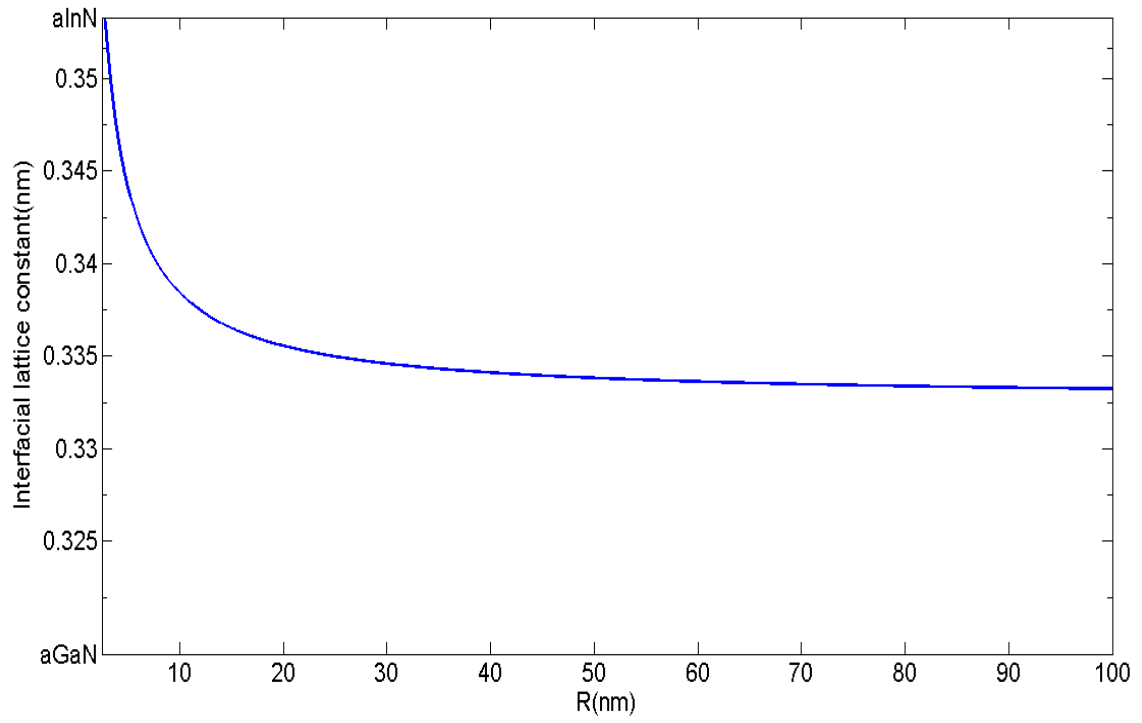


Figure 3-10. Interfacial lattice constant vs. nanorod radius for flexible substrate model

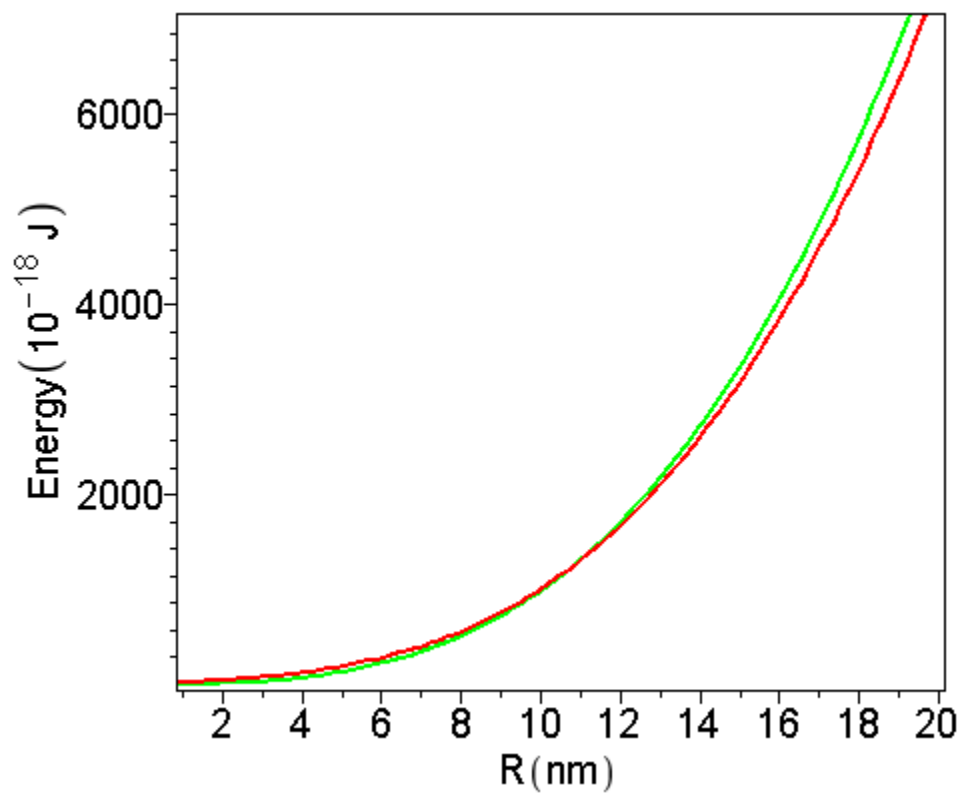


Figure 3-11. Strain Energy vs. nanorod radius (flexible substrate): Red curve is total energy of dislocated system; Green curve is total coherent strain energy

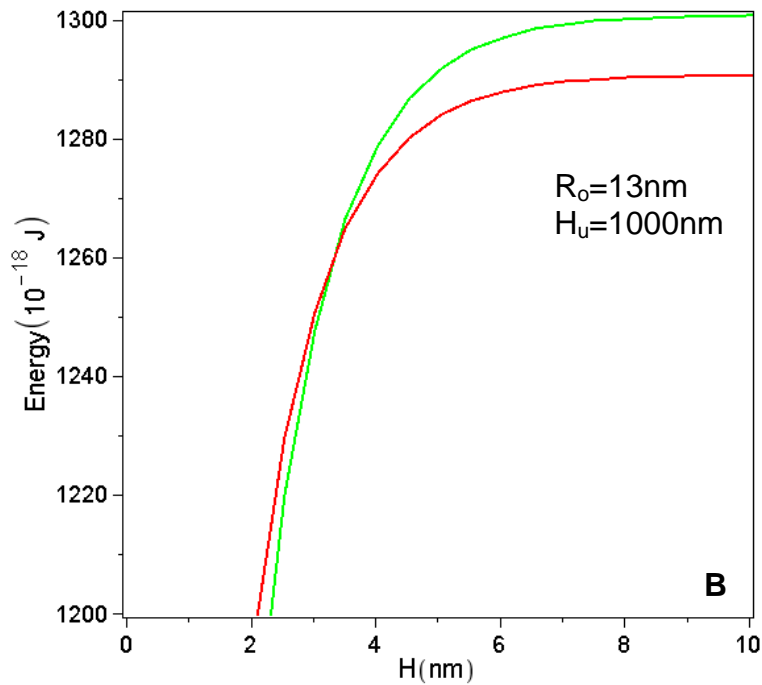
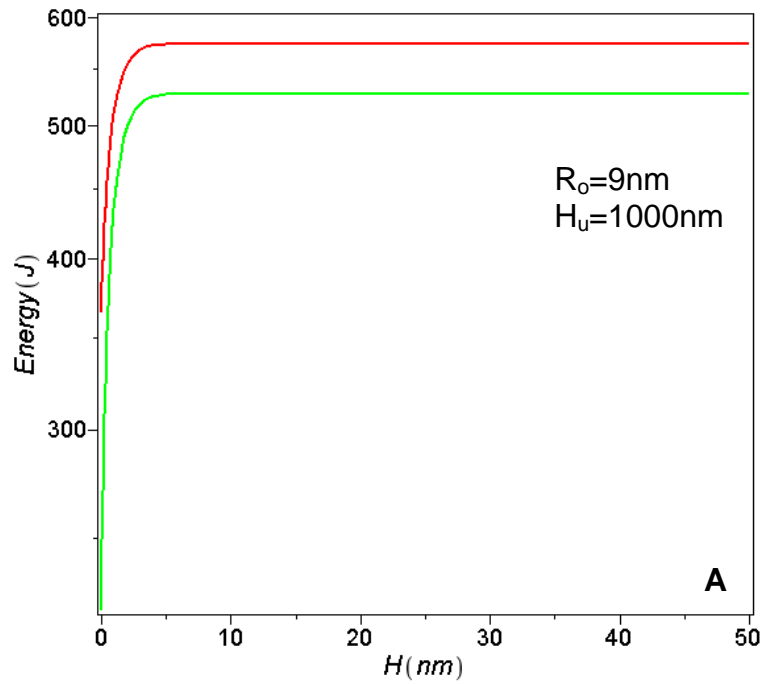


Figure 3-12. Strain Energy vs. nanorod height (H_o) (flexible substrate): Red curve is total energy of dislocated system (E); blue curve is coherent strain energy (E_c) A) for $R_o = 10\text{nm}$ nanorod is coherent at any height, B) for $R_o = 13\text{nm}$ nanorod is coherent only below 3.5nm height

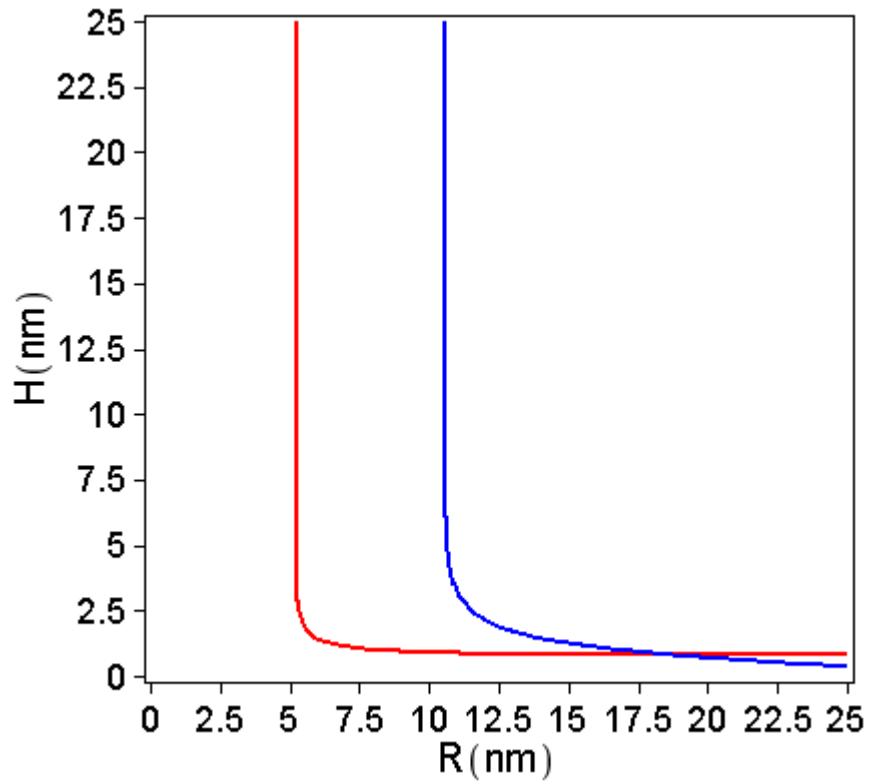


Figure 3-13. Coherency map for InN nanorod on GaN. Red and blue curves are for flexible and rigid substrate case respectively. In area above the red curve dislocations will tend to form or system might acquire S-K growth mode to increase compliance of substrate.

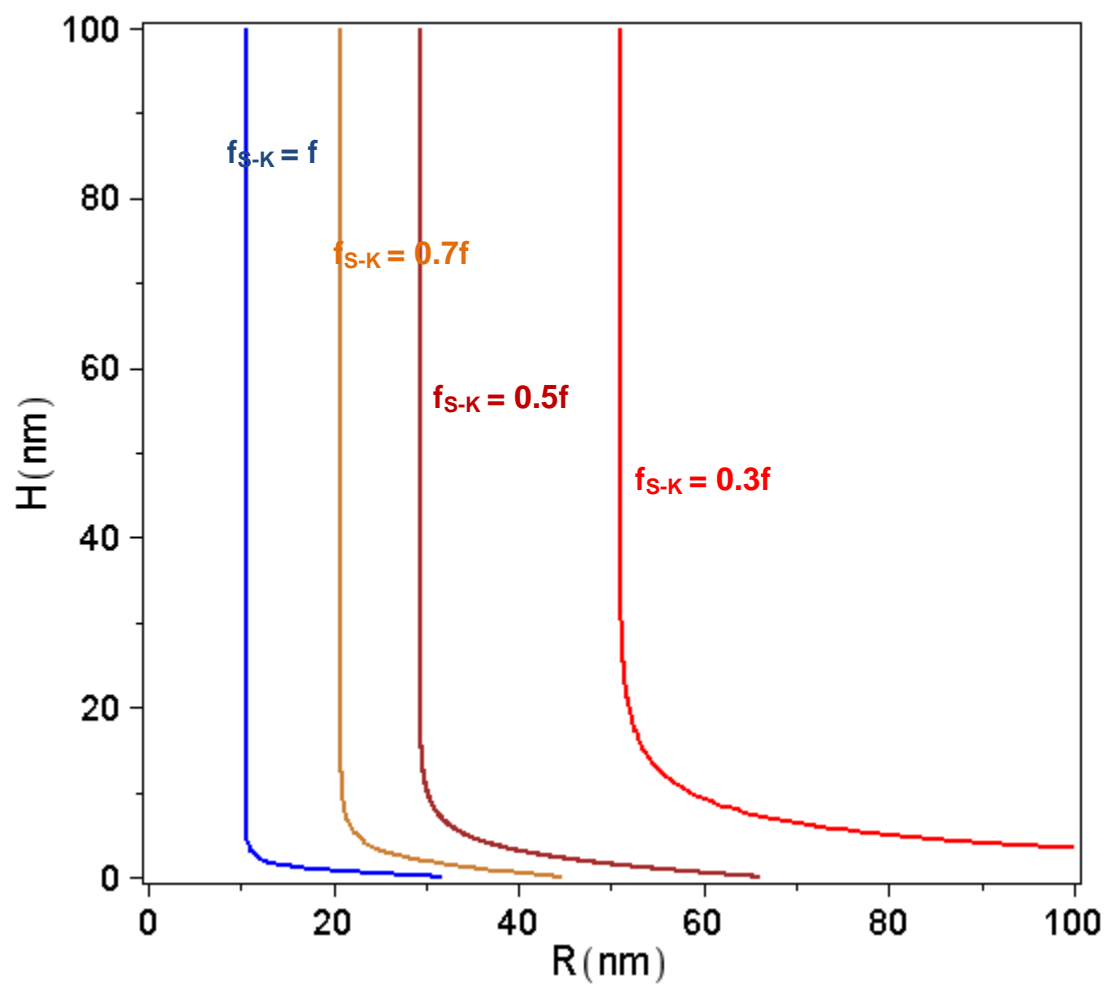


Figure 3-14. Coherency map for InN nanorod on GaN in S-K mode.

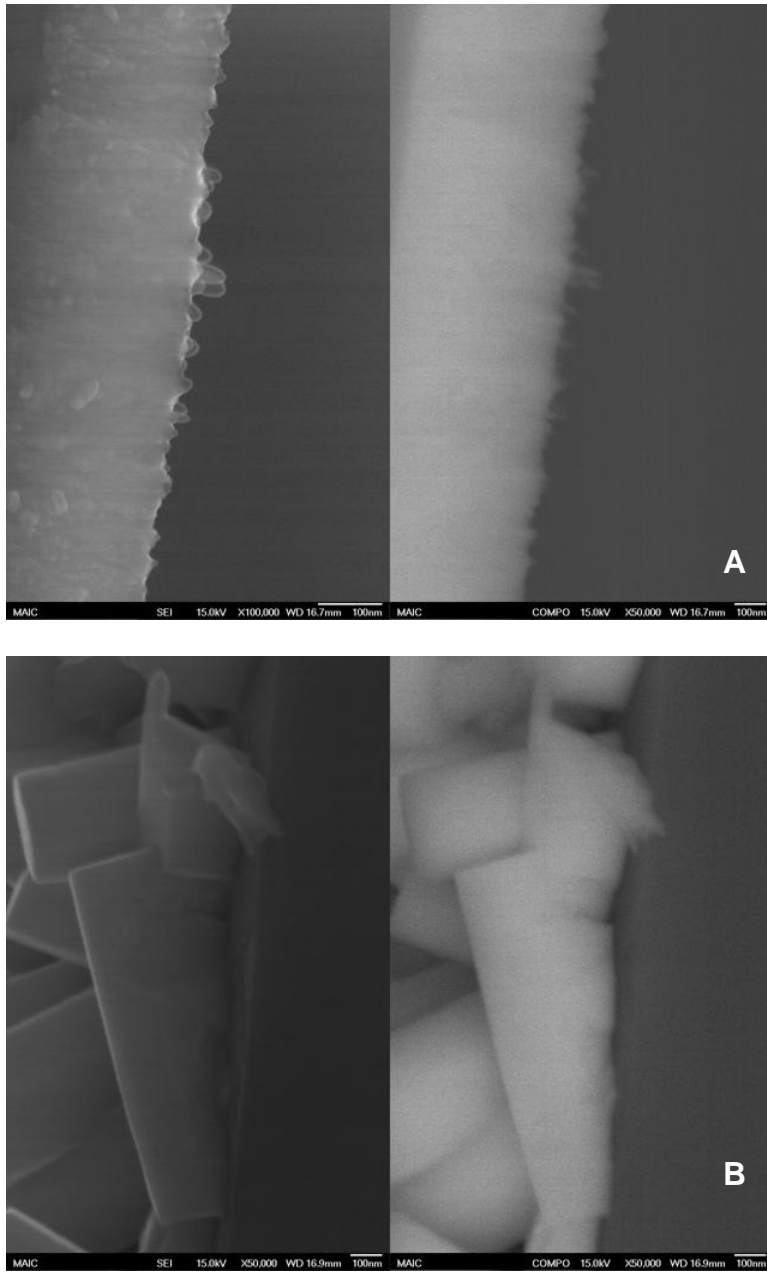


Figure 3-15. SEM and COMPO images showing no evidence of films below InN.
A) InN_{NR} initial stage on GaN film, B) InN_{NR} directly growing on Si

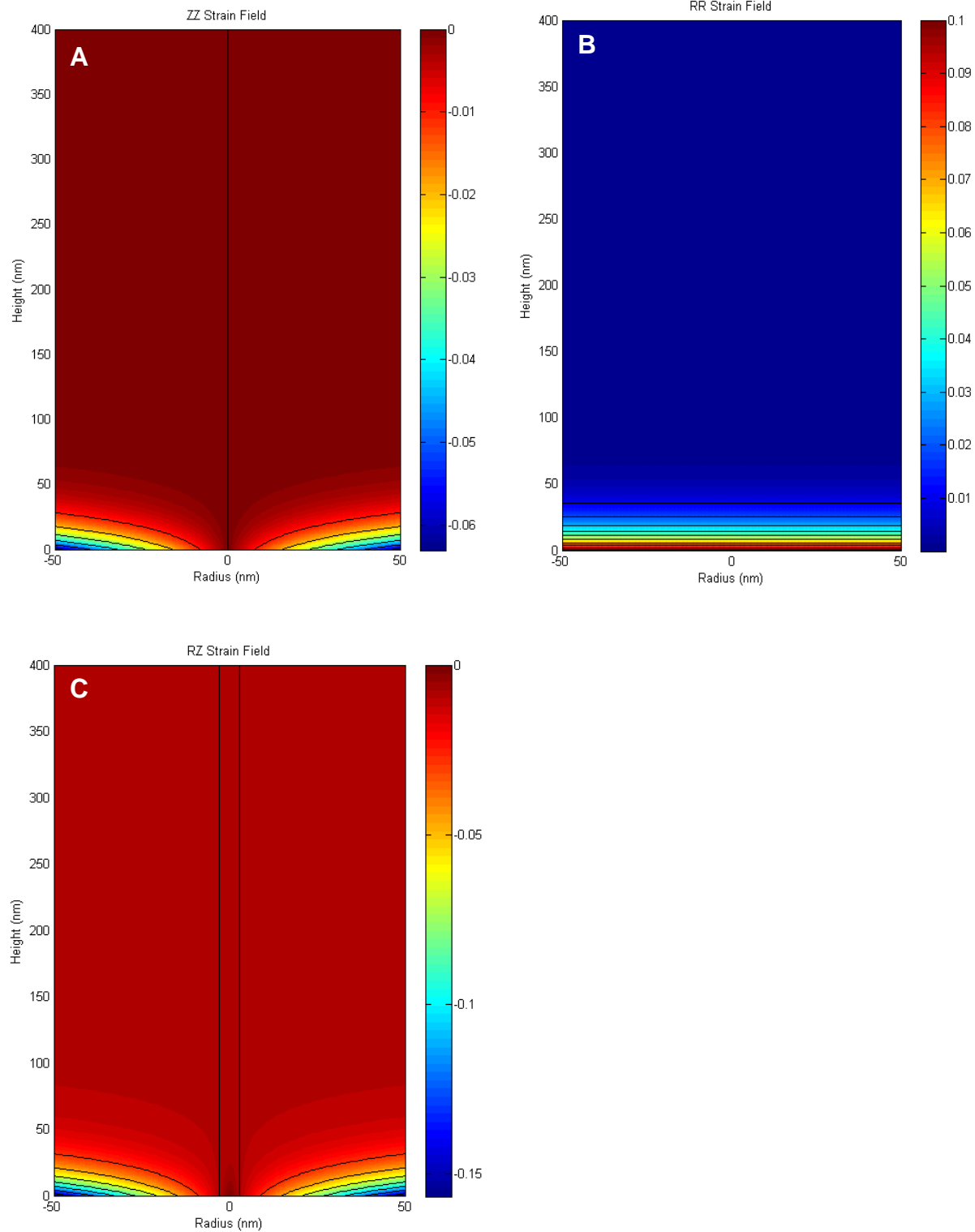


Figure 3-16. Relaxed strain in nanorod bulk. A) Longitudinal strain, B) Radial strain, C) Shear strain

CHAPTER 4 GROWTH OF GALLIUM NITRIDE ON SILICON IN MO-HVPE

GaN Using InN in Literature

In the field of III-V semiconductors GaN has gained lot of importance over last two decades. This is as a result of several material properties such as wide direct band gap of 3.4eV, high temperature stability, high mobility exhibited by GaN. These properties are in fact perfect for variety of applications from public applications to military purposes. GaN has been grown on several substrate materials, among which sapphire is most widely used for several applications such as blue light emitting diodes and laser diodes. With emergence of GaN as very important material for consumer applications, integration of GaN with silicon has become problem of great interests. This is because Silicon is available in fairly large diameters and relatively lower cost. Silicon also has better electrical and thermal conductivities as compared to sapphire. Silicon already has large share of market in semiconductor industry. As a result, the production processes for Silicon devices are well developed. This has been a major driving force behind integrating GaN with Silicon.

On sapphire substrates, AlN is the most widely used buffer layer to grow GaN which has produced very good results. Similar to sapphire, GaN on Si with AlN as buffer layer or by graded AlGaIn layers as buffer has been attempted by various researchers^{56-59,65-67,125,156}. AlN has good lattice match with GaN, but as GaN growth on AlN goes through island growth and coalescence, often dislocation originate at grain boundaries due to slight orientation differences in individual grains. Earlier study also observed that due to strong bond between Si and GaN via AlN, often cracks due to high tensile strain in GaN propagate into the silicon substrate.

Use of InN as buffer layer for providing weak bond between Si and GaN is very promising. InN has lattice constant between Silicon and GaN which makes it better match with Si as well as GaN. InN has low decomposition temperature of around 873K to 973K, which is perfect temperature to grow low temperature GaN⁷³. Just below 873K, InN bonds are weak and it can be very effective in relieving stress in GaN grown on top. Also, at higher temperatures InN can decompose into the elemental Indium and nitrogen, to reduce the bond between GaN and silicon by forming an airgap. Indium can diffuse into GaN forming graded InGaN. Indium is shown to have alloy formation capability with GaN over entire compositional range previously¹²⁶. Both of these things can be effective in reducing the strain. Use of InN film as a buffer layer, getting promising result with sapphire substrate has been reported previously by various researchers^{48,49,157}. This has been employed to GaN growth on Si by MBE more recently¹⁵⁸. No one has employed use of InN nanostructures as template for growth of GaN yet except previous students from our group¹²⁵, although use of nanostructure as an effective way of relieving strain had been shown by many researchers working on NHE^{89,95,96}. Second Chapter was focused on growth of vertical InN nanorod growth on Silicon substrate. In this Chapter, growth of high quality thick crack free GaN on Si using InN nanorod templates will be discussed in details with all intermediate steps.

Growth of GaN in MO-HVPE Reactor

As seen previously Metal-Organic Hydride Vapor Phase Epitaxy (MO-HVPE) is hybrid between conventional Metal Organic Chemical Vapor Deposition (MOCVD) and Hydride Vapor Phase Epitaxy (HVPE). It has three metal organic source lines, two out of which are in use currently. These metalorganic sources can be quickly swapped as

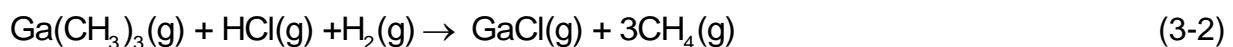
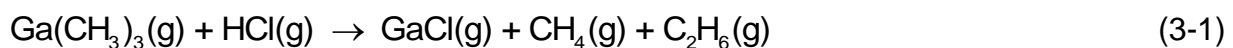
well as turned to vent allowing rapid reactants switching. This makes MO-HVPE more flexible over traditional HVPE where metal sources cannot be transient.

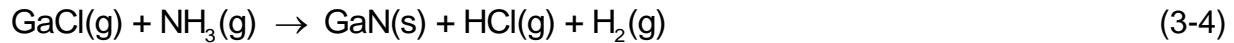
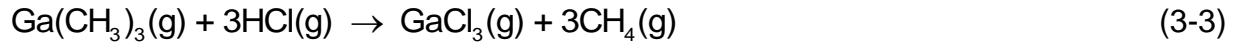
Reactor Setup

The reactor schematic for growth of GaN in reactor is similar to that for InN. It is shown in Figure 3-1. Similar to the InN growth, reactor is capable to be operated with Nitrogen (N₂), Hydrogen (H₂), forming gas (4% H₂, balance N₂) and Helium (He) as sweeping and carrier gases. Typically, 4%H₂ was used as carrier gas for GaN growths, especially at high temperatures to reduce any contamination by oxygen. High sweep gas flows from inlet and gate valve are adjusted so as to minimize wall depositions and confining reactions to growth zone. Typically, growth zone was maintained between 873K and 1173K for GaN growths. As seen in Chapter 2, same reactor can be operated with or without HCl. In both cases GaN forms with different mechanisms. These two modes of operation are explained briefly here

MO-HVPE Operation: HVPE mode

Similar to the case of InN, temperature profile is adjusted in such a way that end of the inlet zone is maintained at 573K to 873K. Generally, inlet is kept at higher end temperatures here for high temperature growths. This temperature profile with shorter metal source tube ensures complete decomposition and reaction of metal organic to form chloride species. This temperature profile also ensures activation of other reactants before they enter the mixing zone. The typical overall reactions that are expected in HVPE of GaN are as follows.

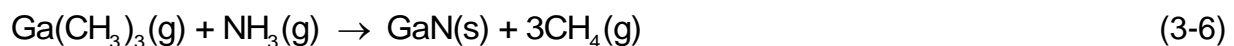




Trimethyl Gallium coming out of innermost tube reacts with, 10% HCl to form either GaCl or GaCl₃ as seen from equations (3-1), (3-2) and (3-3). Generally, with the temperature at the end of the inlet higher than 673K, GaCl is expected to be main Gallium specie. The reaction is generally carried out in presence of some Hydrogen. Introduction of H₂ is found to be helpful in two things. Firstly, it reduces oxygen contamination of GaN film or Gallium oxide formation due to trace amounts of oxygen available in the reactor. Secondly, equilibrium calculations show that it can get rid of carbon contamination of the film¹²⁵. The absence of H₂, however, does not affect GaCl formation. The chlorides GaCl or GaCl₃ react with ammonia to form GaN.

MO-HVPE Operation: MOCVD mode

In absence of HCl gas, the reactions proceed in completely different mechanism, similar to that observed in conventional MOCVD. In this mode, metal organic undergoes irreversible thermal decomposition and then reacts with ammonia to form GaN. In this mode since chloride species reaction with hydride is not present, it is highly dependent on active nitrogen and generally higher NH₃/TMG molar ratios are used to avoid metal contamination and droplet formation in the film. The overall reaction in absence of HCl can be summarized as shown in equation (3-6) below.



Gallium Nitride Growth in MO-HVPE

GaN Growth Conditions

Trimethyl Gallium (TMG) from Epichem and 99.999% pure ammonia from Airgas South were used as Gallium and Nitrogen source respectively. For GaN growth TMG was reacted with 10% HCl (balance nitrogen) from Airgas South in source zone at 673K to form chlorinated species of Gallium. These species were then mixed with ammonia from the concentric inlet in mixing zone. The substrate temperature was maintained at 833K-1173K for growth. The inlet HCl/TMI molar ratio and NH_3 /TMI molar ratio were maintained at 2 and 570 respectively. Ultra high purity Nitrogen or 4% Hydrogen (balance Nitrogen) were used as carrier gases or sweeping gases to avoid wall depositions. The carrier gas flow rate of 1600 sccm was also maintained throughout the runs. When MO-CVD conditions were used, ammonia flowrate was ramped up so that NH_3 /TMG ratio was 2000. Various substrates such as bare Si (100) and Si (111), Indium coated Si (100) were used to grow both low and high temperature GaN. The main focus of this study was to investigate various stages of growth of GaN on InN template.

GaN Growth Stages

The total growth of GaN on Si involves various stages. The temperature time ramp is shown in Figure 4-2. The stages upto the growth of InN_{NR} are covered in Chapter 2. This Chapter covers growth of GaN on InN template. It involved two different stages. They are as follows:

Growth of low temperature GaN capping layer for InN nanorod template

Indium nitride vertical nanorod template was grown as discussed in detail in Chapter 2 at optimum conditions of HCl/TMI and NH_3 /TMI ratios of 4 and 250 respectively at 873K. Once templates were reproducible, growth of GaN was carried out

in the same run without taking out the InN templates. This was done to avoid any exposure of InN_{NR} to the atmosphere. Although oxidation of InN in air is not fast, year old samples only sometimes showed amorphous In₂O₃ few nanometers thin layers on nanorods¹²⁶. This can have detrimental effect on further GaN growth. Indium nitride starts to decompose as temperatures approach 923K. As a result, it is necessary to grow GaN at low temperature first to take advantage of highly crystalline nature and flexibility of InN nanostructured template. It was shown by previous studies that good quality of GaN growth is possible at low temperatures using MO-HVPE technique¹⁵⁹. These optimum conditions were verified and used to grow low temperature GaN (LT-GaN) capping layer. The capping layer was grown for various times for 300 to 900 seconds growths.

Growth of thick high temperature GaN

After first stage ensured the complete coverage of InN_{NR} template, temperature was ramped up to 1123K and GaN was grown. Typical conditions used for growth are HCl/TMG molar ratio of 2 and NH₃/TMG molar ratio of 570 at TMG flow rate of 1 to 2 sccm. After completion of growth reactor was cooled down at desired rate and ammonia was kept flowing until temperature reaches below 773K.

All the materials are characterized for crystallinity by XRD and TEM, morphology by SEM and composition EDS.

Results and Discussion

As seen in section Chapter 2, InN nitride nanorod template with vertically oriented nanorods was grown on Silicon. The vertical nature of nanorod is confirmed by x-ray diffraction (XRD) pattern and secondary electron image from scanning electron microscope image. The XRD pattern suggested presence of vertical nanorods because

of presence of only (0002) InN peak absence of peaks for any other orientations such as $(10\bar{1}0)$, $(10\bar{1}1)$, $(10\bar{1}2)$. SEM images and pole figures also showed that although vertical, nanorods do not have any particular rotational relationship between Silicon substrate. The selected area electron diffraction (SAED) pattern is good indication of crystalline nature as well as it can be used to confirm the crystalline structure of material. The SAED pattern of LT-GaN under layer shows ring pattern indicating highly textured wurtzite GaN (Figure4-3). It means that GaN is crystalline but not a single crystal. This is expected as GaN is grown at low temperature. The SAED of upper InN nanorods shows spot pattern indicating highly ordered planes or single crystalline nature of InN nanorods. The pattern indicates that the single crystals have wurtzite structure $\langle 000\bar{2} \rangle$ growth directions.

Properties of Low Temperature GaN Capping Layer

Due to high crystalline quality of InN nanorods, lower lattice mismatch as compared to silicon, similar crystal structures, it is expected that GaN growth on top would have better crystalline quality. As known from previous section, due to lower decomposition temperatures of InN, GaN cap layer is grown at 873K on InN nanorods. Figure 4-4 shows different stages of capping layer growth in both cross sectional as well as top views. The capping layer growth for 15-20 minutes was found to give full coverage Figure 4-4 (E) and (F). It is also clear from the pictures that all stages the coverage of GaN is uniform. The GaN grew everywhere with similar uniformity. With progress of reaction, gradual growth on walls and bottom surface between nanorods can be clearly seen in Figure 4-4(A) to (D). This eventually led to completely uniform cap of LT-GaN. There was no indication of voids formation. Thus, the growth does not

seem to be limited by mass transfer at interface. The growth rate of GaN, however, is expected to be highly sensitive to temperature. This is because, at lower temperatures, the growth of GaN is found to be in kinetically controlled regime. Only above 800°C it transits from being kinetically limited to mass transfer limited¹⁶⁰. All different stages of these growths were studied to understand the growth of LT-GaN on InN_{NR}.

Crystallinity of LT-GaN capping layer

Though the coverage of LT-GaN was uniform the grown layer is spikey instead of smooth coverage, giving cacti like appearance to InN nanorods. This is very clear in Figure 4-4 (A). It was an indication that LT-GaN growing on InN was having secondary nucleation after initial film growth. This is typical Stranski – Krastanow growth mode that is observed in semiconductors with higher lattice mismatch^{140,141}. Since lattice mismatch between InN and GaN is more than 10%, this behavior is expected. The heterogeneous nucleation behavior is dictated by various things. Surface energetics plays impotent role. Gibbs energy of formation of heterogeneous nuclei depends on various surface forces. It is given by by following equation¹³⁴.

$$\Delta G = -(V / \Omega)\Delta\mu + A_{\text{base}}\Delta\alpha + A_{\text{surface}}\alpha$$

where V = volume of nuclei (m^3)

Ω =molar volume (m^3/mol)

$\Delta\mu$ =chemical potential difference for nucleating specie in vapor and condensed phase (J)

A_{base} , A_{surface} = areas of base and exposed faces of nuclei respectively (m^2)

$\Delta\alpha = (2\alpha - \alpha_s)$

α =surface free energy ($\text{J}/\text{mol}/\text{m}^2$)

α_s =energy of adhesion (J/mol/m²)

InN has lower bond strength (6 eV) as compared to GaN (8eV). Also, bond strength of In_xGa_{1-x}N is expected to be between these two. As a result, GaN does not have special affinity for InN surface. So growth is either expected in island form or film followed by island form. Secondly, when similar materials with different lattice constant are deposited on each other, bonds get in tension or compression. And nature of growth is also dictated by atomic potential interactions. For our case where material of lower lattice constant is deposited on higher lattice constant material, upper layer experiences tensile force. In such case, film formation is favored with dislocation formations¹³⁶. Thirdly, every material can minimize total energy in a process if it grows with equilibrium shape, dictated by Woulf's construction. As a result, GaN grows in the form of hexagonal prisms and since (000 $\bar{2}$) plane is closed pack plane, $\langle 000\bar{2} \rangle$ direction is generally favored growth direction. As a result secondary, nucleation is expected, especially at higher growth rates and lower temperatures.

With growth in S-K mode, still LT-GaN on InN nanorod was also expected to be textured. The powder XRD scan of sample in Figure 4-4(E) and (F) is shown in in Figure 4-5. It shows two peaks for GaN, (10 $\bar{1}1$) GaN and (0002) GaN peak, confirming that indeed growth of GaN was polycrystalline. The presence of (10 $\bar{1}1$) peak indicates that some of the (10 $\bar{1}1$) planes are also parallel to the substrate surface or horizontal direction. If GaN grows in S-K mode, first few layers that form shell on outer surface of InN nanorod are expected to be epitaxial. As a result, the (10 $\bar{1}1$) diffraction peak for GaN is expected to come from the spikes.

To see if indeed this hypothesis is true, the interfacial relationship between LT-GaN over layer and InN under layer, InN-GaN core shell structures was studied. The core shell structures selected for the study were formed by 5 min low temperature growth of GaN on InN nanorods (sample is shown in Figure 4-4(A) and (B)). This kept shell thin enough to be studied in Transmission Electron Microscopy (TEM). TEM is good tool to study structures which are electron transparent, typically specimens below 200nm are desirable for such studies. The TEM bright field image of typical InN-GaN core shell structure is shown in Figure 4-6. In TEM, transmitted electron beam is used to image the samples. The transmitted beam intensity varies because of mainly two reasons when it passes through sample. Firstly, the atomic densities of different atomic planes vary. Thus, depending on their orientation, incoming electron beam transmits defiantly through different planes. Secondly, higher atomic number (high Z) elements hinder or scatter electron beam more than the low Z elements. The latter effect gives darker appearance to higher Z InN core. The difference of tints in images of different spikes as well as shell was, however, mainly because of difference in orientations of GaN planes.

As seen from Figure 4-6, the nanorod core is 100 nm InN core with shell of around 30nm (not including the protruding spikes). In the image of the half nanorod the dark InN core can be clearly while half of the nanorod does not have any core. On closer look, all spikes on GaN shell appear to have their tips oriented in specific sets of angles viz. $(72^\circ \pm 3^\circ)$, $(62^\circ \pm 3^\circ)$ or $(42^\circ \pm 3^\circ)$ approximately to the vertical direction (direction of nanorod growth). The hollowness of certain parts of the core was also surprising, but it

would be discussed latter on. The next section discusses study on orientation and growth direction of nanorod spikes as well as 30 nm GaN film shell.

Orientation and growth directions of GaN secondary nucleation spikes: To further study the growth characteristics of GaN such as growth directions, orientations etc. the high resolution TEM analysis was done of sample similar to that in Figure 4-6. The Figure 4-7 shows high resolution image of a spike on GaN shell. As seen from Figure 4-7(B), the spike is at angle of 62° to the shell. The Figure 4-7(C) shows the high resolution image with arrays of atomic planes visible. On any visible array, the line scan can be done as shown. The average distance between consecutive peaks can be used to determine the d-spacing between the planes. Series of line scans were carried out to determine the d-spacing between the vertical and horizontal arrays of atoms seen in the image. They were found to be 0.24757nm and 0.46215nm respectively. The ideal d-spacing of $(10\bar{1}1)$ is 0.2438 nm. It was closest to the smaller one of observed d-spacing values. But the value of 0.46215nm did not correspond to any lower index planes in GaN.

Since Figure 4-7(C) is an atomic scale image, atomic arrangements can give idea about the orientations and plane in view. The CrystalMaker[®] 2.3.1 can be used to visualize atomic arrangements in space. It was clear from the crystallographic model that regular molecular pattern in high resolution TEM image looked like atomic arrangements viewed from $\langle 1\bar{2}10 \rangle$ direction. The atomic arrangements are shown in Figure 4-8. It is clear from the models that the growth of GaN in $\langle 000\bar{2} \rangle$ direction occurs in ABABAB form i.e. with alternating layers of Ga and N and after every two layers (AB) the structure repeats itself. The Figure 4-8(C), also shows the ball and stick model

superimposed on actual lattice fringe image. The model matches actual lattice fringe image to the scale. Thus, the spikes like structures on GaN shell were GaN secondary nucleation growing in $\langle 000\bar{2} \rangle$ direction. It was, thus, concluded that the lattice spacing of 0.24757nm corresponded to $(10\bar{1}0)$ planes and other to the $\langle 000\bar{2} \rangle$ d-spacing. This particular nano spike was growing at an angle of 62° to vertical nanorods. Since the growth direction of nanorod was $\langle 000\bar{2} \rangle$ direction, it made $(10\bar{1}1)$ parallel to the horizontal plane. In other words in powder $\theta - 2\theta$ XRD pattern, it would contribute to $(10\bar{1}1)$ diffraction peak. Similar analysis on other spikes at other angles can be done. In GaN crystal the angle between $\langle 000\bar{2} \rangle$ direction and $\langle 10\bar{1}2 \rangle$ is 43.23° and that between $\langle 000\bar{2} \rangle$ and $\langle 11\bar{2}1 \rangle$ directions is 73° . Thus these spikes would contribute to $\langle 10\bar{1}2 \rangle$ and $\langle 11\bar{2}1 \rangle$ peaks respectively. It should be, however, noted here that the 62° spikes can also appear to be at higher or lower angle if nanorod on TEM grid is rotated towards or away from viewer respectively. As a result there can be apparent reduction or increase in d-spacing also.

From direct measurement of d-spacing on various lattice fringe images, lattice constants can be estimated. For hexagonal system the d-spacing of plane is related to $(h k l)$ indices and lattice constants through following relationship.

$$\frac{1}{d^2} = \frac{4}{3} \left(\frac{h^2 + hk + k^2}{a^2} \right) + \frac{l^2}{c^2}$$

Knowing the $(h k l)$ indices and d-spacing, lattice constants 'a' and 'c' were calculated. The calculated values of lattice constants from all different spikes were consistently smaller than the actual values. Their average value was found to be 0.3034nm and 0.4939nm respectively. The ideal values of lattice constants for GaN are

$a = 0.3186\text{nm}$ and $c = 0.5189\text{nm}$. It should be noted here that, the observed c/a ratio of 1.6280 was similar to ideal value of 1.6262 for GaN. As a result, the apparent reduction in the measured value by exactly 5% could have been because of either error in TEM calibration or the slight tilt of the nanorod.

Growth direction of GaN shell and its epitaxial relation with InN core: Similar to the secondary nucleation sites, lattice fringe analysis of GaN shell on InN nanorod was done. The Figure 4-9 shows lattice fringe image of shell area of structure. The observed d-spacing from shell was 0.25157nm which again corresponded to the $(10\bar{1}0)$ planes. To confirm the growth direction and epitaxial relationship with InN core selective area electron diffraction was done at hollow shell as well as core-shell tip with InN core still intact. The SADPs (Selective Area Diffraction Patterns) are shown in Figure 4-10. These SADP patterns were superimposed with SADPs generated by kinematical simulations¹⁶¹ generated by Web-EMAPs. The inset images also show the simulated pattern. As seen from the Figure 4-10(A), shell with no InN core SADP matched pattern with $[1\bar{1}00]$ zone axis. This means that core was growing in such a way that $\langle 000\bar{2} \rangle$ direction is parallel to the core and shell wall was increasing in thickness in $\langle 11\bar{2}0 \rangle$ direction. This pattern is similar to that shown for InN nanorod in Chapter 2. It confirmed that $(11\bar{2}0)\langle 000\bar{2} \rangle \text{ GaN}_{\text{shell}} \parallel (11\bar{2}0)\langle 000\bar{2} \rangle \text{ InN}$ at core. The SADP of tip in Figure 4-10(B) showed double diffraction pattern as viewed from $[000\bar{2}]$ zone axis. The bright spots in SADP correspond to reciprocal lattice space, meaning the distance between the spots is inversely proportional to the d-spacing. Thus, inner and lower intensity spots corresponded to InN core and outer brighter spots corresponded to GaN. The SADP confirmed hexagonal nature of InN and GaN and similar pattern also

confirmed highly epitaxial growth of GaN shell on InN core. Thus, lattice relationship between InN core and GaN shell can be summarized as $(11\bar{2}0)\langle 000\bar{2}\rangle \text{ GaN}_{\text{shell}} \parallel (11\bar{2}0)\langle 000\bar{2}\rangle \text{ InN}_{\text{core}}$.

After establishing the epitaxial relationship that is followed between InN and GaN, the lattice constants 'a' and 'c' for GaN were estimated with lattice fringe as well as SAED measurements. The average lattice constants in GaN shell area were found to be 0.3130nm and 0.5068nm respectively with fringe measurement with c/a ratio of 1.6191. The average values of lattice constants with SAED were, however, 0.3154nm and 0.5286nm with c/a ratio of 1.6760 which was much higher than ideal value. SAED patterns were not sharp and hence these calculations become less accurate.

Compositional analysis of InN template capped with LT-GaN

As seen from various images, in the InN – GaN core shell nanostructures, not all were filled with InN nitride. Many of the nanorods were partially filled and some of them empty (Figure 4-11). It is well known that InN is not stable above 923K. In addition, when shell forms, due to absence of ammonia availability, InN can decompose even at 600K to form Indium metal. As a result, partially decomposed InN nanorod cores were visible in GaN shells. During TEM analysis, these dark regions sometimes behaved like liquid and liquid Indium was forced out of shell (Figure 4-11(E) and (F)). It confirmed that these dark regions were Indium metal or partially decomposed InN. It is known that InN and GaN are not very much miscible into each other. Also, SAED patterns showed no evidence of $\text{In}_x\text{Ga}_{1-x}\text{N}$ formation. Thus, it was important to see if InN has diffused into the GaN shell.

Electron dispersive spectroscopy was used for qualitatively looking at the InN. In TEM and SEM, electrons that cannot come out of the sample excite and then again go back to generate X-rays that are characteristics of that particular element. These X-rays coming out of the electron interaction volume in sample as a result have wavelengths characteristic to the composition of that particular region. Hence, with proper detector they can be used for qualitative analysis. When line scan and point scan was done at different points in the core shell structure, no or negligible Indium signal was detected in lighter regions as shown in Figure 4-12. Also, in XRD of similar sample, shown in Figure 4-5, no $\text{In}_x\text{Ga}_{1-x}\text{N}$ peak was detected. For example, (0002) peak, $\text{In}_x\text{Ga}_{1-x}\text{N}$ should be observed between InN (0002) peak and GaN (0002) peak. The EDS, thus, confirmed that there is no significant $\text{In}_x\text{Ga}_{1-x}\text{N}$ formation at interface of InN nanorod surface and GaN cap. Similar to the individual nanorods covered in GaN, samples shown in Figure 4-4(C) were analyzed in TEM and EDS was done. The TEM image of this sample is shown in Figure 4-13. TEM image showed lighter areas at nanorod spots indicating nanorod voids. But, the EDS scans on darker region only detected Gallium and no Indium signal was found. The electron transparent samples are generally 200nm and thinner. Due to such low volume, if Indium is not present in substantial amount in shell it cannot be detected. Samples are prepared in focused ion beam. And it is possible that due to high energy beam InN nanorods were etched away similar to electron beam removing Indium metal from core in TEM.

Annealing of LT-GaN grown on capped template: As seen in previous section, the core shell structures showed absence of Indium in the core. For samples on which GaN was grown for prolonged period of 20 min at 873K, no Indium was detected. The

InN is unstable above 923K. As InN nanorods were capped and were always below 873K for the growths, InN was not expected to completely disappear. To study this phenomenon, the same capped sample was annealed for 10 minutes under ammonia atmospheres from temperatures ranging from 923K to 1123K. After every anneal run the XRD $\theta - 2\theta$ scan was collected. For each run, new sample from same original run at 873K was used to maintain uniformity. As anneal temperature was increased, as seen from plot shown in Figure 4-14, quality of GaN improved as well as InN peak decreased. It was an indication of decomposition of InN. Also, there was no appearance of $\text{In}_x\text{Ga}_{1-x}\text{N}$ peak. So even if it formed it was very limited and was not detectable. It is also clear from the Figure 4-14 that GaN peak becomes sharper till about 1073K and at 1123K InN and GaN (0002) peak heights become equal. The increase in sharpness of GaN was due to improvement in quality due to anneal. On plots of areas under GaN and InN (0002) peaks vs. temperature (Figure 4-15), it was observed that GaN peak started improving after 973K and InN peak started decreasing. The ratio of areas under the InN peak and GaN peak decreased as temperature increased. It was clear indication of InN decomposition without getting much incorporated in GaN.

Estimation of amount of InN in LT-GaN/InN_{NR}/LT-GaN/Si sample: The quantitative estimation of amount of Indium in the sample was done by two methods. Firstly samples were dissolved in concentrated nitric acid overnight. The nitric acid with dissolved sample was then analyzed using ICP-MS. ICP MS estimated Indium fraction to be 2-3 molar percent. It was observed that nitric acid was not able to dissolve sample completely even after 48 hours. As a result, the amount of InN was estimated to be higher than 2-3%.

In another approach, the estimation of amount of Indium in sample similar to one shown in Figure 4-4(C) and (D) was done using SEM imaging. One of the annealed samples was scraped with tweezers lightly to knock off some of the heads. The Figure 4-16 shows the SEM image of the sample with hollow nanotubes of GaN. The core radius was very uniform in diameter with average core diameter of 100nm. From the simple analysis of different images, the amount of Indium that should have been present in the sample can be easily calculated. Knowing area fraction of InN_{NR} core in each core shell structure and area coverage by core shell structures, fraction of area covered by InN in the sample is known. Knowing heights of each layers in the sample, amount of InN present in fully covered InN nanorod sample as shown in Figure 4-4(E) and (F) was calculated out to be 3-5 mole percent. Even lower limit of calculation gave, more estimate than ICPMS analysis. Thus, 3-5% mole is thought to be accurate estimate for amount of InN present.

Although annealing results showed that decomposition of InN core took place, there was no evidence in XRD or TEM for alloy formation. With fully covered sample, some amount out of 3-5% of Indium should be trapped in the sample in some form. The SEM EDS was used for confirming presence of Indium and its distribution in the sample. When EDS was done at the surface it showed Indium atomic fractions of 0.93-1.04% which was close to detection limit. In EDS, characteristic X-rays come out of the sample from depth of up to a micron. Although, sample was not more than 2.5 microns thick, absence of Indium in surface scan meant negligible Indium is present in micron depth. But cross sectional EDS revealed presence 2.85-2.95% Indium in the sample. The point EDS at different points across cross section was done. It revealed presence of 1.25 –

2.1% In, 2.37 – 3.70% In, 2.81 – 4.74% In in capping LT-GaN, bottom of the nanorod and bottom LT-GaN layer respectively. EDS line scans revealed that all concentrations remained constant across the sample whereas along the depth of the sample Indium showed grading. Indium tends to be lower in the concentration at top and its concentration peaked at the boundary where nanorods originate. Secondary Ion Mass Spectrometry also gave similar qualitative profile for Indium. The SEM-EDS profiles and SIMS depth profile are shown in Figures 4-17 and 4-18 respectively.

Properties of High Temperature GaN (HT-GaN) layer

The HT-GaN was grown at 1123K for 1 hour and 5 hours. The one hour grown film was characterized for morphology, crystalline quality, composition. The 5 hour growth was done on various types of templates mainly to produce thick crack free GaN over 1cm x 1cm substrate. It was characterized for surface morphology and for crystalline quality.

Growth conditions for thin and thick HT-GaN

For the 1 hour run the growth rate was low and it produced about 1500nm films, as seen in Figure 4-20(B). The HT-GaN layer in HMOVPE tends to be very rough and nitrogen terminated. This effect is generally because of presence of hydrochloric acid in the system. The HCl gas acts as both scavenger for metal and etchant for GaN film. The HT-GaN in 1 hour run was grown by two methods.

In first method, after growth of InN template GaN was grown, GaN growth was started at 873K. But simultaneously temperature was ramped from 873K to 1123K. During the course of 15-20 minutes that temperature ramped, GaN was continuously kept growing. This method was employed with rationale that growth with continuous and gradual temperature increase will provide gradual change in quality of GaN. As a result,

when HT-GaN is grown at 1123K, it will be much more relaxed. In second approach, LT-GaN was first grown for 20minutes. Then temperature was raised to 1123K and then HT-GaN was grown for 1 hour. The samples grown from both cases are shown in Figure 4-19 and Figure 4-20 respectively.

Thick GaN was grown on various samples. They included A) vertical InN nanorod templates as discussed in Chapter 2, B) random InN nanorods grown on Si, C) bare Silicon substrate and D) vertical InN nanorod templates covered with 15 min of LT-GaN. All the samples were loaded into the reactor in a single run to maintain the uniformity of conditions. Initially, another layer of LT-GaN was grown at 873K to form buffer layer on bare silicon and capping layer on InN nanorod samples. It also gave one more coat of LT-GaN on already capped sample D. Then temperature was increased to 1173K and high temperature GaN was grown for 4 hours at high growth rate of about 10 microns per hour.

Properties of thinner HT-GaN

In first case contrary to expectations, GaN films showed lots of cracks and GaN films peeled off. The peeling of GaN film from substrate silicon is expected because of low bonding between LT-GaN and Silicon. But in this case GaN peeled off from both silicon as well as initial LT-GaN layer as seen in Figure 4-19(A). High temperature GaN tends to crack if grown on bare silicon, because of thermal expansion mismatch and lattice mismatch. But initial LT – GaN gives some relaxation. In first case, when GaN was grown on InN nano rods grown on the initial LT – GaN with continuously increasing temperatures, process of capping GaN formation and decomposition of InN were going on simultaneously. This resulted in lower bonding between initial LT-GaN and upper GaN layer that resulted in peeling of later. The peeled off layers are shown in Figure 4-

19(B) and it also shows back side of uppermost layer of GaN. It is a hollow structure, with voids instead of nanorods. No nanorods were found on anywhere on the sample. The EDS was done on the same sample on both front and back side. On front side as expected Indium concentration was below 1%, while on back side it was 3% which is just above the detection limit of EDS. Figure 4-19(C) and (D) show close view underlying LT-GaN buffer layer and HT-GaN. While HT-GaN films are rough, LT-GaN show high texture with c-faces of GaN crystallites visible. Grains in HT-GaN are however much bigger.

In second case, films did not crack similar to first case, but often self-separated from substrate due to low adhesion between LT-GaN buffer and silicon. This is good, if standalone thick GaN is desired product. As discussed in previous section, at higher temperatures InN decomposes. Same thing was seen here. Both cross sectional SEM image in Figure 4-20 (B) and TEM image in Figure 4-21 showed voids of InN instead of nanorod. SIMS depth profile was done to study diffusion of Indium into the film similar to in case of LT-GaN growth. The SIMS profile as seen in Figure 4-22, showed that Indium that is diffused in LT-GaN does not penetrate into upper GaN crystal. Due to high temperature, even $\text{In}_x\text{Ga}_{1-x}\text{N}$ alloy formation is not possible. Also, due to high crystalline quality, Indium may not have as much accumulation sites such as grain boundaries in HT-GaN as in LT-GaN.

The SAED analysis of upper GaN layer produced very sharp dot pattern with was indication on grain growing in $\langle 000\bar{2} \rangle$ direction. This better quality growth was expected at high temperature. The grain sizes were found to be in micron range, with 700nm as shown in Figure 4-21. The lattice parameters of high temperature GaN were $a = 0.3164$

nm and $c/a = 0.5167$ and c/a ratio of 1.633 which was near to ideal ratio. The film was not, however, single crystal GaN growing in $\langle 000\bar{2} \rangle$ direction, and various grains had different zone axes. As a result film was believed to be polycrystalline.

Properties of thick HT-GaN

Thick GaN grown was 50 μm in thickness. Different substrates produced different results in terms of growth without cracks. The GaN grown directly on silicon and random InN nanorods cracked. The GaN grown on samples C and D did not crack, but were self-separated. Both of them were highly crystalline and textured in $\langle 000\bar{2} \rangle$ direction. But, only HT-GaN grown on LT-GaN capped InN template showed best ω - 2θ FWHM which was less than 350 arc sec. The XRD spectra however revealed that the GaN grown was polycrystalline. The powder XRD spectra showed a very small $(10\bar{1}3)$ peak which is common facet that can provide strain relaxation during growth. The SEM images and powder XRD scan for best result are shown in Figure 4-23 and Figure 4-24 respectively.

The results showed that if GaN is grown on LT-GaN capped InN templates that have been allowed to relax at room temperature produced good results. This means that the samples of LT-GaN should be allowed to relax before any extra stress is added to them by taking to higher temperature and growing GaN. Self-separation could have been another reason why samples did not crack. Due to lower adhesion between the bottom LT-layer and silicon, developing crack the samples self-separated and relaxed.

Summary and Conclusions

In this Chapter, crack free thick GaN was successfully grown using vertical $\text{InN}_{\text{NR}}/\text{LT-GaN}/\text{Si}$ template developed in Chapter 2. The growth of GaN was crack free

for nanorod templates over area of 1 cm x 1 cm. The GaN grown separated from Si due to weak adhesion. Although crack free high quality GaN could be grown, the results showed the polycrystalline nature of final film, though film seems to be highly textured in $\langle 000\bar{2} \rangle$ direction. The polycrystalline nature of HT-GaN might have origins in bottom LT-GaN nature which was also found to be polycrystalline.

Polycrystalline nature of LT-GaN was arising from SK type growth with secondary nucleations. TEM results revealed that LT-GaN growth started as epitaxial, but did not continue as epitaxial due to high strains and more favorable energetics for secondary nucleations. As a result although InN nanorods were single crystalline, GaN growth was not.

Main reason behind relaxation provided by InN template can be low decomposition temperatures of InN. The decomposition of InN provided nano voids where LT-GaN was able to relax as temperatures increased. This was clear from the fact that HT-GaN films cracked when these conditions were not uniform. For example, when nanovoids were in non-uniform distribution, in case of random nanorods films cracked. When InN mediating layer was not used on bare Silicon, films cracked. Also, when capping of GaN was not complete and simultaneous decomposition and deposition of InN nanorods and GaN respectively was allowed, films cracked. So uniformity of relaxation provided by nanovoids created by InN was must to get good thick GaN growth. Another relaxation mechanism can be formation of alloy of InN and GaN, though no evidence was found for that.

It was also found that although InN is decomposing, Indium metal was not leaving the sample. The Indium mole fraction was calculated to be 3-5% in capped LT-GaN

grown sample. The presence of Indium in the LT-GaN after anneal was confirmed by SEM EDS and the concentration values matched to calculated values. Qualitative analysis by SIMS also confirmed that Indium concentration is distributed in the LT-GaN film with Indium sometimes higher at boundary where nanorods originated.

Thus, this Chapter presents complete study of GaN growth on InN with step by step investigation at different stages of growth. Although relaxation provided by InN nanostructured template can produce crack free GaN, to avoid polycrystalline nature of HT-GaN, the quality and orientation of LT-GaN layers must be improved.

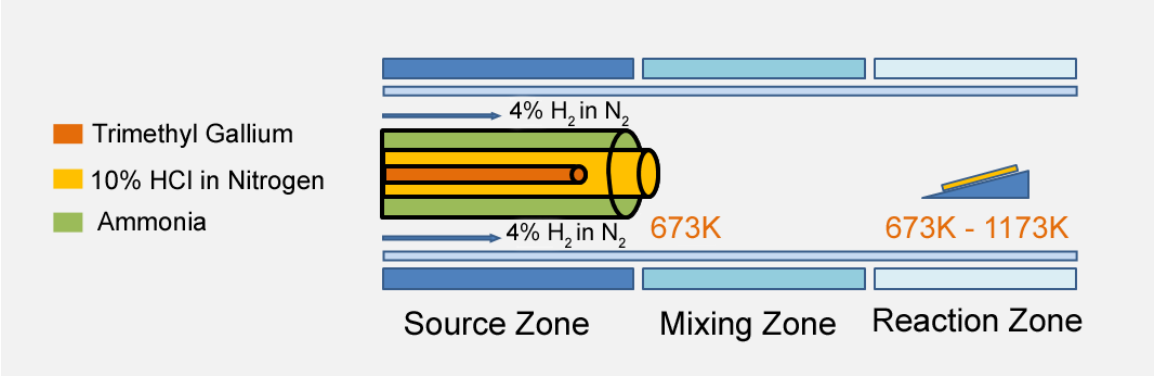


Figure 4-1. Schematic of MO-HVPE for GaN growth

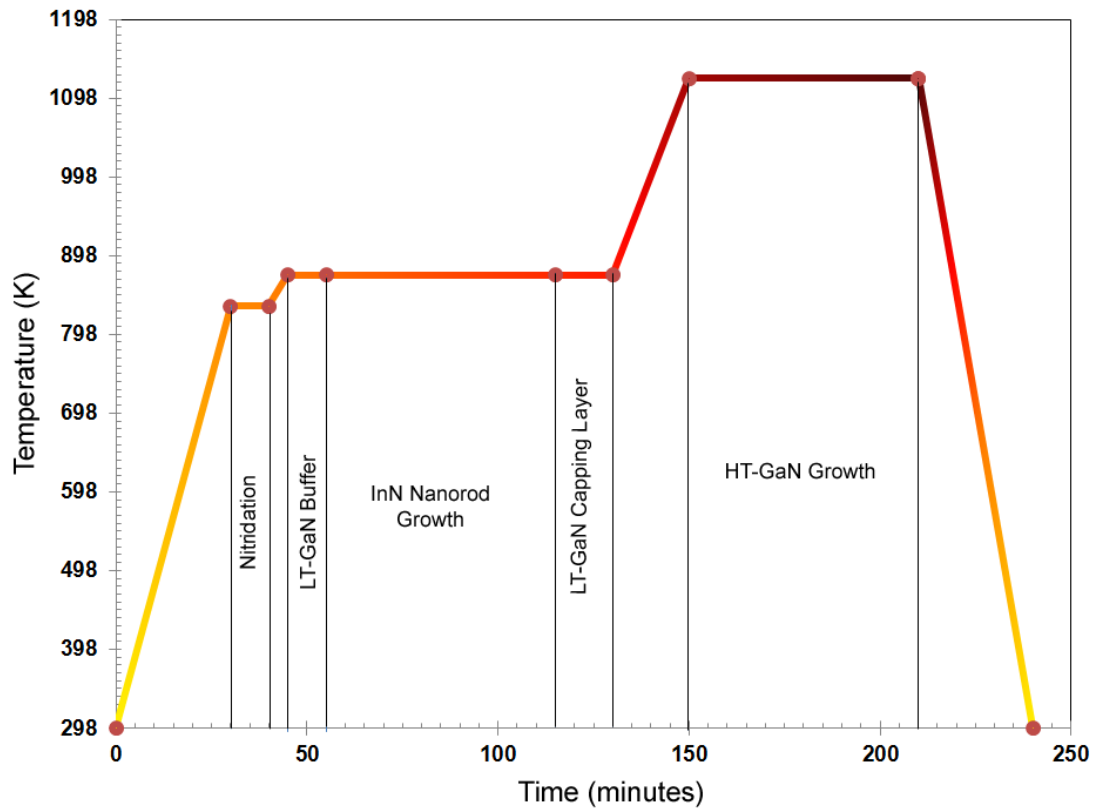


Figure 4-2. Typical growth scheme for thick HT-GaN growth

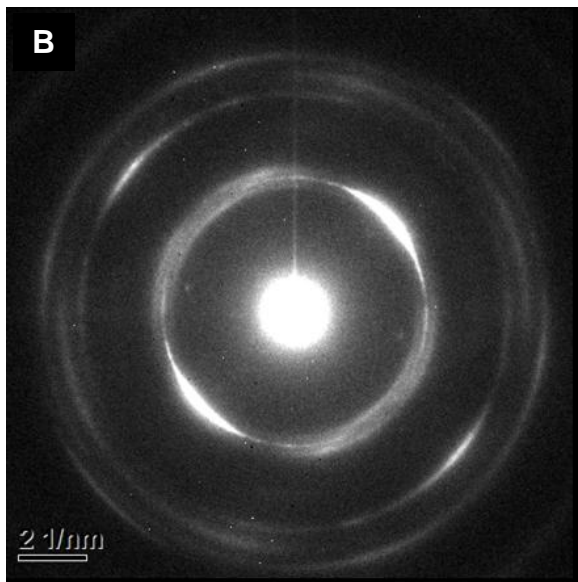
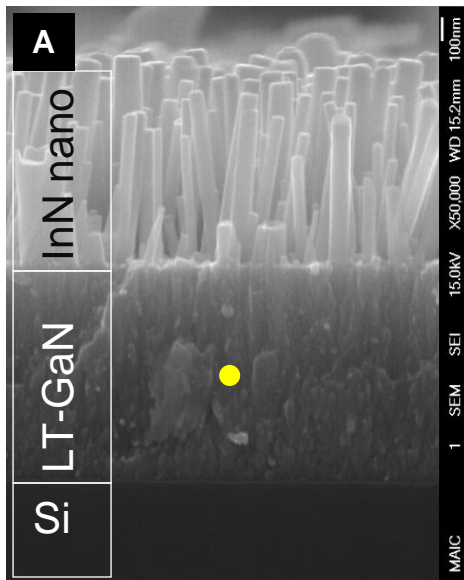


Figure 4-3. SAED pattern for LT-GaN buffer in vertical InNNR template. A) Cross sectional view (The yellow spot gives idea of position of SAED pattern taken FIB sample of similar type), B) SAED ring pattern showing polycrystalline nature of LT-GaN

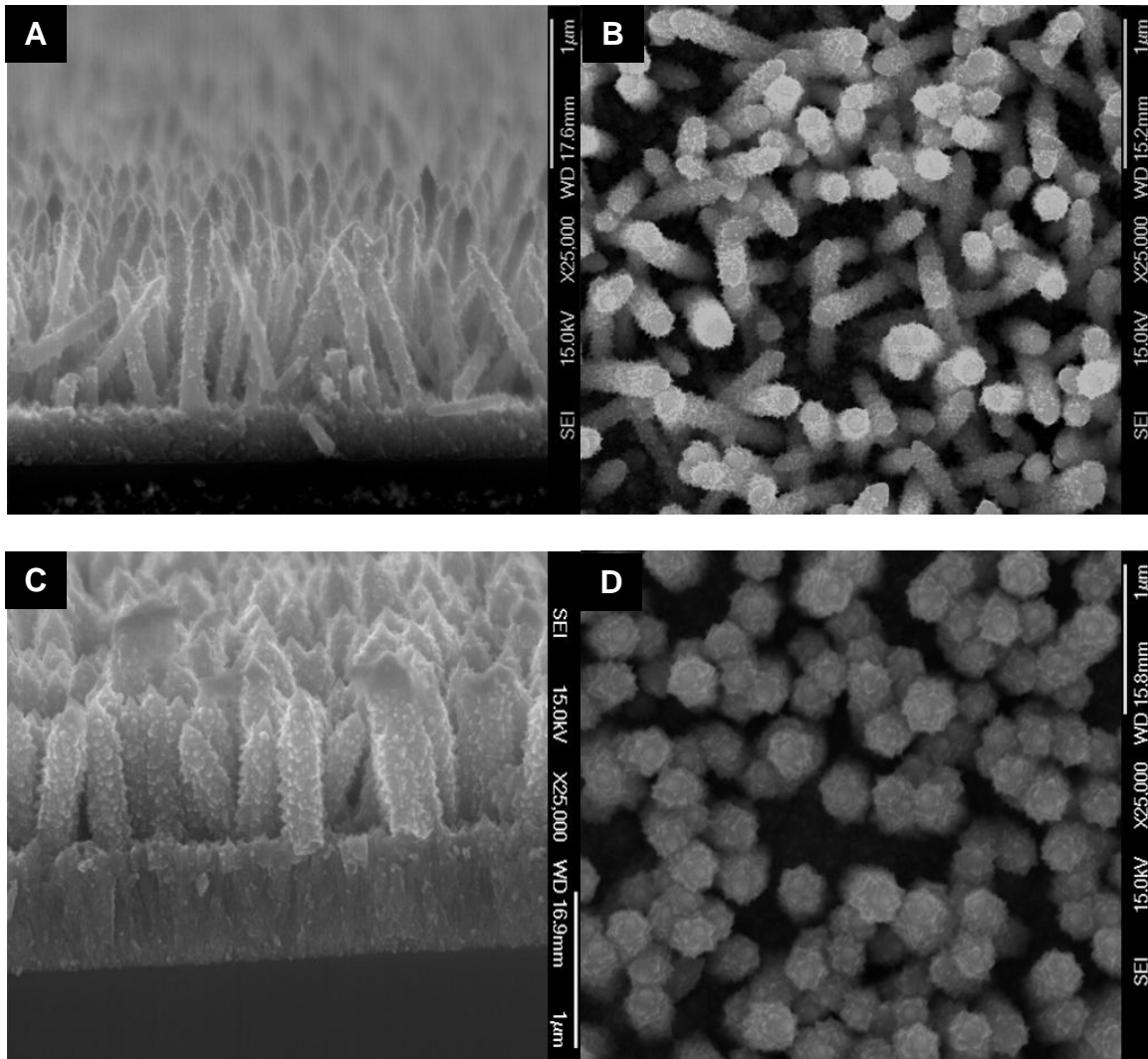


Figure 4-4. Different stages of capping layer growth. A) Cross sectional view and B) Top view of 5 minutes LT-GaN growth, C) Cross sectional view and D) Top view of 10 minutes LT-GaN growth, E) Cross sectional view and F) Top view of 15-20 minutes LT-GaN growth

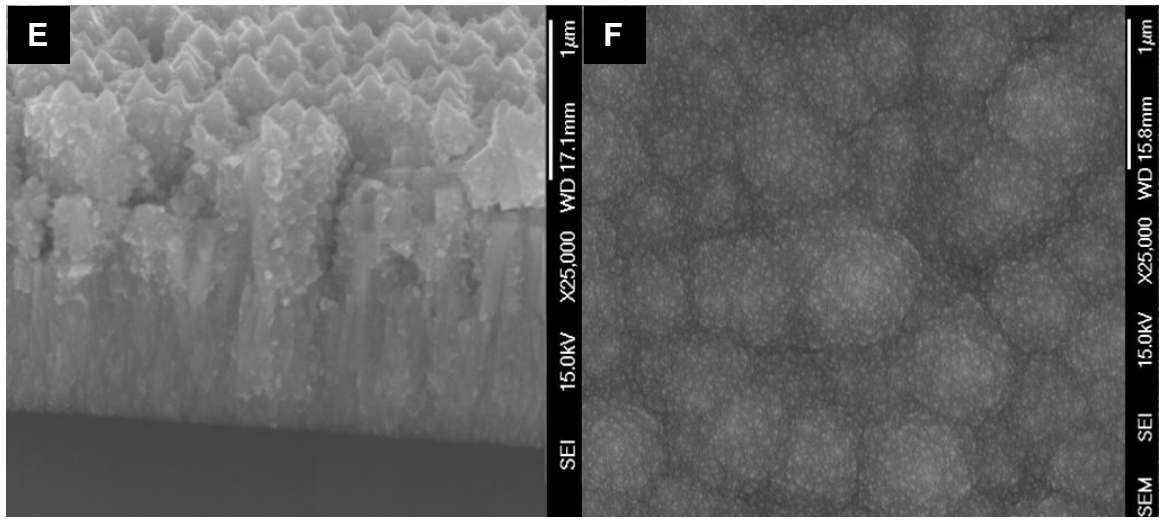


Figure 4-4. Continued...

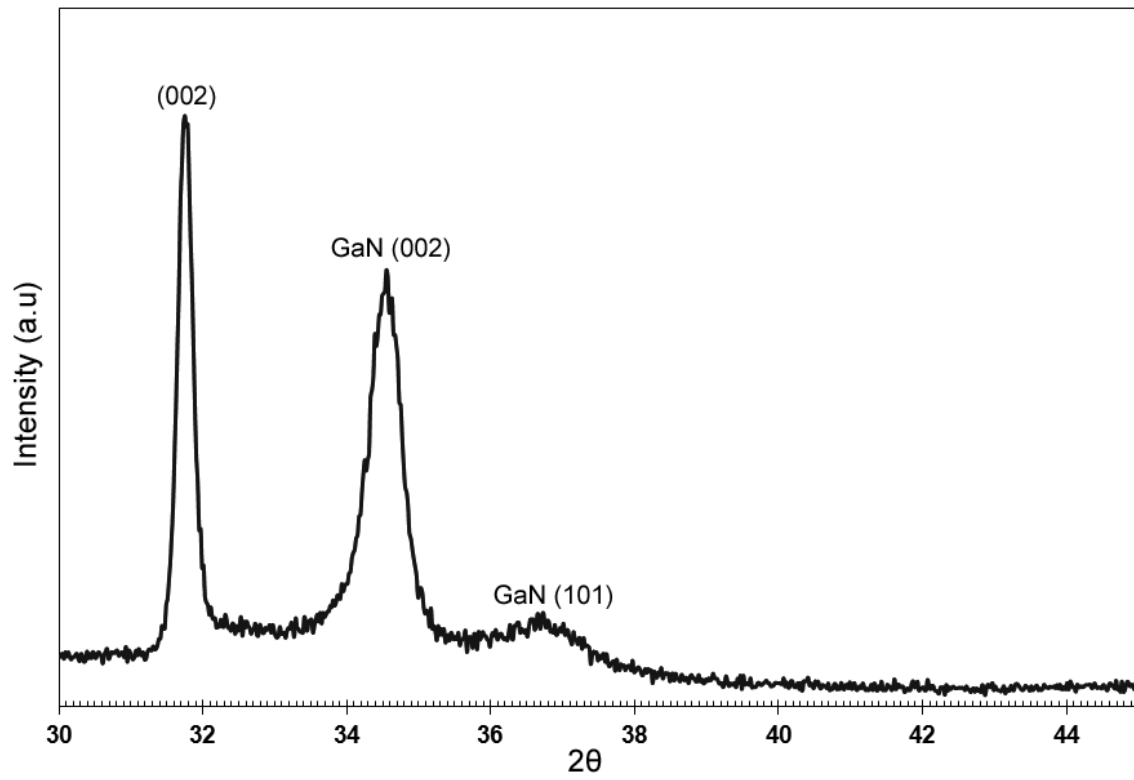


Figure 4-5. XRD (θ - 2θ) pattern for vertically oriented InN nanorod capped by LT-GaN for 15 min

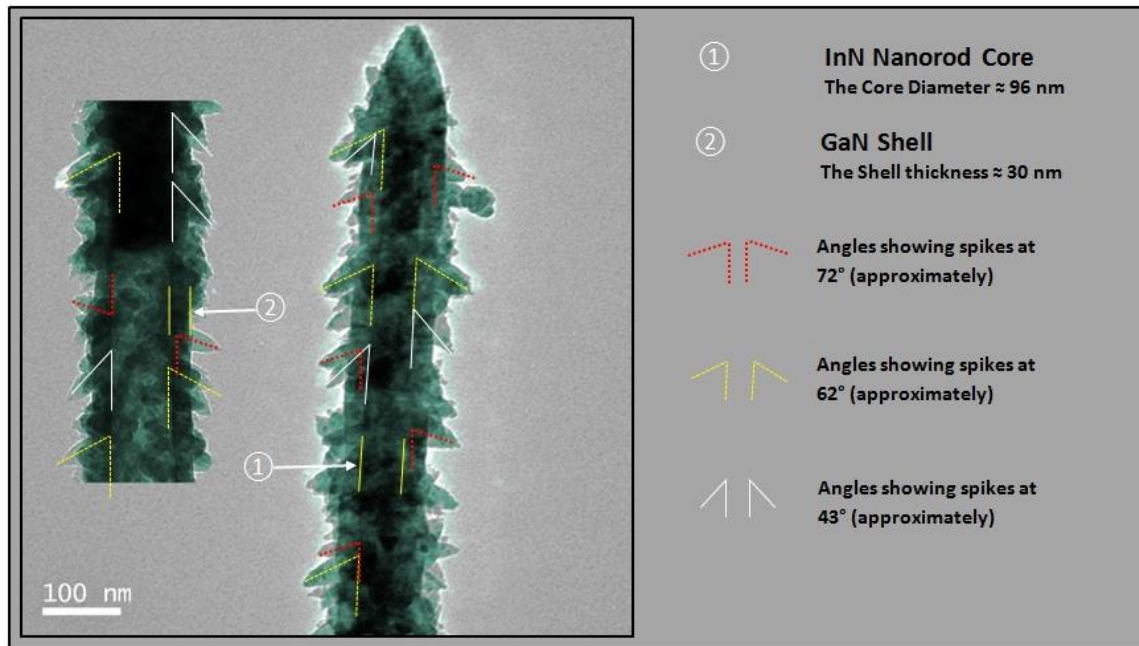


Figure 4-6. TEM image of InN-GaN core shell structure

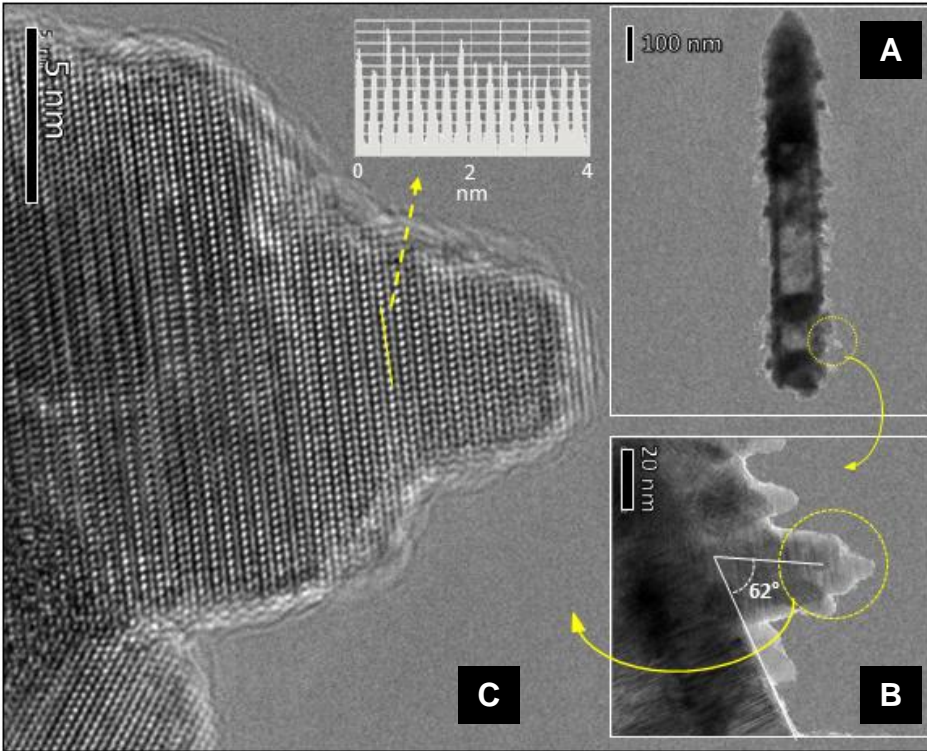


Figure 4-7. HRTEM of GaN spike: A) actual core-shell rod, B) magnified view spike showing spike is at 62° to shell, C) high magnification image with line scan

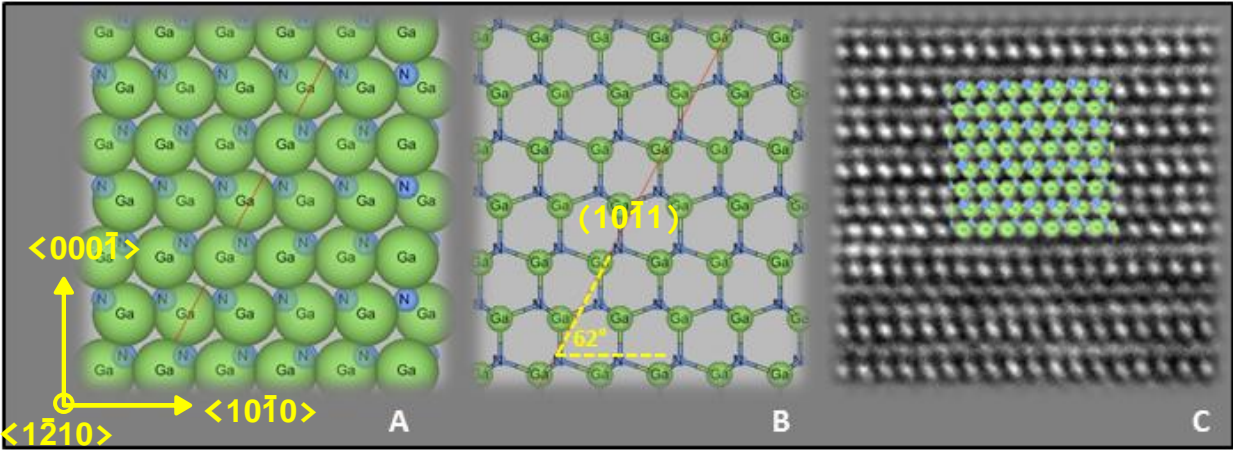


Figure 4-8. GaN as viewed in $\langle \bar{1}2\bar{1}0 \rangle$ direction represented in different models. A) space filled model, B) ball-stick model Ball-stick model shows $(10\bar{1}1)$ plane at an angle of 62° to $\langle 10\bar{1}0 \rangle$ plane, C) Space filled model superimposed on actual lattice fringes showing exact fit.

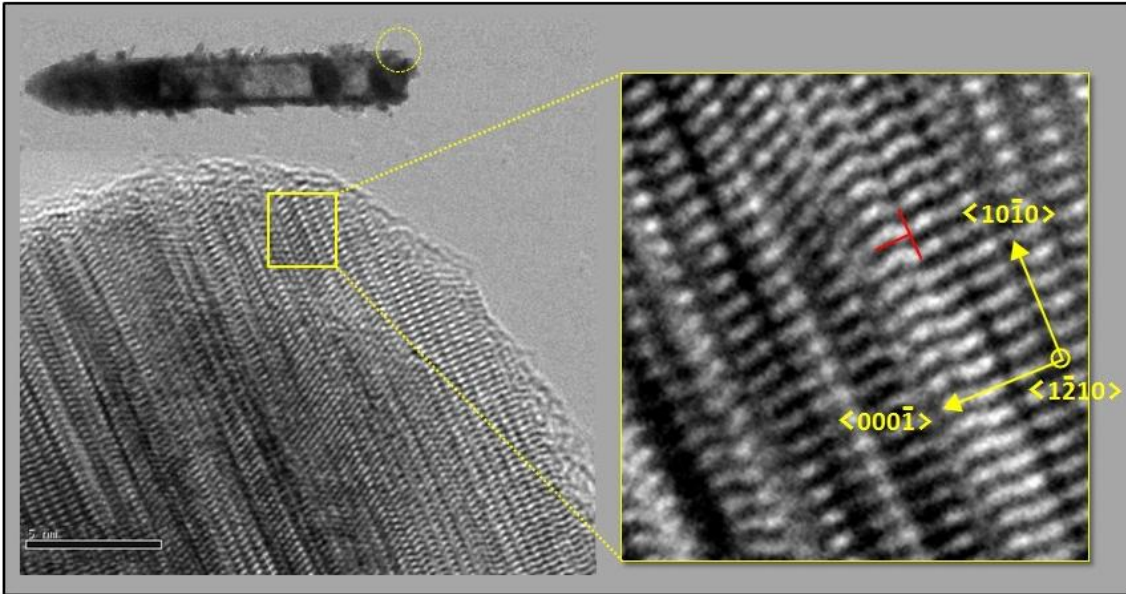


Figure 4-9. GaN shell lattice fringe image. Image in inset shows growth direction of $\langle 000\bar{2} \rangle$ as well as an edge dislocation in red. Edge dislocations of $|b| = a$ are common in wurtzite GaN.

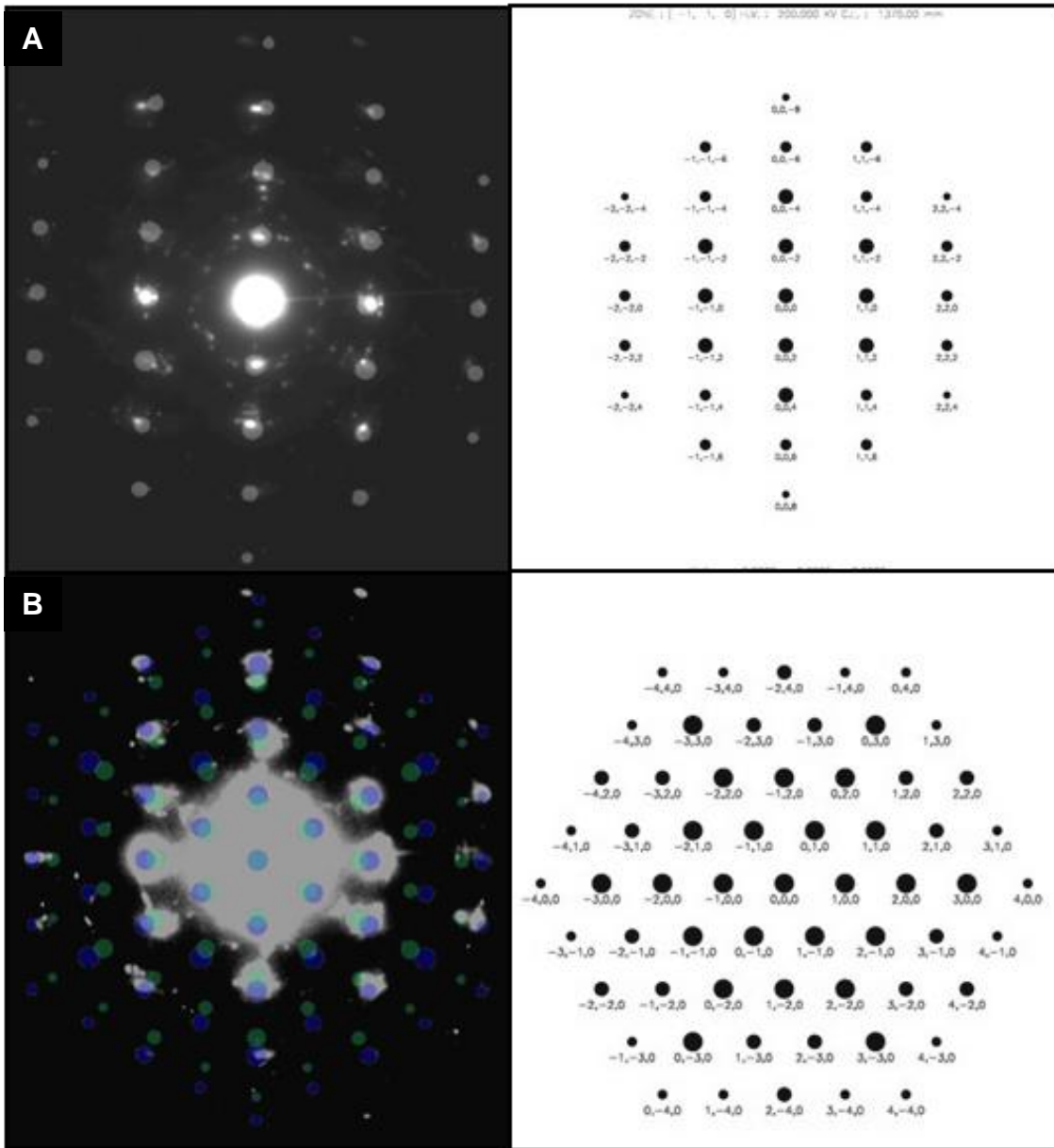


Figure 4-10. SAED patterns of InN – GaN core shell structure shown in Figure 4-6. A)SAED of shell showing pure GaN as viewed in $[1\bar{1}00]$ zone axis, presence of some other bright spots indicate polycrystalline nature, B) SAED of tip showing double pattern as viewed in $[000\bar{2}]$ zone axis, with superimposed blue GaN pattern and green InN pattern. Simulated SAED patterns on right are generated by Web-EMAPs¹⁶¹

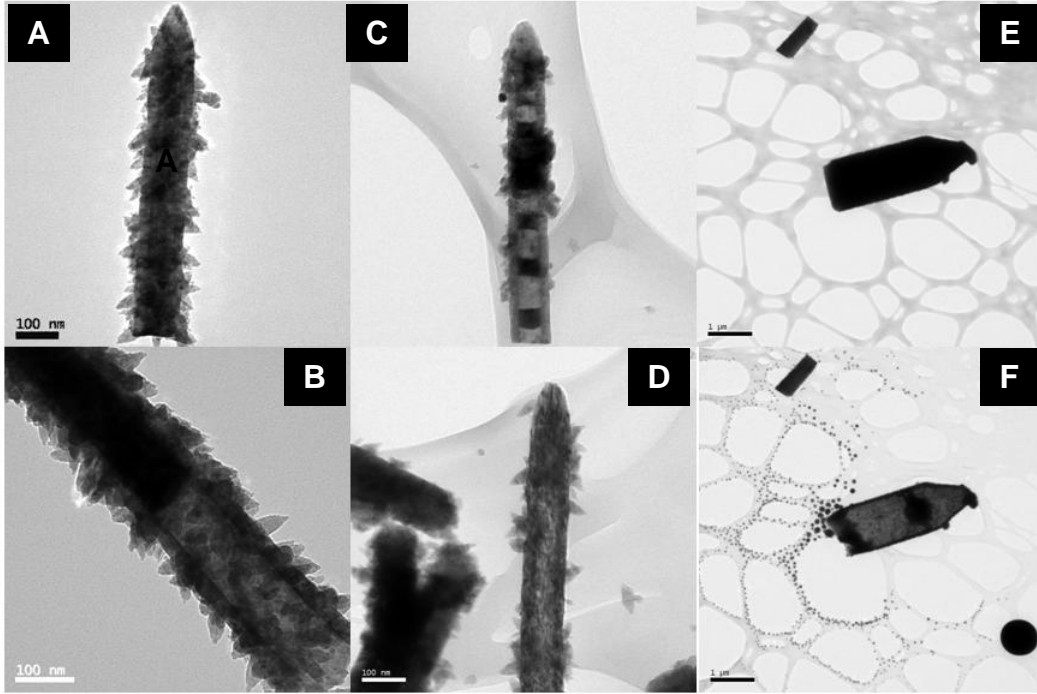


Figure 4-11. TEM Image showing InN-GaN core shell structures filled with Indium nitride or Indium metal. A) Completely filled, B) and C) partially filled, D) Empty GaN shell. E) Micro core-shell filled with Indium, F) Indium forced out on focusing with electron beam

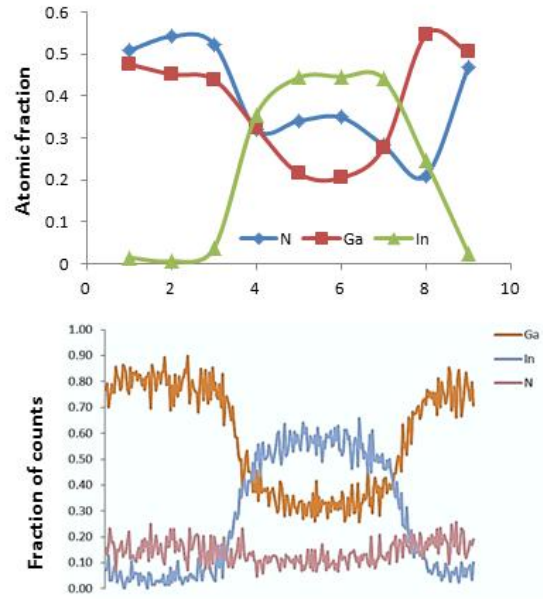
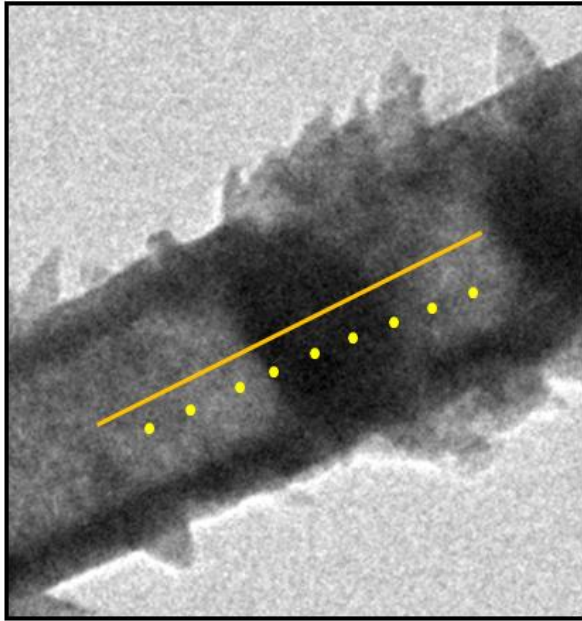


Figure 4-12. Point scan and line scan EDS in TEM both showing absence of Indium in shell possibility of Indium liquid in dark regions.

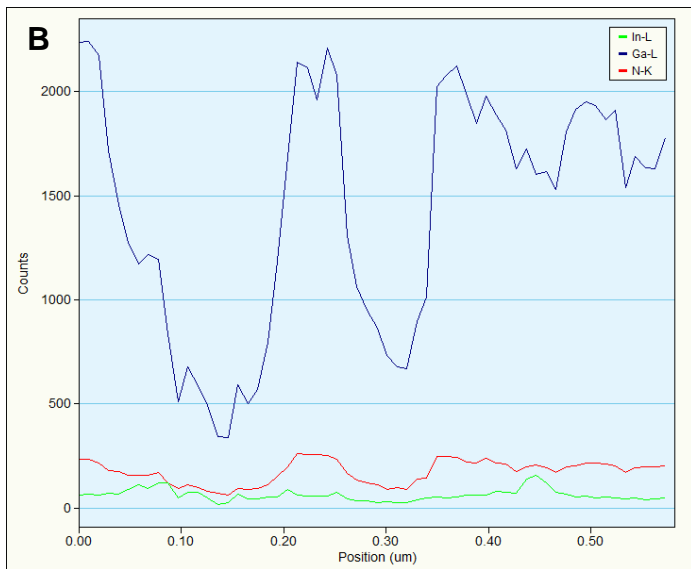
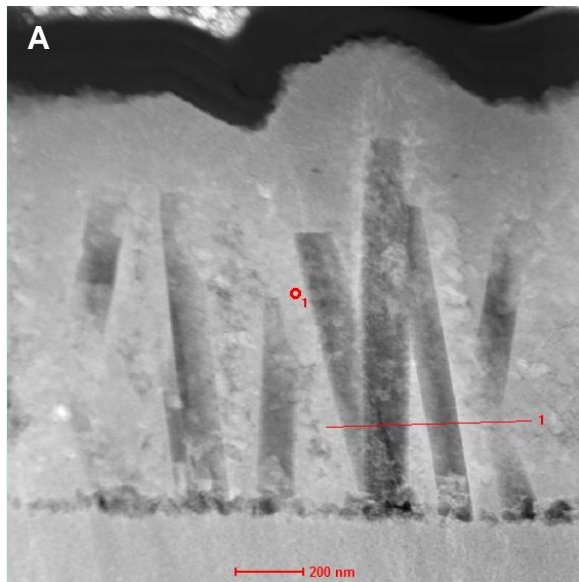


Figure 4-13. TEM and TEM EDS of InN template completely covered in LT-GaN. A) Lighter areas show InN voids, B) Line scan showing total absence of Indium in films.

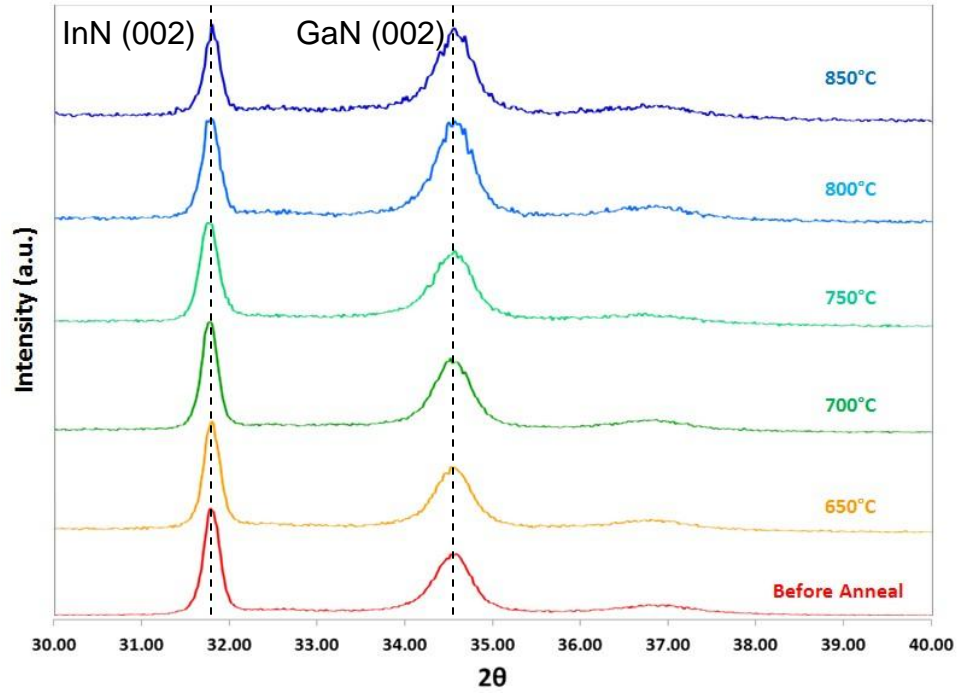


Figure 4-14. Annealing of LT-GaN/InN_{NR}/Si under ammonia atmosphere for 10 minutes at different temperatures showing decomposition of InN

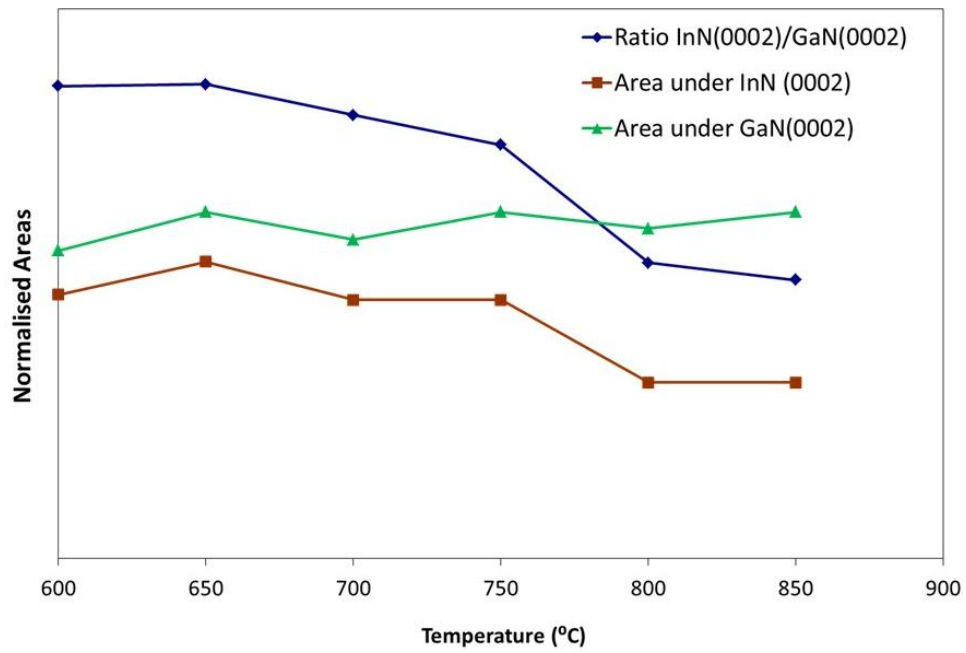


Figure 4-15. Areas under (0002) GaN and InN peaks and area ratio vs. anneal temperature

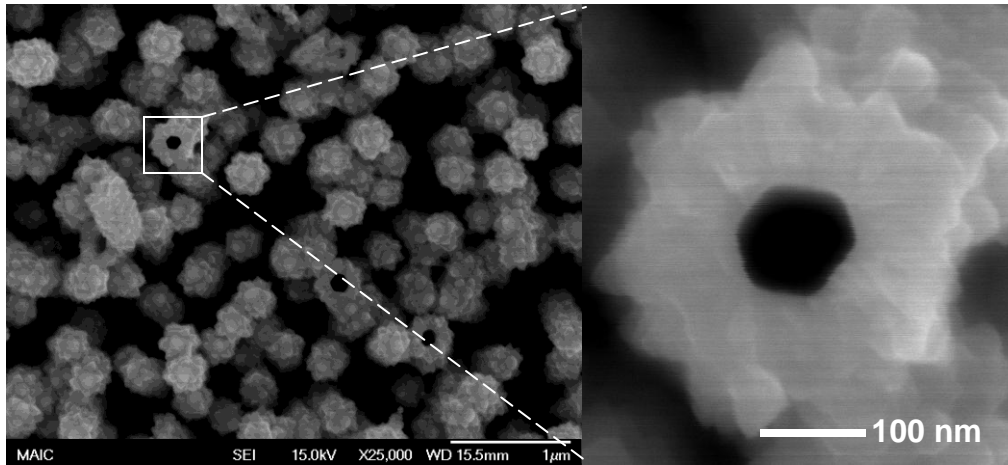


Figure 4-16. Annealed LT-GaN/InN_{NR}/GaN sample. Absence of InN core creates empty GaN shells with 100nm bore and 80nm thick shell.

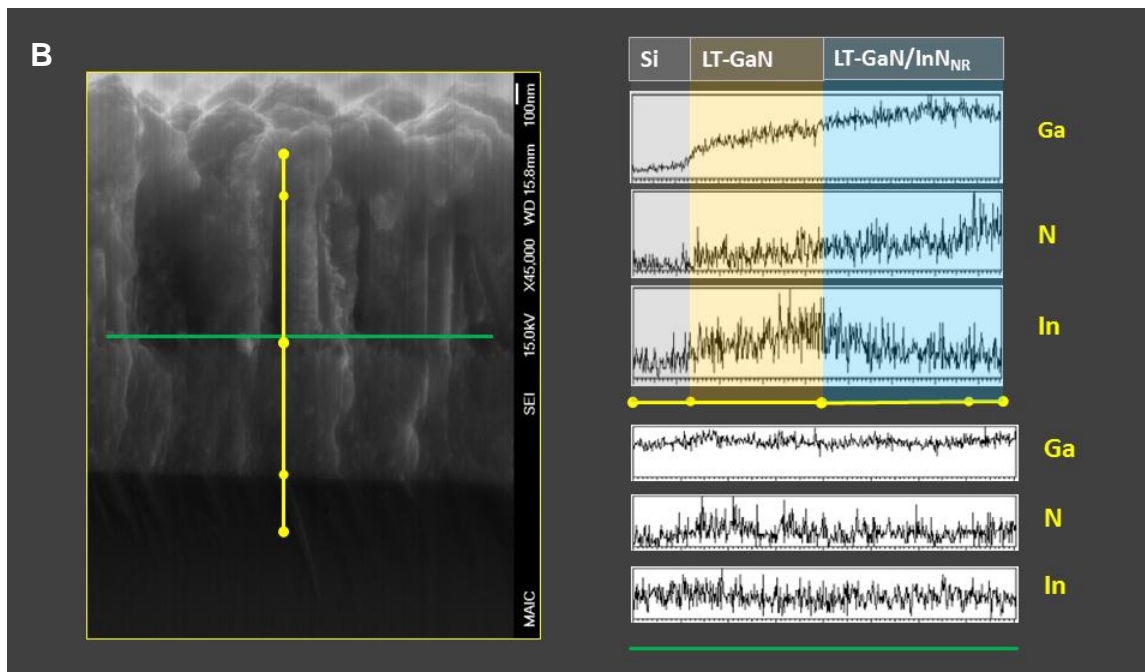
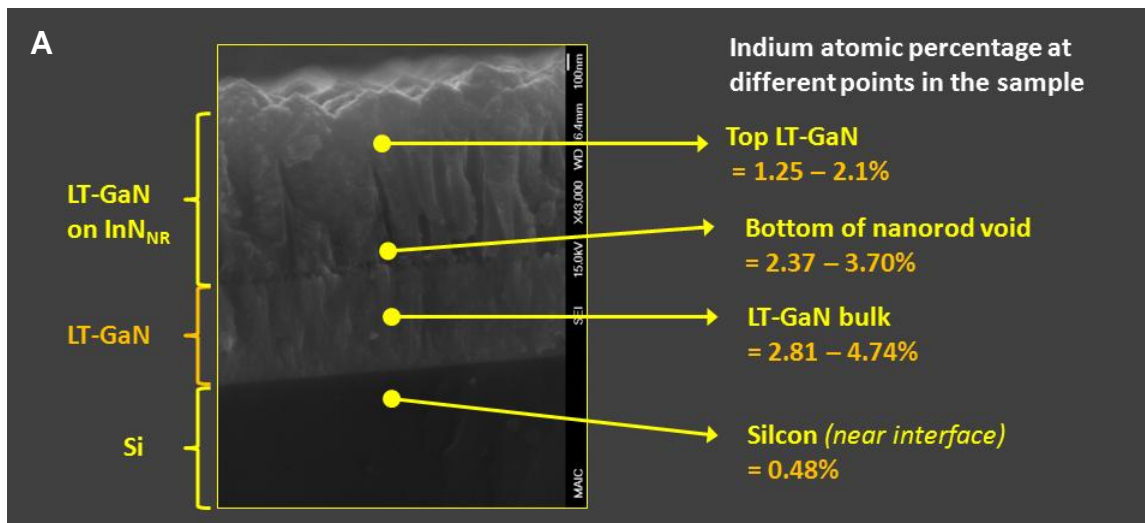


Figure 4-17. SEM EDS of annealed LT-GaN/InN_{NR}/GaN sample. A) Point EDS scans at selected points in different layers, B) EDS scans showing counts of different species along specified horizontal and vertical lines.

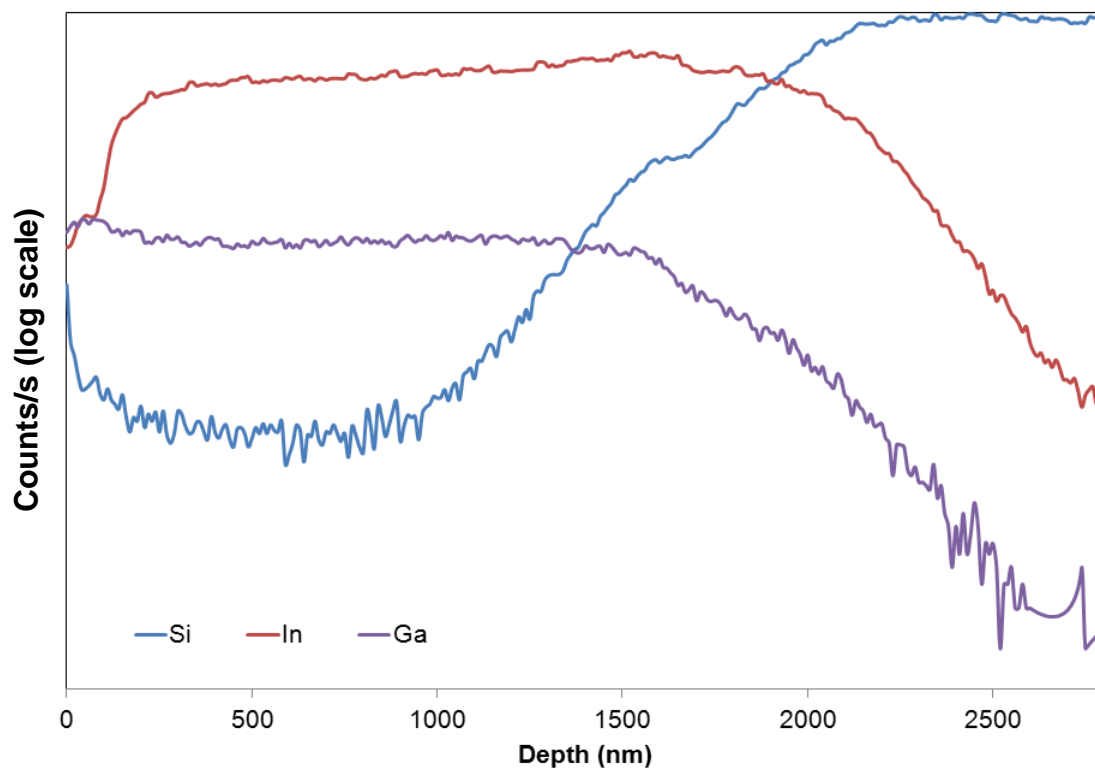


Figure 4-18. SIMS depth profile showing In, Ga and Si for annealed LT-GaN/InN_{NR}/GaN sample.

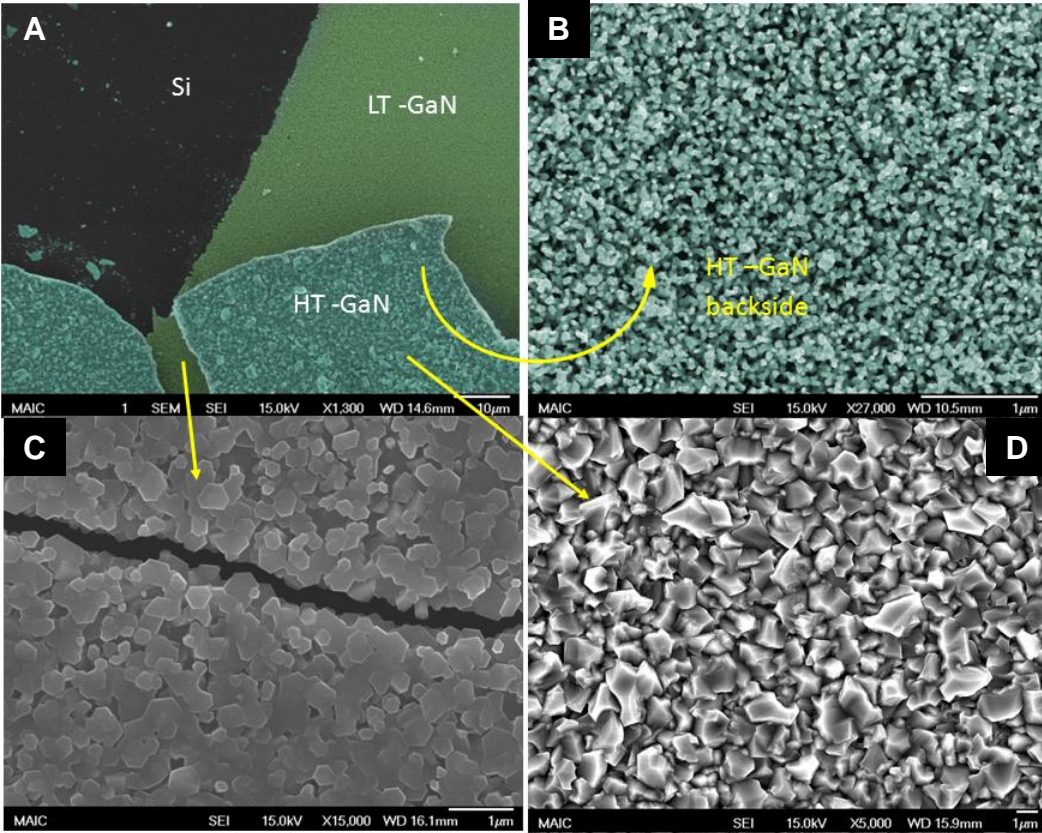


Figure 4-19. Cracked HT-GaN layer on Si ($2\mu\text{m}$) thick). A) Image showing all the layers in growth, B) Back side of thick GaN which has LT-GaN grown on InN template connected to it, C) Image showing crack in lower LT-GaN and morphology with hexagonal c-plane faces, D) High temperature GaN image showing rough surface due to presence of HCl

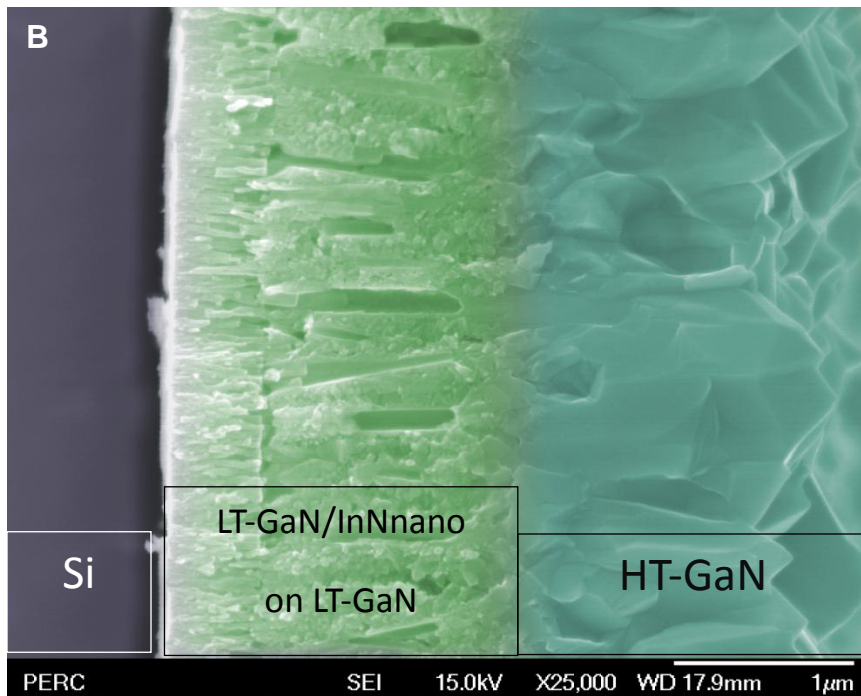
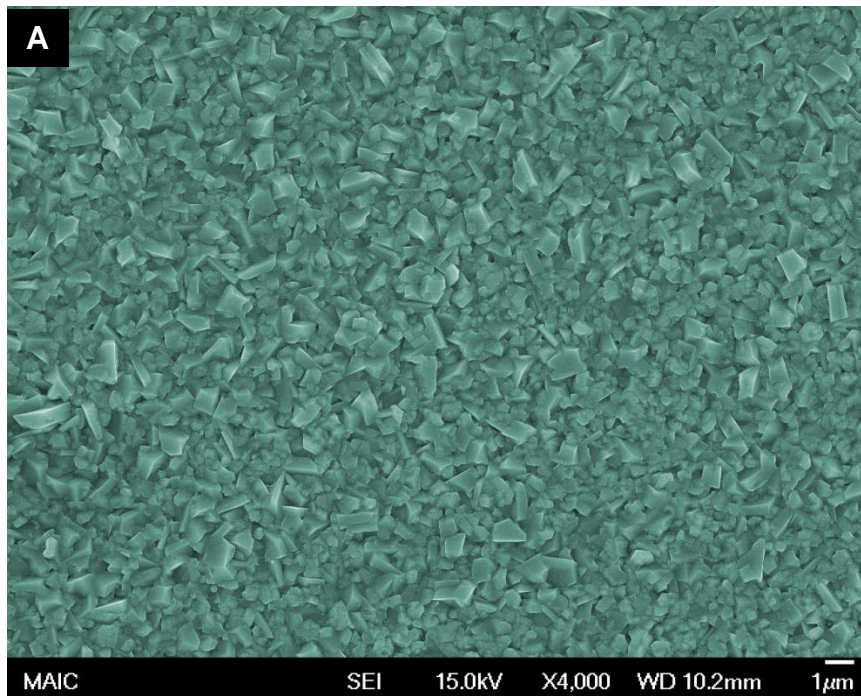


Figure 4-20. GaN (2 μ m thick) film without cracks, A) Image showing surface roughness, B) Cross sectional image showing voids where nanorods were and quality difference in LT- GaN and HT-GaN is clear

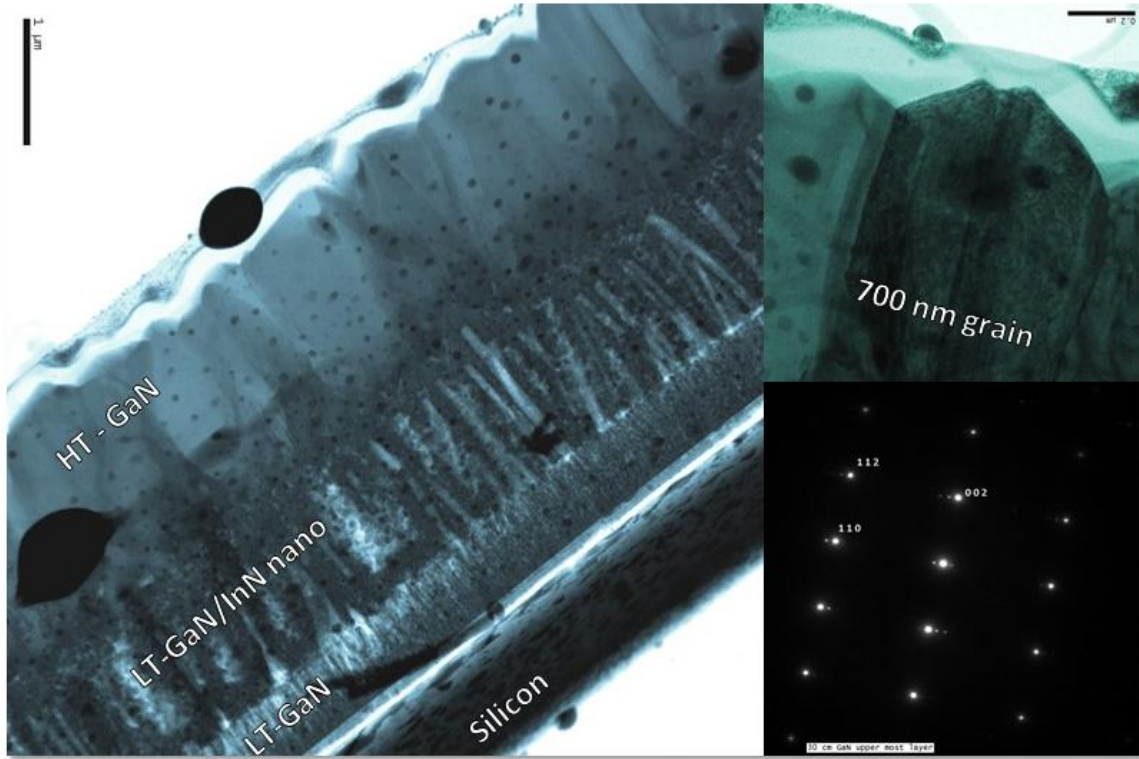


Figure 4-21. TEM cross sectional image of HT-GaN sample, 700 nm grain is single crystal growing in $\langle 000\bar{2} \rangle$ direction

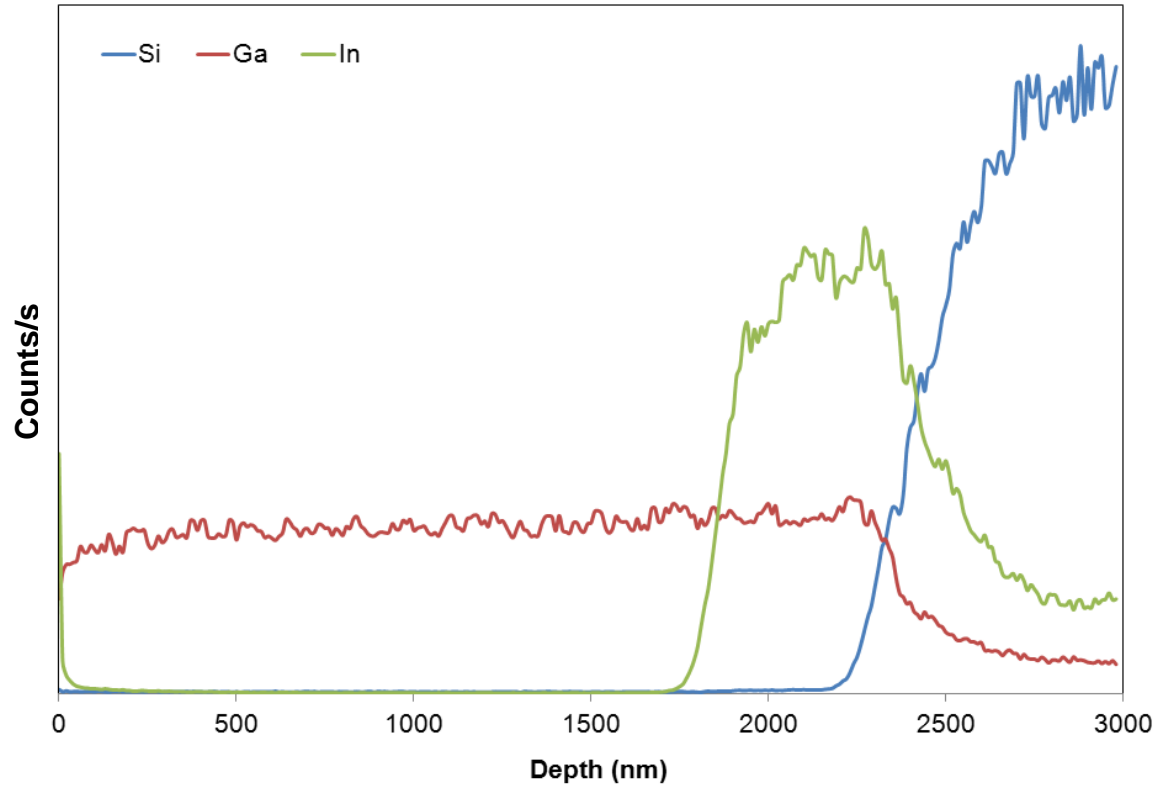


Figure 4-22. SIMS depth profile of 1.5 micron thick GaN showing no diffusion of Indium in upper HT-GaN layer

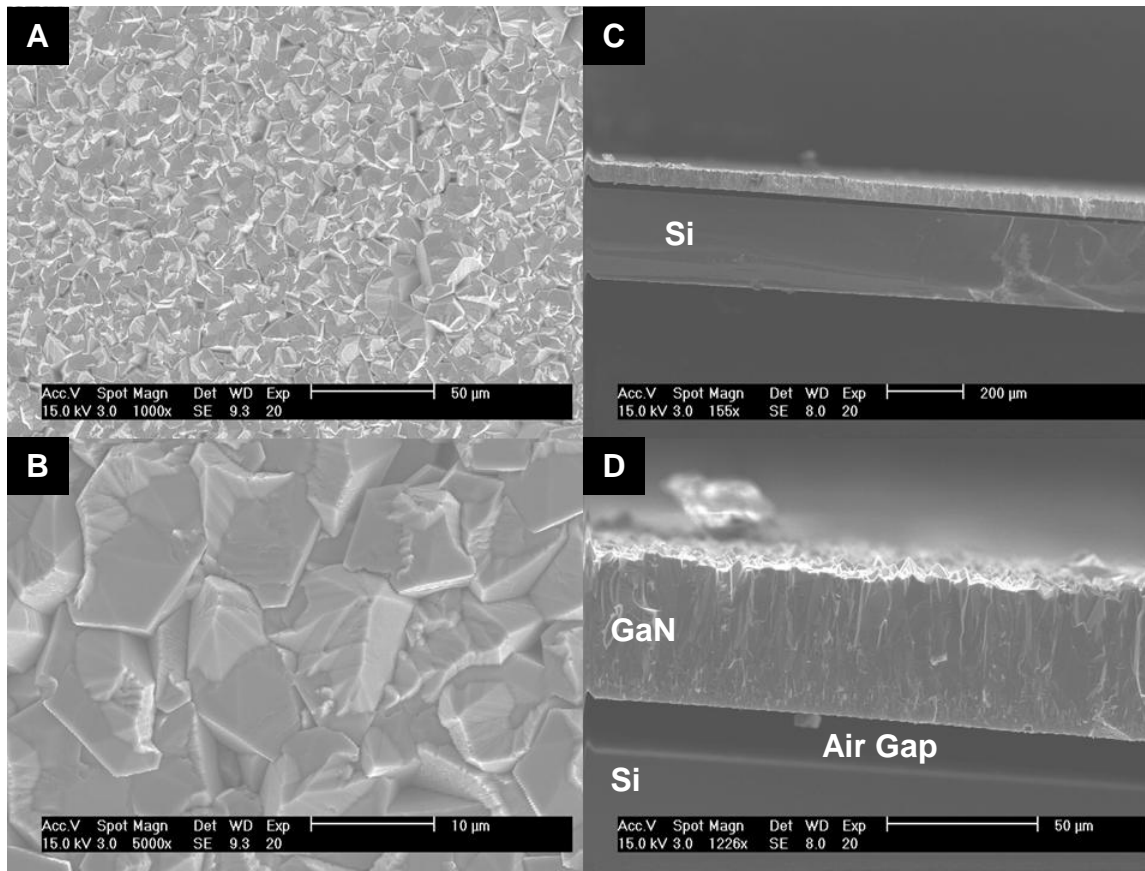


Figure 4-23. SEM image of 50 μm thick GaN grown on InN template. A) Top view at lower magnification showing coverage, B) Top view showing big grains of 10 μm size, C) Cross sectional view showing uniform crack free growth, D) Cross sectional view at higher magnification showing self-separation from Si substrate.

CHAPTER 5 EXPLORATORY STUDY ON GROWTH OF GALLIUM NITRIDE OVER INDIUM TEMPLATED SILICON

Overview

From Chapter 4, it is clear that the main role InN plays in the growth of thick GaN growth is because of flexibility offered by nano template. This Chapter explores growth of GaN using very novel technique i.e. the use of thin Indium metal film as a template to grow GaN on Silicon. Although there is no report on using metal templates to deposit semiconductor material films, there are numerous reports on growing InN and GaN nanostructures on substrates patterned with metals ^{120,123,124,162,163}. Often in MOCVD techniques that are developed for nanowire growths, the growths take place via Vapor-Liquid-Solid (VLS) mechanism. The metal that catalyzes the process often comes from either patterning or reaction can be self-catalyzed by metal from one of the source materials ^{114,122,124,126,132,139,164}. The motive behind this study was to see if Indium metal deposited on Silicon can be used as template for GaN nanostructure or film growth. Metal films deposited on forging substrates when heated above melting point often self-assemble and resulting semiconductor nanowires that grow via VLS mechanism will be self-assembled. Another reason for exploring Indium metal deposited on Silicon as a for GaN growth was that use of Indium metal at interface can form alloy of InN and GaN which may decrease the lattice mismatch between Silicon substrate and GaN similar to InN use. As a result, it can also prove to be a template for thick GaN growth.

Growth Conditions for Different Layers in Growth

Silicon (100) was used as a substrate for this study. Silicon wafer was degreased using RCA cleaning method described in Chapter 2 in detail. The method includes cleaning of Silicon wafer in boiling trichloroethylene, acetone, and methanol baths for 5

minutes each. The Silicon was then cleaned in buffered oxide etch to remove any SiO₂, of which are in use currently. The wafers were then deposited with Indium metal and GaN at different conditions. They are described as follows:

Deposition of Indium Metal Film

Indium metal was deposited using electron beam physical vapor deposition system located at microfab. In this method high electron beam is bombarded on anode made of material to be deposited. High energy of electron beam causes material to evaporate, the vapors then deposited on complete chamber, which includes the substrate. The thickness of deposited material is measured precisely by piezoelectric crystal sensor.

In this case, Indium was used as anode material; e-beam was operated with 15mA emission current. The chamber pressure was maintained at 10⁻⁶ torrs. The thickness of Indium deposited was 100 nm.

Deposition of GaN in MO-HVPE Reactor

GaN films were deposited in same MO-HVPE reactor chamber as described in Chapters 2 and 4. The films were grown in two steps.

Thin GaN films

The Indium metal films were deposited with 10 minutes GaN films first which produced about 1 μm films. All films of this type were grown under MO-CVD mode, i.e. no HCl was used. The HCl gas being good scavenger of metals can react with Indium to form gaseous chlorides. As a result, no HCl was used to deposit first layer of GaN. The GaN depositions were carried out at 973K as lower temperature and 1073K-1123K as higher temperature. The temperatures were chosen to avoid any InN formations. The

ammonia to TMG ratio was maintained at 1000 which was previously optimized value for good GaN deposition. Nitrogen was used as carrier gas with flow rate of 1600 sccm.

Thick GaN films

Once thin MOCVD film was deposited on In/Si template, they were deposited with high temperature GaN films for longer times. Thick films of GaN were all grown at high temperature of 1123K. GaN films were deposited in both MOCVD and HVPE mode. For MOCVD mode, same conditions as described for thin GaN layer were used. MOCVD growths were done for 2hours. For HVPE mode films, HCl was introduced into the reactor. The HCl/TMG and NH_3 /TMG molar ratios were maintained at 2 and 600 which are previously optimized values for good HT-GaN growth.

Films at all the stages of growths were characterized using SEM and XRD.

Results and Discussion

The SEM image shows deposited Indium on Si substrate in Figure 5-1. From cross sectional view (Figure 5-1(A)), it is clear that the film was precisely 100 nm. But as seen in planar view (Figure 5-1(B)), film was not continuous but formed islands for Indium metal. This type of equilibrium shapes of metal are expected in various systems of heteroepitaxy as well as depositions on amorphous materials¹³⁴. The size distribution of Indium islands varied from 100nm to 700nm, with most of the islands showing hexagonal geometry. It is in fact equilibrium shape on Indium droplets with {111} faces parallel to substrate surface^{165,166}. The substrate was approximately 70% covered with big Indium crystals. On heat treatment, Indium was expected melt at 433K and form $\text{In}_x\text{Ga}_{1-x}\text{N}$ at growth temperatures used.

Thin GaN films

The SEM image in Figure 5-2 (A) and (B) shows as deposited GaN film at 973K on Si (100) and In/Si(100) samples respectively. On bare Silicon substrate film formed as expected, but on other sample, GaN deposited in the form of semispherical cabbage like structures. The semispherical shapes are clearly visible in SEM cross sectional image of the same sample (Figure 5-2 (C)). Also, there was a noticeable deposition of thin film of about 150nm thickness between the spheres. The cabbage type nanostructures themselves had average diameter of 700 nm. The EDS measurements showed that sample contained 56.73% Ga, 40.86% N and 2.41% Indium. The XRD spectrum of the sample is shown in Figure 5.3. The spectra showed that GaN film formed is polycrystalline GaN. There was a sharp peak of at 30.82° which is attributed to $(\text{In,Ga})_2\text{O}_3$. The highly textured oxide with $\langle 222 \rangle$ peak was attributed to the fact that Indium metal deposited was preferentially oriented in $\langle 111 \rangle$ direction. Presence of oxides is detectable sometimes when forming gas is not used as carrier gas for GaN growth.

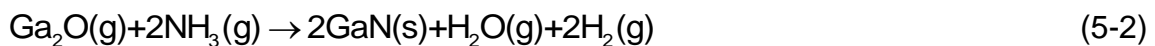
On the other hand, GaN grown at higher temperatures on Indium template showed completely different morphologies. The planar views of thin GaN deposited on In/Si at 1123K and 1073K are shown in Figure 5-4(A) and Figure 5-4(B). As seen from the images, there are apparent bright hexagonal GaN nucleations, embedded in darker matrix. The nucleations were denser but smaller in case of GaN grown at 1073K whereas nucleations in case of GaN grown at 1123K were sparse bigger hexagonal discs. At initial judgment, the discs and matrix were thought to be different materials, but XRD spectra showed only presence of GaN as seen in Figure 5-5. Also, XRD data is

noisy due to very weak signals. It is indicator of sparse deposition. When In/Si samples were annealed at 1123K for 10 min under nitrogen atmosphere, the surface of Si showed morphology similar matrix structure (Figure 5-4(C)). The EDS analysis showed only presence of Gallium, Nitrogen and approximately 5% oxygen. No Indium was found in annealed samples. This meant that due to high temperatures Indium films evaporated. The deposition of Gallium nitride or Gallium oxynitride on Silicon in absence of any metal organic flow was coming from parasitic wall depositions from previous runs in the hot wall reactor. At higher temperatures, when metal organic was flowing; hexagonal diskettes formed might be due to new seeding of GaN. The smaller diskettes at lower temperature and bigger diskettes at higher temperatures can be explained by higher mobility of Gallium at higher temperatures. Due to higher surface mobility at higher temperatures and Ostwald's ripening, bigger diskettes are able to grow and only bigger and sparse diskettes remain. The Indium metal has been shown to work as surfactant at these temperatures¹⁶⁷. Because of surfactant like behavior, reduction in substrate surface energy can in turn increase Gallium surface mobility. Because of sparse GaN diskettes formation, however, a weaker XRD spectrum was also expected as the matrix only contributed to amorphous signal or noise.

Thick GaN films

All the thick GaN films were grown at 1123K. The MO-GaN films were grown under higher TMG/NH₃ molar ratios of 1000 whereas those under HVPE mode were grown at the ratio of 600. The SEM images of MOVPE are shown in Figure 5-6 (A) and (B) in planar view and cross sectional view respectively. The growth of GaN under these conditions was not film like. Contrary to that the GaN showed highly dense wafer structures. These wafers were approximately 8 μm in height and 100 nm in thickness.

From the cross sectional view it is clear that the GaN wafers are originating from underlying 1 μm seed layer. All the seed layers, grown at temperatures ranging from 973K-1123K, showed similar results. The EDS analysis showed presence of Gallium and nitrogen only both in seed layer as well as GaN wafers. . The powder XRD θ - 2θ scans for samples grown on both 973K LT-GaN and 1123K LT-GaN are shown in the Figure 5-7 (A) and (B) respectively. They confirmed absence of any Indium species. All the GaN peaks are present as wafers do not have any preferred growth direction. SEM images did not show any Gallium droplets on any part of sample either. Absences of Indium meant that it is not playing any role in GaN wafer growth. Absence of Gallium metal droplet meant no VLS mechanism was involved in GaN growth. Absence of any stable oxide in the film, confirmed that oxygen might have played role in the formation of these GaN diskettes. Growth of GaN by oxide mediated growth is studied by various researchers¹⁶⁸⁻¹⁷⁴. The overall reactions for oxide mediate GaN growth are given as follows:



In oxygen poor environment Ga_2O may readily form over more complex Ga_2O_3 . Although Ga_2O_3 is a stable oxide, at growth conditions of high temperatures in ammonia rich environment, gaseous Ga_2O can form. This oxide can be further reduced on reaction with ammonia either in presence or absence of carbon catalyst to GaN (Reactions (5-1) and (5-2) respectively). In such Vapor Solid reactions reaction sites play important role, resulting in preferred direction or plane growths forming nanostructures.

The other type of GaN growth was done in HVPE mode for higher time intervals of 4 hours. From former discussion it is clear that there was no or little Indium left in the film when thin GaN was grown at 1123K. Also, deposition consisted of sparse GaN diskettes. As a result, when this template was used for high temperature GaN growth, films cracked as expected. When high temperature GaN was grown on template with 973K GaN grown for 10 minutes, films showed excellent composure. The films did not show any crack similar to films grown on InN nanorod template. Unlike InN nanorod template samples, most of the time Indium film underneath had not completely broken contact between silicon and upper film. As a result, GaN films grown on Indium film did not self-separate. The SEM planar and cross sectional view of 40 μm GaN film grown on In/Si (100) template is shown in the Figure 5-8 (A) and (B) respectively. As seen from SEM images, the film grown on this template, like every other HVPE films, is very rough due to presence of HCl in growths. The powder XRD θ -2 θ scan (Figure 5-9) showed results similar to HVPE thick films grown on InN nanorod sample meaning GaN grown by this method was also polycrystalline.

Summary and Conclusions

This Chapter presented study about growth of GaN using novel Indium on Si template. By changing the mode of growth and temperatures, it was shown that growth of GaN can be changed drastically from nanostructures growth to film growths.

A thick GaN layer, similar to that presented in last Chapter, was achieved, without cracks on 1cm x1cm Si (100). The GaN layer grown here did not self-separate similar to that grown on InN nanorod template. This behavior was attributed to fact that Indium

metal layer although can act as stress relieving layer; it does not prevent GaN to form bonds with Si.

In MO-CVD mode, high temperature growths produced nanostructures. Absence of any evidence for VLS mechanism and presence of oxygen in low temperature grown layers showed Gallium oxide mediated growth as a possible mechanism for GaN wafer growths. Wafers showed no preferred orientations, but showed uniform thickness of 100 nm. It was thought that they are grown from diskettes of GaN that form at high temperature growths on In/Si templates. The diskettes formations can be a result of high mobility of GaN at higher temperatures. In heightened motilities of Gallium molecules on substrate can be attributed to effect of Indium as a surfactant that plays part in reducing surface energies.

To conclude, use of In/Si as a template for thin and thick GaN is shown here. Although, thick GaN films were polycrystalline in nature, the preliminary results are promising and need further investigation to improve quality. Growth of GaN wafers on Si(100) has never been reported. Although wafers have shown uniformity of thickness, uniformity of direction is highly desired. If all wafers grow in one direction, the method can be improved on to harvest even bigger sizes of wafers. Hence, further studies will be needed to improve orientation of the GaN wafer structures.

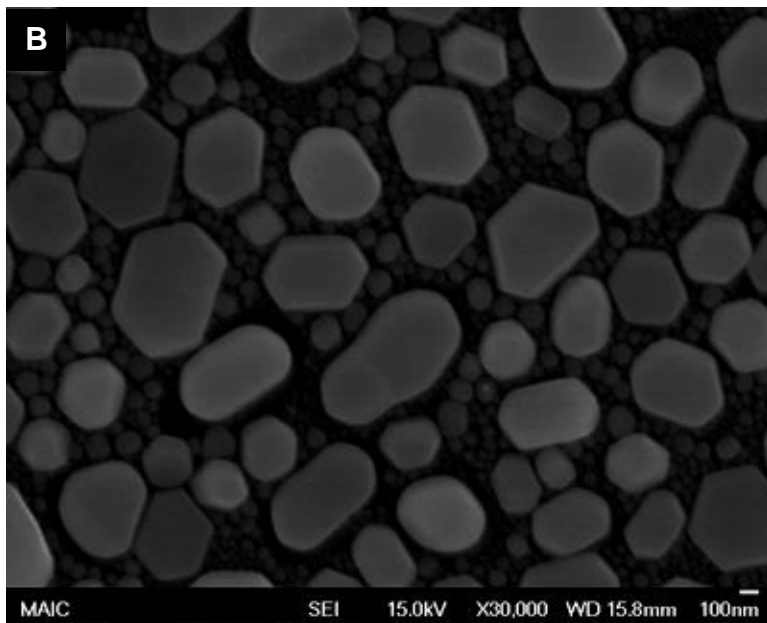
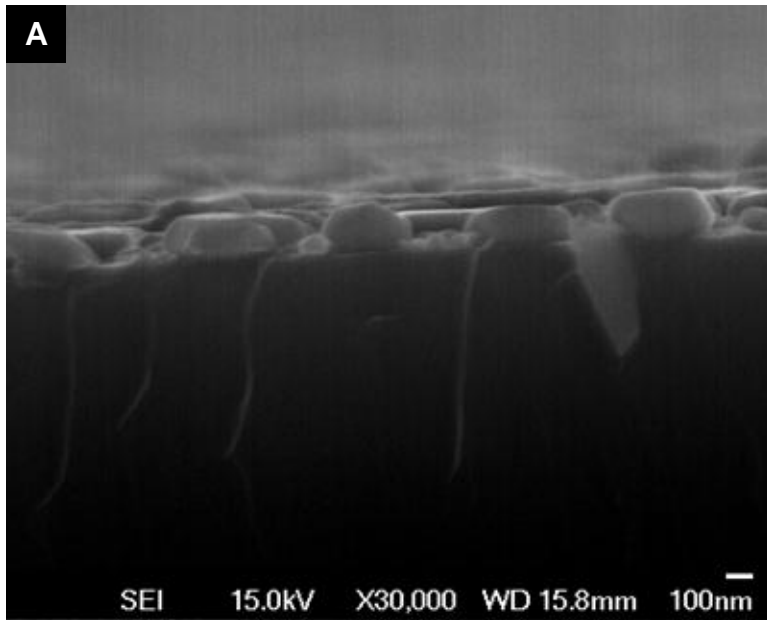


Figure 5-1. SEM images of Indium on Silicon (100). A) Cross sectional view showing 100nm islands of Indium, B) Top view showing self-assembled Indium islands structure

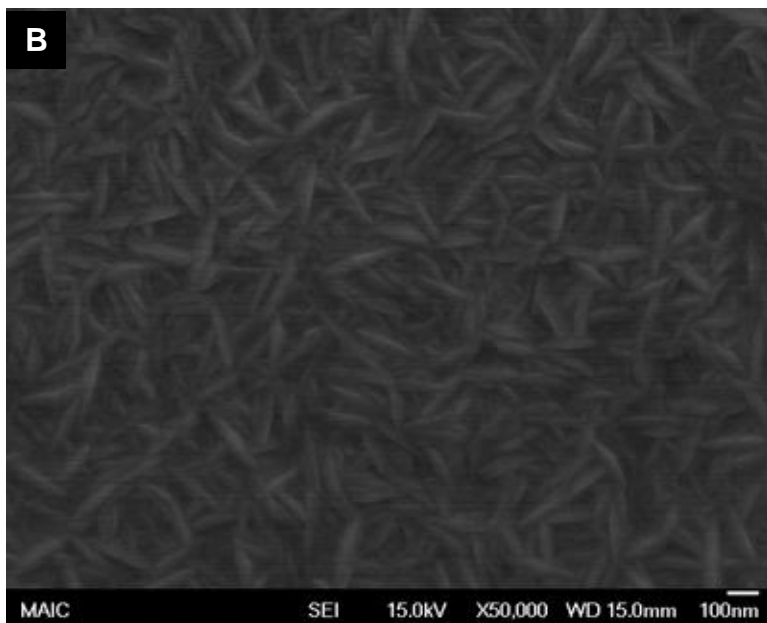
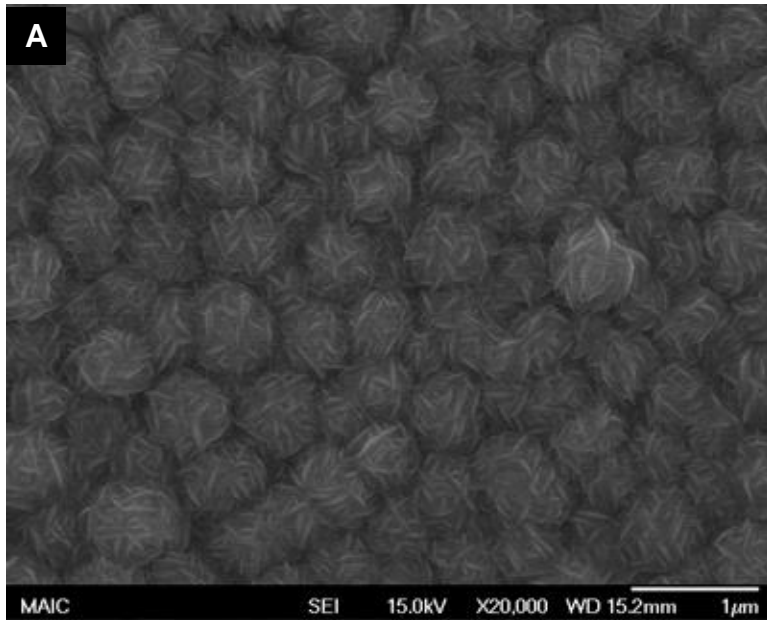


Figure 5-2. SEM images of GaN grown at $T=873\text{K}$ for 10 min. A) Growth on In/Si(100) as template, B) Growth on Si(100) as template, C) Cross sectional view of growth on In/Si(100) template

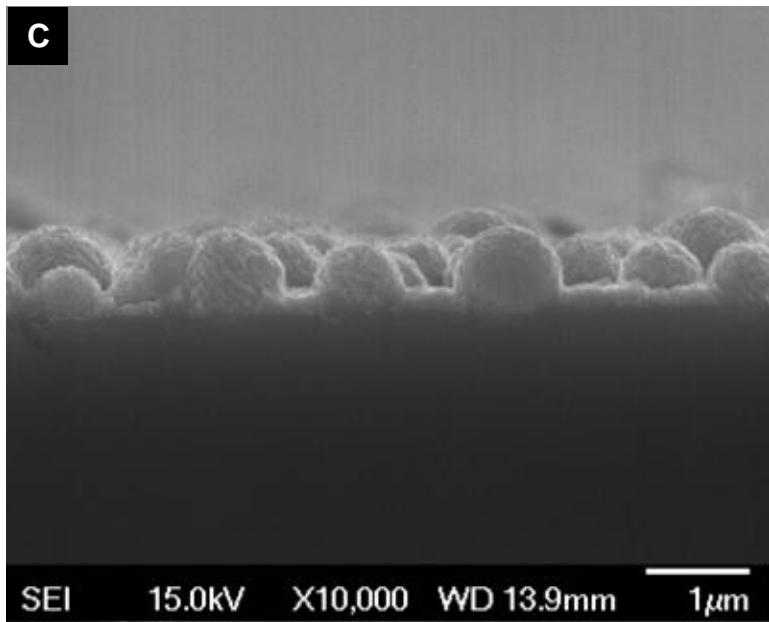


Figure 5-2. Continued

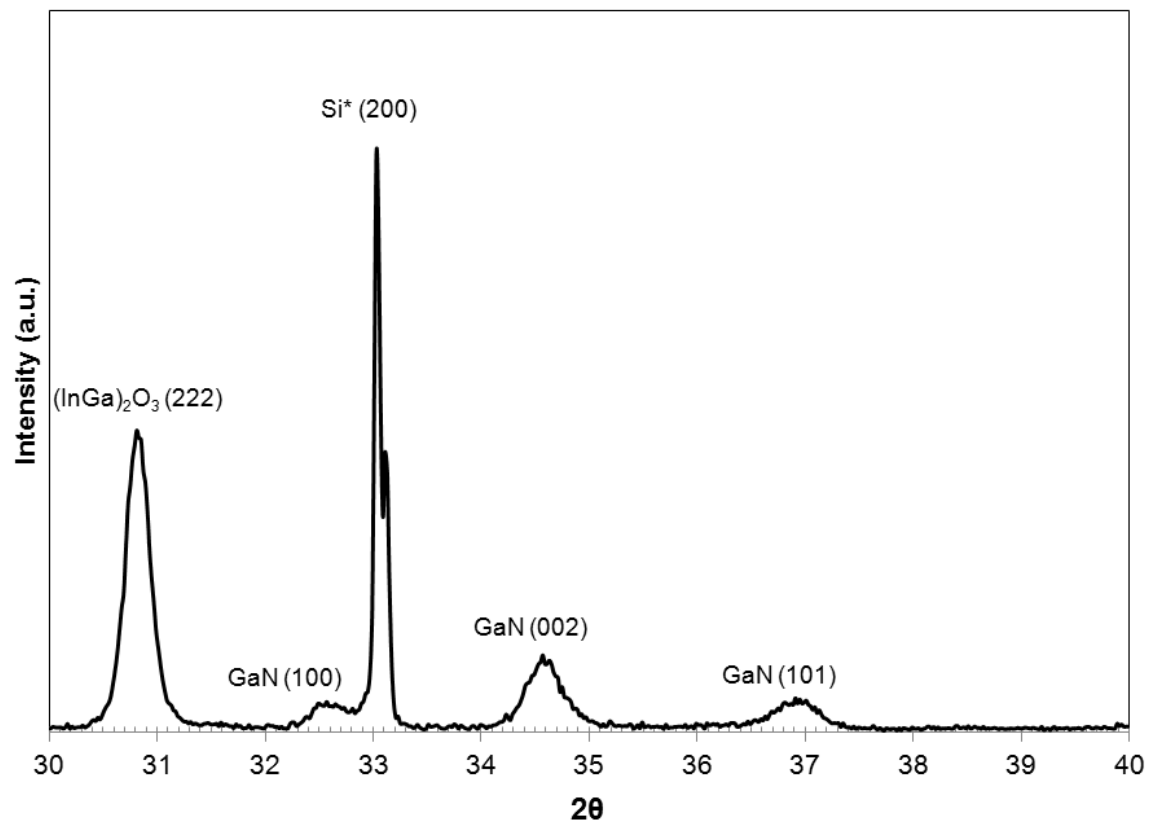


Figure 5-3. XRD θ - 2θ scan of GaN grown on In/Si template for 10 min at 973K

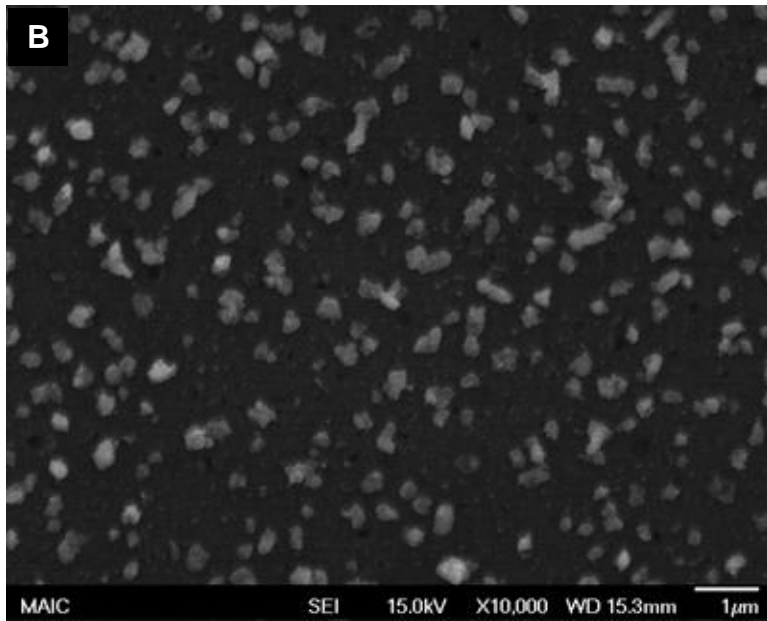
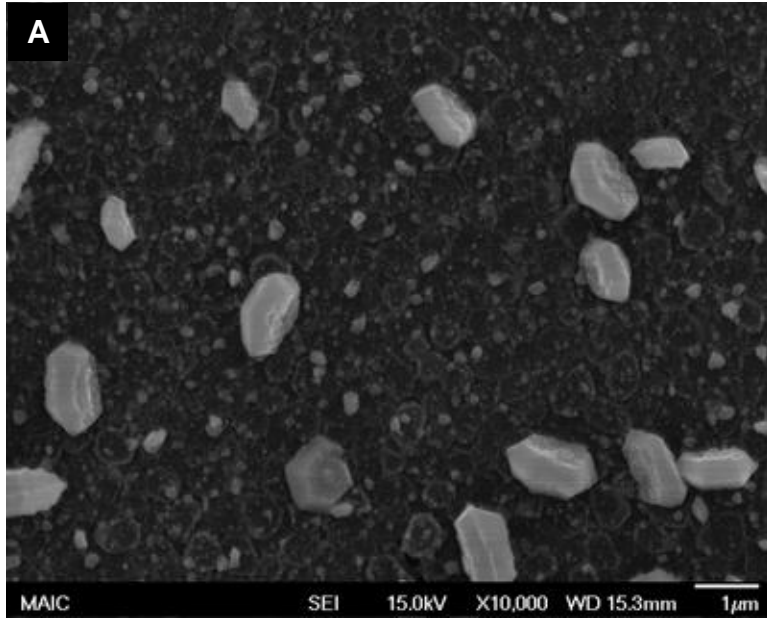


Figure 5-4. SEM images of growth on In/Si at higher temperatures for 10 min. A) Growth at $T=1123\text{K}$ showing bigger and sparse diskettes in matrix, B) Growth at $T=1073\text{K}$ showing smaller but dense diskettes in matrix, C) Growth under only nitrogen flow at $T=1123\text{K}$

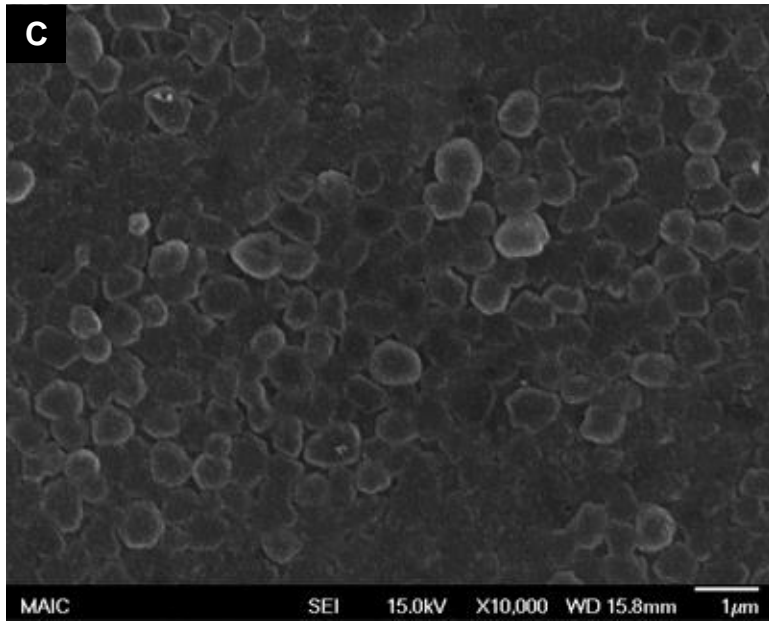


Figure 5-4. Continued...

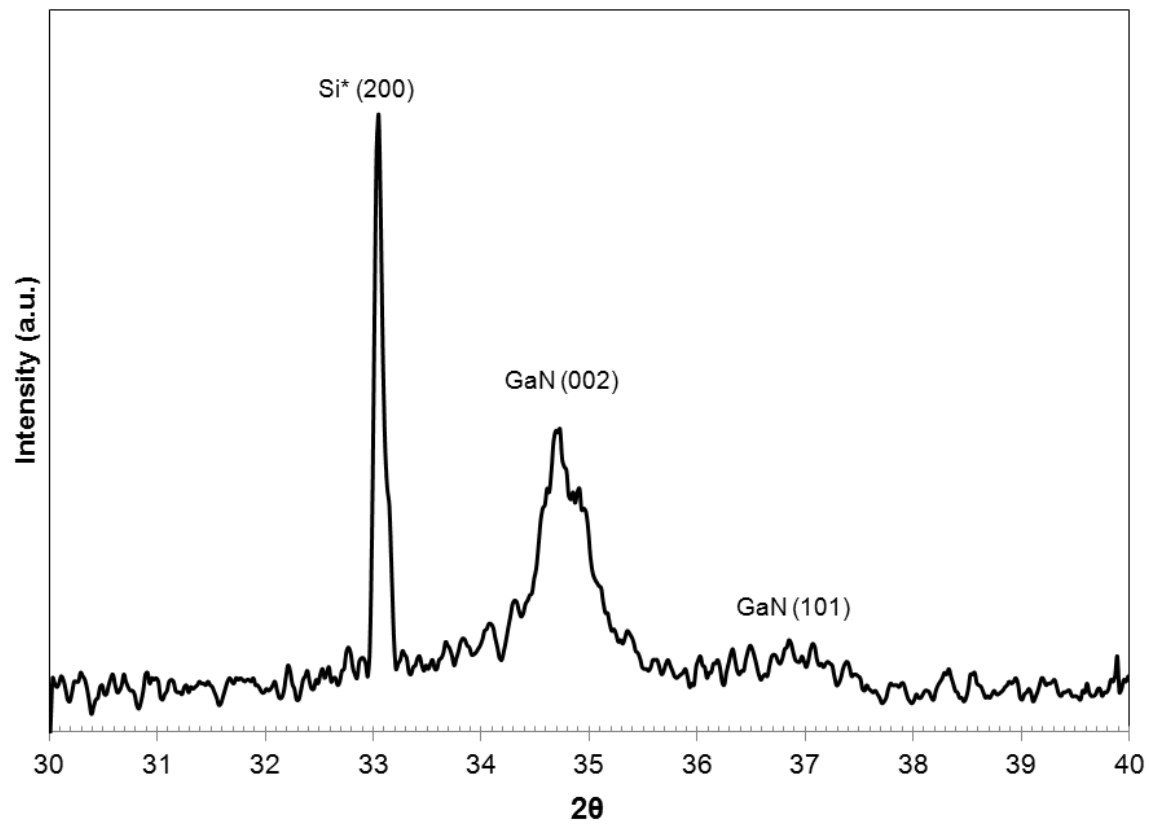


Figure 5-5. XRD θ - 2θ scan of GaN grown on In/Si template for 10 min at 1123K.

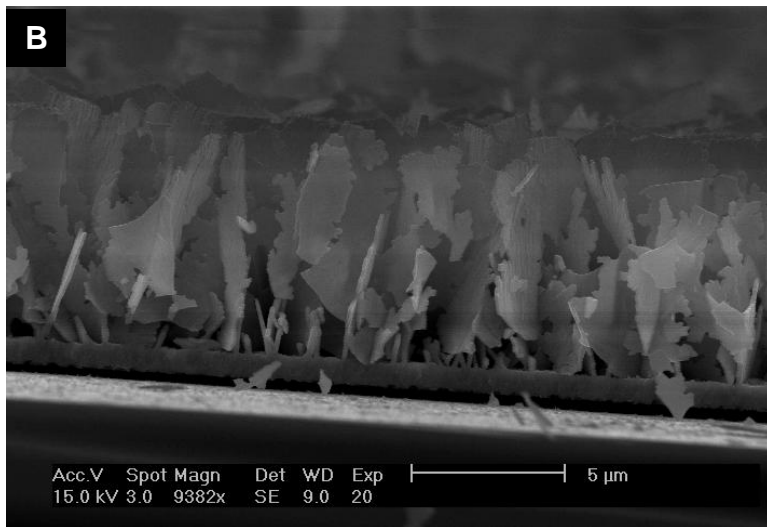
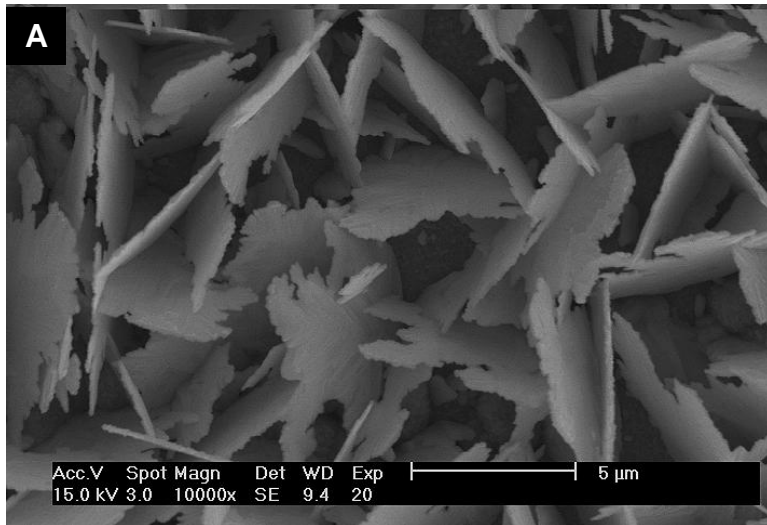


Figure 5-6. SEM images of thick MOCVD GaN growth on In/Si at 1123K for 120 min.
A) Top view showing rough GaN wafers B) Cross sectional view showing height about 8 μ m

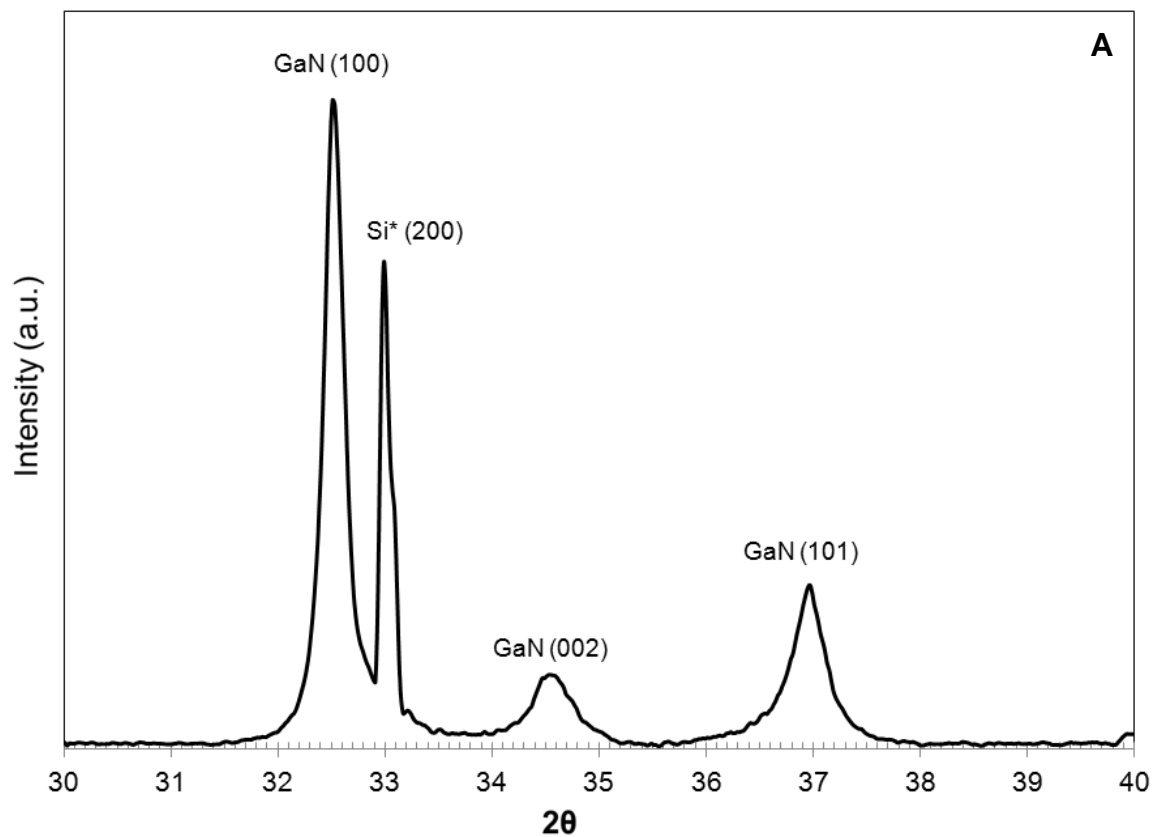


Figure 5-7. XRD θ - 2θ scan of GaN wafers grown at 1123K in MOCVD mode. A) Grown on GaN/In/Si(100) template grown at 973K, B) Grown on GaN/In/Si(100) template grown at 1123K

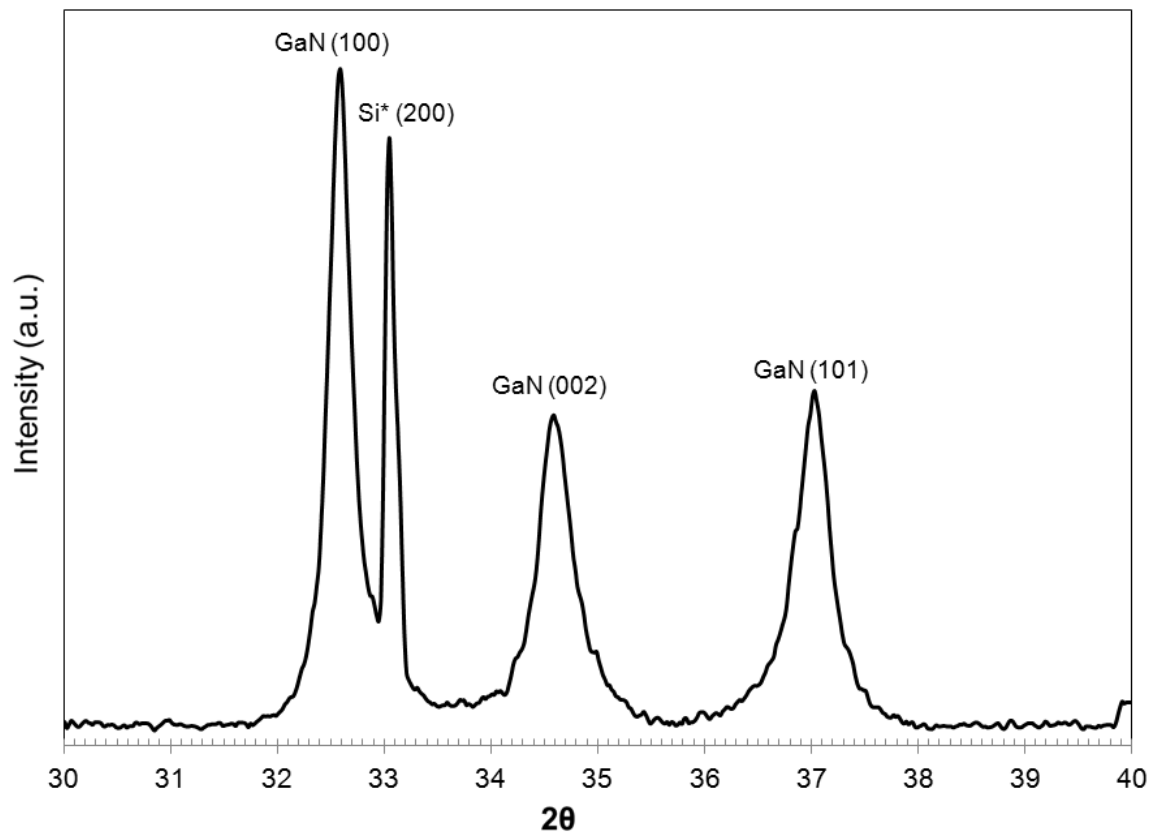


Figure 5-7. Continued

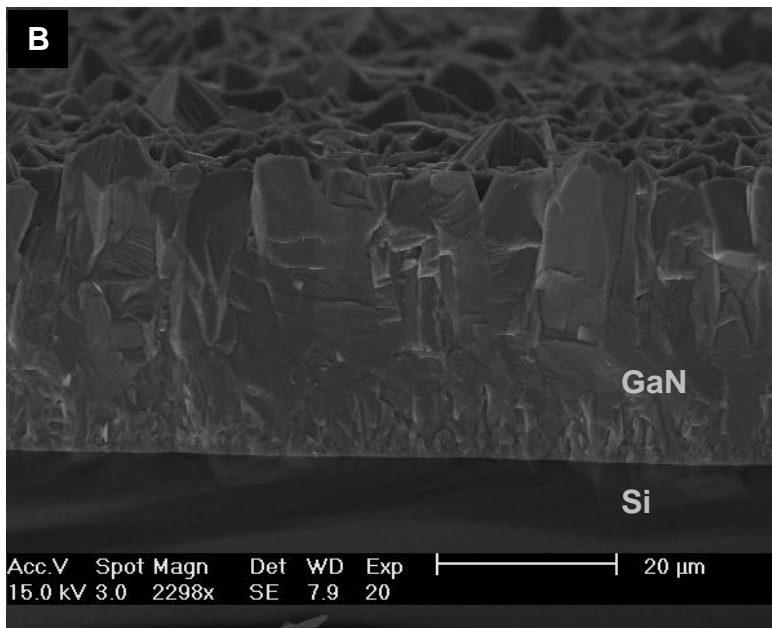
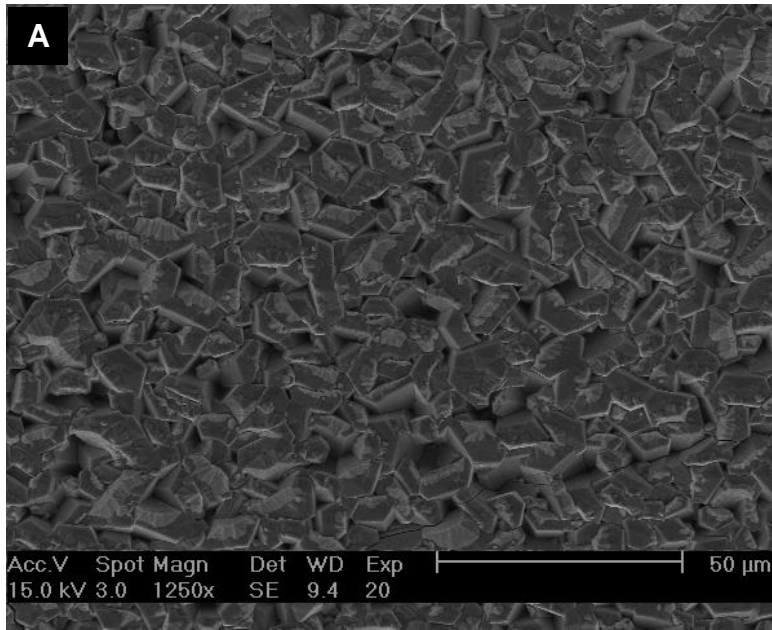


Figure 5-8. SEM images of 40 μ m thick HVPE GaN growth on LT-GaN/In/Si at 1123K for 240 min. A) Top view showing rough GaN surface B) Cross sectional view showing height about 40 μ m free growth without self-separation

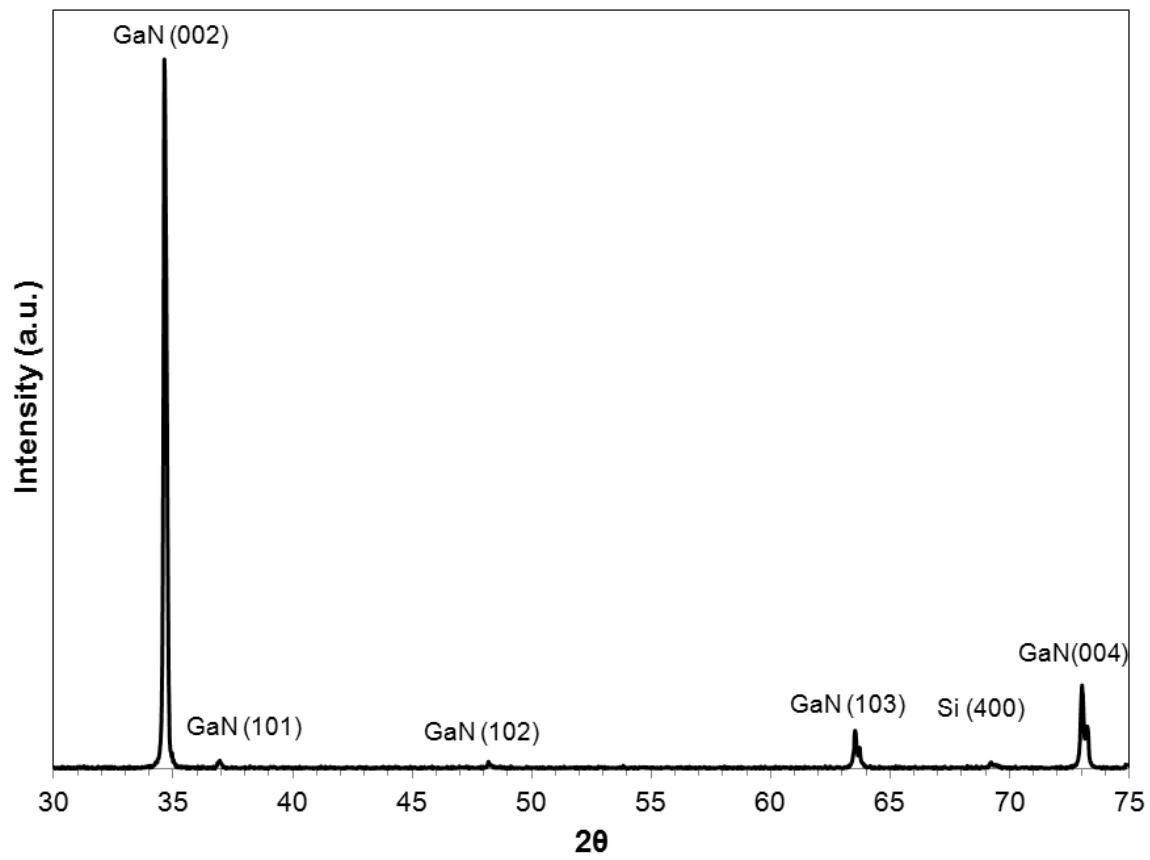


Figure 5-9. XRD θ - 2θ scan of thick GaN grown on LT-GaN/In/Si template at 1123K.

CHAPTER 6 CONCLUSIONS AND RECOMMENDATIONS OF FUTURE WORK

Conclusions

This study had final goal to achieve crack free thick and thin GaN on substrates such as Silicon which has very large lattice mismatch with GaN. The goal was successfully achieved, though various challenges still remain. The key conclusions from this study are as follows.

Chapter 2 dealt with question of how the growth direction of InN nanorods is affected by different substrate preparations for Silicon. Chapter showed that major improvement in directionality is possible by changing surface properties structurally. Nitridation formed Silicon oxynitride layer, which changed the surface to either hexagonal geometry or amorphous. In both cases, directionality of InN nanorods in c-axis direction improved. The c-axis growth happens to be the preferred growth direction of nitride crystals. If formation of oxynitride layer formed a crystalline layer, the oxynitride being geometrically more similar to basal plane of InN, it improved the growth in vertical direction. If oxynitride created the amorphous layer, then it disconnected all the epitaxial requirements for growth, and that resulted in improvement in natural growth direction. This direction happened to be vertical direction in case of InN nanorods. More than nitridation, presence of good quality c-directional nucleation layer of GaN improved growth of InN in vertical direction. With optimum nucleation layer, all the nanorods with high crystallinity were grown in vertical direction. And results from pole figures showed that InN nanorods orientation was only dependent on underlying nucleation layer.

The InN nanorods grown were high quality crystals, with very few defects and dislocations concentrated towards bottom. This was thought to be because of possible

lateral relaxation in nanostructures as they grow. This relaxation was modeled and model qualitatively showed relaxation into the bulk material was possible. Model also showed that coherency can be greatly improved if lower layer also shares the strain and assumed to be flexible. The results predicted were observed were confirmed with many similar experimental observations.

InN nanorods grown on Silicon substrate were used as possible template for thick GaN growth. The thick growth without cracks was shown to be absolutely feasible. But, large lattice mismatches and lower temperature growths of GaN made it impossible to grow epitaxial GaN on nanorods. This resulted in secondary nucleations and GaN ended up to be highly textured in $\langle 000\bar{2} \rangle$ direction but polycrystalline. It can be concluded here, that only if GaN capping layer quality can be improved, a very big improvement in quality of thick high temperature GaN is achievable. Use of InN definitely helped relaxing strain, as after cooling films did not crack but completely self-separated. The importance of role of InN nanorod layer was also confirmed by the fact that, films cracked if InN nanorods decomposed before formation of capping layer. Decomposed InN when completely covered by GaN, produced porous matrix on GaN which helped relaxation of the layer. Also, Indium was found to be graded throughout the lower part of structure, which should have influenced relaxation. So use of InN nanostructured template was successful for crack free growth of GaN was possible.

Similar to InN, Indium metal was deposited on silicon and used as template for high temperature GaN growth. It was shown that Indium layer served similar purpose as InN layer. As a result, thick GaN growth was also achieved on In/Si substrates. There was no self-separation, but GaN showed similar properties and polycrystalline nature. In

absence of strong reducing agents such as hydrogen and HCl in the reactor, GaN growth on In/Si template produced GaN wafer growth. The wafer growth may have been influenced by formation of diskettes of GaN. The diskette formation was attributed to increased mobility of Gallium due to surfactant like effect of trace Indium atoms on substrate surface. The wafers growth was possible due to small amount of oxide present in the reactor and reactions proceeding with oxide mediated vapor solid growth.

Recommendations for Future Work

Improvements in InN nanorod orientations

Although InN nanorod size and density can be controlled pretty well in MO-HVPE system, major improvement is needed in the rotational relationship with substrate. If all the nanorods could be grown in exact same rotation with Silicon substrate, it would influence quality of material grown on it. This uniformity will also allow better devices of these nanostructures. This can be done two ways. First approach would be to use patterned substrate. If silicon is patterned with Indium catalyst dots and other area is covered with oxide or nitride layer of silicon, resulting nanorods growth will be symmetric. Similar approach would be to use porous alumina as template. Improvement in orientation in InN nanorods will be better for its application for devices as well as for template usage. Second way it could be achieved by using template that retains epitaxial relationship with the substrate. It is possible by layer by layer growth process such as ALD. If the ALD films of GaN can be used as substrates for InN nanorod growth, InN nanorods will have epitaxial relationship with substrate Silicon as nucleation layer will be minimal.

Growth of GaN and $\text{In}_x\text{Ga}_{1-x}\text{N}$ nanostructures in MO-HVPE

With advance of semiconductor industry, there is major shift in how semiconductor materials are going to be grown. With arrival of 3D transistors, growth of nanostructures of materials such as GaN, $\text{In}_x\text{Ga}_{1-x}\text{N}$ is highly desirable. Nanostructures tend to be highly crystalline and as a result devices can perform better. GaN nanostructures growth however is challenging due to nature of GaN growth. Like many other semiconductors, GaN tends to grow polycrystalline, as it is effective way to relieve strain in material growth. But, use of patterned substrates has shown to be effective in achieving GaN growth.

In MO-HVPE, there is added advantage of control over HCl to metal ratio. Due to this nanorod of InN can be grown in HVPE without any catalyst or patterning. But growth of nanostructures of GaN has not been studied in great detail. The major problem has been guessing the growth conditions for GaN nanostructure growth. The great starting point would be to grow Gallium poor $\text{In}_x\text{Ga}_{1-x}\text{N}$ nanostructures and then go towards GaN growth. Second hurdle has been the substrate. With understanding of nature of GaN in this study it is clear that first growth of nucleation layer of GaN would be essential step towards getting GaN nanostructures. The path of oxide mediated growth of GaN is also worth exploring if controlled and oriented nucleation of the GaN diskettes is achieved. If GaN nanostructures can be grown in MO-HVPE with uniformity in orientation and size, it would be important step in terms of achieving GaN nano devices such as nano lasers, high brightness LEDs and nanostructured solar cells.

Furthermore, well oriented GaN nanostructures will prove to be much better substrate to achieve thick single crystal growth of GaN on any substrate.

LIST OF REFERENCES

- 1 Y. J. Dong, B. Z. Tian, T. J. Kempa, and C. M. Lieber, *Nano Letters* **9**, 2183 (2009).
- 2 R. H. Horng, S. T. Lin, Y. L. Tsai, M. T. Chu, W. Y. Liao, M. H. Wu, R. M. Lin, and Y. C. Lu, *IEEE Electron Device Letters* **30**, 724 (2009).
- 3 G. H. Jessen, R. C. Fitch, J. K. Gillespie, G. D. Via, N. A. Moser, M. J. Yannuzzi, A. Crespo, J. S. Sewell, R. W. Dettmer, T. J. Jenkins, R. F. Davis, J. Yang, M. A. Khan, and S. C. Binari, *IEEE Electron Device Letters* **24**, 677 (2003).
- 4 M. A. Khan, A. Bhattarai, J. N. Kuznia, and D. T. Olson, *Applied Physics Letters* **63**, 1214 (1993).
- 5 M. A. Khan, Q. Chen, J. W. Yang, C. J. Sun, and M. S. Shur, *Silicon Carbide and Related Materials 1995* **142**, 985 (1996).
- 6 M. A. Khan and M. S. Shur, *Materials Science and Engineering B-Solid State Materials for Advanced Technology* **46**, 69 (1997).
- 7 M. A. Khan, X. Hu, G. Sumin, A. Lunev, J. Yang, R. Gaska, and M. S. Shur, *IEEE Electron Device Letters* **21**, 63 (2000).
- 8 V. Kumar, A. Kuliev, R. Schwindt, M. Muir, G. Simin, J. Yang, M. A. Khan, and I. Adesida, *Solid-State Electronics* **47**, 1577 (2003).
- 9 B. W. Liou, *Japanese Journal of Applied Physics* **48** (2009).
- 10 B. W. Liou, *IEEE Photonics Technology Letters* **22**, 215 (2010).
- 11 J. K. Sheu, C. C. Yang, S. J. Tu, K. H. Chang, M. L. Lee, W. C. Lai, and L. C. Peng, *IEEE Electron Device Letters* **30**, 225 (2009).
- 12 G. Simin, A. Koudymov, H. Fatima, J. P. Zhang, J. W. Yang, M. A. Khan, X. Hu, A. Tarakji, R. Gaska, and M. S. Shur, *IEEE Electron Device Letters* **23**, 458 (2002).
- 13 S. Westwater, in *Compound Semiconductors; Vol. 16, August/September* ed. (**Angel Business Communications Ltd**, Watford, Herts WD17 1JA, UK, 2010), p. 99.
- 14 J. R. Brodrick, B. Consulting., N. C. Inc., R. A. Inc., S. Consulting., and S. S. L. S. Inc., May 2011 ed., edited by U. S. D. o. Energy (Lighting Research and Development Building Technologies Program,

Office of Energy Efficiency and Renewable Energy,
U.S. Department of Energy, Washington, D.C, 2011).

- 15 S. Nakamura, N. Senoh, N. Iwasa, and S. I. Nagahama, *Japanese Journal of Applied Physics Part 2-Letters* **34**, L797 (1995).
- 16 S. Nakamura, M. Senoh, N. Iwasa, S. Nagahama, T. Yamada, and T. Mukai, *Japanese Journal of Applied Physics Part 2-Letters* **34**, L1332 (1995).
- 17 S. Nakamura, *Diamond and Related Materials* **5**, 496 (1996).
- 18 J. W. Yang, Q. Chen, C. J. Sun, B. Lim, M. Z. Anwar, M. A. Khan, and H. Temkin, *Applied Physics Letters* **69**, 369 (1996).
- 19 A. Avramescu, T. Lerner, J. Muller, C. Eichler, G. Bruederl, M. Sabathil, S. Lutgen, and U. Strauss, *Applied Physics Express* **3** (2010).
- 20 S. Lutgen, A. Avramescu, T. Lerner, D. Queren, J. Muller, G. Bruederl, and U. Strauss, *Physica Status Solidi a-Applications and Materials Science* **207**, 1318 (2010).
- 21 S. Nakamura, M. Senoh, S. Nagahama, N. Iwasa, T. Yamada, T. Matsushita, H. Kiyoku, and Y. Sugimoto, *Japanese Journal of Applied Physics Part 2-Letters* **35**, L74 (1996).
- 22 S. Nakamura, *Mrs Bulletin* **23**, 37 (1998).
- 23 G. F. Brown, J. W. Ager, W. Walukiewicz, and J. Wu, *Solar Energy Materials and Solar Cells* **94**, 478 (2010).
- 24 H. Hamzaoui, A. S. Bouazzi, and B. Rezig, *Solar Energy Materials and Solar Cells* **87**, 595 (2005).
- 25 M. Anani, C. Mathieu, M. Khadraoui, Z. Chama, S. Lebid, and Y. Amar, *Microelectronics Journal* **40**, 427 (2009).
- 26 X. Chen, K. D. Matthews, D. Hao, W. J. Schaff, and L. F. Eastman, *Physica Status Solidi a-Applications and Materials Science* **205**, 1103 (2008).
- 27 C. McCormick, *Mrs Bulletin* **34**, 151 (2009).
- 28 L. A. Reichertz, I. Gherasoiu, K. M. Yu, V. M. Kao, W. Walukiewicz, and J. W. Ager, *Applied Physics Express* **2** (2009).
- 29 M. Song, Z. Wu, Y. Fang, R. Xiang, Y. Sun, H. Wang, C. Yu, H. Xiong, J. Dai, and C. Chen, *Journal of Optoelectronics and Advanced Materials* **12**, 1452 (2010).
- 30 A. Tarakji, X. Hu, A. Koudymov, G. Simin, J. Yang, M. A. Khan, M. S. Shur, and R. Gaska, *Solid-State Electronics* **46**, 1211 (2002).

- 31 I. P. Smorchkova, M. Wojtowicz, R. Sandhu, R. Tsai, M. Barsky, C. Namba, P. S. Liu, R. Dia, M. Truong, D. Ko, J. Wang, H. Wang, and A. Khan, *Ieee Transactions on Microwave Theory and Techniques* **51**, 665 (2003).
- 32 R. Dwilinski, J. M. Baranowski, M. Kaminska, R. Doradzinski, J. Garczynski, and L. Sierzputowski, *Acta Physica Polonica A* **90**, 763 (1996).
- 33 R. Dwilinski, R. Doradzinski, J. Garczynski, L. Sierzputowski, R. Kucharski, M. Zajac, M. Rudzinski, R. Kudrawiec, J. Serafinczuk, and W. Strupinski, *Journal of Crystal Growth* **312**, 2499 (2010).
- 34 T. Hashimoto, E. Letts, M. Ikari, and Y. Nojima, *Journal of Crystal Growth* **312**, 2503 (2010).
- 35 D. Ehrentraut and T. Fukuda, *Journal of Crystal Growth* **312**, 2514 (2010).
- 36 T. Sasaki and T. Matsuoka, *Journal of Applied Physics* **64**, 4531 (1988).
- 37 T. Sasaki, T. Matsuoka, and A. Katsui, *Applied Surface Science* **41-2**, 504 (1989).
- 38 S. A. Kukushkin, A. V. Osipov, V. N. Bessolov, B. K. Medvedev, V. K. Nevolin, and K. A. Tcarik, *Reviews on Advanced Materials Science* **17**, 1 (2008).
- 39 M. E. Lin, B. Sverdlov, G. L. Zhou, and H. Morkoc, *Applied Physics Letters* **62**, 3479 (1993).
- 40 R. F. Davis, S. Tanaka, L. B. Rowland, R. S. Kern, Z. Sitar, S. K. Ailey, and C. Wang, *Journal of Crystal Growth* **164**, 132 (1996).
- 41 S. Tanaka, S. Iwai, and Y. Aoyagi, *Journal of Crystal Growth* **170**, 329 (1997).
- 42 P. Waltereit, O. Brandt, A. Trampert, M. Ramsteiner, M. Reiche, M. Qi, and K. H. Ploog, *Applied Physics Letters* **74**, 3660 (1999).
- 43 S. Yoshida, S. Misawa, and S. Gonda, *Applied Physics Letters* **42**, 427 (1983).
- 44 M. A. Khan, J. N. Kuznia, D. T. Olson, and R. Kaplan, *Journal of Applied Physics* **73**, 3108 (1993).
- 45 I. Akasaki, H. Amano, Y. Koide, K. Hiramatsu, and N. Sawaki, *Journal of Crystal Growth* **98**, 209 (1989).
- 46 H. Amano, I. Akasaki, K. Hiramatsu, N. Koide, and N. Sawaki, *Thin Solid Films* **163**, 415 (1988).
- 47 H. Amano, K. Hiramatsu, and I. Akasaki, *Japanese Journal of Applied Physics Part 2-Letters* **27**, L1384 (1988).

- 48 T. Kachi, T. Tomita, K. Itoh, and H. Tadano, *Applied Physics Letters* **72**, 704 (1998).
- 49 K. H. Lee, S. H. Park, J. H. Kim, N. H. Kim, M. H. Kim, H. Na, and E. Yoon, *Thin Solid Films* **518**, 6365 (2010).
- 50 E. Calleja, M. A. Sanchez-Garcia, F. J. Sanchez, F. Calle, F. B. Naranjo, E. Munoz, S. I. Molina, A. M. Sanchez, F. J. Pacheco, and R. Garcia, *Journal of Crystal Growth* **201**, 296 (1999).
- 51 A. Ohtani, K. S. Stevens, and R. Beresford, *Applied Physics Letters* **65**, 61 (1994).
- 52 K. S. Stevens, A. Ohtani, M. Kinniburgh, and R. Beresford, *Applied Physics Letters* **65**, 321 (1994).
- 53 D. J. As, T. Frey, D. Schikora, K. Lischka, V. Cimalla, J. Pezoldt, R. Goldhahn, S. Kaiser, and W. Gebhardt, *Applied Physics Letters* **76**, 1686 (2000).
- 54 F. Schulze, A. Dadgar, J. Bläsing, and A. Krost, *Journal of Crystal Growth* **272**, 496 (2004).
- 55 V. Lebedev, J. Jinschek, U. Kaiser, B. Schroter, W. Richter, and J. Krausslich, *Applied Physics Letters* **76**, 2029 (2000).
- 56 J. R. Gong, M. F. Yeh, and C. L. Wang, *Journal of Crystal Growth* **247**, 261 (2003).
- 57 H. P. D. Schenk, E. Frayssinet, A. Bayard, D. Rondi, Y. Cordier, and M. Kennard, *Journal of Crystal Growth* **314**, 85 (2011).
- 58 F. Schulze, A. Dadgar, J. Blasing, and A. Krost, *Applied Physics Letters* **84**, 4747 (2004).
- 59 J. Wan, R. Venugopal, M. R. Melloch, H. M. Liaw, and W. J. Rummel, *Applied Physics Letters* **79**, 1459 (2001).
- 60 L. S. Chuah, Z. Hassan, S. S. Ng, and H. Hassan, *Journal of Nondestructive Evaluation* **28**, 125 (2009).
- 61 Y. Cordier, J. C. Moreno, N. Baron, E. Frayssinet, J. M. Chauveau, M. Nemoz, S. Chenot, B. Damilano, and F. Semond, *Journal of Crystal Growth* **312**, 2683 (2010).
- 62 A. Dadgar, J. Blasing, A. Diez, A. Alam, M. Heuken, and A. Krost, *Japanese Journal of Applied Physics Part 2-Letters* **39**, L1183 (2000).
- 63 F. Reiher, A. Dadgar, J. Blasing, M. Wieneke, and A. Krost, *Journal of Crystal Growth* **312**, 180 (2010).

- 64 F. Schulze, A. Dadgar, J. Blasing, A. Diez, and A. Krost, *Applied Physics Letters* **88** (2006).
- 65 A. Dadgar, M. Poschenrieder, J. Blasing, K. Fehse, A. Diez, and A. Krost, *Applied Physics Letters* **80**, 3670 (2002).
- 66 P. Chen, R. Zhang, Z. M. Zhao, D. J. Xi, B. Shen, Z. Z. Chen, Y. G. Zhou, S. Y. Xie, W. F. Lu, and Y. D. Zheng, *Journal of Crystal Growth* **225**, 150 (2001).
- 67 E. Feltin, B. Beaumont, M. Laugt, P. De Mierry, P. Vennegues, M. Leroux, and P. Gibart, *Physica Status Solidi a-Applied Research* **188**, 531 (2001).
- 68 S. Joblot, E. Feltin, E. Beraudo, P. Vennegues, M. Leroux, F. Omnes, M. Laugt, and Y. Cordier, *Journal of Crystal Growth* **280**, 44 (2005).
- 69 D. M. Follstaedt, J. Han, P. Provencio, and J. G. Fleming, *Mrs Internet Journal of Nitride Semiconductor Research* **4**, art. no. (1999).
- 70 J. Y. Huang, Z. Z. Ye, L. Wang, J. Yuan, B. H. Zhao, and H. M. Lu, *Solid-State Electronics* **46**, 1231 (2002).
- 71 T. Lei, M. Fanciulli, R. J. Molnar, T. D. Moustakas, R. J. Graham, and J. Scanlon, *Applied Physics Letters* **59**, 944 (1991).
- 72 T. Lei, T. D. Moustakas, R. J. Graham, Y. He, and S. J. Berkowitz, *Journal of Applied Physics* **71**, 4933 (1992).
- 73 M. A. Mastro, O. M. Kryliouk, and T. J. Anderson, *Materials Science and Engineering B-Solid State Materials for Advanced Technology* **127**, 91 (2006).
- 74 Y. E. Romanyuk, D. Kreier, Y. Cui, K. M. Yu, J. W. Ager, and S. R. Leone, *Thin Solid Films* **517**, 6512 (2009).
- 75 T. N. Bhat, M. K. Rajpalke, B. Roul, M. Kumar, and S. B. Krupanidhi, *Journal of Applied Physics* **110**, 6 (2011).
- 76 R. Grun, *Acta Crystallographica Section B* **35**, 800 (1979).
- 77 R. F. Davis, T. Gehrke, K. J. Linthicum, E. Preble, P. Rajagopal, C. Ronning, C. Zorman, and M. Mehregany, *Journal of Crystal Growth* **231**, 335 (2001).
- 78 R. F. Davis, T. Gehrke, K. J. Linthicum, T. S. Zheleva, P. Rajagopal, C. A. Zorman, and M. Mehregany, *Zeitschrift Fur Metallkunde* **92**, 163 (2001).
- 79 R. F. Davis, T. Gehrke, K. J. Linthicum, T. S. Zheleva, E. A. Preble, P. Rajagopal, C. A. Zorman, and M. Mehregany, *Journal of Crystal Growth* **225**, 134 (2001).

- 80 R. F. Davis, T. Gehrke, K. J. Linthicum, P. Rajagopal, A. M. Roskowski, T. Zheleva, E. A. Preble, C. A. Zorman, M. Mehregany, U. Schwarz, J. Schuck, and R. Grober, *Mrs Internet Journal of Nitride Semiconductor Research* **6**, 1 (2001).
- 81 T. Gehrke, K. J. Linthicum, E. Preble, P. Rajagopal, C. Ronning, C. Zorman, M. Mehregany, and R. F. Davis, *Journal of Electronic Materials* **29**, 306 (2000).
- 82 K. Linthicum, T. Gehrke, D. Thomson, E. Carlson, P. Rajagopal, T. Smith, D. Batchelor, and R. Davis, *Applied Physics Letters* **75**, 196 (1999).
- 83 T. Zheleva, S. Smith, D. Thomson, K. Linthicum, P. Rajagopal, and R. Davis, *Journal of Electronic Materials* **28**, L5 (1999).
- 84 N. P. Kobayashi, J. T. Kobayashi, X. G. Zhang, P. D. Dapkus, and D. H. Rich, *Applied Physics Letters* **74**, 2836 (1999).
- 85 P. Kung, D. Walker, N. Hamilton, J. Diaz, and M. Razeghi, *Applied Physics Letters* **74**, 570 (1999).
- 86 K. Y. Zang, Y. D. Wang, S. J. Chua, and L. S. Wang, *Applied Physics Letters* **87** (2005).
- 87 E. Suhir, *Journal of Applied Mechanics-Transactions of the Asme* **53**, 657 (1986).
- 88 S. Luryi and E. Suhir, *Applied Physics Letters* **49**, 140 (1986).
- 89 D. Zubia and S. D. Hersee, *Journal of Applied Physics* **85**, 6492 (1999).
- 90 S. D. Hersee, D. Zubia, X. Y. Sun, R. Bommena, M. Fairchild, S. Zhang, D. Burckel, A. Frauenglass, and S. R. J. Brueck, *IEEE Journal of Quantum Electronics* **38**, 1017 (2002).
- 91 D. Zubia, S. H. Zaidi, S. R. J. Brueck, and S. D. Hersee, *Applied Physics Letters* **76**, 858 (2000).
- 92 D. Zubia, S. H. Zaidi, S. D. Hersee, and S. R. J. Brueck, *Journal of Vacuum Science & Technology B* **18**, 3514 (2000).
- 93 X. Wang, G. Yu, C. Lin, M. Cao, H. Gong, M. Qi, and A. Li, *Electrochemical and Solid-State Letters* **11**, H273 (2008).
- 94 X. Y. Sun, R. Bommena, D. Burckel, A. Frauenglass, M. N. Fairchild, S. R. J. Brueck, G. A. Garrett, M. Wraback, and S. D. Hersee, *Journal of Applied Physics* **95**, 1450 (2004).
- 95 J. Liang, S. K. Hong, N. Kouklin, R. Beresford, and J. M. Xu, *Applied Physics Letters* **83**, 1752 (2003).

- 96 K. Y. Zang, Y. D. Wang, L. S. Wang, S. Tripathy, S. J. Chua, and C. V. Thompson, *Thin Solid Films* **515**, 4505 (2007).
- 97 L. S. Wang, S. Tripathy, B. Z. Wang, and S. J. Chua, *Applied Surface Science* **253**, 214 (2006).
- 98 A. Strittmatter, A. Krost, V. Turck, M. Strassburg, D. Bimberg, J. Blasing, T. Hempel, J. Christen, B. Neubauer, D. Gerthsen, T. Christmann, and B. K. Meyer, *Materials Science and Engineering B-Solid State Materials for Advanced Technology* **59**, 29 (1999).
- 99 F. Hamdani, M. Yeadon, D. J. Smith, H. Tang, W. Kim, A. Salvador, A. E. Botchkarev, J. M. Gibson, A. Y. Polyakov, M. Skowronski, and H. Morkoc, *Journal of Applied Physics* **83**, 983 (1998).
- 100 X. H. Luo, R. M. Wang, X. P. Zhang, H. Z. Zhang, D. P. Yu, and M. C. Luo, *Micron* **35**, 475 (2004).
- 101 D. C. Park and S. Fujita, *Physica Status Solidi a-Applied Research* **176**, 579 (1999).
- 102 R. F. Xiao, X. W. Sun, Z. F. Li, N. Cue, H. S. Kwok, Q. Z. Liu, and S. S. Lau, *Journal of Vacuum Science & Technology a-Vacuum Surfaces and Films* **15**, 2207 (1997).
- 103 K. Black, A. C. Jones, P. R. Chalker, J. M. Gaskell, R. T. Murray, T. B. Joyce, and S. A. Rushworth, *Journal of Crystal Growth* **310**, 1010 (2008).
- 104 V. A. Ferreira and H. W. Leite Alves, *Journal of Crystal Growth* **310**, 3973 (2008).
- 105 S. Nishimura and K. Terashima, *Materials Science and Engineering B-Solid State Materials for Advanced Technology* **75**, 207 (2000).
- 106 S. Nishimura and K. Terashima, *Materials Science and Engineering B-Solid State Materials for Advanced Technology* **82**, 25 (2001).
- 107 S. Nishimura, S. Matsumoto, and K. Terashima, *Optical Materials* **19**, 223 (2002).
- 108 S. Nishimura, H. Hanamoto, K. Terashima, and S. Matsumoto, *Materials Science and Engineering B-Solid State Materials for Advanced Technology* **93**, 135 (2002).
- 109 K. S. A. Butcher and T. L. Tansley, *Superlattices and Microstructures* **38**, 1 (2005).
- 110 B. Onderka, J. Unland, and R. Schmid-Fetzer, *Journal of Materials Research* **17**, 3065 (2002).
- 111 O. Kryliouk, H. J. Park, Y. S. Won, T. Anderson, A. Davydov, I. Levin, J. H. Kim, and J. A. Freitas, *Nanotechnology* **18** (2007).

- 112 H. J. Park, O. Kryliouk, T. Anderson, D. Khokhlov, and T. Burbaev, *Physica E-Low-Dimensional Systems & Nanostructures* **37**, 142 (2007).
- 113 I. Shalish, G. Seryogin, W. Yi, J. M. Bao, M. A. Zimmler, E. Likovich, D. C. Bell, F. Capasso, and V. Narayanamurti, *Nanoscale Research Letters* **4**, 532 (2009).
- 114 B. S. Simpkins, A. D. Kansal, and P. E. Pehrsson, *Crystal Growth & Design* **10**, 3887 (2010).
- 115 Y. H. Kim, W. S. Yun, H. Ruh, C. S. Kim, J. W. Kim, Y. H. Shin, M. D. Kim, and J. E. Oh, *Journal of Crystal Growth* **312**, 662 (2010).
- 116 C. Y. Chang, G. C. Chi, W. M. Wang, L. C. Chen, K. H. Chen, F. Ren, and S. J. Pearton, *Journal of Electronic Materials* **35**, 738 (2006).
- 117 C. K. Chao, J. I. Chyi, C. N. Hsiao, C. C. Kei, S. Y. Kuo, H. S. Chang, and T. M. Hsu, *Applied Physics Letters* **88** (2006).
- 118 M. C. Johnson, C. J. Lee, E. D. Bourret-Courchesne, S. L. Konsek, S. Aloni, W. Q. Han, and A. Zettl, *Applied Physics Letters* **85**, 5670 (2004).
- 119 J. Zhang, B. L. Xu, F. H. Jiang, Y. D. Yang, and J. P. Li, *Physics Letters A* **337**, 121 (2005).
- 120 C. H. Liang, L. C. Chen, J. S. Hwang, K. H. Chen, Y. T. Hung, and Y. F. Chen, *Applied Physics Letters* **81**, 22 (2002).
- 121 J. Zhang, L. Zhang, X. S. Peng, and X. F. Wang, *Journal of Materials Chemistry* **12**, 802 (2002).
- 122 S. N. Mohammad, *Journal of Applied Physics* **106**, 11 (2009).
- 123 T. Kuykendall, P. J. Pauzauskie, Y. F. Zhang, J. Goldberger, D. Sirbuly, J. Denlinger, and P. D. Yang, *Nature Materials* **3**, 524 (2004).
- 124 G. W. Xu, Z. Z. Li, J. Baca, and J. D. Wu, *Nanoscale Research Letters* **5**, 7 (2010).
- 125 H. J. Park, Thesis, University of Florida, 2006.
- 126 J. L. Mangum, Thesis, University of Florida, 2007.
- 127 S. W. Kang, Thesis, University of Florida, 2004.
- 128 S. A. Kukushkin, *Reviews on advanced materials science* **17**, 1 (2008).
- 129 L. Liu and J. H. Edgar, *Materials Science and Engineering: R: Reports* **37**, 61 (2002).

- 130 J. A. Venables, G. D. T. Spiller, and M. Hanbucken, Reports on Progress in Physics **47**, 399 (1984).
- 131 Y. S. Won, Y. S. Kim, O. Kryliouk, and T. J. Anderson, Journal of Crystal Growth **310**, 3735 (2008).
- 132 S. Vaddiraju, A. Mohite, A. Chin, M. Meyyappan, G. Sumanasekera, B. W. Alphenaar, and M. K. Sunkara, Nano Letters **5**, 1625 (2005).
- 133 A. Y. Timoshkin, H. F. Bettinger, and H. F. Schaefer, Inorganic Chemistry **41**, 738 (2002).
- 134 E. I. Givargizov, *Oriented Crystallization on Amorphous Substrates*, Vol. 1 (Plenum Press, New York, 1991).
- 135 B. Maleyre, S. Ruffenach, O. Briot, B. Gil, and A. Van der Lee, Superlattices and Microstructures **36**, 517 (2004).
- 136 C. Goyhenex, H. Bulou, J. P. Deville, and G. Trégia, Applied Surface Science **177**, 238 (2001).
- 137 A. O. Ajagunna, A. Adikimenakis, E. Iliopoulos, K. Tsagaraki, M. Androulidaki, and A. Georgakilas, Journal of Crystal Growth **311**, 2058 (2009).
- 138 S. D. Hersee, X. Y. Sun, and X. Wang, Nano Letters **6**, 1808 (2006).
- 139 N. Wang, Y. Cai, and R. Q. Zhang, Materials Science & Engineering R-Reports **60**, 1 (2008).
- 140 I. N. Stranski and V. L. Krastanow, Akademie der Wissenschaften und Literatur Mainz, Mathematisch-Naturwissenschaftliche Klasse IIb **146**, 797 (1939).
- 141 D. J. Eaglesham and M. Cerullo, Physical Review Letters **64**, 1943 (1990).
- 142 B. Elman, E. S. Koteles, P. Melman, C. Jagannath, J. Lee, and D. Dugger, Applied Physics Letters **55**, 1659 (1989).
- 143 J. H. Vandermerwe, Discussions of the Faraday Society, 201 (1949).
- 144 J. H. Vandermerwe, Proceedings of the Physical Society of London Section A **63**, 616 (1950).
- 145 J. H. Vandermerwe, Journal of Applied Physics **34**, 117 (1963).
- 146 J. H. Vandermerwe, Journal of Applied Physics **34**, 123 (1963).
- 147 J. W. Matthews, Journal of Vacuum Science & Technology **12**, 126 (1975).

- 148 J. W. Matthews, D. C. Jackson, and A. Chambers, *Thin Solid Films* **26**, 129 (1975).
- 149 E. Ertekin, P. A. Greaney, D. C. Chrzan, and T. D. Sands, *Journal of Applied Physics* **97** (2005).
- 150 M. A. Slawinski, *Waves and rays in elastic continua*, Vol. 1, 2 ed. (World Scientific Publishing Company, 2007).
- 151 S. Raychaudhuri and E. T. Yu, *Journal of Vacuum Science & Technology B* **24**, 2053 (2006).
- 152 L. C. Chuang, M. Moewe, C. Chase, N. P. Kobayashi, C. Chang-Hasnain, and S. Crankshaw, *Applied Physics Letters* **90**, 3 (2007).
- 153 J. P. Hirth and J. Lothe, *Theory of dislocations* (McGraw-Hill Book Company, New York, 1968).
- 154 M. K. a. V. C. a. A. T. a. H. Riechert, *Nanotechnology* **21**, 245705 (2010).
- 155 Y. H. Kim, H. J. Park, K. Kim, C. S. Kim, W. S. Yun, J. W. Lee, and M. D. Kim, *Applied Physics Letters* **95** (2009).
- 156 R. F. Xiang, Y. Y. Fang, J. N. Dai, L. Zhang, C. Y. Su, Z. H. Wu, C. H. Yu, H. Xiong, C. Q. Chen, and Y. Hao, *Journal of Alloys and Compounds* **509**, 2227 (2011).
- 157 A. Yamamoto, Y. Hamano, T. Tanikawa, B. K. Ghosh, and A. Hashimoto, *physica status solidi (c)* **0**, 2826 (2003).
- 158 F. R. Hu, K. Ochi, Y. Zhao, B. S. Choi, and K. Hane, *Journal of Crystal Growth* **294**, 197 (2006).
- 159 M. A. Mastro, Thesis, University of Florida, 2001.
- 160 M. D. Reed, Thesis, University of Florida, 2002.
- 161 J. M. Zuo and J. C. Mabon, in *Microsc Microanal; Vol. 10 (Suppl 2)* (2004).
- 162 M. Law, J. Goldberger, and P. D. Yang, *Annual Review of Materials Research* **34**, 83 (2004).
- 163 G. Seryogin, I. Shalish, W. Moberlychan, and V. Narayanamurti, *Nanotechnology* **16**, 2342 (2005).
- 164 M. Zervos and A. Othonos, *Journal of Crystal Growth* **312**, 2631 (2010).
- 165 T. Yanagihara, *Japanese Journal of Applied Physics Part 1-Regular Papers Short Notes & Review Papers* **21**, 1554 (1982).

- 166 M. K. Zayed and H. E. Elsayed-Ali, *Thin Solid Films* **489**, 42 (2005).
- 167 J. E. Northrup and J. Neugebauer, *Physical Review B* **60**, R8473 (1999).
- 168 C. Xue, Y. Wu, H. Zhuang, D. Tian, Y. a. Liu, X. Zhang, Y. Ai, L. Sun, and F. Wang, *Physica E: Low-dimensional Systems and Nanostructures* **30**, 179 (2005).
- 169 Y. Ai, C. Xue, C. Sun, L. Sun, H. Zhuang, F. Wang, H. Li, and J. Chen, *Materials Letters* **61**, 2833 (2007).
- 170 W. Han, S. Fan, Q. Li, and Y. Hu, *Science* **277**, 1287 (1997).
- 171 H. Y. Peng, X. T. Zhou, N. Wang, Y. F. Zheng, L. S. Liao, W. S. Shi, C. S. Lee, and S. T. Lee, *Chemical Physics Letters* **327**, 263 (2000).
- 172 P. Sahoo, J. Basu, S. Dhara, H. Fang, C.-P. Liu, T. Ravindran, S. Dash, and A. Tyagi, *Journal of Materials Science* **47**, 3447 (2012).
- 173 B. S. Simpkins, L. M. Ericson, R. M. Stroud, K. A. Pettigrew, and P. E. Pehrsson, *Journal of Crystal Growth* **290**, 115 (2006).
- 174 X. Sun and Y. Li, *Angewandte Chemie International Edition* **43**, 3827 (2004).

BIOGRAPHICAL SKETCH

Vaibhav Chaudhari was born in Delhi, India. He received his Bachelor of Chemical Engineering degree (B.Chem.Engg.) in July 2004 from Mumbai University Institute of Chemical Technology. After B.Chem.Engg., he joined University of Toledo, Ohio for Master of Science in Chemical Engineering in the Fall of 2004. At Toledo, he worked under guidance of Dr. Dong-Shik Kim towards his M.S. degree. His M.S. thesis work involved use of genetically modified bacteria for production of ethanol biofuel from different bio-wastes. He graduated from University of Toledo in summer 2004. Right after M.S. degree, he joined Ph.D. program at the University of Florida in August 2006. He joined the electronic materials processing group (EMPG) to work under guidance of Dr. Tim Anderson. His work at EMPG involved studying growth of gallium nitride and indium nitride on silicon substrates using merged metal organic hydride vapor phase epitaxy.